Assessment of seismic displacements of existing landslides through numerical modelling and simplified methods

Mara Mita

THÈSE DE DOCTORAT

Université Gustave Eiffel

PARIS EST SUP

« Assessment of seismic displacements of existing landslides through numerical modelling and simplified methods »

Thèse de doctorat de l'Université Gustave Eiffel

École doctorale n° 531, SIE – Sciences, Ingénierie et Environnement
Doctorat en Géotechnique

Thèse préparée dans l'unité de recherche **GERS/SRO**
sous la direction de **Luis-Fabian BONILLA HIDALGO**, Dr.,
la co-direction de **Luca LENTI**, Dr.,
l'encadrement de **Céline BOURDEAU-LOMBARDI**, CR,
et le co-encadrement de **Salvatore MARTINO**, MCF.

Thèse soutenue à l'Université Gustave Eiffel, le 18 Décembre 2023, par

Mara MITA

Composition du jury

Lisa BORGATTI, Dr., Univ. Bologne	Rapportrice
Haris SAROGLOU, MCF, NTUA	Rapporteur
Céline GÉLIS, Ingénieur-Chercheur, IRSN	Examinatrice
Hans-Balder HAVENITH, MCF, Univ. Liège	Examinateur
Etienne BERTRAND, Dr., Univ. G. Eiffel	Examinateur
Luis-Fabian BONILLA HIDALGO, Dr., Univ. G. Eiffel	Directeur de thèse
Luca LENTI, Dr., CEREMA	Co-directeur de thèse
Céline BOURDEAU-LOMBARDI, CR, Univ. G. Eiffel	Encadrante
Salvatore MARTINO, MCF, La Sapienza, Univ. Rome	Invité

GERS/SRO: Département GERS - Géotechnique, Environnement, Risques Naturels et Sciences de la Terre/Laboratoire SRO - Sols, Roches et Ouvrages Géotechnique

Abstract

Landslides are common secondary effects related to earthquakes which can be responsible for greater damages than the ground shaking alone. Predicting these phenomena is therefore essential for risk management in seismic regions. Nowadays, landslides permanent co-seismic displacements are assessed by the traditional « rigid-sliding block » method proposed by Newmark (1965). Despite its limitations, this method has two advantages: i) relatively short computation times, ii) compatibility with GIS software for regional-scale analyses. Alternatively, more complex numerical analyses can be performed to simulate seismic waves propagation into slopes and related effects. However, due to their longer computation times, their use is usually limited to slope-scale analyses. This study aims at better understanding in which conditions (i.e. combinations of introduced relevant parameters), analytical and numerical methods predict different landslides earthquake-induced displacements. At this regard, 216 2D landslide prototypes were designed by combining geometrical and geotechnical parameters inferred by statistical analysis on data collected by literature review. Landslide prototypes were forced by 17 signals with constant Arias Intensity (AI $\sim$ 0.1 m/s) and variable mean period. Results allowed defining a preliminary Random Forest model to predict *a priori*, the expected difference between displacements by the two methods. Analysis of results allowed: i) identifying parameters affecting displacement variation according to the two methods, ii) concluding that in here considered AI level, computed displacements differences are negligible in most of the cases.

Key words: Earthquake-induced landslides, numerical analyses, Newmark (1965)'s method, Random Forest predictive model.

Résumé

Les glissements de terrain sismo-induits sont des effets secondaires fréquents des séismes qui peuvent provoquer des dommages plus importants que les séismes eux-mêmes. Prévoir ces phénomènes est donc essentiel pour la gestion des risques dans les régions sismiques. Les déplacements co-sismiques sont généralement évalués par la méthode « bloc rigide » de Newmark (1965). Malgré ses limites, cette méthode a deux avantages: i) des temps de calcul relativement courts, ii) une compatibilité avec les logiciels SIG pour des analyses à l'échelle régionale. Les modélisations numériques complexes permettent quant à elles de simuler la propagation des ondes sismiques dans les versants et les effets associés. Cependant, elles sont caractérisées par des temps de calcul longs, ce qui limite leur utilisation à l'échelle des versants. L'objectif de cette étude est de mieux comprendre dans quel cas les méthodes analytiques et numériques prédisent des valeurs de déplacements différentes. 216 prototypes de glissements de terrain ont été définis en 2D en combinant des paramètres géométriques et géotechniques déduits de la littérature. Ces modèles ont été soumis à 17 signaux sismiques

d'Intensité Arias constante (IA~ 0,1 m/s) et de période moyenne variable. Les résultats ont permis de définir un modèle « Random Forest » préliminaire pour prédire *a priori* la différence entre les valeurs de déplacements des deux méthodes. Les résultats ont ainsi permis : i) d'identifier les paramètres qui contrôlent les déplacements dans les deux méthodes, ii) de conclure que les différences entre les valeurs de déplacements sont négligeables dans la plupart des cas pour cette valeur de IA.

Mots clés: Glissements de terrain induits par des séismes, modélisation numérique, méthode de Newmark (1965), modèle « Random Forest ».

Acknowledgments

I would like to express my deepest gratitude to my mentors: Salvatore Martino, who has followed me since my Master's Degree; Céline Bourdeau-Lombardi, and Luca Lenti. Their invaluable guidance has been fundamental in completing this doctoral thesis. In particular, I would like to offer a special thanks to Céline Bourdeau-Lombardi for her support and understanding throughout the past three years.

My thanks also go out to Luis Fabian Bonilla Hidalgo for his contribution as the director of this thesis and to Leonardo Giannini and Carlo Esposito of the University of Rome « La Sapienza » for their collaboration in developing the Random Forest model integrated into this thesis.

Finally, I would like to express my thanks to the individuals who have accompanied and supported me during this journey, including my colleagues, friends, and family.

INDEX

Chapter 1: Introduction

1.1 Earthquake-induced landslides in risk management perspective

Landslides are generally considered as common secondary effects (i.e., ground-cracks, liquefactions and superficial faultings) induced by earthquakes. A demonstration of the frequency of these phenomena is provided by the Italian Catalogue of Earthquake-Induced Ground Failures (CEDIT, Martino et al., 2014), which reports that landslides are the most frequent secondary effects associated to seismic events in Italy in the period between 1000 AD and the present time. In this perspective, landslides triggered by earthquakes can be regarded as the result of a « domino-effect » sequence of events in which an independent triggering event (i.e., earthquake) is responsible for their re-/activation (Martino, 2017). The just described sequence of events can become more complex if landslides trigger in turn other hazard events. At this regard, an example is provided by the Scilla rock avalanche (Italy, Calabria), detached from the Monte Pacì coastal slope on 6th February 1783 triggered by the « Terremoto delle Calabrie » seismic sequence (Bozzano et al., 2011a). This landslide is sadly known since it induced a tsunami wave responsible for more than 1500 casualties (Bozzano et al., 2011a). In this perspective, seismic hazard predictions should be considered more properly as « multi-hazard » predictions. The events that define the multi-hazard can be concatenated (such as the sequence earthquake-landslides or earthquake-landslide-tsunami) or independent. The latter case may result when a given event predisposes to the occurrence of another one. In this regard, an example could be rainfall preceding earthquakes that can predispose to the re-/activation of landslides. Such sequence of events is documented in literature by the exceptional spatial distribution of earthquake-induced landslides in Montecilfone (Italy) after the M_w 5.1 seismic event that hit the site on 16th August 2018 (Martino et al., 2022). Indeed, the area was subjected to intense rainfall before the earthquake that were responsible for a general increasing of soil saturation.

The topic of multi-hazard is particularly stressed since earthquake-induced landslides can significantly impact on human activities. For this reason, identifying hazard sources becomes crucial for seismic risk management. Bird & Bommer (2004) report that in mountainous regions, where the susceptibility to mass movements is high, losses caused by earthquake-induced landslides can overcome those produced by the ground shaking itself. Indeed, these phenomena are well known to be responsible for destruction of hillside villages, failures of roads and river embankments (Bird & Bommer, 2004).

Beyond economic consequences, loss of life due to landslides is not uncommon. According to Petley (2012), between 2004 and 2010, non-seismically-induced landslides were responsible for 32 322 fatalities at worldwide scale (= 2620 fatal landslides in 7 years). As it regards fatal earthquake-induced landslides, recent estimations were provided by Seal et al. (2022). The authors collected data on landslides related to 281 worldwide historical earthquakes occurred between 1772-2021. They report that out of these seismic events, ~58% of them (i.e., 162 cases), triggered landslides that resulted in fatalities. According to Keefer (1984) seismically-

induced landslide types producing the greatest loss of human lives are rock avalanches, rapid soil flows and rock falls. Rock avalanches and rapid soil flows are relatively uncommon during earthquakes; nevertheless, they can travel for several kilometres at high velocities, also on low-inclined slopes, hitting villages even far from the landslide source (Keefer, 1984). In contrast, according to Keefer (1984)'s inventory, the most abundant landslides type occurring during seismic events are rock falls, as they can involve all slopes with inclination greater than 40°. However, in this case, the risk area is limited to the distance boulders can reach by rolling or bounding (Keefer, 1984). To reduce the number of casualties, appropriate land use planning of the territory should be implemented to prevent the construction of buildings in highly susceptible areas (Bird & Bommer, 2004). However, these problems are still particularly enhanced at the periphery of cities in developing countries, where the demand for land is high and the control is poor (Bird & Bommer, 2004). Land use planning requires site-specific investigations to identify susceptible areas to these phenomena. Moreover, a reliable prediction of co-/post-seismic landslides re-/activations must account for all factors (i.e., geology, topography, seismic waves properties) contributing to slope response under dynamic solicitations. For these reasons, earthquake-induced landslide hazard evaluation is a complex topic that has received great attention by the scientific community. Some main progresses about this topic are described in the following.

1.2 State of art

Understanding the conditions leading to landslides re-/activation by seismic shaking has always been a challenging topic for engineering-geologists. At this regard, identifying the relationships existing between landslides and their triggering earthquakes is fundamental to predict slope responses to future seismic events. The study by Keefer (1984) was a pioneer on that sense. To correlate earthquake magnitudes with maximum areas (i.e., the sum of the areas of the localities in which landslides clusters are documented during a seismic event) and epicentral distances (i.e., the distance between epicenter and the farthest landslide), the author collected data from 40 historical worldwide earthquakes in the period between 1811 and 1980. Findings by Keefer (1984) demonstrated that the concentrations of landslide areas and maximum epicentral distances tend to increase with magnitude. Upper-bound curves for 3 landslide typologies (i.e., disrupted landslides/falls, coherent slides, and lateral spread/flows) were defined according to the compiled database. An extension of this study was provided by Rodríguez et al. (1999) who included 36 extra worldwide earthquakes that increased the analysis time-period up to 1997. Nowadays, Keefer (1984)'s curves are recognized as an important predictive tool for earthquake-induced landslides distribution in the framework of seismic hazard evaluations. However, since Keefer (1984)' s curves are based on worldwide data, it may be more accurate to realize site-specific curves at smaller scale (i.e., regional, national) for more reliable seismic hazard predictions. Martino (2017) made a comparison between the Keefer (1984)'s curve (maximum epicentral distance vs M_w) for rock falls and rock slides and the upper-bound curve realized for rock falls and rock slides occurred in Italy in the period between 1908 and 2016 according to the CEDIT catalogue (cf. paragraph 1.1). The study revealed that landslides occurred in Italy after 2016 fit preferentially the curve obtained from the CEDIT. This result demonstrates that national historical

catalogues can contribute to refine upper-bound curves and that historical datasets can well operate in a prevision perspective (Martino, 2017).

However, independently from the scale of analysis, upper-bound curves are not always reliable. For instance, Rodríguez et al. (1999) identified outliers that occurred at greater distances than those predicted by such kind of curves. The authors explained these outliers by the presence of highly susceptible slopes in the investigated areas. Similar observations are made by Delgado et al. (2011) using the 270 worldwide earthquakes database they created. According to Delgado et al. (2011), conditions responsible for slopes high susceptibility, for which far-field landslides occur, are determined by the presence of jointed rock-masses, marls and/or clayey soils, alluvial and colluvial sediments, volcanic soils, and residual soils in slopes. In addition, antecedent rainfall preceding the seismic event could lead to far-field activations due to pore pressures built up during the ground shaking.

Finally, site effects (i.e., effects due to geology and topography as well as impedance contrasts causing local modifications of ground shaking amplitude and duration, cf. paragraph 1.2.1) represent another important factor responsible for an increase in slopes susceptibility under dynamic solicitations (Delgado et al., 2011).

At this regard, it is worth mentioning two case studies from Italy:

- the Salcito landslide (Italy, Molise) re-actived by the M_l 5.4 Molise earthquake on 31st October 2002, 30 km away from the epicenter (Bozzano et al., 2008)
- the Cerda landslide (Italy, Sicily) re-actived by the M_s 5.4 Palermo earthquake on 6th September 2002, 50 km way from the epicenter (Bozzano et al., 2011b)

The two landslides took place in similar geological contexts. According to Bozzano et al. (2008) and Bozzano et al. (2011b), the far-field activations of the Salcito and the Cerda landslides could be explained by a « self-excitation » process consisting in an amplification of seismic waves caused by the presence of soft materials (i.e., the landslide mass) lying over a deeper and stiffer layer (i.e., the bedrock) resulting in a high seismic impedance contrast between them.

In agreement with this interpretation, the landslide seismic response could be comparable to that of a 2D basin (Bard and Bouchon, 1985). For this reason, second generation landslides (i.e., existing landslides) would be more prone to be self re-activated, as their softer mass is responsible for wave trapping and ground-motion amplification (Bozzano et al., 2011b).

The topic of the impact of site-specific conditions on slope responses under dynamic inputs is however very complex since it must account for several factors. In this regard, it is worth specifying that the definition « slope/landslide response » not only includes the possibility of re-/activation of the landslide but it also refers to intensity of displacements that can occur when the slope failure takes place. Quantifying these displacements has been the main goal of this research project.

1.2.1 Local seismic response inferring earthquake-induced landslides

Local seismic response of slopes refers to changes of the ground-motion (in terms of amplitude and duration) if compared with sites located on bedrock, due to the combination of the following features:

- properties of seismic inputs
- geological setting
- morphological features
- geometry of the seismic waves incidence and shaking (i.e., directivity and polarisation)

A general overview of the above-listed factors is provided below.

Properties of seismic inputs: earthquakes can be regarded as external triggers exercising a destabilizing action on slopes/landslides. Consequently, it can be expected that the greater the energy, the greater the destabilizing effect (Delgado et al., 2011). Magnitude, Arias Intensity and Peak Ground Acceleration (PGA) are seismic parameters that are generally used for seismic slope stability predictions (cf. paragraph 1.2.2). As previously mentioned (cf. paragraph 1.2), Keefer (1984) makes use of earthquake magnitude to predict maximum areas and maximum epicentral distances of occurrence of landslides. According to the author, a minimum magnitude between 4.0 and 5.0, basing on the landslide type, would be required to induce slope instabilities. Arias Intensity is instead used to compute expected earthquake-induced displacements of landslides (cf. paragraph 3.2.2.1). Further findings on the topic (cf. paragraph 3.7.1.2) demonstrated, however, that in addition to the above-mentioned parameters, the frequency content of the seismic solicitations must be considered for reliable predictions. Generally, in slope stability analyses, seismic input frequency content is expressed using the « mean period (T_m) » parameter. According to Rathje et al. (1998), T_m is the best simplified frequency content characterization parameter for seismic inputs, and it can be computed as (eq. 1.1):

$$T_m = \frac{\sum_i C_i^2 * (\frac{1}{f_i})}{\sum_i C_i^2} \qquad \text{[Eq.1.1]}$$

where C_i are the Fourier amplitudes of the entire accelerogram and f_i are the discrete Fourier transform frequencies between 0.25 and 20 Hz.

Geological setting: properly refers to the geological setting of the site hit by seismic shaking. Relevant features of the site that can affect the seismic response of slopes are:

- presence of soft layers over stiffer ones in the stratigraphy. Among them, the existence of a sufficient impedance contrast (i.e., the ratio between the products of shear wave velocity and density computed for the two layers, cf. paragraph 2.3.2.3, eq. 2.7) may cause ground-motion amplifications that can predispose to slope failures. If the softer layer contains an already existing landslide, a self-excitation of the landslide itself might be expected (cf. paragraph 1.2). Seismic slope analyses on first time failures and existing landslides require different approaches (Martino, 2015). For pre-existing landslides, geometries, dimensions, and material composition are already known.

Basing on such features, the interaction of landslides with incoming seismic waves can be assessed. It may be more or less effective in reactivating the landslides depending on characteristic period ratios. The use of landslide characteristic periods in comparison with input mean periods is nowadays recognized as an important tool for predicting landslide re-activations. The topic will be more deeply addressed in the following chapters (cf. paragraph 3.7.1.2) since, before that, more information about landslide geometrical parameters must be provided

- material internal fracturing: Gischig et al. (2015) demonstrated that compliant large-scale discontinuities in existing deep-seated landslides may contribute to amplify the ground-motion, predisposing to slope failures. This phenomenon may be also enhanced during the co-seismic phase, when additional internal fracturing may be generated
- hydrogeological conditions: soil saturation due to water tables or rainfall is a fundamental predisposing factor for slope instabilities since it directly controls soils effective strength. It is well known that in saturated soils subjected to ground-motion, pore water pressures may be built up; they may be drained after a time interval that depends on the material permeability (if the permeability is low the drainage phase will occur during the post-seismic phase). Until the drainage is not started, the material opposes an undrained shear strength against driving stresses that, basing on the material type, can imply a temporary increasing (over consolidated OC clays – dense sands) or decreasing (normally consolidated NC clays, loose sands) of shear strength with respect to the pre-seismic phase. At the end of the dissipation process, drained shear strength will increase for NC clays and loose sands and decrease for OC clays and dense sands because of the drainage. Consequently, most critical conditions in terms of material shear strength may occur in the pre- or post- drainage phase. Such processes are quite important because they can justify landslide activations in the post-seismic phase. This was the case of the Calitri landslide in Italy activated few hours after the end of the mainshock of the M_S 6.9 Irpinia earthquake (Martino & Scarascia Mugnozza, 2005). Additionally to post-seismic activations, reduction of material shear strength due to pore pressure build-up can also be responsible for far-field re-/activations (cf. paragraph 1.2) or exceptional landslide spatial distribution during seismic events (cf. paragraph 1.1)
- presence of faults can affect landslide distribution during a seismic event. From a geotechnical point of view, fault zones are characterized by the presence of weak materials because of the high deformations caused by the fault movement. The presence of such kind of high-deformed materials together with the great energy released in these zones during the seismic event, may control earthquake-induced landslides clustering (Rault et al., 2019; Meunier et al., 2008). In addition, fault rupture mechanism is another important factor to be considered for interpreting/predicting the distribution of earthquake-induced landslides. Fan et al. (2019) conducted a literature review about this topic summarizing that landslides tend to concentrate along fault hanging walls in the presence of reverse and normal faults. Conversely, they are symmetrically distributed along strike-slip faults but in a narrower area (fig. 1.1)

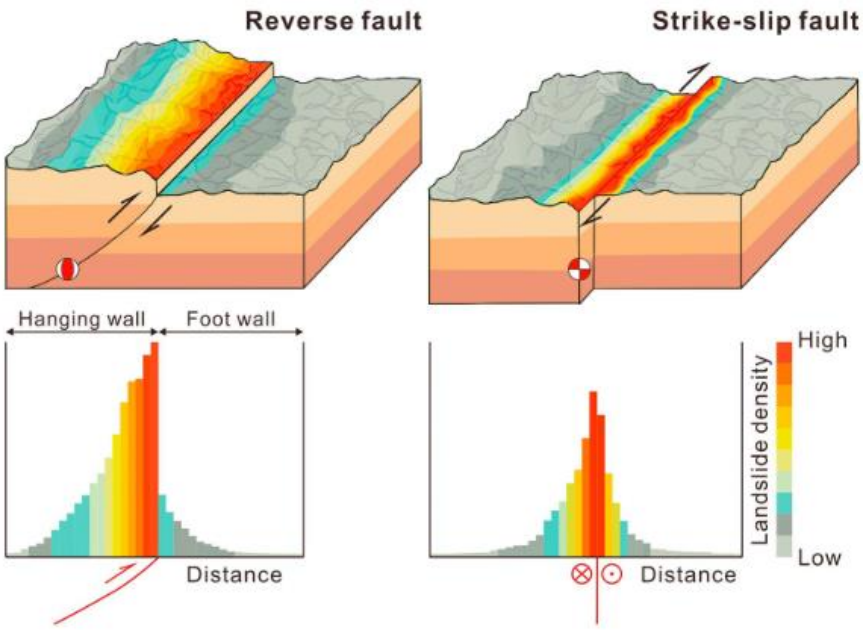

Figure 1.1: *Distribution of earthquake-induced landslides with respect to reverse and strike-slip fault (from Fan et al., 2019).*

As it regards the last feature, according to the review proposed by Fan et al. (2019), several factors may contribute to control different earthquake-induced landslide distributions basing on fault rupture mechanism:

- reverse and normal faults present longer fault plane segments close to the ground surface compared to vertical faults (i.e., strike-slip faults) due to their lower inclination. In these conditions, greater energy is released close to the ground surface, especially at the hanging wall, where landslides would concentrate (fig. 1.1)
- trapping of seismic waves at faults hanging walls in the presence of dipping faults (i.e., reverse, and normal faults). Indeed, in these cases, it would be possible to identify a « wedge » corresponding to a portion of the hanging wall included between the ground surface and the fault plane where waves are trapped (fig. 1.1). In these conditions, constructive interferences responsible for ground-motion amplification may take place. This phenomenon would predispose to an asymmetrical distribution of landslides as in figure 1.1

Case studies in which earthquake-induced landslides mainly concentrate at fault hanging walls are documented in China during the 12th May 2008 M_w 7.9 Wenchuan earthquake (Gorum et al., 2001), in Pakistan during the 8th October 2005 M_w 7.6 Northern Pakistan earthquake (Sato et al., 2007) and in Japan during the 14th June 2008 M_{JMA} 7.2 Iwate-Miyagi Nairiku earthquake (where M_{JMA} is magnitude value according to the seismic intensity scale proposed by the Japan Meteorological Agency), (Sato et al., 2007).

Another scenario that is worth considering is when earthquakes are caused by blind faults (i.e., fault plane does not propagate until the ground surface). The latter is the case of the 12th January 2010 M_w 7.0 Haiti earthquake. Gorum et al. (2013) compared co-seismic landslide inventory related to the 2010 Haiti seismic event with other earthquake-induced landslide inventories in literature (i.e., the 1999 Chi-Chi earthquake, Taiwan; the 2008 Wenchuan

earthquake, China; the 2008 Iwate-Miyagi Nairiku earthquake, Japan and the 1994 Northridge earthquake, California) and demonstrated that blind-rupture earthquakes trigger a minor number of landslides compared to surface-ruptures.

Morphological features: landscape morphological features are well-known to be responsible for amplification/de-amplification of seismic waves. More in particular, amplifications at hill tops and de-amplifications at hill toes are generally registered (Bakavoli & Haghshenas, 2010) due to peculiar reflections and refractions that develop in the presence of convex (i.e., reliefs) and concave (i.e., depressions) topographical shapes. Similarly, crest points of step-like slopes are crucial topographical points that can give rise to complex amplification patterns at their location or within short distance beyond them (Zhang et al., 2018; Bouckovalas & Papadimitriou, 2005). In some cases, topographical effects can be strongly enhanced by the presence of low-velocity layers constituted by weathered materials (Havenith et al., 2002). Amplification effects related to topography are particularly important since nowadays many cities and villages are built on hill tops (Glinsky et al., 2019). For instance, large accelerations may develop at hill crests due to the combination of local geological and topographical factors: they may be responsible for the collapse of the Hotel Dekelia that occurred during the 1999 Athens earthquake (Athanasopoulos et al., 2001). For the same reason, ground-motion amplifications caused by topography at hill crests exercise a strong influence also on earthquake-induced landslides clustering: indeed landslides often cluster at slope crests. Some examples are documented by Rault et al. (2019) in the epicentral areas of the: 17th January 1994 M_w Northridge earthquake (California), 21st September 1999 M_w 7.6 Chi-Chi earthquake (Taiwan) and 12th May 2008 M_w 7.9 Wenchuan eartquake (China). Other cases are also reported in Chile during the 21st April 2007 M_w 6.2 Aysén Fjord earthquake (Sepúlveda et al., 2010).

Geometry of the seismic waves incidence and shaking (i.e., directivity and polarisation) must be accounted for reliable landslide predictions in near-field sites where incidence angle can be different than 0° (Alfaro et al., 2012). Seismic wave incidence angles between 0° and 50° would be the cause of the activation of the first-time Lorca rockslide (Spain) during the M_w 5.1 Lorca earthquake on 11th May 2011, 10 km away from the epicenter (Alfaro et al., 2012).

1.2.2 Methods for assessing landslides seismic displacements

In engineering-geology, the proneness of slopes to failure is traditionally expressed through the « Safety Factor (SF) » parameter. This parameter represents the ratio between the maximum shear strength available to the opposing material and the shear stresses effectively acting (including those related to eventual external triggers such as dynamic solicitations, rainfall) along a defined sliding surface (cf. paragraph 3.1). Following this definition, SF values lower than 1 indicate that slopes are unstable in the considered conditions.

In seismic areas, evaluating if slopes are prone to earthquake-induced landslides is not sufficient for reliable seismic hazard predictions. Indeed, additionally to SF, earthquake-induced displacements of landslides must be assessed. At this aim, the rigid-block method by Newmark (1965) is widely used (cf. paragraph 3.2.2). As the name suggests, in Newmark (1965)'s method, the landslide mass is considered as a rigid block with an elastic-perfectly

plastic behaviour (cf. paragraph 3.2.2). Newmark's method is easily applicable and allows estimating a unique value of co-seismic displacement for the whole landslide mass. Data required for the application of this kind of approach include the critical acceleration of the landslide (i.e., maximum acceleration to which a landslide can be subjected before failure, cf. paragraph 3.2.1) and the time history acceleration of the earthquake. Indeed, according to Newmark's approach, landslide SF would decrease below 1 when time history acceleration overcomes landslide critical acceleration: during these moments, permanent displacements are cumulated. In this manner, the total cumulated co-seismic displacement is given by the double integration of the time history acceleration values that remain above the landslide critical acceleration.

More recently, semi-empirical equations were derived by several authors (such as: Hsieh & Lee, 2001; Jibson, 1993; Jibson, 2007; Saygili & Rathje, 2008; Ambraseys & Menu, 1998 and Romeo, 2000) to identify relationships between computed Newmark's displacements and other parameters. The latter include: i) parameters related to landslide masses (such as their critical acceleration) and ii) parameters related to seismic solicitations (such as Arias Intensity, PGA, moment magnitude and so forth).

Moreover, implementations of the original Newmark (1965)'s method were developed in GIS (Geographic Information System). The utility of such kind of tools is that they allow increasing the scale of analysis from the single slope to wider regions. That latter aspect is fundamental for risk management and land use planning over large areas.

Nevertheless, in Newmark's method some limitations can be found. Indeed, all effects related to pore pressures build-up during ground shaking (cf. paragraph 1.2.1) and/or to de-/amplifications of ground-motion (i.e., site effects, cf. paragraph 1.2.1) are not accounted for. For the latter reasons, predictions provided by the simplified Newmark's approach are not always reliable.

Beyond analytical approaches, more complex stress-strain analyses by numerical tools can be performed (cf. paragraph 3.4.1). Since the use of these softwares allows simulating the propagation of seismic waves into models reproducing slopes under investigation, site effects and pore pressure modifications can be accurately modelled. However, numerical modelling requires high expertise level as well as longer computation times compared to analytical approaches. For the latter reason, they are hardly applied at larger scales than the slope scale.

Analytical and numerical methods will be more deeply described in chapter 3. The aim here was to provide the reader with a general overview of current achievements in the framework of predictive methods for seismic displacements of landslides.

1.3 Aims and contents of the research project

The aim of this research has been to understand why and which conditions lead analytical and numerical approaches to return different predictions in terms of earthquake-induced displacements. In other words, this study aims at identifying factors leading methods commonly used for regional scale predictions (i.e., analytical methods) to under-/over-estimate displacements compared to more complex numerical methods which use is usually

limited to slope scale analyses. Indeed, either under- or over- estimated displacements, may lead to economic losses because of under- and over- dimensioning of mitigation measures to prevent damages related to the occurrence of earthquake-induced landslides.

In this regard, 216 translational and rotational 2D landslide prototypes were defined by combining geometrical and geotechnical parameters inferred by literature review (cf. chapter 2). The term « landslide prototype » as adopted here, refers to simplified slope models representative of real and more complex landslides. In this perspective, the landslide prototypes can be considered as representative of common real landslides in terms of geotechnical composition and geometrical features.

This research is mainly addressed to existing rotational and translational mass movements: indeed, in the designed landslide prototypes, a basal sliding surface is introduced. On the contrary, peculiar failure mechanisms such as falls, topples, deep-seated landslides and flows will not be treated.

The landslide prototypes were forced by 17 signals (cf. paragraph 2.6) in order to compute earthquake-induced displacements via simplified and numerical methods (cf. chapter 3). The resulting dataset contains: i) data related to geometrical and geotechnical features of the prototypes, ii) data referring to the dynamic solicitations, iii) displacements computed by the two adopted methodologies.

Finally, a random forest analysis was performed on the compiled dataset (cf. chapter 4) in order to define a predictive model for estimating *a priori*, and in case of real landslides, the expected difference in terms of predictions provided by numerical and simplified approaches.

1.4 Thesis organization

In addition to the present introductive chapter, the thesis includes 4 more chapters whose contents are shortly summarized below.

Chapter 2: 2D prototypes of landslide-involved slopes

The main focus of chapter 2 is on designing the 2D landslide prototypes used for the analysis of seismically-induced displacements. More in particular, this chapter places particular relevance on the selection of the geometrical and geotechnical parameters used for designing the landslide prototypes. The role of each parameter in terms of seismically-induced mobility of landslides is also discussed. Additionally, the chapter describes statistical analyses performed on the datasets compiled for each selected parameter. Finally, the last paragraph introduces the set of seismic inputs selected for performing displacements analyses.

Chapter 3: Computation of seismic displacements by analytical and numerical methods

Chapter 3 is further divided into two parts as in the following:

PART 1: Newmark's method-based analysis

In this first part, static safety factors for the 2D landslide prototypes are computed. Following, the main assumptions, advantages, and limitations of the Newmark (1965)'s method are discussed. Results returned by such an analysis are presented in the last paragraph.

PART 2: FDM numerical modelling

The second part focuses on seismic displacements computed by a FDM (Finite Difference Method) solution through the software FLAC (Itasca). Main functionalities of this software are also described to better identify differences, either in terms of advantages or in terms of disadvantages, between numerical and analytical methods.

Chapter 4: Machine Learning (ML) Random Forest (RF) analysis

This chapter describes the procedure of definition of the preliminary predictive model for earthquake-induced displacements of landslides by the random forest algorithm. The methodology proposed in this chapter is still at its early experimental phase; consequently, drawbacks of the obtained results are also discussed.

Chapter 5: Conclusions and future perspectives

The chapter summarizes the main findings of the research. Additionally, it discusses its limitations, advances, and future perspectives.

Chapter 2: 2D prototypes of landslide-involved slopes

This chapter outlines the procedure for deriving 2D simplified landslide prototypes, which will serve as the basis for computing earthquake-induced displacements in chapter 3. More in particular, chapter 2 discusses the outcomes of the conducted literature review, which aimed to compile sub-datasets for geometrical and geotechnical parameters of landslides. The goal was to compute their representative values at worldwide scale. Finally, seismic inputs selected for simulating the interaction between seismic waves and landslide prototypes (cf. chapter 3) are presented at the end of the chapter.

2.1 Criteria for the identification and selection of the parameters

The identification and selection of the most adapt parameters is a key point in the procedure of generation of simplified landslide prototypes. Indeed, this choice must satisfy the following conditions:

1) the selected parameters must describe the geometrical features of the slopes, the shape and the size of the landslides and the geotechnical properties of the involved materials
2) the selected parameters allow investigating relevant aspects of the seismic input – landslide interaction in terms of seismically-induced displacements; at this regard, the strategy of selection cannot neglect the identification of more than one value for each parameter to perform parametric analyses of the displacements
3) the combination of the selected parameters (cf. paragraph 2.5) returns landslide prototypes that are representative of the most common real landslides in terms of morphology, dimensions, geotechnical properties, and failure mechanism. Concerning the latter, in this research, exclusively landslides induced by the exceeding of the shear strength along defined circular (rotational slides, sensu Varnes, 1978) and planar (translational slides, *sensu* Varnes, 1978) sliding surfaces were accounted for. Therefore, types of landslides that involve peculiar failure mechanisms such as deep-seated landslides, falls, toppling, and flows were not considered

In accordance with the condition n.3, the best approach was to extract topographical and morphological parameters, along with geotechnical properties of materials, from the available literature. Then, statistical analyses were performed on the dataset defined for each considered parameter to determine their most frequent values at worldwide scale.

2.2 Parameters related to landslides geometry and morphology

In order to design 2D simplified landslide slope geometries, parameters quantifying the topography of the slopes (i.e., slope angles), the shapes (i.e., thickness (D) to length (L) ratio) and the dimensions (i.e., volume) of the landslides were extracted from existing landslide inventories and statistically analysed to compute associated mean values.

Before the above-mentioned parameters are more deeply described, it is necessary to highlight the following. The parameter « width » (i.e., the parameter describing the extension of a landslide body in the third dimension) will not be considered in this research, since exclusively 2D prototypes will be modelled. Schematizing real landslides (i.e., 3D bodies) with 2D models in which the third dimension is not defined (i.e., it is approximated to be infinite) leads to some uncertainties in the results. Indeed, the assumption of approximating three-dimensional bodies with two-dimensional ones is reliable only when real landslides are characterized by:

- homogeneity of the material in the third direction, that is the case here considered as it will be discussed later
- width dimension much larger compared to the longitudinal length. If this condition is not met, the third dimension cannot be assumed infinite. This becomes particularly important when the propagation of seismic waves is modelled, as seismic waves might be reflected and/or refracted at the landslide edges and their reciprocal interference could result in local amplification or de-amplification of ground-motion that could in turn affect the final displacements of the mass

Nonetheless, the width is indirectly considered into the parameter « volume », for which a statistical analysis was performed. Indeed, even if the final models will be 2D and not 3D, the « volume » parameter will serve as reference dimensional value for calculating landslide length (cf. paragraph 2.5.1).

A short description of the inventories used to compile sub-datasets for the selected geometrical parameters is provided in the following.

2.2.1 Description of landslide inventories used for deriving slope angle, D/L and volume

Inventories of earthquake-induced landslides are necessary to better understand the cause-effect relationship between the occurrence of a landslide and its triggering earthquake (Tanyaş et al., 2017).

Nevertheless, available inventories are generally variable in terms of data quality, completeness and format depending on the methodologies employed for their collection and on the objectives of the work (Tanyaş et al., 2017). Because of this issue, in the framework of this study, different landslide inventories were considered to collect a statistically relevant amount of data for the parameters of interest.

More in particular, the inventories selected in the framework of this study are:

1) the chronological inventory by Domej & Pluta (2018) which compiles data on 277 well-known landslides from 40 different countries. This database focuses on slide-type landslides (*sensu* Varnes, 1978) that were seismically and non-seismically activated during/since ancient geological times until nowadays (Domej et al., 2017). Each landslide is described by geometrical parameters related to the 3D and 2D shape of the rupture mass (i.e., volume and area), as well as its depth, length and width and the topography of the slope (i.e., slope angle). The aim of such an inventory was to study the variability of landslide geometrical parameters and to identify statistical correlations among them (Domej et al., 2017; 2020)
2) the database by Martino et al. (2019), which is an event-based database inventorying hundreds of landslides triggered by the mainshocks of the 2016-2017 Central Italy seismic sequence (M_w 6.5) in the Central Apennines. The landslides inventoried by Martino et al. (2019) consist mainly of rock falls and rockslides. In this case, the purpose of such a database was to study the landslide spatial distribution as a function of natural (i.e., geology, earthquake) and anthropogenic (i.e., presence of roads) factors. According to the collected data, the authors propose a frequency-density distribution of volume values that was also compared to other volume distributions from literature (i.e., Hungr et al., 1999; Wieczorek et al., 1999; RTM, 1996 cited in Dussauge-Peisser et al., 2002; Jeannin et al., 2001 cited in Dussauge-Peisser et al., 2002; Dussauge et al., 2003; Guzzetti et al., 2004; Stock et al., 2013; Barlow et al., 2015; Royánet et al., 2015; and Corominas et al., 2018)
3) the Tanyaş et al. (2019) database which aims at identifying the driving factors with respect to frequency-area distributions for earthquake-induced landslide inventories. At this regard, the authors considered data from 45 different earthquake-induced landslide inventories related to seismic events in the period 1976-2016. This database offers the opportunity to have information on the distribution of seismically-induced landslides dimensions, in terms of areas in different geological contexts. In literature, it is quite common to express the size of a landslide in terms of area instead of volume, indeed, measuring the latter is a difficult task that requires information on the surface (that can be done by digital landslide mapping) and on the sub-surface geometry of the slope failure (Guzzetti et al., 2009)

2.2.2 Volume (V)

Volume (V) is a key parameter in the definition of simplified landslide prototypes since it quantifies the three-dimensional extension of landslide bodies.

Landslide volume infers on:

1) the runout: the size of a landslide exercises a strong control on its expected runout (i.e., propagation distance from the source area) (Roback et al., 2018) and consequently on the number of anthropogenic elements at risk in the area of interest in case of occurrence of the phenomenon. For this reason, the estimation of landslide volume cannot be neglected in evaluating the associated risk and for planning

mitigation measures (Tang et al., 2018). In some cases, the runout can be enhanced by erosive processes associated to landslide movement that lead to incorporate material from the substratum, which leads to increase in a sort of domino effect: volume, mobility, and impact force of the landslide (Pudasaini & Krautblatter, 2021). These processes are, however, more peculiar of avalanches (Huggel et al., 2005) and debris flows (Hungr et al., 2005) that will not be treated in this manuscript

2) the landform evolution over time: landslides can be seen as mass-wasting phenomena able to produce landscape modifications. Depending on the size and the velocity of landslide events, landform modifications can be slow or immediate as well as negligible or highly modifying the existing landscape. This is the case for catastrophic large landslides such as: the 1980 Mount St. Helens rockslide-avalanche in U.S. (Voight et al., 1983), the 1963 Vajont rockslide in Italy (Hendron et al., 1985) or the 2001 Las Colinas landslide in El Salvador (García-Rodríguez & Malpica, 2010). As it regards long-term landscape modifications, their « slowness » can be quantified through the estimation of the erosion rates associated to landslide occurrences. Malamud et al. (2004) estimated that the erosive rates related to landslide events in seismically active subduction zones are approximately between 0.2 and 7 mm/y for landslides triggered by earthquakes with magnitudes major than 4

Despite the importance of V parameter, as already discussed (cf. paragraph 2.2.1), its quantification is so far a challenging subject. Indeed, V quantification requires the acquisition of detailed information on the shape and the location of the sliding surface at depth from geotechnical and/or geophysical field investigations that cannot be performed for regional-scale studies because of economical and time constraints.

To overcome this limit, empirical relationships were developed to estimate landslide volume (m^3) starting from measured landslide area (m^2) (Guzzetti et al., 2008,2009; Martin et al., 2002; Guthrie & Evans, 2004; Larsen & Sanchez, 1998; Simonett, 1967 and so forth). Further details on this topic will be provided in the following.

2.2.2.1 Step 1: extraction of volume values from available landslide inventories

A multiple strategy was pursued to infer a volume distribution reliable for worldwide landslides. Indeed, one of the main difficulties of this kind of work, as previously observed by Tanyaş et al. (2017), is that information such as landslide size and/or type are generally complete only in high-detail earthquake-induced landslide inventories that are generally scarce.

Therefore, to select volume values for landslide prototypes, ranges of volumes associated to available landslide inventories were used, instead of individual landslide volumes. That means quantifying at least the volume of the smallest (V_{min}) and largest (V_{max}) landslides that occurred during particular seismic events at specific sites (Martino et al., 2019; Tanyaş et al., 2019) or at worldwide scale (Domej & Pluta, 2018). In more detail, the following procedure was adopted:

1) extraction of volume values from landslide inventories when available as in the case of those by Domej & Pluta (2018) and Martino et al. (2019). In the worldwide database

by Domej & Pluta (2018), for each inventoried landslide, an equivalent volume (Domej et al., 2017) is available. These values were computed by using the equation proposed by Cruden & Varnes (1996) that approximates rupture geometries by perfect half ellipsoids. Similarly, in the event-based dataset by Martino et al. (2019) a volume value is associated to each catalogued landslide. The latter values were summarized by the authors into a frequency-density distribution plot (cf. fig.3 from Martino et al., 2019), where volume ranges from similar landslide inventories in literature (cf. paragraph 2.2.1 for full list) are reported for comparison. The latter were additionally considered for this study

2) extraction of landslide areas from the frequency-area distribution plots in figure 2 by Tanyaş et al. (2019) that report information related to 45 worldwide earthquake-induced landslide inventories. Landslide areas were converted into volume values using empirical equations expressing surface vs volume (tab.2.1). The most appropriate equation for surface to volume conversion was selected using volume ranges indicated in table 2.1

The use of both event-based and worldwide inventories has some advantages. Indeed, the worldwide catalogue by Domej & Pluta (2018) primarily includes large and well – known worldwide landslides. Consequently, relying exclusively on this inventory would have caused an under-estimation of the frequency of small-medium-size landslides, which on the contrary, occur more frequently than the large-catastrophic ones. The relative abundance of small vs large landslides is a complex topic and still widely discussed in literature. Previous studies (Guzzetti et al., 2002; Malamud et al., 2004a; Tanyaş et al., 2019) demonstrated that the frequency-area distribution of medium-large-size landslides follows a power law from which the distribution of small-size landslides diverges defining an exponential roll-over point below which the frequency of smaller area landslides decreases. In some cases, this roll-over can be explained by the incompleteness of the inventory due to erosive processes and/or mapping technique resolution (Guzzetti et al., 2002). However, when the inventory is considered as complete, the roll-over cannot be interpreted as an artifact and additional causes (such as the coalescence of small landslides) are identified as possible contributors to this effect (Guzzetti et al., 2002; Tanyaş et al., 2019).

On the other hand, the minimum/maximum landslide size in an area can be controlled by the existing geomorphological setting (Guzzetti et al., 2002), therefore, considering a worldwide inventory avoids any constraint from site-specific effects.

Table 2.1: *List of empirical equations used for converting the landslide area (A) into the landslide volume (V) from Amirhadi et al. (2016).*

EMPIRICAL EQUATION	A_l range (m^2)	REFERENCE
$V = 1.0359A^{0.880}$	$2x10^2 – 5.2x10^4$	Martin et al. (2002)
$V = 0.1549A^{1.0905}$	$7x10^2 – 0.5 x 10^5$	Guthrie and Evans (2004)
$V = 0.0844A^{1.4324}$	$1x10^1 - 1x10^9$	Guzzetti et al. (2008)
$V = 1.826A^{0.898}$	$5x10^1 - 1.6x10^4$	Larsen and Sanchez (1998)

2.2.2.2 Step 2: selection of reference values

Using values of volume from available landslide inventories (cf. paragraph 2.2.2.1), a frequency distribution was calculated to derive values representative of small, medium, and large-size landslide prototypes.

At this regard, a geometric average (eq. 2.1) was computed starting from V_{min} and V_{max} for each inventory to compute an average volume value (V_{av}).

$$V_{av} = \sqrt{(V_{min} * V_{max}} \quad \text{[Eq. 2.1]}$$

From those average values a compiled distribution is obtained (fig. 2.1).

From figure 2.1, it can be inferred that the average volume value representing the worldwide inventory by Domej & Pluta (2018) is larger (roughly one order of magnitude higher) in comparison to the average values computed using data from Martino et al. (2019) and Tanyaş et al. (2019). This result is consistent with previous observation (cf. paragraph 2.2.2.1), which emphasized the importance of considering both event-based and worldwide landslide inventories for more reliable representation of existing landslide volume classes. Using figure 2.1, it is possible to infer volume values for representing small, medium, and large-size landslide prototypes. The first selected value is the distribution mode corresponding to a volume of 1000 m^3. Therefore, the latter is the most frequent landslide volume at worldwide scale. In addition, since the mode of the distribution ($Log_{10}(V) = 3$) is very close to the mean volume ($Log_{10}(V) = 3.4$) it can be assumed that the selected value is representative of medium-size landslides according to the reference system (i.e., the collected dataset). Two additional values must be selected to represent smaller and larger landslides. According to that principle, 2 orders of magnitude of difference with respect to the medium-size value were judged sufficient and additional values of 10 m^3 and 100 000 m^3 were finally selected to design smaller and larger size landslide prototypes.

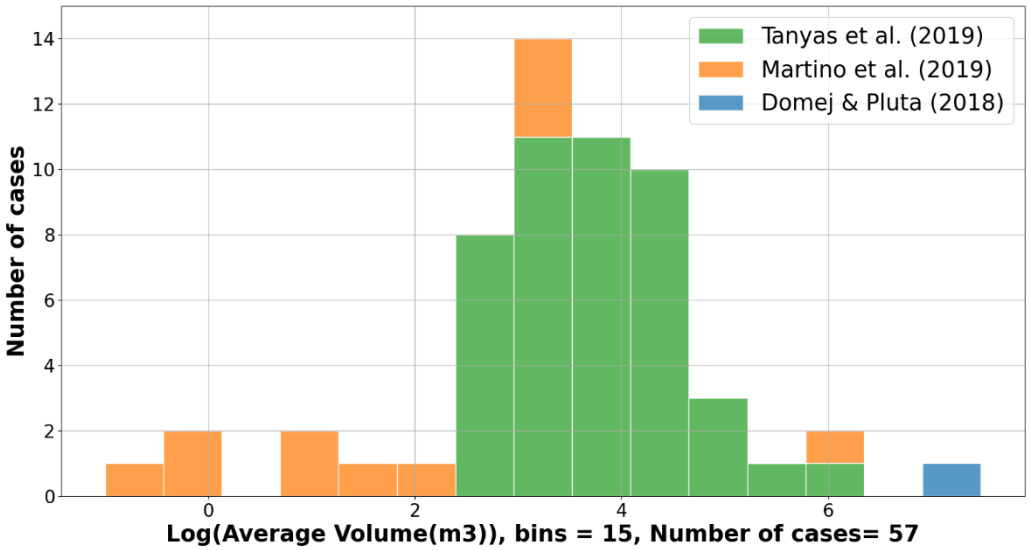

Figure 2.1: *Distribution of average volumes inferred from Domej & Pluta (2018), Martino et al. (2019) and Tanyaş et al. (2019). Statistical attributes of the distribution calculated according to the equations presented in paragraph 2.2.2: Mode: 3; Mean: 3.4; Median: 3.4; σ: 1.5; $σ^2$: 2.1.*

2.2.3 Thickness/Length ratio (D/L)

D/L (Skempton & Hutchinson, 1969) expresses the ratio between the thickness and the longitudinal length of a landslide (fig.2.2). This dimensionless parameter provides with information on the landslide morphometry independently from its size.

Beyond the ratio, if taken separately, length and thickness measure the extension of the landslide along the main direction of sliding (longitudinal length) and perpendicularly to the slope face (thickness). The topic of the importance of landslide size is crucial in the complex seismic waves – landslide body interaction and will be addressed in more detail in paragraph 3.7.1.2.

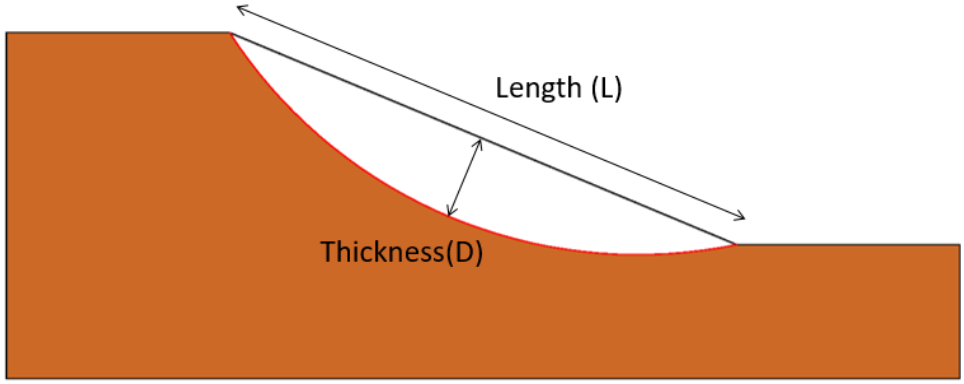

Figure 2.2: *Identification of the landslide thickness and length in a simplified landslide scheme.*

Specifically, the longitudinal length and the thickness of a landslide enter directly in the equations of its characteristic periods (T_I (Hutchinson, 1987; 1994) and T_S (Rathje & Bray, 2000)) that play an important role in explaining landslide earthquake-induced mobility.

D/L provides with information about the kinematics of slides. Indeed, according to Skempton & Hutchinson (1969), rotational slides show peculiar D/L ranging from 0.15 and 0.33. On the contrary, this ratio is lower than 0.1 for translational slides.

In accordance with the condition n.3 (cf. paragraph 2.1), and assuming the variability of D/L depending on the sliding type, two different reference values for D/L must be defined: one for rotational landslides and another one for translational landslides.

Therefore, two separated distributions were generated by extracting values from the worldwide inventory by Domej & Pluta (2018). Even if not all the landslides catalogued in this database are seismically triggered, it was chosen since:

- it collects mass movements from all over the world: that fact allows excluding any possible morphological constraint of the landslides due to particular geological/geomorphological features that can characterize specific areas
- it directly specifies the value of the parameter of interest
- there is not any evidence of differences between the morphology of seismically-induced landslides and that of non-seismically-induced landslides

However, due to the presence of different mass movement types from those considered in this work (such as deep-seated landslides, flows and landslides involving sensitive clays), data filtering was necessary before extrapolating the distributions.

In addition, since the goal was to define representative D/L values exclusively for purely rotational and translational landslides, some of the landslides into the database were re-classified. In particular, the so-defined « roto-translational » landslides were re-classified to be re-located between the groups of the purely rotational and translational slides. The criterion adopted for the re-classification is the following: if more than 50% of the total length of the landslide is affected by a translational failure mechanism, that landslide can be considered predominantly of translational type and *vice versa*.

In literature, the term « roto-translational landslide » generally refers to landslides having a simultaneous rotational and translational kinematics. These landslides can be more properly defined as « compound slides » according to Cruden & Varnes (1958) or « complex landslides » according to Varnes (1978). Although in nature the distinction between rotational and translational landslides is not always clear and intermediate types generally exist between the two end-members (purely translational and rotational slides), in order to design landslide prototypes, a simplification is necessary, since it is not possible to represent all the intermediate cases.

Figures 2.3 a-b show the distributions of D/L values extracted from Domej & Pluta (2018) for rotational and translational landslides after the re-classification.

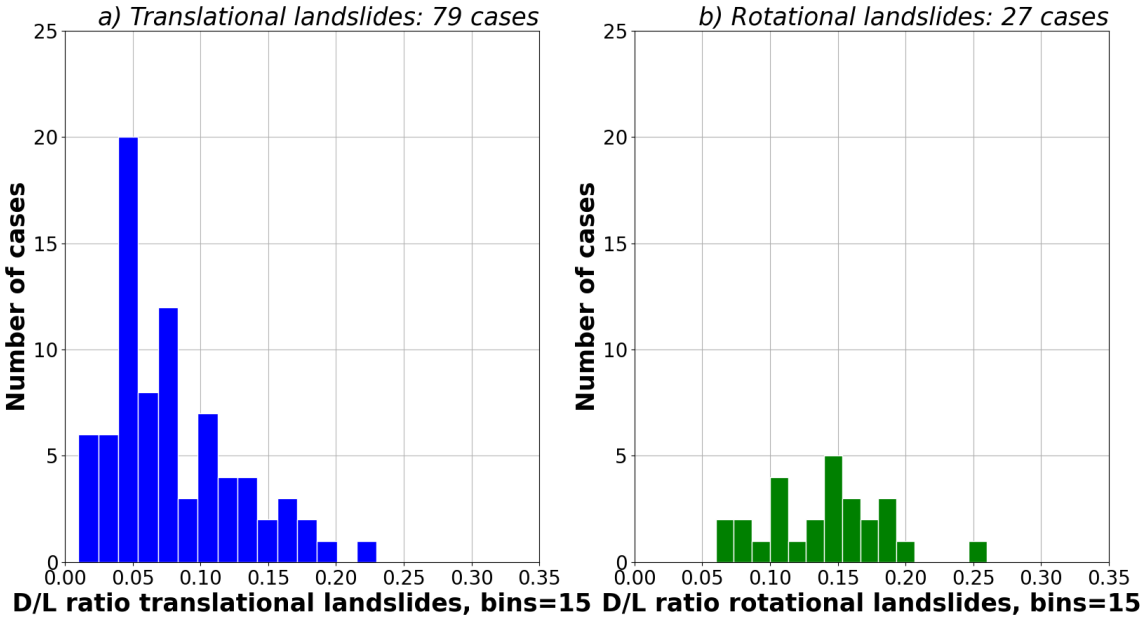

Figure 2.3: *Distribution of D/L derived from the dataset by Domej & Pluta (2018) for a) translational landslides (Mode: 0.05; Mean: 0.08; Median: 0.06; σ: 0.05; σ^2: 0.002) and b) rotational landslides (Mode: 0.16; Mean: 0.14; Median: 0.14; σ: 0.04; σ^2: 0.002).*

Distributions in figures 2.3a-b were statistically characterized by calculating the following attributes:

- the mode: corresponding to the most frequent value of the two distributions

- the median: equivalent to the middle value of the datasets
- the mean: calculated as the arithmetic mean (μ) of the sets of data
- the variance (σ^2) and the standard deviation (σ): the first one is a measure of the degree of dispersion of the data with respect to the mean value (eq. 2.2) whereas the second one is its squared root

$$\sigma^2 = \frac{\sum_{i=1}^{n}(x_i - \mu)^2}{n} \qquad \text{[Eq. 2.2]}$$

where μ is the mean, n is the total number of samples in the dataset, and x_i is a value.

The analysis of the distributions in figures 2.3a-b allows inferring that:

- translational landslides (79 total cases) are more frequent than rotational landslides (27 total cases) at worldwide scale according to the considered dataset. This result is consistent with observations by Varnes (1978). Indeed, according to the author, purely rotational landslides (i.e., landslides delimited by failure surfaces that are curved concavely upward) are infrequent since they typically affect homogenous materials that are not very common in nature. For the same reason, natural slides are more often characterized by complex mechanisms since the shape of the sliding surface is usually controlled by material internal discontinuities. Nevertheless, even if they represent the minority, rotational landslides raise interest in the engineering field for their predisposition to occur in artificial embankments or dams
- the modes of the two distributions are 0.05 for translational landslides and 0.16 for rotational landslides. These values are consistent with the ranges previously documented by Skempton & Hutchinson (1969), and consequently can be selected for the next phases of the procedure
- the two distributions share common values and intersect each other (fig. 2.4) due to the presence of landslides having intermediate kinematics (i.e., re-classified roto-translational landslides)

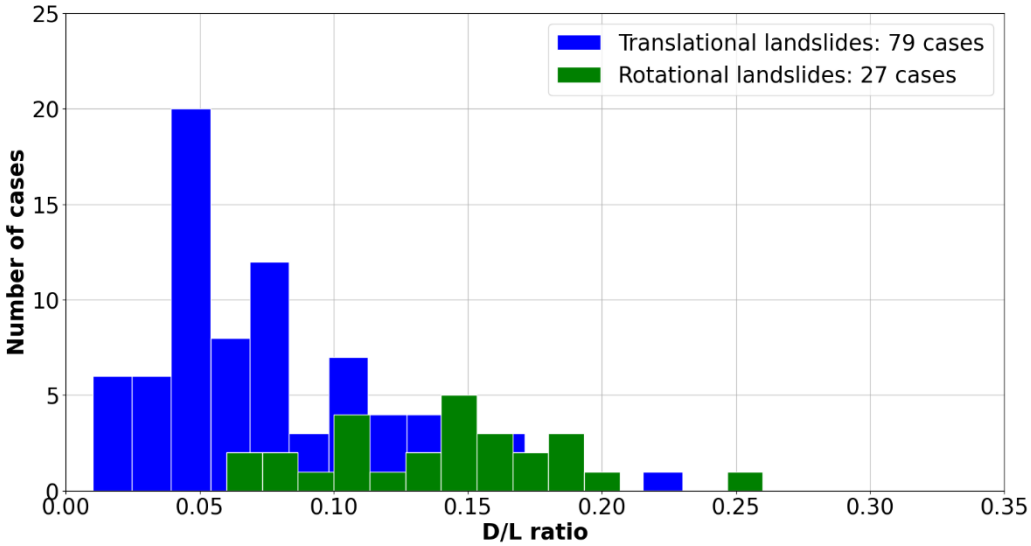

***Figure 2.4**: Comparison of D/L distributions obtained for translational landslides and rotational landslides.*

2.2.4 Slope angle (α)

Slope angle is the parameter that quantifies the average inclination of the slope. It is generally measured as the clockwise angle between the horizontal and the slope (fig. 2.5).

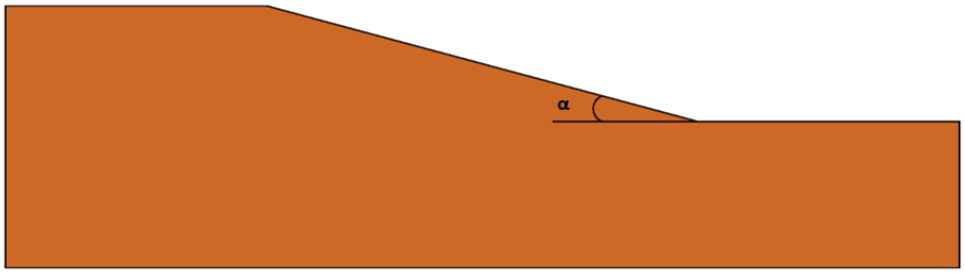

***Figure 2.5**: Definition of slope angle (α) in a simplified slope scheme.*

In general, high-angle slopes are more prone to induce landslides due to the force of gravity. However, in the presence of ground shaking, it is more complex. Lenti & Martino (2012; 2013) performed parametric analyses on landslide models and investigated the role of the slope angle on their resulting earthquake-induced mobility.

Main outcomes from Lenti & Martino (2012; 2013) are summarized below:

- unsheared slopes (first-time failures): high-angle configurations are associated to significant values of the Progressive Failure Index (PFI). The latter is the index quantifying the portion of the slope significantly involved into the progressive failure process (i.e., the process leading to the development of a shear zone). In contrast, this index is zero for low-angle configurations (being equal the geotechnical properties of materials and the applied inputs). Moreover, high-angle models can fail (transition from shear zone to real sliding surface) after several applications of a given input. The number of applications inducing the failure depends on the Arias Intensity (energy) of the input (Lenti & Martino, 2012)
- sheared slopes (pre-existing landslides): low-angle configurations exhibit amplification effects along the slope face at frequencies related to the thickness of the landslide and the impedance contrast with the stiffer bedrock. This effect is drastically reduced when the slope angle is increased up to 35° - 45°. Indeed, in this case the sole de-amplification related to topography is visible. This variation of ground-motion response leads to: i) larger and highly variable earthquake-induced displacements with the Arias Intensity for low-angle configurations, ii) poorly variable and lower earthquake-induced displacements for high-angle configurations (Lenti & Martino, 2012). Because of the de/amplification phenomena, the authors also highlight a discrepancy between predictions by numerical modelling and Newmark's method: Newmark's method can return lower (for low-angle configurations) and higher (for high-angle configurations) displacements than numerical simulations. A similar result is also proposed by Lenti & Martino (2013)

Results by Lenti & Martino (2012; 2013) highlight how being constant the geology and the properties of the dynamic solicitations, the variation of the slope dip can be decisive in the

final response of a slope under seismic shaking. For this reason, the slope angle represents an important parameter to consider when studying the interaction between landslides and seismic waves. Therefore, it must be carefully selected.

In order to design landslide prototypes representative of most of the real cases, the selection of a single slope angle value cannot be considered sufficient and a minimum of two values must be accounted for. Clearly, it would have been more convenient to select more values to represent more real cases and to perform more robust parametric analyses. However, due to time constraints, it was not possible to investigate all the possibilities. Therefore, two values representative of low- and high-slope angles were considered following Domej et al. (2020, fig.7b). The latter report the distribution of average slope angles measured for landsliding slopes at worldwide scale with respect to landslide volume. Excluding possible outliers, according to Domej et al. (2020), the majority of worldwide landslides occurred along slopes with mean slope angles in the range 15° - 30°. These extreme values were therefore selected for the next phases of this study.

To furtherly support this choice, slope angle distribution from Domej et al. (2020) was compared to the frequency distribution that Tanyaş et al. (2017) report in fig. 5. More in particular, according to Tanyaş et al. (2017), mean dip of slopes affected by earthquake-induced landslides from 61 digital inventories is approximately 27°, which is very close to the maximum value selected from Domej et al. (2020). Furthermore, Tanyaş et al. (2017) argued that 80% of the landslides occurred on slopes with a mean dip angle of 10°-15° (equally consistent with the minimum value inferred from Domej et al., 2020) and a maximum value ranging from 40 up to 45°. This is 10°- 15° more than the maximum value extrapolated from Domej et al. (2020). To further confirm the choice of 30° (and not 45°) as the upper-bound slope angle it must be considered that:

1) 80% of the data collected by Tanyaş et al. (2017) are related to landslides that occurred along major mountain belts (such as the Andes or Himalayas) that are therefore constrained by specific geomorphological conditions
2) plot in fig.7b, proposed by Domej et al. (2020) is exclusively based on data collected for slide type slope movements that is specifically the failure mechanism treated in this research

2.3 Analysis of geomechanical properties to characterize landslide prototypes

In order to attribute geomechanical properties to the landslide prototypes, a data collection from the available literature was performed.

The selection of material types is a crucial step since it affects wave propagation. Consequently, the choice must go towards material types that are more frequently involved in slope movements. Obviously, as previously mentioned, there is a large variability in nature and the identification of main groups and/or reference values is a necessary simplification for deriving landslide prototypes. Indeed, as it regards material types, the geotechnical

composition of landsliding slopes is mainly conditioned by the combination of geological and climatic conditions that are necessarily different in different geographical locations.

These typologies of material were identified by referring to the commonly used landslide classification by Varnes (1978). This classification allows classifying through a double entry matrix slope movements accounting for: i) the failure mechanism, ii) the material type. Material groups indicated by Varnes (1978) as principal for classifying landslides are: rocks and engineering soils. The latter are further distinguished in debris and earth. As reviewed by Hungr et al. (2014), the term « debris » does not have clear equivalents in geotechnical terminology but in geology and landslide science, it is still commonly used to indicate mixtures of sand, gravel, cobbles, and boulders with variable amount of silt and clay. This group of low-cohesion materials will be referred to as « loose soils». In a similar way, the term « earth » could sound ambiguous but in landslide topic issues it is often used with the meaning of cohesive, plastic, and clayey soils (Hungr et al., 2014). The latter group, including high-cohesion materials, will be indicated with the term « cohesive soils » in this study.

Finally, it is worth specifying that even if the soil/rock types mentioned by Varnes (1978) and Hungr et al. (2014) are intended as mixtures of particles with different sizes and jointed rock-masses or layered rocks with different mechanical properties, the spatial heterogeneity of the material and its effect on the landslide mobility will not be investigated in this study. Indeed, exclusively homogeneous materials will be attributed to the « landslide » in the designed prototypes in order to reduce the number of variables.

2.3.1 Geotechnical parameters attribution to rocks, cohesive and loose materials

In order to attribute the geotechnical properties to rocks, cohesive and loose materials, relevant parameters describing their geomechanical behaviour must be identified.

Since the present research is mainly devoted to the study of the dynamic response of landslides, the choice of these parameters must be done in the perspective of investigating the interaction between seismic inputs and landslide masses.

As explained in paragraph 1.2.1, site effects related to amplification phenomena generated by difference in shear wave velocity and density between a landslide body and its below bedrock (known as impedance contrast between them) might play an important role in landslide mobility. For this reason, parameters describing materials dynamic response (i.e., shear wave velocity, impedance contrast, shear modulus decay curves) must be considered in addition to those related to their shear strength (i.e., cohesion, friction angle) and their physical properties (i.e., unit weight).

This selection resulted into a set of 11 different geotechnical parameters (tab. 2.2) defined in addition to 3 average shear modulus decay curves. Among these 11 parameters, 3 parameters were inferred from literature (i.e., unit weight, friction angle, cohesion) and the remaining 8 were analytically calculated from the first ones (i.e., residual cohesion and friction angle, shear modulus, bulk modulus, elastic modulus, shear wave velocity and peak and residual tension cut-off). The parameters inferred from literature are average values calculated basing on sets

of data gathered from the existing literature. Indeed, in this case, a previous literature review aiming at collecting the values attributed to the above-listed parameters in available landslide/geotechnics studies for the material types of interest was performed. More detailed information on the datasets defined for each material type will be provided in the next paragraphs.

Finally, it has to be noticed that in the list of parameters reported in tab. 2.2, the impedance contrast (IC) between the landslide mass and the substratum was not mentioned. Indeed, at this regard, a short anticipation of the next phases of the work must be provided to explain how the parameter « impedance contrast » is calculated for each considered material type. In this work, the term « substratum » or « bedrock » is used to indicate the area or the material below the designed landslide geometry. Since the focus of this study is on the landslide behaviour, a rock-type material with a shear wave velocity of 800 m/s was considered for all the designed cases. Starting from this assumption, as it will be better explained in the next paragraphs, 2 different impedance contrasts were defined for each material type attributed to the landslide.

Table 2.2: *List of geotechnical parameters used to characterize the material types.*

PARAMETERS INFERRED FROM LITERATURE	ANALYTICALLY CALCULATED PARAMETERS
Unit weight (γ)	Shear modulus (G_0)
Cohesion (c)	Elastic modulus (E)
Friction angle (ϕ)	Bulk modulus (B)
_	Shear wave velocity (v_s)
_	Tension cut-off (t)
_	Residual tension cut-off (t_{res})
_	Residual cohesion (c_{res})
_	Residual friction angle (ϕ_{res})

2.3.2 Rocks (R)

2.3.2.1 Introduction

The term « rock » is commonly used to indicate an aggregate of minerals from earth's crust that basing on its genesis is classified as igneous, sedimentary, or metamorphic type.

Outcrops of rocks in nature are generally variable not only in terms of type but also in terms of geotechnical quality. Indeed, basing on the tectonic history of the site as well as the intensity of local weathering, rocks develop, in addition to the eventual initial layering, sets and/or randomly oriented joints that can become sources of slope instabilities (falls, topples, slides), since they represent planes with lower shear strength compared to the intact matrix. In engineering geology, these types of rocks (i.e., rocks characterized by matrix and joints) are generally known as jointed rock-masses.

Based on the previous considerations, it is not surprising if in literature, measured values of rocks parameters are highly variable. Indeed, they depend on the contribution of several factors such as lithology and presence of joints. This variability also regards the kind and the number of parameters that are documented, since it is directly influenced by the aim of the

study and the available economical resources for the geotechnical tests (further distinguished between *in situ* tests and laboratory tests).

In order to generalize the results of this study as much as possible, it was established to not focus on specific lithologies and to collect, from literature, measured values for parameters in table 2.2 independently from the rock type. Moreover, as previously explained (cf. paragraph 2.3), only homogeneous materials without discontinuities were considered, therefore, information related to the shear strength of the joints was not looked for. Indeed, to reduce the number of variables, rock materials were considered as intact rocks instead of as jointed rock-masses.

2.3.2.2 Literature review on geotechnical parameters for rock-type materials

The literature review on rock-type materials allowed collecting a reasonable number of cases for the following geotechnical parameters:

1) unit weight (ɣ): it measures the weight per unit of volume of material. It is here considered in conditions of natural degree of saturation
2) friction angle (ϕ): it is a shear strength parameter that for intact materials measures the friction that the material itself would oppose to the sliding along a plane
3) cohesion (c): as the friction angle, it is used to characterize shear strength. In particular, it measures the strength that holds together the particles composing the material

If a theoretical elastic-perfectly plastic material behaviour is assumed, cohesion and friction angle contribute together to the maximum available shear strength (τ) according to the Mohr-Coulomb failure criterion (eq. 2.3):

$$\tau = c + \sigma'(\tan\phi) \qquad \text{[Eq. 2.3]}$$

where c is the cohesion, ϕ is the friction angle and σ' is the effective normal stress on the plane. When shear stress overcomes τ, failure occurs. Through this relationship, it can be better understood how much the choice of reliable shear strength parameters is important in slope stability studies.

The distributions obtained for the above-listed parameters are reported in figure 2.6.

From the distributions a-c in figure 2.6, it can be argued that the datasets defined for the 3 considered parameters are quite different in terms of degree of completeness. Indeed, it appears evident that the parameter « unit weight » is reported in the consulted references much more frequently (72 cases) than the other parameters (each one is reported 12 times). This lack of information introduces a higher degree of uncertainty for cohesion and friction angle compared to unit weight.

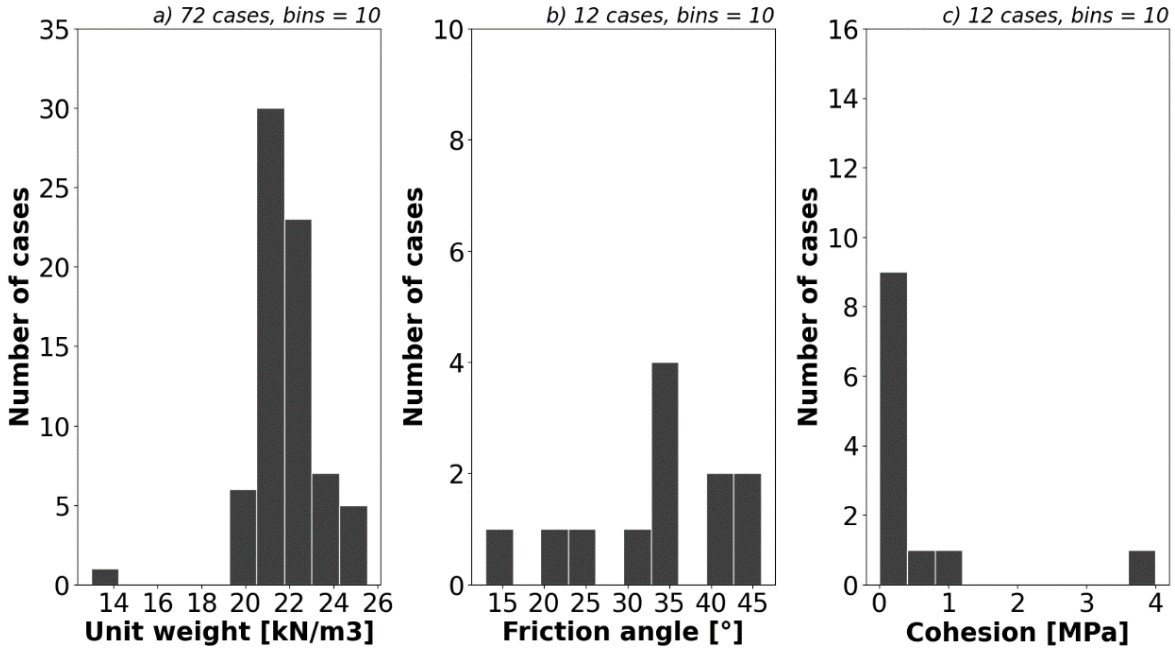

Figure 2.6: *Distributions of values collected for a) unit weight, b) friction angle and c) cohesion for rock-type materials.*

Data were used to calculate average values of the above-mentioned parameters to define an average geomechanical behaviour of rock-type materials. More in particular:

- weighted averages were calculated for unit weight and friction angle to account the « weight » in terms of number of cases of each collected value into the final average according to the distributions in figures 2.6 a and b. Indeed, from the latter it can be argued that there is a clear peak of cases in the range $21 < \gamma[kN/m^3] < 23$ and even if less evident, a peak at $\phi \sim 35°$. Equation 2.4 allowed calculating the weighted average:

$$\text{weighted average} = \frac{\sum_{i=1}^{n} x_i * p_i}{\sum_{i=1}^{n} p_i} \qquad \text{[Eq. 2.4]}$$

  where p_i is the weight (the frequency of occurrence) of each value (x_i) and n is the total number of cases. More in particular, equation 2.4 was applied to unit weight and friction angle distributions by considering the central value (x_i) of each bar and counting the corresponding number of cases (p_i). The resulting values correspond to $\gamma \sim 22$ kN/m^3 and $\phi \sim 33°$ that were judged reliable for rock-type materials
- the geometric average was used for cohesion because of the higher range spanned by data. This effect is probably related to the co-existence, into the dataset, of harder (such as marbles) and weaker rocks (such as marls). However, the limited amount of data collected does not provide a comprehensive overview of the variability of this parameter for all the existing rock lithologies. This raises the question of the necessity to expand the dataset with new values in the future to achieve a more reliable geotechnical parameterization. The calculated average value for cohesion according to equation 2.5 is 0.13 MPa (~130 kPa):

$$\text{geometric average} = \sqrt[n]{\prod_{k=1}^{n} x_k} \qquad \text{[Eq. 2.5]}$$

where n is the total number of cases (x_k)

Before discussing on other parameters defined to characterize rock geomechanical behaviour it must be mentioned that:

- cohesion and friction angle values previously discussed are intended as peak cohesion and peak friction angle. It means that they represent the strength that the material opposes when it is subjected to the maximum possible stress before reaching the plastic deformation: after this moment the material experiences a decreasing of the available strength (residual strength)
- due to an insufficient amount of data found in literature, residual strength parameters were derived, basing on expert judgement, from the peak ones in the following manner: residual friction angle (ϕ_{res}) was calculated as half peak value, whereas residual cohesion was computed by decreasing peak value by one order of magnitude
- in this research, peak shear strength parameters are attributed to the domains representing landslide body and substratum, whereas residual ones are used to simulate post-failure conditions existing along the sliding surface

The final computed values for cohesion, friction angle and unit weight are summarized in table 2.3.

Table 2.3: *Unit weight, cohesion and friction angle computed for rock-type materials.*

PARAMETER	CORRESPONDENT CALCULATED VALUE
Unit weight (γ) – [kN/m^3]	22
Cohesion (c) – [kPa]	130
Friction angle (ϕ) – [°]	33
Residual cohesion (c_{res}) – [kPa]	13
Residual friction angle (ϕ_{res}) – [°]	16.6

2.3.2.3 Attribution of values to shear wave velocities and impedance contrasts

The evaluation of consistent shear wave velocities (v_s) values for landslides in rock materials is here discussed. Two different values were selected in order to analyse, in the next chapters, how seismic displacements are affected by different landslide-bedrock impedance contrasts.

As previously mentioned (cf. paragraph 2.3.1), an elastic bedrock composed of rocks (geotechnical properties in tab. 2.3) characterized by a shear wave velocity of 800 m/s will be introduced in all the designed landslide configurations.

Material shear wave velocity is computed according to equation 2.6:

$$v_S = \sqrt{G_0 / \rho} \qquad \text{[Eq.2.6]}$$

where G_0 is the elastic shear modulus and ρ is the density.

In order to select two different values of shear wave velocities for rock materials (corresponding to two different IC with respect to the below bedrock), the procedure described below was followed:

1) shear wave velocity values of rock materials were collected from available literature in order to obtain the frequency distribution in figure 2.7

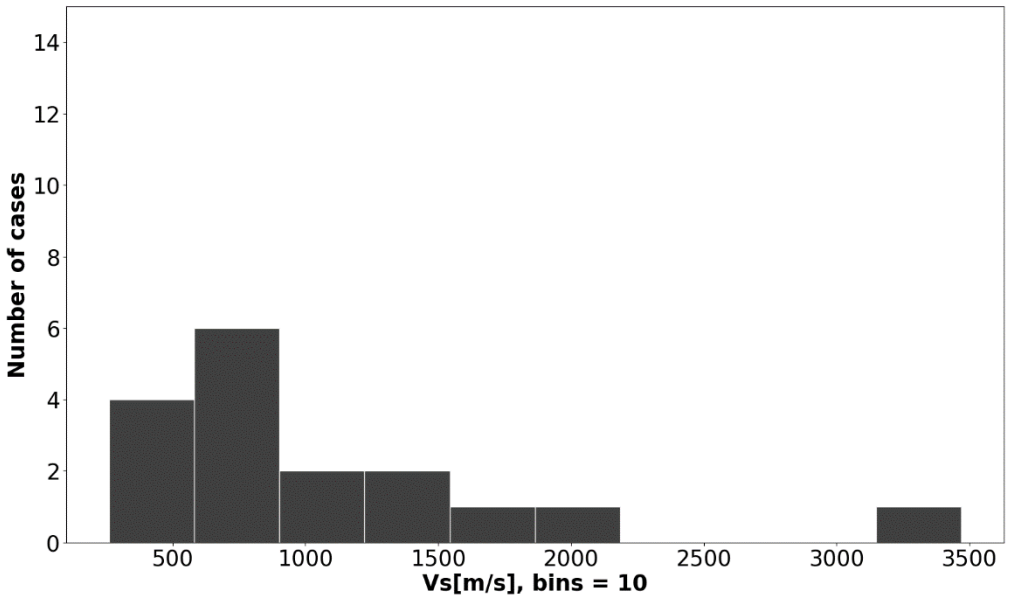

Figure 2.7: *Distribution of shear wave velocity (17 cases) for rocks (Mode: 600 m/s; Mean: 1044 m/s; Median: 775 m/s).*

2) having fixed the shear wave velocity of the seismic bedrock at 800 m/s and having calculated an average unit weight for rocks (that can be converted in terms of density) valid for both the landslide and the substratum; equation 2.7 was inverted to compute shear wave velocity of the landslide body after having hypothesized a sequence of values of IC (it was judged realistic to assume values between 1.5 and 4 with an interval of 0.5):

$$IC = \frac{\rho_{land} * V_{land}}{\rho_{bed} * V_{bed}} \qquad \text{[Eq. 2.7]}$$

where ρ_{land} and ρ_{bed} are, respectively, the density of the bedrock and landslide, that in this case are coincident since both are composed of rocks. On the contrary, v_{land} and v_{bed} are respectively the shear wave velocity into the landslide body (the value that must be computed) and the shear wave velocity into the bedrock (=800 m/s). The configuration landslide-bedrock here mentioned is schematized in figure 2.8 to help to understand the procedure

3) the resulting values in terms of shear wave velocity of the landslide mass are compared with the distribution in figure 2.7 to verify that the results of the calculations are consistent with real values documented in literature

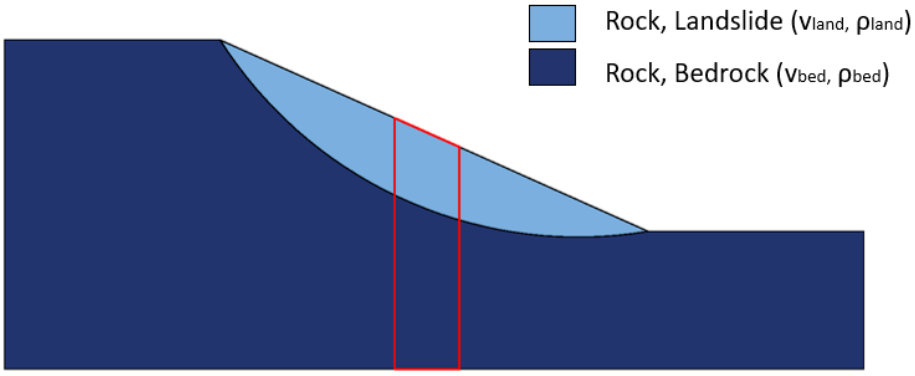

Figure 2.8: *Representation of landslide body and bedrock. The difference in terms of shear wave velocity between the two layers contribute to define an IC between them.*

Results are summarized in table 2.4. From obtained results, it is possible to infer that the computed v_{land} values are between 200 and 533 m/s: the first value corresponds to the highest hypothesized IC (=4), while the second one corresponds to the lowest hypothesized IC (=1.5). After comparing this list of values with the distribution in figure 2.7, it is possible to argue that among the computed values, only those included between 266 and 533 m/s (IC from 3 to 1.5) are consistent with documented values of shear wave velocities for rocks. Indeed, the dataset compiled for this parameter includes values ranging from 260 and 3470 m/s, underlining its high natural variability.

As the v_{land} value corresponding to an IC of 3 appears borderline with respect to the distribution in figure 2.7, values judged more reliable are those between 320 and 533 m/s. As final choice, the selection went towards IC of 1.5 and 2.5, whereas the IC = 2 was excluded. Indeed, having to select a restricted number of values, it was judged more convenient to opt for values that are not too close, as they could return too similar results in terms of modelling of displacements.

Table 2.4: *Parameters used for computing shear wave velocities of landslide bodies according to the procedure listed in 1-3. Density was obtained by conversion from unit weight (multiplying for 1000/g, with g equal to 9.81 m/s^2). The « green » values are those consistent with distribution in figure 2.7, the orange cell contains a value judged borderline for rocks, and finally the values in the red cells were excluded because too small with respect to collected data.*

IC	v_{bed} [m/s]	Υ [kN/m^3]	ρ [kg/m^3]	v_{land} [m/s]
1,5	800	22	2230	533.3
2	800	22	2230	400.0
2,5	800	22	2230	320.0
3	800	22	2230	266.7
3,5	800	22	2230	228.6
4	800	22	2230	200.0

2.3.2.4 Parameters computed by analytical equations

To complete the geomechanical characterization of rock-type materials additional parameters were calculated. More in particular they are:

1) the tension cut-off (t): together with cohesion and friction angle, tension cut-off is used to quantify material strength, particularly if it is subjected to tensile stresses. The quantification of this parameter is important when evaluating the possibility of fracturing in rock masses. In these conditions, empirical studies demonstrated that the theoretical linear stress-strain relationship expressed by the Mohr-Coulomb criterion does not well approximate the behaviour of rocks, whereas it results more reliable for soils (Conti, 2012). In this case, it is preferable to refer to the Griffith's criterion (Conti, 2012). According to the latter, t can be computed as half the cohesion assuming an effective normal stress equal to zero (Conti, 2012). This parameter was here computed in peak (t) as well as residual (t_{res}) conditions
2) Poisson's ratio (ν): this ratio measures shortening in the transverse direction compared to elongation in the direction of applied compression (ISMR, 1975). Basing on expert judgement it was fixed at a value of 0.25 for all material types
3) Elastic modulus (E), Bulk modulus (B) and Shear modulus (G_0): these parameters, in addition to Poisson's ratio serve to characterize the elastic behaviour of materials (Conti, 2012). More in particular, E (also known as Young's modulus) expresses the ratio between the longitudinal stress and the corresponding deformation (extension or shortening depending on if it is subjected to tensile or compressive stress), G_0 (also known as shear rigidity modulus) similarly to E is the ratio between the applied shear stress and the induced shear deformation. Finally, B measures the propensity of the material to decrease its volume when subjected to compression, therefore it can be expressed as the ratio between the applied compressive stress and the resulting volumetric deformation

To compute G_0, equation 2.6 was used as it expresses shear wave velocity as function of G_0 and ρ. In particular, the average density calculated for rock-type materials and the v_s values defined in paragraph 2.3.2.3 were substituted into eq. 2.6 to compute G_0. Then:

1) having fixed Poisson's ratio (ν) at 0.25 (cf. par. 2.3.2.2), E can be determined by inverting equation 2.8:

$$G_0 = \frac{E}{2(1+\nu)} \qquad \text{[Eq. 2.8]}$$

2) B values are finally given by equation 2.9:

$$B = \frac{E}{(3(1-(2\nu))} \qquad \text{[Eq. 2.9]}$$

The described sequence of computation was repeated 3 times by using the two shear wave velocity values determined for landslide bodies to simulate impedance contrasts of 1.5 and 2.5 (cf. paragraph 2.3.2.3) and the shear wave velocity of 800 m/s fixed for the bedrock. This last step will not be repeated for other materials since, as already mentioned, only one bedrock type consisting of rocks will be considered for all landslide prototypes. In summary, the landslide prototypes designed in this study will be characterized by one bedrock type and 6 landslide body types (corresponding to the three selected materials, each in two different v_s

combinations) for each designed configuration as will be better explained in the next paragraphs.

Finally, it has to be noticed that tension cut-off computed for rocks, as well as cohesion, friction angle and density do not change with the impedance contrast. The only difference is given in this case by shear wave velocity. Moreover, as it will be better explained later, a purely elastic behaviour will be considered for the bedrock.

The final three sets of parameters are summarized in tab. 2.5 a-c. From the latter it can be inferred that an increasing shear wave velocity of the material corresponds to an increasing rigidity. Indeed, the parameter G_0 is at least one order of magnitude higher for rock materials constituting the bedrock compared to the rock involved in the landslide process.

Table 2.5: *Summary of the parameters calculated for rocks in the landslide (a-b) and the bedrock (c). Parameters G, B and E are different between tables as they result from the different shear wave velocities assumed for rocks.*

a) Rock, Landslide : IC = 1.5, v_s = 533 m/s, ρ = 2230 kg/m ^{3}, ν = 0.25	
Griffith's tension cut-off (t) - [kPa]	62.5
Residual Griffith's tension cut-off (t_{res}) - [kPa]	6.25
Shear modulus (G_0)-[MPa]	634
Elastic modulus (E)-[MPa]	1590
Bulk modulus (B)-[MPa]	1060

b) Rock, Landslide : IC = 2.5, v_s = 320 m/s, ρ = 2230 kg/m ^{3}, ν = 0.25	
Griffith's tension cut-off (t) - [kPa]	62.5
Residual Griffith's tension cut-off (t_{res}) - [kPa]	6.25
Shear modulus (G_0)-[MPa]	228
Elastic modulus (E)-[MPa]	571
Bulk modulus (B)-[MPa]	381

c) Rock, Bedrock : v_s = 800 m/s, ρ = 2230 kg/m ^{3}, ν = 0.25	
Shear modulus (G_0)-[MPa]	1430
Elastic modulus (E)-[MPa]	3570
Bulk modulus (B)-[MPa]	2380

2.3.2.5 Average shear modulus decay curve inferred for rock-type materials

Once shear modulus was computed for different v_s values, it was necessary to quantify the amount of reduction that this parameter can experience during seismic shaking. At this regard, an average shear modulus decay curve was defined for rock-type materials.

Decay curves are used in geotechnical applications to return the variation of shear modulus (and consequently of material rigidity) with the strain level experienced by the material when stressed by cyclic loads (i.e., seismic waves). These curves are also known as G/G_0 curves (with: G_0, initial shear modulus; G reduced shear modulus at a given strain level).

Generally speaking, G/G_0 curves have peculiar shapes and identify three different dynamic material behaviours (corresponding to three different segments of the curve) once characteristic strain thresholds are overcome:

1) strain level is lower than the linearity threshold and the material shows an elastic behaviour where shear modulus is not subjected to reductions ($G/G_0 = 1$)
2) strain level is between the linearity and the volumetric thresholds: the material has a non-linear stable behaviour and G_0 is subjected to a progressive reduction. In that phase, the decreasing material rigidity is combined to an increasing damping (D [%], corresponding to the capacity of the material to dissipate seismic shaking energy converting it into deformations of the material itself) according to a hysteretic model
3) strain level exceeds the volumetric threshold: the material has a non-linear unstable behaviour, D and G/G_0 depend on the number of dynamic cycles due to the developed pore water pressures. In this phase, material may experience strain « hardening » or « softening » basing on material type

In order to account for these processes, decay curves derived for rock-type lithologies in the framework of activities for the III-level microzonation of 140 municipalities hit by the 24 August 2016 M_w 6 seismic event occurred in Central Italy (OPCM24/2017) were collected (data available on www.centromicrozonazionesismica.it). Such a database has the advantage to provide directly with a sequence of measured G/G_0 – strain (ε) [%] value pairs which are usually poorly documented in literature. Among the curves proposed in the above-cited dataset, 17 were attributed to rock-type materials. The 17 selected curves were implemented into the open-source software WebPlotDigitizer 4.5 (Rohatgi, 2021) in order to measure, for each curve, the strain [%] corresponding to given G/G_0 between 0 and 1 each 0.05. Finally, geometric average of the measured strain values was calculated to obtain an average strain [%] for each selected G/G_0. The G/G_0 – average strain [%] value pairs resulting from this procedure are plotted in figure 2.9a. The Hardin & Drnevich (1972) model was then used to approximate the shape of the curve in figure 2.9a. The advantage of using this model is that is directly implemented by the software used for numerical modelling (cf. paragraph 3.4.2) to simulate non-linear behaviour (Seed & Idriss, 1969) of materials. More in particular, it assumes that in presence of seismic shaking in the strain range between the linearity and volumetric thresholds, the decay of the rigidity and the increasing of the damping are exclusively dependent on the stress level. According to Hardin & Drnevich (1972), G/G_0 is given by equation 2.10:

$$\frac{G}{G_0} = \frac{1}{1+\frac{\varepsilon}{\varepsilon_{ref}}} \qquad \text{[Eq. 2.10]}$$

where ε_{ref} is the reference value that corresponds to the strain of the material when G/G_0 is 0.5 and ε is the generic deformation at the generic G/G_0. This equation was applied to recalculate the amount of decay of shear modulus (G). The resulting approximated curve is shown in figure 2.9b.

Decay curves are only considered for rock materials composing the « landslides ». For rocks composing the « substratum », a fully elastic behaviour is assumed in all simulations.

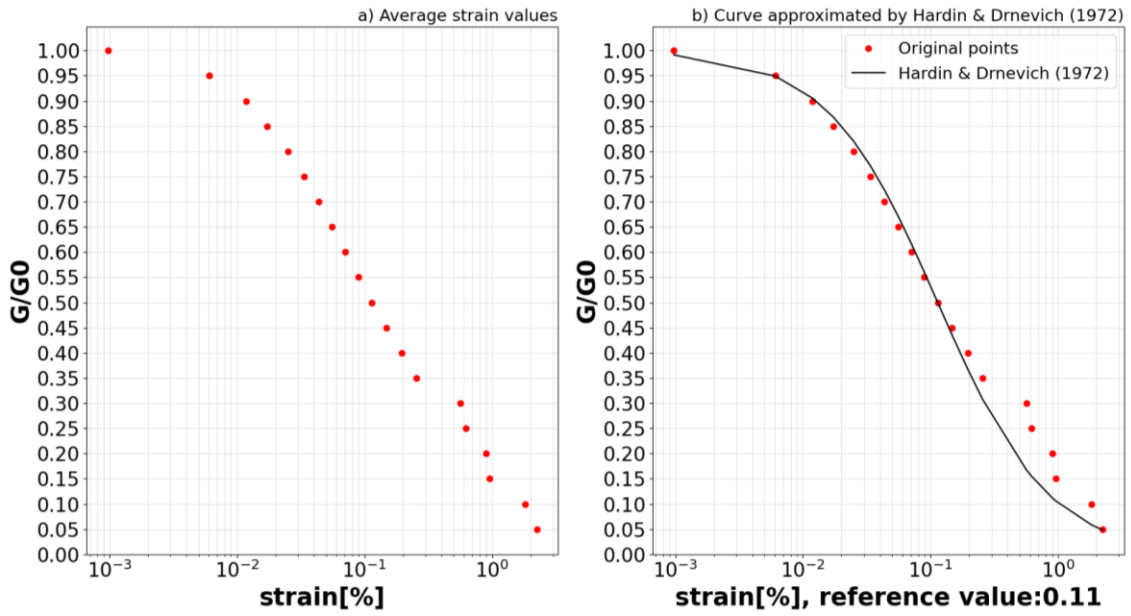

Figure 2.9: *Average strain values computed for fixed G/G_0 values (a) and shear modulus decay curve (b) approximated by the Hardin & Drnevich (1972) model for rocks.*

2.3.3 Cohesive Soils (CS)

2.3.3.1 Introduction

As previously mentioned (cf. paragraph 2.3), in this study, the term « cohesive soil » refers to materials characterized by a dominant clay component. Clayey materials have peculiar geotechnical strength properties dominated by the cohesion resulting from the electrostatic attraction between particles. This cohesion significantly contributes to the maximum available strength according to the Mohr-Coulomb yield criterion (eq. 2.3). Clay particles have, by definition, a diameter minor or equal to 0.002 mm (ISO/FDIS 14688-1:2017), however, natural soil mixtures contain in most of the cases also particles of different sizes in various percentages.

The « cohesive soil » group includes:

1) unconsolidated materials: they are mixtures of particles of different sizes present in different percentages generally originated from physical and/or chemical erosive processes. According to the Unified Soil Classification System (USCS), if the clayey/silty component is dominant into the soil mixture, the latter will be classified as fine-grained soil. Into this macro-category, then, sub-groups can be identified basing on peculiar soil properties such as plasticity and liquid limit
2) consolidated materials: they are originated from sedimentary depositional processes. In this category, the deposit can be further distinguished as normally consolidated (NC) and over-consolidated (OC). NC clays are currently subjected to an effective pressure that corresponds to the maximum ever experienced, whereas, if the current effective stress is lower than that the deposit experienced in the past, they will be better defined as OC clays. The geotechnical behaviour of OC and NC clays subjected to

static/dynamic stresses is quite different. Indeed, in drainage conditions, this response will go towards the strain softening (OC materials) or hardening (NC materials)

Consolidated and unconsolidated deposits give rise to slope movements in different modalities. For instance, unconsolidated materials generally generate flows either fast or slow, wet or dry (Varnes, 1978). Since the aim of this study is to analyse the mobility of landslides along well-defined sliding surfaces, such as block-slides or slumps (*sensu* Varnes, 1978), the selection of the geotechnical parameters for cohesive materials was mainly focused on data related to consolidated deposits.

2.3.3.2 Literature review on geotechnical parameters for cohesive soils

To compute geotechnical properties for cohesive materials, a literature review was carried out to collect a reasonable amount of data for unit weight, cohesion, and friction angle to deduce their average values. The final aim of this research was to define an average geotechnical behaviour of cohesive materials for parameterizing the landslide masses in the sketched slope models.

The sets of data collected for the 3 above-mentioned parameters are summarized in the distributions in figures 2.10 a-c. As for rocks, parameters quantifying material shear strength (i.e., cohesion and friction angle) were poorly accessible compared to unit weight. Indeed, 28 cases were found for unit weight and only 12 and 17 cases were collected for cohesion and friction angle respectively. As it regards cohesion, friction angle and unit weight, the average values were computed using the following procedure:

- weighted averages (eq. 2.4) were calculated to assess average values of unit weight and friction angle. Indeed, as it can be argued from figures 2.10 a and b, the obtained distributions show peaks located at γ[kN/m^3] ~20 and 20 < ϕ [°] < 25 respectively. Basing on these distributions, the values computed according to equation 2.4 are $\gamma \sim$ 18 kN/m^3 and $\phi \sim 21°$
- geometric average (eq. 2.5) was selected for calculating an average cohesion. The collected values span over a wider range (from 4e^{-4} MPa to 1.5e^{-1} MPa) compared to friction angle and unit weight. Also in this case, this effect can be related to the co-existence of materials with different consolidation conditions within the dataset, in addition to their natural compositional variability. Since in this study the main interest is on landslides failing along well-defined sliding surfaces, it was judged more appropriate to exclude from the calculation, cohesions < 6e^{-2} MPa to not underestimate this parameter with respect to the purpose of the study. According to this filtering, the calculated average cohesion is 1.4e^{-1} MPa (~140 kPa). However, in the future it is necessary to increase the dataset for a more reliable quantification of this parameter

Above-mentioned cohesion and friction angle have to be considered as their respective peak values. Corresponding residual values were determined according to the criteria already explained for rocks (cf. paragraph 2.3.2.2).

The full list of parameters is finally given in table 2.6.

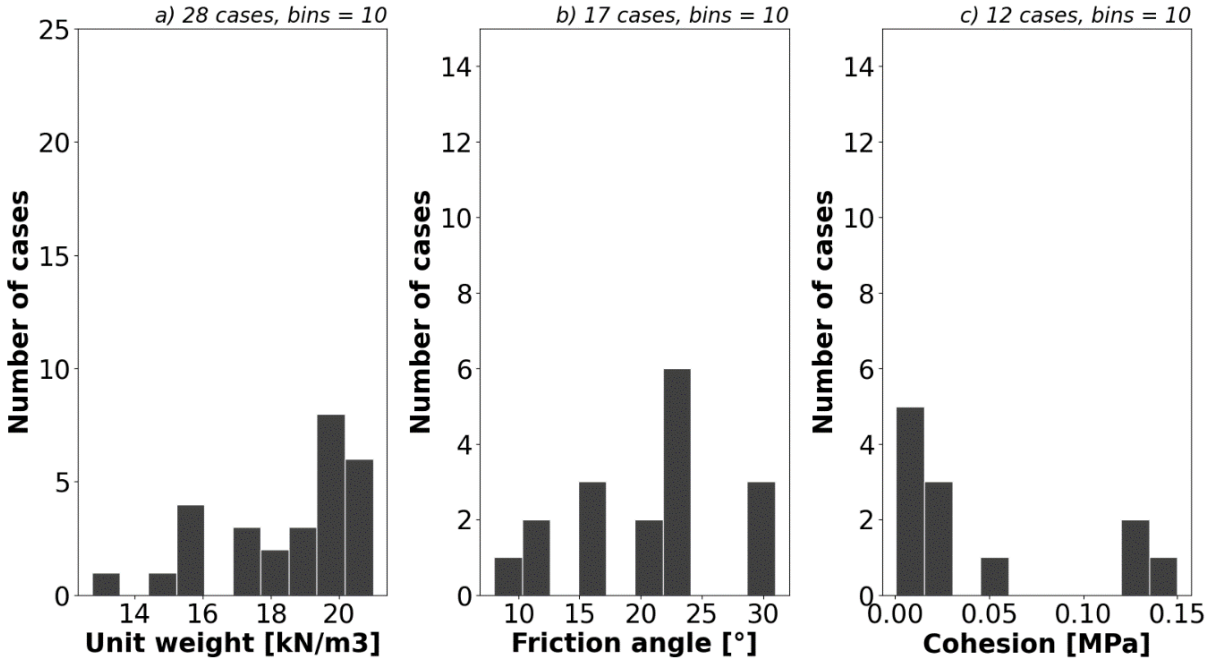

***Figure 2.10**: Distributions of values collected for a) unit weight, b) friction angle and c) cohesion for cohesive materials from literature review.*

***Table 2.6:** Final values computed for unit weight, peak and residual cohesion, and friction angle for cohesive materials.*

PARAMETER	CORRESPONDENT CALCULATED VALUE
Unit Weight (ɣ) – [kN/m^3]	18
Cohesion (c) – [kPa]	140
Friction angle (ϕ) – [°]	21
Residual cohesion (c_{res}) – [kPa]	14
Residual friction angle (ϕ_{res}) – [°]	10.5

2.3.3.3 Selection of values for shear wave velocities and impedance contrasts

In addition to cohesion, friction angle and unit weight, shear wave velocity was defined for characterizing landslides involving cohesive materials. The procedure used to compute this parameter is analogous to that already described for rocks (cf. paragraph 2.3.2.3). Also in this case, a bedrock composed of rock-type materials with a shear wave velocity of 800 m/s was hypothesized as reference for selecting two v_s values and consequently simulating two different impedance contrasts between the landslide and the substratum.

As starting point, documented v_s values for cohesive soils were collected from literature to obtain the distribution in figure 2.11. Distribution in figure 2.11 suggests that v_s values are quite variable since they span from less than 100 m/s to more than 1000 m/s. This variability can be interpreted as the result of the presence of materials characterized by different consolidation states into the dataset.

The following step was to hypothesize a sequence of realistic IC values (as before this parameter was varied between 1.5 and 4 each 0.5) and to invert equation 2.7 to compute v_{land}.

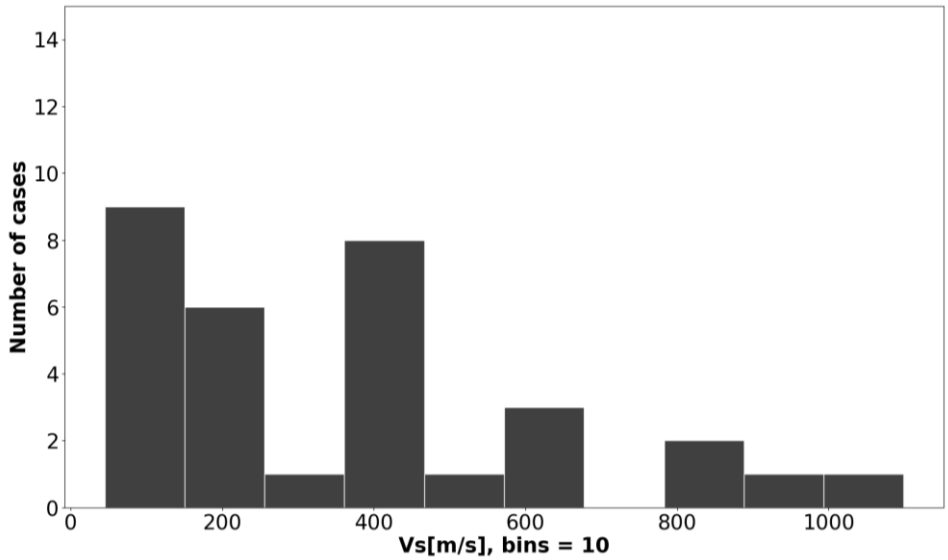

Figure 2.11: *Distribution of shear wave velocities (32 cases) for cohesive materials (Mode: 400 m/s; Mean: 354.5 m/s; Median: 370.5 m/s).*

In this case, it is important to stress that the density of the landslide (ρ_{land}) is different from that of the bedrock (ρ_{bed}). Indeed, the landslide density, which was computed for conversion from the unit weight, is that of cohesive materials, whereas the bedrock density is that of rock-type materials. Table 2.7 reports the full sequence of calculations. From table 2.7 it can be argued that all the v_s values computed to represent landslides (v_{land}) are consistent with the distribution in figure 2.11. For this reason, the choice of the most appropriate IC – v_s values must be done based on expert judgement. At this regard, a first filtering was done by excluding v_s values > 800 m/s (i.e., the shear wave velocity of the bedrock) from the distribution in figure 2.11. Cutting the tail of the distribution, the range of v_s variability is reduced until a maximum of ~ 600 m/s. Consequently, v_s value corresponding to an IC = 1.5 becomes borderline with respect to the distribution and, therefore, it was excluded from the selection. At this point, the lowest selectable IC value is 2 (i.e., v_s = 474.9 m/s). This result is geologically realistic because it is reasonable to assume a higher IC between rocks and cohesive materials compared to the rock-rock combination, where the lowest selectable IC value was equal to 1.5.

Table 2.7: *Summary of the calculations performed to derive consistent shear wave velocities for landslides involving cohesive soils. As before, the density of the landslide (ρ_{land}) was obtained by converting the unit weight selected in the paragraph 2.3.3.2. In the « green » cells there are the values consistent with distribution in fig.2.11 whereas the « orange » cell contains a value judged as borderline.*

IC	v_{bed} [m/s]	ρ_{bed} [kg/m^3]	ρ_{land} [kg/m^3]	v_{land} [m/s]
1,5	800	2230	1879	633.2
2	800	2230	1879	474.9
2,5	800	2230	1879	379.9
3	800	2230	1879	316.6
3,5	800	2230	1879	271.7
4	800	2230	1879	237.4

The second IC value must be sufficiently different from the first one while remaining consistent with the distribution in figure 2.11. Following this criterion, IC = 2.5 was excluded as it was too close to the first selected value (i.e., IC = 2). After considering the remaining possibilities, an IC value of 4 was chosen based on expert judgement.

2.3.3.4 Parameters calculated by analytical equations

Once consistent v_s values for cohesive soils were derived, G_0, E and B were calculated by inverting/applying equations 2.6, 2.8 and 2.9 and assuming ν = 0.25. This sequence of equations is repeated two times to account for the different v_s values selected in the previous paragraph.

Finally, peak and residual values for tension cut-off (t, t_{res}) were computed according to the Mohr-Coulomb criterion as in the equation 2.11:

$$t = c/\tan \phi \qquad \text{[Eq.2.11]}$$

where c is the cohesion and ϕ is the friction angle (cf. paragraph 2.3.3.2). As t is not affected by shear wave velocity variations, it was calculated just once. All the parameters are finally summarized in tables 2.8 a (lowest IC) - b (highest IC).

Table 2.8: *Summary of the parameters calculated for landslide involving cohesive soils assuming different shear wave velocity values (a-b).*

a) Cohesive soil, Landslide : IC = 2, v_s = 474.9 m/s, ρ = 1879 kg/m ^{3}, ν = 0.25	
Mohr-Coulomb's tension cut-off (t) - [kPa]	370
Mohr-Coulomb's tension cut-off (t_{res}) - [kPa]	76
Shear modulus (G_0) - [MPa]	420
Elastic modulus (E) - [MPa]	1100
Bulk modulus (B) - [MPa]	710

b) Cohesive soil, Landslide : IC = 4, v_s = 237.4 m/s, ρ = 1879 kg/m ^{3}, ν = 0.25	
Mohr-Coulomb's tension cut-off (t) - [kPa]	370
Mohr-Coulomb's tension cut-off (t_{res}) - [kPa]	76
Shear modulus (G_0) - [MPa]	110
Elastic modulus (E) - [MPa]	270
Bulk modulus (B) - [MPa]	180

2.3.3.5 Average shear modulus decay curve assumed for the cohesive soils

An average G/G_0 curve was defined for cohesive soils in order to account for the decay of the material maximum shear modulus (G_0) in response to the dynamic solicitation in the next phases of this study.

Also in this case, the decay curves for cohesive materials were extracted among those derived (20 in total) in the framework of the III-level microzonation of 140 Central Italy municipalities hit by the 24/08/2016 seismic event (cf. paragraph 2.3.2.6). The final curve (cf. paragraph 2.3.2.6) is shown in figure 2.12b.

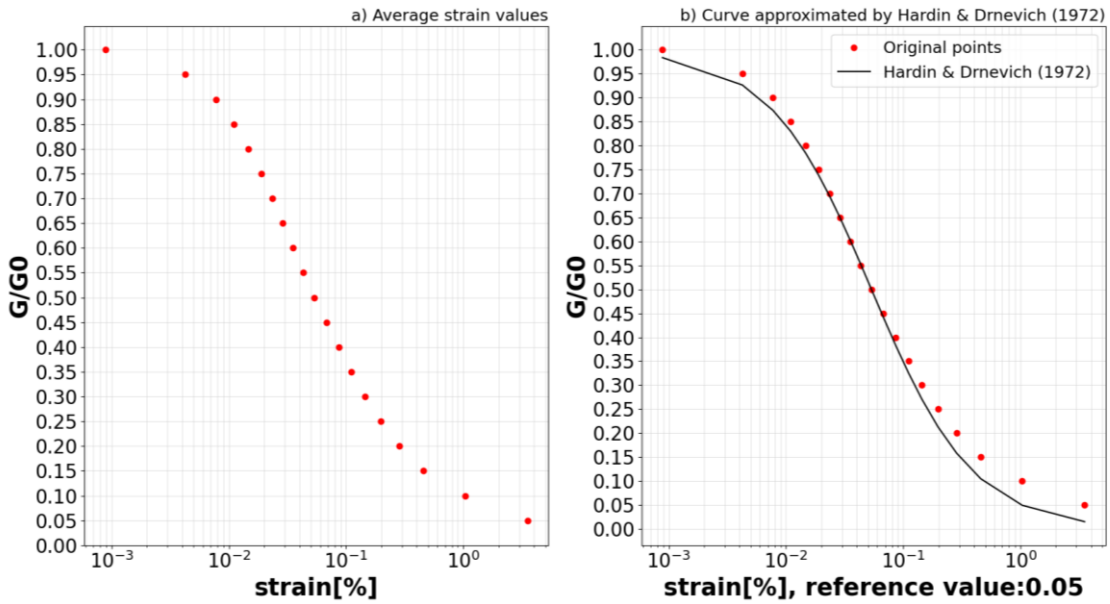

Figure 2.12: *Average strain values computed for fixed G/G_0 values (a) and (b) shear modulus decay curve approximated by the Hardin & Drnevich (1972) model for cohesive soils.*

2.3.4 Loose Soils (LS)

2.3.4.1 Introduction

The term « loose soils » is here used with the general meaning of coarse-grained soils with dominant gravel and/or sand component (less than 50% of the material passes the n.200 sieve, corresponding to a diameter of 0.075 mm according to the Unified Soil Classification System) and various percentages of silt and/or clay.

For this kind of materials, the main contribution to the shear strength is given by the internal friction between the soil particles quantified through the parameter « friction angle », which represents the inclination of Mohr-Coulomb's strength upper envelope.

In the common geological language granular soils covering slope surfaces originated from processes such as weathering, glacial transportation or pyroclastic activity are indicated under the generic term of « debris » (Hungr et al., 2014). From the point of view of slope movements of interest for this study, granular soils most likely give rise to shallow planar slides of material parallel to the substratum that can change into flow-like slides after moving a short distance from the source area (Hungr et al., 2014).

2.3.4.2 Literature review on geotechnical parameters for loose soils

Using the same procedure as for the other materials, unit weight, friction angle and cohesion values of loose soils were collected by literature review. Obtained distributions are reported in figures 2.13 a-c. As previously commented for rocks and cohesive soils, the parameter most frequently documented in literature is unit weight (55 cases), whereas data for quantifying shear strength of material are scarce (i.e., cohesion and friction angle for which respectively 5 and 29 cases were found).

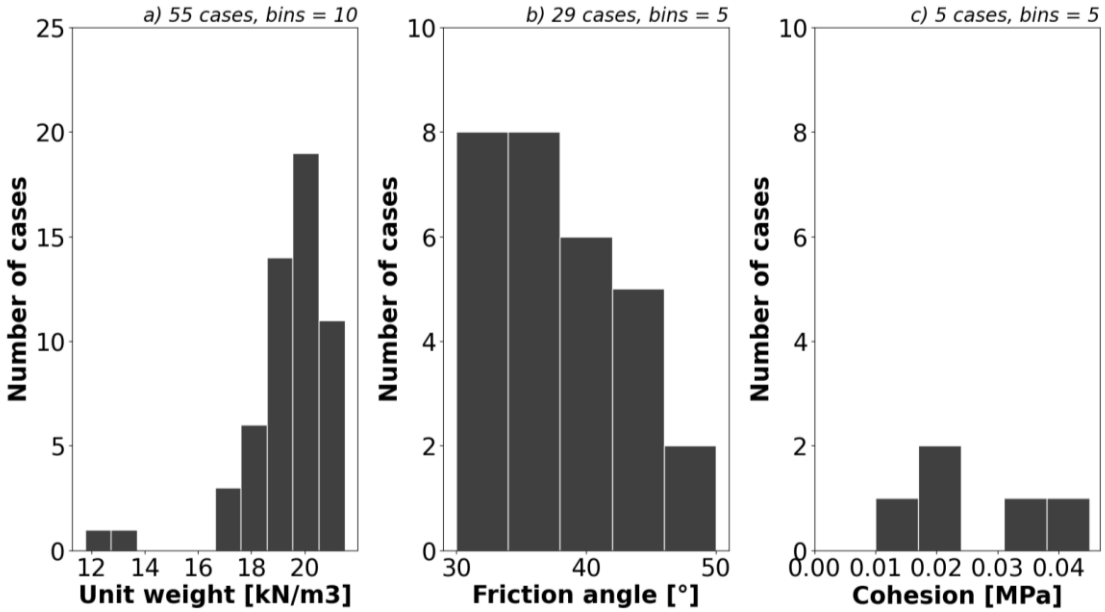

***Figure 2.13**: Distributions of a) unit weight, b) friction angle and c) cohesion obtained for granular soils by literature review.*

To compute average parameters, the procedure already discussed for rocks and cohesive soils was adopted:

- weighted averages were calculated for unit weight and friction angle by equation 2.4. Regarding unit weight distribution (fig.2.13a) a clear peak of cases is identifiable at $\gamma[kN/m^3] \sim 20$. In agreement with this result, the resulting average unit weight by equation 2.4 was $\sim$19 kN/m^3. On the contrary, the friction angle distribution shows a reverse trend with a decreasing number of cases with the increasing friction angle. The average value computed for this parameter by equation 2.4 was $\sim$ 38°. This outcome is geotechnically reliable. Indeed, as previously mentioned, granular soils are characterized by a predominant frictional shear strength compared to cohesive materials for which a smaller value (i.e., 21°) was computed
- geometric average (eq.2.5) was used to derive an average cohesion. Also in this case, the collected number of cases is not sufficient for having a comprehensive representation of the real variability of this parameter. Nevertheless, since shear strength of granular soils is mainly controlled by friction between the particles rather than cohesion among them, it can be assumed that this parameter is secondary in the framework of the geotechnical characterization of this material type. The average cohesion calculated for granular soils is $2.4e^{-2}$ MPa ($\sim$24kPa), i.e., approximately one order of magnitude minor than the value computed for cohesive materials

From the computed peak friction angle and cohesion, corresponding residual values were derived.

The full list of parameters is finally summarized in table 2.9.

Table 2.9: *Final values computed for unit weight, Poisson's coefficient, cohesion, and friction angle for loose materials*.

PARAMETER	CORRESPONDENT CALCULATED VALUE
Unit weight (ɣ) – [kN/m^3]	19
Cohesion (c) – [kPa]	24
Friction angle (ϕ) – [°]	38
Residual cohesion (c_{res}) – [kPa]	2.4
Residual friction angle (ϕ_{res}) – [°]	19

2.3.4.3 Selection of values for shear wave velocities and impedance contrasts

Shear wave velocities for loose soils were collected from literature to identify two different representative values for this parameter. The distribution summarizing the collected v_s data is in figure 2.14.

From figure 2.14 it can be observed that cases span between 125 m/s and 700 m/s. This result can be interpreted as the effect of the natural compositional variability of loose soils (depending on percentages of sand/gravels/silts/clays into the soil mixture) as well as the densification state in which they are found (especially in the case of sandy materials).

Distribution in figure 2.14 was used to verify the reliability of the shear wave velocities computed by inverting the expression of the IC (eq. 2.7) and by assuming a shear wave velocity of 800 m/s for the rocky bedrock.

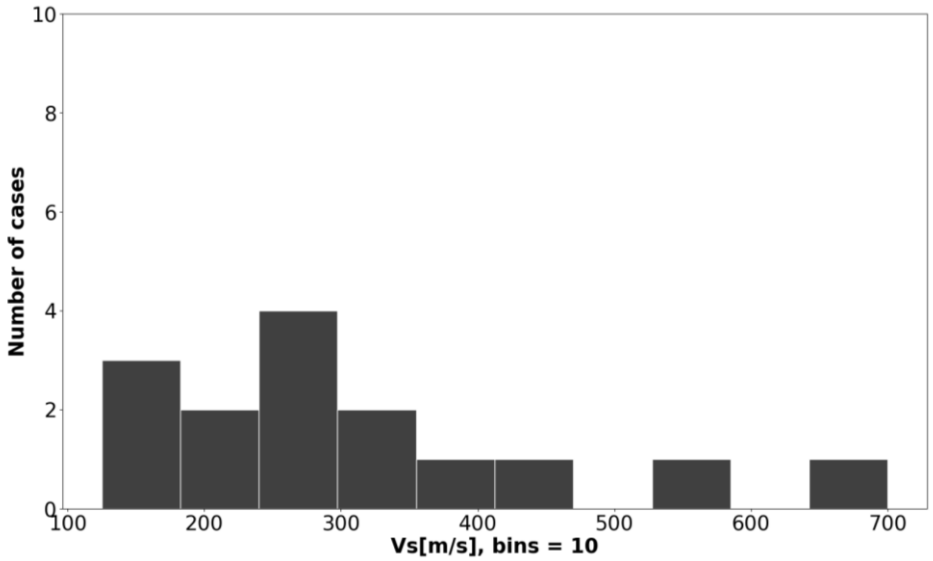

Figure 2.14: *Distribution of shear wave velocities for loose soils (15 cases) from literature (Mode: 300 m/; Mean: 305.5 m/s; Median: 275 m/s).*

A sequence of IC values between 1.5 and 4 each 0.5 was considered in order to derive v_{land} values for loose soils. The performed sequence of calculations is summarized in table 2.10.

From table 2.10 it can be noticed that all the calculated values are consistent with the distribution in figure 2.14. Expert judgement was used to select two velocity values among

those reported in table 2.10: the maximum resulting value (i.e., IC =1.5) and a smaller value corresponding to an IC = 2.5.

Table 2.10: *Summary of shear wave velocities for landslides involving loose soils. Landslide density (ρ_{land}) was obtained by converting the unit weight selected in the paragraph 2.3.4.2. In the « green » cells there are the values consistent with distribution in figure 2.14.*

IC	v_{bed}[m/s]	ρ_{bed} [kg/m^3]	ρ_{land} [kg/m^3]	v_{land}[m/s]
1,5	800	2230	1975	602.4
2	800	2230	1975	451.8
2,5	800	2230	1975	361.5
3	800	2230	1975	301.2
3,5	800	2230	1975	258.2
4	800	2230	1975	225.9

2.3.4.4 Parameter values computed by analytical equations

Table 2.11a-b summarizes the two sets of parameters computed by varying the shear wave velocity between the selected two values (cf. paragraph 2.3.4.3). As previously done for rocks and cohesive soils, G, E and B were computed by inverting/applying equations 2.6, 2.8 and 2.9 and by assuming ν = 0.25. On the contrary, peak and residual values for tension cut-off (t, t_{res}) were calculated according to equation 2.11.

Table 2.11: *Summary of the parameters calculated for landslide involving cohesive soils assuming different shear wave velocity values (a-b).*

a) Loose soil, Landslide : IC = 1.5, v_s = 602.4 m/s, ρ = 1975 kg/m^3, ν = 0.25	
Mohr-Coulomb's tension cut-off (t) - [kPa]	31
Residual Mohr-Coulomb's tension cut-off (t_{res}) - [kPa]	6.9
Shear modulus (G_0)-[MPa]	720
Elastic modulus (E)-[MPa]	1800
Bulk modulus (B)-[MPa]	1200

b) Loose soil, Landslide : IC = 2.5, v_s = 361.5 m/s, ρ = 1975 kg/m^3, ν = 0.25	
Mohr-Coulomb's tension cut-off (t) - [kPa]	31
Residual Mohr-Coulomb's tension cut-off (t_{res}) - [kPa]	6.9
Shear modulus (G_0)-[MPa]	260
Elastic modulus (E)-[MPa]	650
Bulk modulus (B)-[MPa]	430

2.3.4.5 Average shear modulus decay curve inferred for loose soils

The geotechnical characterization of loose soils is concluded by defining an average G/G_0 curve. As for rocks and cohesive materials, curves related to loose materials (36 in total) derived in the framework of activities for the III-level microzonation of 140 municipalities hit by the 24 August 2016 Magnitude 6 seismic event occurred in Central Italy (OPCM24/2017) were selected (source : www.centromicrozonazionesismica.it). Then, these curves were digitalized in WebPlotDigitizer 4.5 (Rohatgi, 2021) in order to compute average strains [%]

corresponding to pre-fixed G/G_0 values. Computed average values, as well as the resulting approximated curve by the Hardin & Drnevich (1972) model are in figures 2.15a-b.

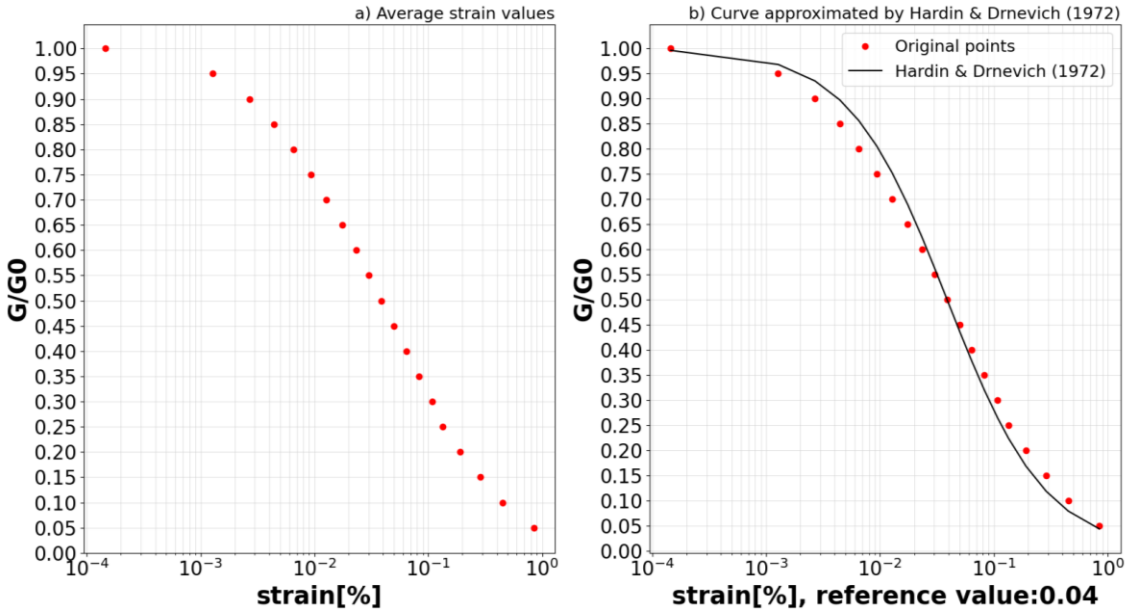

Figure 2.15: *Average strain values computed for fixed G/G_0 values (a) and (b) shear modulus decay curve approximated by the Hardin & Drnevich (1972) model for loose soils.*

2.4 Design of slope sheared-slope configurations

Real landslides are differentiated not just by their geological composition, geometry, and failure mechanism but also by the location of the crown and main scarp with respect to the slope face. As it regards rotational and translational slides, it is possible to sketch 3 main slope configurations by portioning them into different percentages of unstable mass:

1) configuration n.1 (fig. 2.16 a-b): the landslide crown is located approximately at the level of the slope crest and the unstable mass involves the total slope length (L_{slope}). In this case it is possible to assume that 100% of the L_{slope} is involved by the unstable mass (given by: [L_{land}/L_{slope}] x 100 % and being L_{land} = L_{slope}). Documented real cases representative of this configuration type are for instance the Büyükçekmece landslide in Turkey (Martino et al., 2018) and the Las Colinas landslide in El Salvador (García-Rodríguez & Malpica, 2010). On smaller scale, this type of landslides can occur in presence of slope debris covering the total slope length that once triggered (earthquakes, rainfall) give rise to shallow planar landslides
2) configuration n.2 (fig. 2.16 c-d): the landslide crown is located along the slope at various distances from the slope crest (it changes from case to case) generating landslides involving mainly the slope bottoms. Configuration n.2 is typical of landslides caused by road cuts. Martino et al. (2019) report that as consequence of the 2016-2017 Central Italy seismic sequence, approximately 70% of the triggered landslides detached from road cuts impacting transportation routes. A documented case for con-

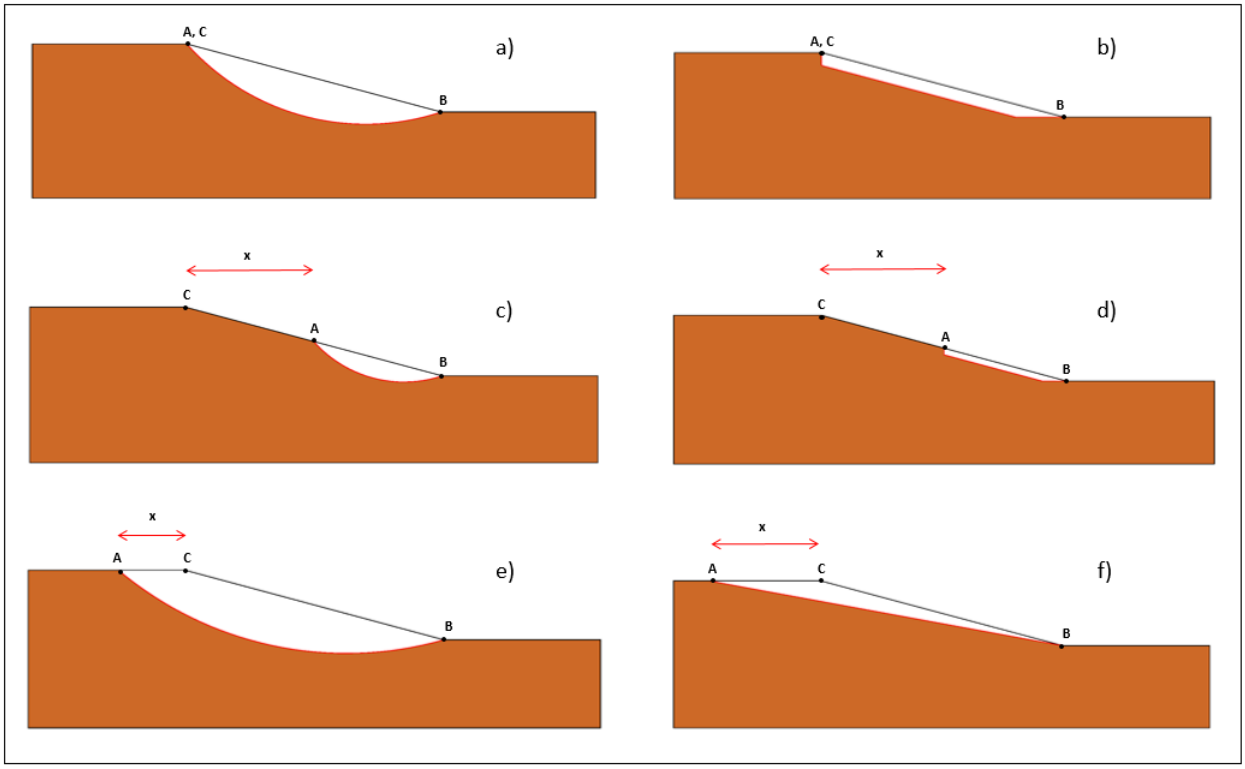

***Figure 2.16**: Schematization of the different configurations identified for rotational (a, c, e) and translational (b, d, f) landslides involving simplified step-like slopes. In the figures: C= slope crest, A= landslide top, B = landslide tip, CB = L_{slope}, AB = L_{land}, x = horizontal crown-crest distance.*

figuration n.2 is the Diezma landslide, in Spain, whose instability was caused by the construction of the A-92 highway (Delgado et al., 2015). Evidence of co-seismic landslides clustering at slope toes are also documented by Rault et al. (2019) and Meunier et al. (2008) in the epicentral areas of the Northridge, California (1994), Chi-Chi, Taiwan (1999), and Wenchuan, China (2008) earthquakes. Rault et al. (2019) interpret this pattern as the result of the combination of specific geological conditions due to the presence of highly fractured or weathered materials near major fault zones where highest deformations occur. Due to the high variability of the crown – crest distance that can be found for real landslides, a simplification was necessary to draw simplified landslide prototypes. More in particular, it was assumed: $L_{land} = L_{slope} / 2$ (i.e., 50% of slope length is involved into the slope movement)

3) <u>configuration n.3</u> (fig. 2.16 e-f) represents landslides whose crown is extended beyond the slope crest. Since as previously explained (cf. paragraph 1.2.1), slope crest is a crucial topographical point where complex amplification pattern can occur; this configuration was here accounted to include this group of effects. At this regard, configuration n.1 was modified by moving the landslide crown beyond the crest of an amount equal to $L_{land}/4$. In this manner, the portion of slope affected by the landslide movement becomes more than 100% due to $L_{land} > L_{slope}$. For geometrical reasons (cf. paragraph 2.5), the shape of the sliding surface designed for translational landslides in configuration n.3 it is not parallel to the slope face as for configurations n. 1 and 2, but

it defines a wedge – like landslide with decreasing thickness in the downstream direction

2.5 Sizing of geometries for the landslide-slope prototypes

To design 2D landslide prototypes it was assumed that:

1) slope profiles have a simplified step-like morphology that can be described by slope angle (α), slope length (L_{slope}) and height (H), as schematized in figure 2.17. According to this representation, α is the clockwise angle between the horizontal and the slope face; H is the altitude difference between the slope crest and the slope toe ($H = y_C - y_B$) and L_{slope} is the distance between the crest and the toe measured along the slope dip direction
2) to simplify the design process, circular geometries are used for representing the sliding surfaces of rotational slides, while planar geometries are employed for translational slides. The parameters describing dimension and morphology of the landslides are thickness and length as well as their ratio and the volume (fig. 2.18). The thickness is here intended as the perpendicular distance between the slope and the sliding surface taken at $L_{land}/2$, whereas the length is the distance between the landslide top and tip. Since the models here represented are in « 2D », the designing processes cannot account directly for the 3D parameter « volume ». For this reason, the selected volume values were used to compute the parameter « L_{land} » through the L-V correlation inferred by Domej et al. (2020, fig.7c) on the basis of volume and length values measured for worldwide landslides

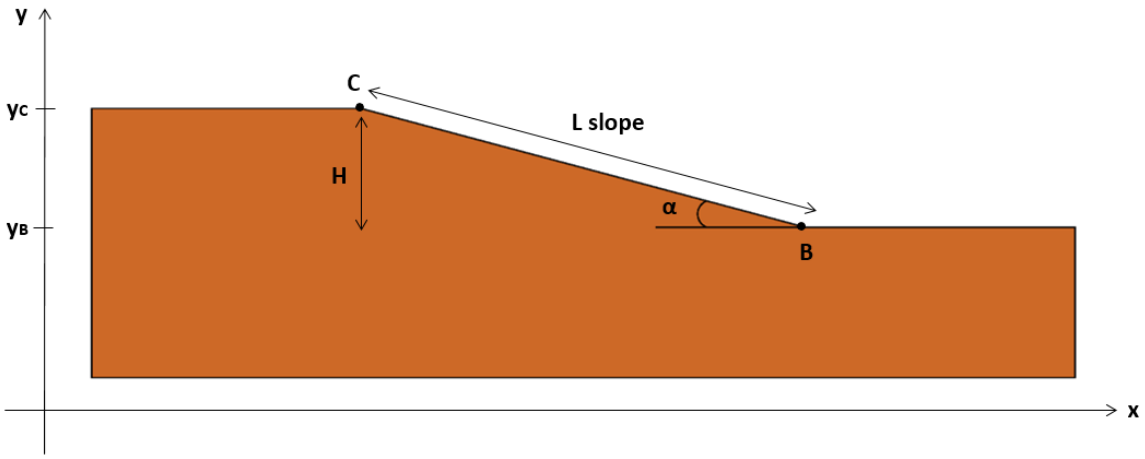

Figure 2.17: *Identification of the main geometrical parameters characterizing step-like slopes.*

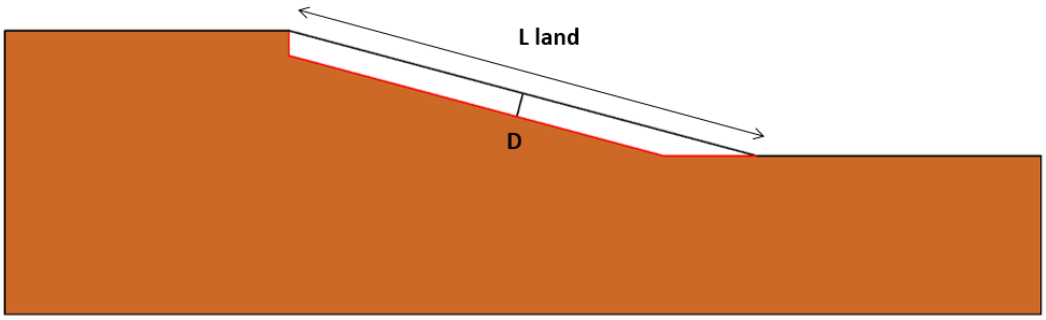

***Figure 2.18**: Identification of landslide length and thickness in a generic translational landslide model.*

Slope angles, D/L_{land} and volume values computed by statistical analyses on data collected from literature review are summarized below:

1) slope angle: 15° and 30°
2) D/L_{land}: 0.05 (for translational landslides) and 0.16 (for rotational landslides)
3) volume: 10 m^3, 10^3 m^3, 10^5 m^3

In addition, before designing 2D landslide prototypes it is necessary:

- to infer missing parameters for slope/landslide dimensioning, i.e., D and L_{land} taken singularly and slope H
- to identify all possible landslide/slope geometries which can be generated by the combination of the above-mentioned parameters

The three different procedures were used to compute landslide length, depth, and slope height values for the three considered landslide configurations are presented below. Each of them was repeated to consider all the possible combinations in terms of D/L, volume, and slope angle as in table 2.12 a-c'.

***Table 2.12:** Steps for the definition of landslide models in configuration 1 (a-a'), 2 (b-b') and 3 (c-c').*

a) ROTATIONAL LANDSLIDES IN CONFIGURATION N.1
1) Given D/L_{land} = 0.16
2) Given the volume = 10 m^3
3) Given the slope angle = 15°
4) Given L = L_{land} = L_{slope}, calculate L by the L-V regression proposed by Domej et al. (2020)
5) Compute D by inverting the D/L_{land} ratio fixed at 0.16 having computed L_{land} in the step 4)
6) Compute H as L_{slope} x sin(α) having computed L_{slope} in the step 4) and according to figure 2.17
7) Repeat steps 1) – 3) x 2 by assuming before V = 10^3 m^3 and then V = 10^5 m^3
8) Repeat steps 1) -7) by assuming α = 30°

a') TRANSLATIONAL LANDSLIDES IN CONFIGURATION N.1
1) Given $D/L_{land} = 0.05$
2) Given the volume = 10 m^3
3) Given the slope angle = 15°
4) Given $L = L_{land} = L_{slope}$, compute L by the L-V regression proposed by Domej et al. (2020)
5) Compute D by inverting the D/L_{land} ratio fixed at 0.05 having computed L_{land} in the step 4)
6) Compute H as L_{slope} x sin(α) having computedL_{slope} in the step 4) and according to figure 2.17
7) Repeat steps 1) – 3) x2 by assuming $V = 10^3$ m^3 and then $V = 10^5$ m^3
8) Repeat steps 1) -7) by assuming α = 30°

b) ROTATIONAL LANDSLIDES IN CONFIGURATION N.2
1) Given $D/L_{land} = 0.16$
2) Given the volume = 10 m^3
3) Given the slope angle = 15°
4) Use L_{slope} computed in table 2.9a for the reference volume class and derive L_{land} as $L_{slope}/2$
5) Compute D by inverting the D/L_{land} ratio fixed at 0.16 having computed L_{land} in the step 4)
6) Compute H as L_{slope} x sin(α) having computed L_{slope} in the step 4) and according to figure 2.17
7) Repeat steps 1) – 3) x2 by assuming $V = 10^3$ m^3 and then $V = 10^5$ m^3
8) Repeat steps 1) -7) by assuming α = 30°

b') TRANSLATIONAL LANDSLIDES IN CONFIGURATION N.2
1) Given $D/L_{land} = 0.05$
2) Given the volume = 10 m^3
3) Given the slope angle = 15°
4) Use L_{slope} computed in table 2.9a' for the reference volume class and derive L_{land} as $L_{slope}/2$
5) Compute D by inverting the D/L_{land} ratio fixed at 0.05 having calculated L_{land} in the step 4)
6) Compute H as L_{slope} x sin(α) having computed L_{slope} in the step 4) and according to figure 2.17
7) Repeat steps 1) – 3) x2 by assuming $V = 10^3$ m^3 and then $V = 10^5$ m^3
8) Repeat steps 1) -7) by assuming α = 30°

c) ROTATIONAL LANDSLIDES IN CONFIGURATION N.3
1) Given $D/L_{land} = 0.16$
2) Given the volume = 10 m^3
3) Given the slope angle = 15°
4) Having computed L_{slope} for the reference volume as in table 2.9a calculate analytically L_{land} according to figure 2.19
5) Compute D by inverting the D/L_{land} ratio fixed at 0.16 having computed L_{land} in the step 4)
6) Compute H as L_{slope} x sin(α) having computed L_{slope} in the step 4) and according to figure 2.17
7) Repeat steps 1) – 3) x2 by assuming $V = 10^3$ m^3 and then $V = 10^5$ m^3
8) Repeat steps 1) -7) by assuming α = 30°

c') HIGH-ANGLE SLOPE TRANSLATIONAL LANDSLIDES IN CONFIGURATION N.3
1) Given $D/L_{land} = 0.05$
2) Given the volume = 10 m^3
3) Given the slope angle = 30°
4) Having computed L_{slope} for the reference volume as in table 2.9a' calculate analytically L_{land} according to figure 2.19
5) Compute D by inverting the D/L_{land} ratio fixed at 0.05 having computed L_{land} in the step 4)
6) Compute H as L_{slope} x sin(α) having computed L_{slope} in the step 4) and according to figure 2.17
7) Repeat steps 1) – 3) x2 by assuming $V = 10^3$ m^3 and then $V = 10^5$ m^3

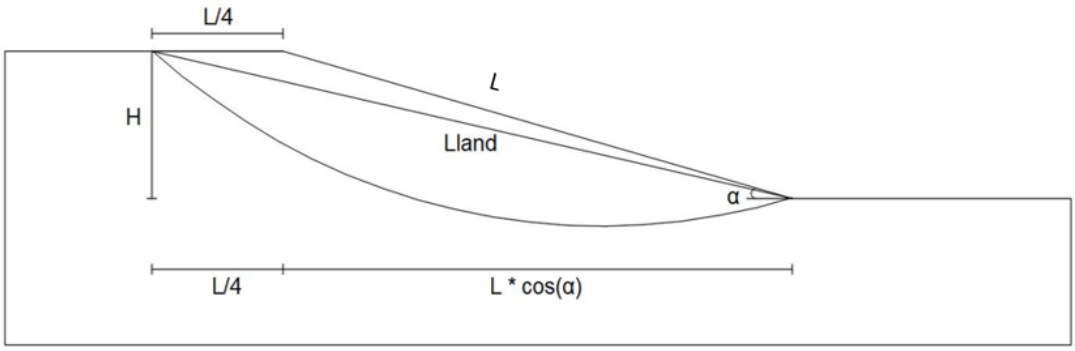

$$L_{land} = \sqrt{(H^2 + (L/4 + (L\cos\alpha))^2}$$

Figure 2.19: *Calculation of L_{land} for rotational/translational landslides in configuration n.3.*

It is necessary to specify that the landslide extension behind the crown (i.e., the tip-to-top planar distance) was arbitrarily fixed at $L_{slope}/4$ for all the rotational landslides and the high-angle slope translational landslides. Due to geometrical constraints, for low-angle slope translational landslides, it was not possible to maintain this distance. Therefore, the following approach was adopted:

- the extension of the landslides beyond the slope crest was increased up until it reached $L_{slope}/2.25$. This specific value was determined by progressively increasing the length of the landslides until their resulting D/L_{land} was as close as possible to the theoretical value adopted for other configurations (i.e. a ratio of 0.04 instead of 0.05). These landslides represent the only cases where L_{land} and D values are measured directly from the designed geometry, rather than being calculated analytically as in table 2.12 a-c'
- the shape of the sliding surface was changed from planar and parallel to the slope face to assume the shape schematized in figure 2.16f for both low and high-angle translational landslides in configuration n.3. This choice was linked to the necessity of representing in a correct manner parameters calculated according to the procedure in table 2.12c'. In addition, the resulting 2D « wedge » slide appears more kinematically compatible with respect to real landslides. Indeed, this geometry can be

representative of landslides occurring in the presence of alternance of rocks-soils or rocks with different shear strength properties which layering is less dip than the slope

Finally, a total number of 36 simplified landslide geometries was generated in AutoCAD (Autodesk). Each landslide was assigned an identification code indicating:

- failure mechanism and consequently D/L_{land}. In particular: « T » indicates translational landslides and « R » indicates rotational landslides
- number of configuration: from 1 to 3 as explained in paragraph 2.4
- volume: « 101 » is 10^1 m^3; « 103 » is 10^3 m^3 and « 105 » is 10^5 m^3
- slope angle « 15 » means α= 15° and «30 » means α= 30°

An example is reported below (fig.2.20).

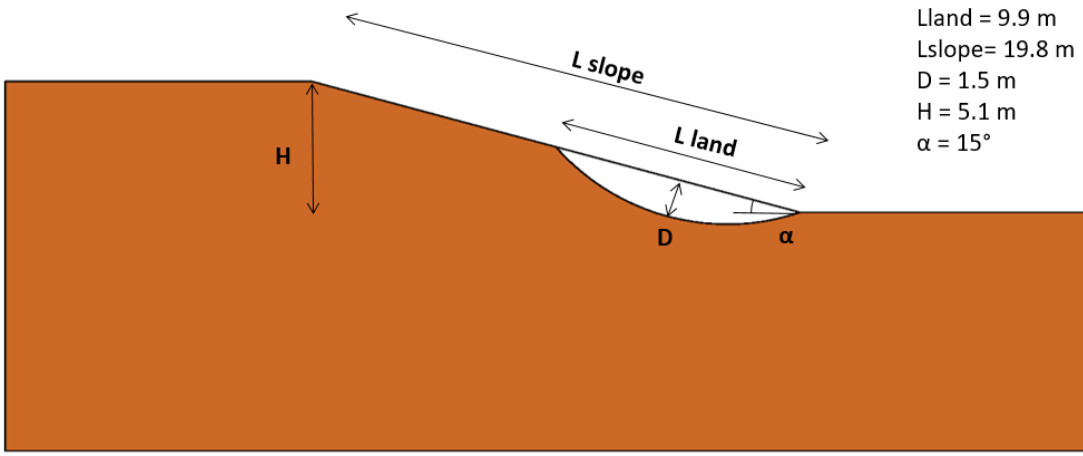

Figure 2.20: *Geometry « R2_103_15 » inferred by the procedure in table 2.12b.*

2.5.1 Sheared-slope prototypes resulting from the combination of slope/landslide schemes and geotechnical parameters

The final step to define sketched landslide slopes was to combine the 36 obtained geometries with the 3 groups of materials (i.e., cohesive soils – CS, loose soils – LS, rocks – R) and their corresponding properties.

The combination of all the parameters (as in table 2.13) resulted in a total number of 216 sheared-slope prototypes. Among them, 108 models are rotational landslides, whereas the remaining 108 represent translational ones.

Table 2.13: *Example of the combination of the geometry « R1_101_15 » with geotechnical parameters.*

GEOMETRY	MATERIAL	IC
R1_101_15	Cohesive Soils - CS	2
		4
	Loose Soils - LS	1.5
		2.5
	Rock-type Materials - R	1.5
		2.5

2.6 Forcing dynamic signals

In the present paragraph seismic inputs used to compute earthquake-induced displacements of landslide prototypes (cf. chapter 3) are presented.

For studies on earthquake-induced effects, the selection of seismic signals can go towards two directions:

- use of real accelerograms recorded during earthquakes
- use of synthetics signals

Real accelerograms allow simulating more accurately the interaction between landslide bodies and dynamic triggers in the frequency and energy spectrum of interest. Nevertheless, the latter generally have longer duration that can lead to large computation times. For this reason, synthetics signals were adopted in this study. Reasons that support this choice are:

- large number of landslide prototypes to be analysed: if the analytical methodology here adopted for computing earthquake-induced displacements (cf. chapter 3 part 1) is not affected by total duration of the signals, numerical stress-strain analyses (cf. chapter 3 part 2) are significantly impacted by this feature, becoming very time-consuming when long-duration signals are introduced
- necessity to select a sufficient number of signals: the designed landslide prototypes are characterized by a wide dimensional variability, consequently, the number of selected seismic signals must be large enough to represent a sufficiently wide mean period interval to ensure the reaching of peculiar characteristic periods ratios (cf. paragraph 3.7.1.2) of the landslides that are fundamental for seismic displacements interpretation

For these reasons, equivalent signals derived through the LEMA_DES (Levelled-Energy Multifrequential Analysis for Dynamic Equivalent Signals) approach (Lenti & Martino, 2010) were finally considered. The latter approach aims at generating multifrequential signals shorter than the real accelerograms from which they are derived to reduce calculation times satisfying criteria of spectral, energetic, and kinematic equivalence (Lenti & Martino, 2010). The use of LEMA_DES signals in the framework of earthquake-induced landslide studies is documented in literature by several publications (such as Bozzano et al., 2010; Bozzano et al., 2011b; Lenti & Martino 2012,2013; Martino et al., 2016 and Martino et al., 2018).

A set of 17 different LEMA_DES signals was used in this study. The original earthquakes from which they were derived (source: European Strong-Motion Database) are indicated in table 2.14.

The 17 selected LEMA_DES signals are characterized by duration between 0.25 and 9.11 s and mean periods (Rathje et al., 1998) ranging from 0.08 to 2.04 s. On the contrary, the Arias Intensity of the inputs is almost constant, remaining in the order of magnitude of 0.1 m/s. This particular AI level is not referred to a specific seismic scenario. Indeed, the choice of this energy level was done as: i) lower AI values may not have been enough to induce relevant displacements in the designed landslides prototypes, ii) higher AI could have induced too many failures, preventing from the study of earthquake-induced displacements, which is the main goal of this study. A nearly constant AI level implies that this study will not be able to explore the variability of seismically-induced displacements with the AI level. Nevertheless, understanding this variability is crucial for offering reliable predictions in seismic scenarios different from those investigated here. As a result, this aspect will deserve further investigations in future. PGA and PGV for each input are also reported in table 2.14. Velocity time histories of selected inputs are in Annex 1.

Table 2.14: *Characteristic of the LEMA_DES signals considered in this study. Earthquake: is the location of the original earthquake from which they were derived (for which is also reported the magnitude (M_w) and the date of occurrence), PGA is the peak ground acceleration, PGV is the peak ground velocity, AI is the Arias Intensity and T_m is the signal mean period (Rathje et al., 1998).*

Original earthquakes			**LEMA_DES signals**					
Earthquake	**Date**	**M_w**	**Name**	**Duration [s]**	**PGA [m/s^2]**	**PGV [m/s]**	**AI [m/s]**	**T_m [s]**
South_Iceland (aftershock)	21/06/2000	6.49	**a**	9.11	0.92	1.29	0.12	2.04
Montenegro	15/04/1979	7	**b**	5.65	1.65	0.96	0.15	1.42
Izmit	17/08/1999	7.64	**c**	4.57	1.72	0.91	0.12	1.09
Umbria_Marche	26/09/1997	5.72	**d**	3.43	1.86	0.76	0.19	0.84
Friuli (aftershock)	11/09/1976	5.6	**e**	3.93	1.42	0.43	0.16	0.67
Campano_Lucano	23/11/1980	6.93	**f**	7.83	1.38	0.44	0.12	0.56
Friuli (aftershock)	11/05/1976	4.99	**g**	1.83	2.11	0.69	0.11	0.44
Montenegro	15/04/1979	7	**h**	1.73	2.41	0.48	0.16	0.41
Friuli (aftershock)	11/09/1976	5.6	**i**	4.13	1.39	0.24	0.18	0.34
South_Iceland (aftershock)	21/06/2000	6.49	**l**	1.45	3.49	0.45	0.16	0.30
Kozani	13/05/1995	6.61	**m**	0.75	2.71	0.44	0.12	0.26
Umbria_Marche (aftershock)	03/04/1998	5.19	**n**	0.91	2.96	0.37	0.11	0.19
Umbria	29/04/1984	5.68	**o**	0.45	2.99	0.32	0.12	0.16
Umbria_Marche (aftershock)	03/10/1997	5.33	**p**	0.87	4.33	0.32	0.21	0.16
Umbria_Marche (aftershock)	06/10/1997	5.58	**q**	0.61	3.79	0.22	0.13	0.13
South_Iceland	17/06/2000	6.57	**r**	0.55	4.87	0.26	0.16	0.11
Umbria_Marche (aftershock)	16/10/1997	4.39	**s**	0.25	7.14	0.22	0.35	0.08

Chapter 3: Computation of seismic displacements via analytical and numerical methods

PART 1: Newmark's method– based analysis

This chapter focuses on the computation of the expected co-seismic displacements for the 216 simplified landslide prototypes presented in chapter 2, using conventional methods. Before that, stability in static conditions (i.e., in the absence of seismic shaking) is assessed for each landslide prototype by calculating the « Safety Factor (SF) » according to the assumptions of limit equilibrium methods.

3.1 Sheared-slopes stability under static conditions

Slope stability along existing (second-time landslides) or hypothesized (first-time landslides) sliding surfaces is evaluated in the common engineering-geology practice by the « Safety Factor (SF) » parameter, defined as the ratio between the available shear strength and the acting shear stress. When the shear strength opposed by the material overcomes the shear stress (i.e., SF > 1) the slope is stable. In the opposite situation (i.e., SF < 1), the slope is unstable, and the landslide movement may occur. Finally, when, shear strength is equal to shear stress (i.e., SF $\sim$ 1), it signifies critical stability conditions that require the consideration of stabilisation and reinforcement measures.

The SF can change over time because of force balance modifications caused by external perturbations (such as seismic shaking, rainfall, or human activities) that can bring the slope from equilibrium (stability) to disequilibrium conditions (instability).

Nowadays, several methods are available to compute SF for slopes. The choice of the most appropriate method depends on the failure mechanism and the shape of the sliding surface reconstructed or hypothesized for the landslide. At this regard, limit equilibrium methods are commonly used. More in particular:

- the methods by Fellenius (1927; 1936) and Bishop (1955) for circular sliding surface landslides
- the Janbu (1954)'s method for landslides with non-circular sliding surfaces
- the infinite slope method (Skempton & De Lory, 1957) for planar translational landslides

According to limit equilibrium methods, the landslide is regarded as a rigid block with an elastic-perfectly plastic behaviour for which the sliding starts once the maximum shear strength is exceeded. Moreover, the failure occurs simultaneously along all the points of the sliding surface and the unstable mass is not subjected to internal deformations during the movement (i.e., rigid body assumption).

Hypotheses at the basis of limit equilibrium approaches are quite restrictive and for this reason are difficult to generalize. Indeed, the non-deformability can be assumed only for few categories of materials such as intact and stiff rocks or over consolidated clays, whereas it is less appropriate for weak rocks or unconsolidated soils characterized by a higher deformability. Additionally, in real conditions, processes leading to slope failures are not immediate and simultaneous but, in most of the cases, they occur progressively over time and space. Indeed, it is more common to observe a progressive increase of permanent deformations until a generalized collapse of the slope. Studying such types of processes is however complex and cannot be performed via analytical methods since it requires the analysis of the evolution of the stress-strain field by numerical methods (Lenti & Martino, 2012).

Nevertheless, methods based on the limit equilibrium assumptions are largely employed by engineers and engineering-geologists since they are easier to be managed compared to numerical methods that require a higher degree of expertise. The following paragraphs will provide a brief introduction to the selected methods used for performing slope stability analyses for the designed landslide prototypes. Then, the results of these analyses are presented in paragraph 3.1.3.

3.1.1 Slope stability analyses on rotational landslides

Conventional methods by Fellenius (1927; 1936) and Bishop (1955) are commonly adopted by engineering-geologists to evaluate the predisposition of slopes to first/second-time rotational landslides.

The latter methods consist in dividing the landslide body into vertical slices (fig. 3.1) for which the force balance is separately evaluated. Finally, the SF is computed as the ratio of the sum of the shear strengths and that of the shear stresses at the base of each slice. This concept was firstly introduced by Fellenius (1927; 1936), which method is also known as the ordinary method of slices.

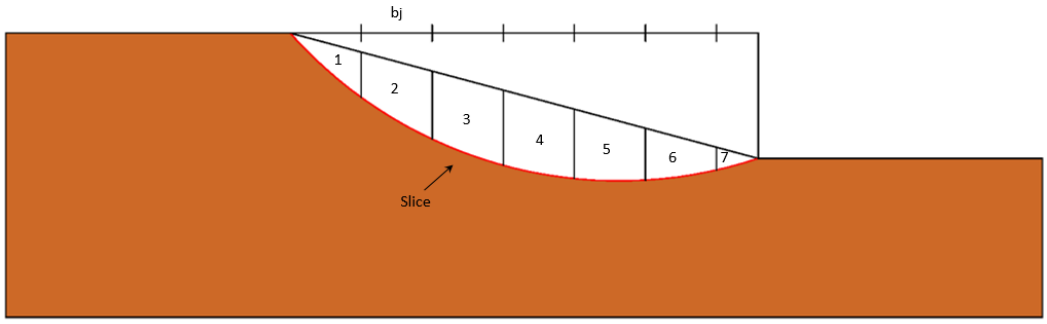

Figure 3.1: *Example of landslide volume portioning into slices.*

To explain the conceptual difference between the two methods a short premise must be done.

Theoretically, slope-landslide systems are considered stable or in equilibrium when the sums of vertical (F_v) and horizontal (F_h) forces and the one of moments (M) are null (i.e., $\sum F_v = 0$, $\sum F_h = 0$ and $\sum M = 0$). The above-mentioned forces include forces acting along the predefined sliding surface (such as slice weight components) and forces acting between two

slices (i.e., perpendicular, or tangential forces due to adjacent slices interactions) as schematized in figure 3.2. Due to the higher number of unknowns compared to the number of equations, the equilibrium problem is generally indefinite.

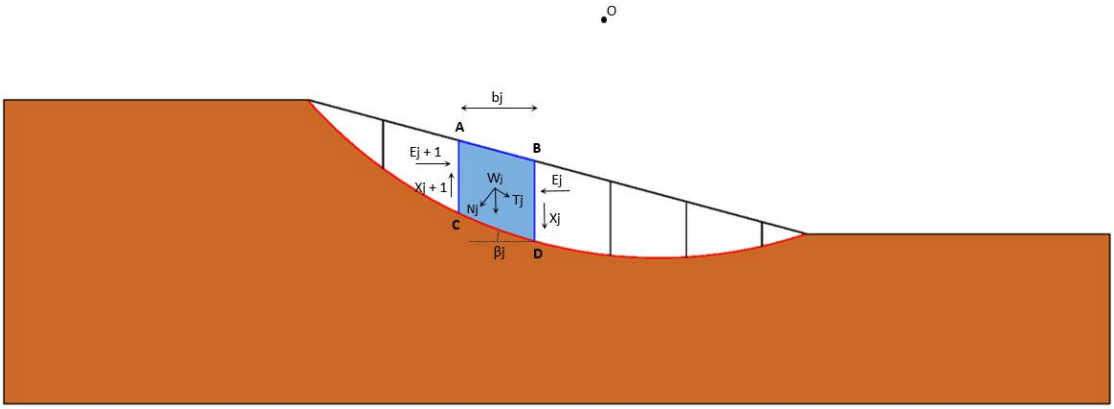

Figure 3.2: *Sketch illustrating forces acting at the slices surfaces. « O » is the center of rotation of the landslide body. Due to the perfectly circular shape of the sliding surface, « O » corresponds to the center of the designed arc of circumference (i.e., failure surface).* W_j *is the slice weight and* T_j *and* N_j *are its tangential and normal components respectively.* E_j*+1 and* E_j *are the normal interslice forces at the right and left sides of the slice, whereas* X_j *+1 and* X_j *are the tangential interslice forces. Finally,* β_j *quantifies the inclination of the segment of sliding surface delimitating the slice at its base and the distance CD measured along the arc is* l_j *in the equation 3.1.*

Fellenius (1927; 1936) and Bishop (1955) solved the equilibrium problem by two different approaches:

1) Fellenius (1927; 1936) satisfies moment balance only and neglects interslice forces. Consequently, he provides with a linear SF equation (Fredlund & Krahn, 1977). Fellenius's method is therefore extremely simple. In this method, the Newmark's principle of « action equal reaction » is not respected between slices because resultant interslice forces of adjacent slices do not have same intensity and direction (Fredlund & Krahn, 1977). The SF calculated according to this approach is following reported (eq. 3.1) in the most simplified case of dry slopes in static conditions:

$$SF = \frac{\sum[(c_j * l_j) + (W_j * \cos\beta_j * \tan\phi_j)]}{\sum W_j * \sin\beta_j} \qquad \text{[Eq.3.1]}$$

where c_j and ϕ_j correspond to the cohesion and the friction angle of the material respectively

2) the simplified Bishop's method (1955) satisfies both the equations of vertical forces and that of the moment. The method neglects interslice shear forces assuming their resultant is zero and considers that a normal force adequately defines the interslice forces (Fredlund & Krahn, 1977). In this manner, the stability problem becomes indeterminate, and the calculation of the slope safety factor must be done by an iterative procedure (eq. 3.2):

$$SF = \frac{\sum[(c_j * b_j) + (W_j * \tan\phi_j)] * m_j}{\sum W_j * \sin\beta_j} \qquad \text{[Eq.3.2]}$$

with:

$$m_j = \frac{1}{[\cos\beta_j + \frac{\sin\beta_j * \tan\phi_j}{SF_{hypothesized}}]}$$

The SF computed by equation 3.2 is suitable for dry slopes and in the absence of seismic shaking. The iterative calculation proceeds by hypothesizing an initial value of the SF factor to assess the coefficient m_j. Then, the SF according to equation 3.2 is computed: the correct solution is the one for which the hypothesized SF and the calculated SF converge

3.1.2 Slope stability analyses on translational landslides

Slope stability analyses on translational landslides are generally performed by the infinite slope method (Skempton & De Lory, 1957). The latter, is particularly suitable for planar and shallow landslides that satisfy the following conditions:

1) the length of the landslide is much larger compared to its depth. Theoretically, the infinite slope model (fig. 3.3) would assume infinite dimensions of the length, however, this assumption is not realistic for natural slopes
2) the slope angle (β) is constant
3) the sliding surface is planar and parallel to the slope face
4) the material involved in landslide movement is homogenous and eventual layering must be parallel to the slope dip (i.e., according to a vertical homogeneity condition)

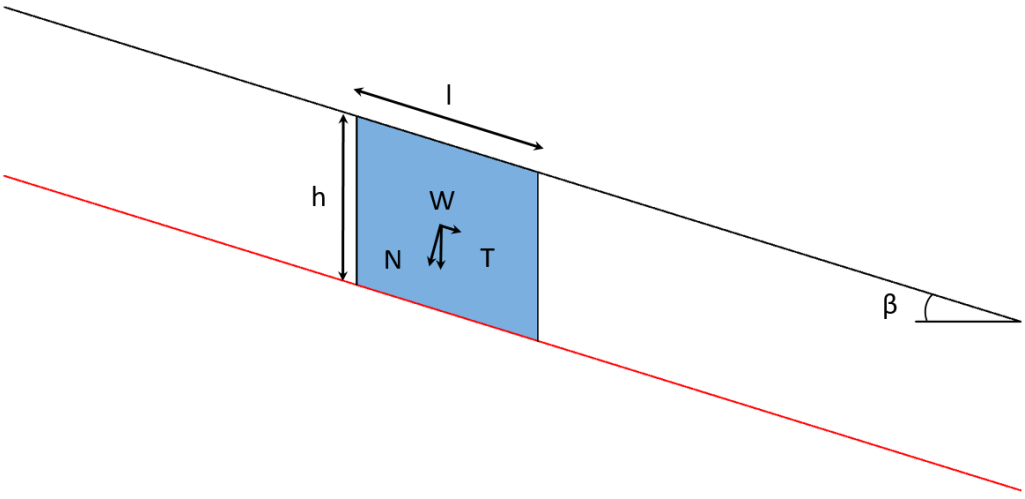

***Figure 3.3**: Sketch representation of the infinite slope model. In the picture, forces acting at the base of the sliding surface in a generic unit width (l =1) element are also shown.*

The static safety factor, according to the infinite slope method, is expressed by equation 3.3 for dry slopes under static conditions:

$$SF = \left(\frac{c}{\gamma h \cos\beta \sin\beta}\right) + \left(\frac{\tan\phi}{\tan\beta}\right) \quad \text{[Eq.3.3]}$$

where c, ɣ and ϕ are respectively the cohesion, the unit weight and the friction angle of the material.

3.1.3 Application to landslide prototypes

The methods presented in the previous paragraphs (cf. paragraphs 3.1.1 and 3.1.2) were used to compute safety factors for the landslide prototypes. More in particular:

- static SFs for rotational landslide prototypes were quantified by Fellenius's method (1927; 1936) rather than Bishop's method (1955). This choice significantly reduced the number of calculations required to assess initial static stability of the prototypes. It is reasonable to assume that results from the two methods would not have been too different. This assumption is supported by a previous study conducted by Skempton & Hutchinson (1969), in which they compared SFs computed for few real landslides by several limit equilibrium approaches. Among the landslides investigated by the two authors, the case study closest to the landslide geometries designed in this study is the Northolt landslide, characterized by a circular sliding surface and a D/L = 0.14. Skempton & Hutchinson (1969) used for the Northolt landslide both Fellenius's and Bishop's methods, obtaining very close SF values as output. Indeed, the first method returned a SF =0.94, whereas the second method, therefore considered less conservative, computed a SF = 1
- static SFs for « T1 » and « T2 » translational landslides were computed by adopting the infinite slope method. Indeed, these landslide configurations fully satisfy infinite slope method's hypotheses, since they are characterized by planar sliding surfaces and D/L = 0.05 (i.e., D << L). On the contrary, « T3 » models (cf. paragraph 2.5.1) do not satisfy hypotheses n.1 and 3 of the infinite slope method due to sliding surface – slope face different inclination that determines a not constant landslide thickness. In lack of more appropriate theoretical models representing wedge-like geometries, SFs for « T3 » models were computed as the ratio between the soil shear strength (according to the Mohr-Coulomb's equation) and the shear stress related to the shear component (T) of the landslide mass weight (eq.3.4):

  $$SF = \frac{[cl + (W\cos\beta \tan\phi)]}{W\sin\beta} \quad \text{[Eq.3.4]}$$

  where l is the length of the sliding surface and Wcosβ and Wsinβ are respectively the normal (N) and the shear (T) components of the weight (W)

As it regards geotechnical properties, since the limit equilibrium analysis does not account for material shear wave velocity or shear modulus, the SF computed for landslides involving a given material type (i.e., cohesive soils, loose soils, and rocks) are not altered by landslide-bedrock impedance contrast modifications. Indeed, the parameters of interest for SFs computation (i.e., cohesion, friction angle and density) were defined (cf. chapter 2) by

statistical approaches and are therefore independent from shear wave velocity modifications. In this manner, the number of calculations is reduced to 108.

To compute the SF of landslide prototypes, residual shear strength properties (i.e., c_{res}, ϕ_{res}) were used. Indeed, since the landslide prototypes here proposed aim at schematising real second-time landslides (i.e., landslides that have already experienced failure in the past), it can be assumed that at least along the sliding surface, the unstable material is found in residual strength conditions (i.e., post failure).

Variations of the geotechnical properties and/or of the geometrical conditions of landslide masses/slopes determine modifications of the SF. Since in this study, different combinations of geotechnical and geometrical parameters were assumed for designing the landslide prototypes (cf. paragraph 2.5.1), the results will be presented by comparing SF calculated for different models that differ for just one specific parameter to:

- emphasize the effect of the single parameter on the overall stability
- identify the combinations of parameters that are less favourable for equilibrium

Effect of geomechanical properties on the SF: figures 3.4 a-b show factors of safety distributions calculated for models « R1_103_15 » and « T1_103_15 ». In both cases, stability is verified for all the considered material types. Nevertheless, figures 3.4 a-b highlight that for medium volume – low angle landslides, stability is strongly affected by reductions of the material cohesion: indeed, low-cohesion materials (i.e., loose soils) are associated to the lowest SF values.

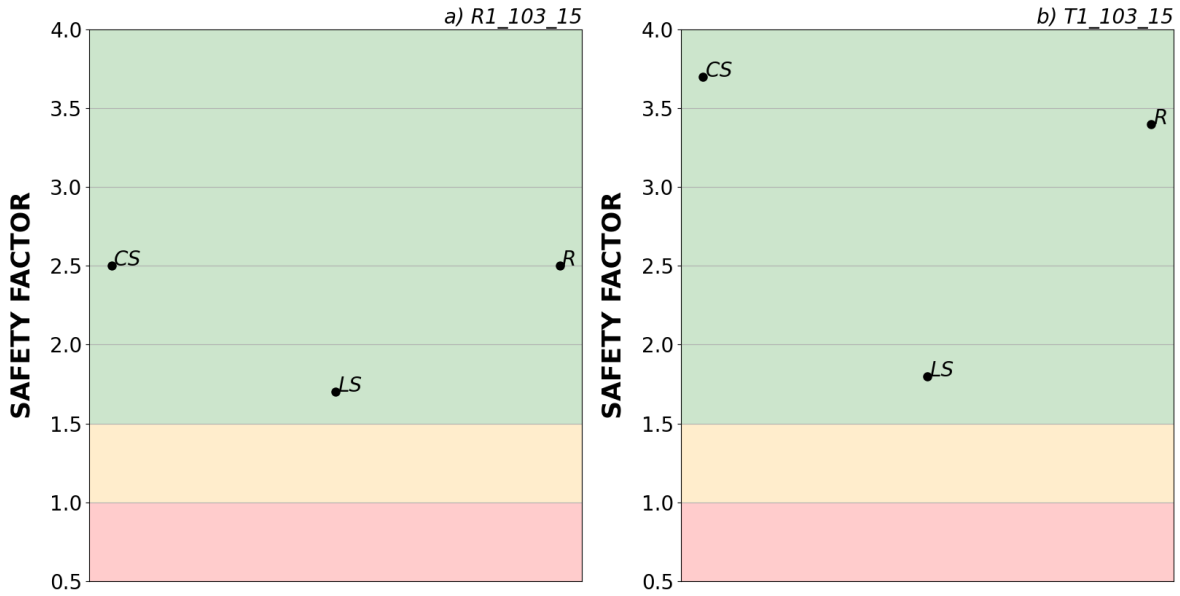

Figure 3.4: *Distributions of safety factors for models a) « R1_103_15 » and b) « T1_103_15 » computed for cohesive soils (CS), loose soils (LS) and rocks (R). In the plot: green area (SF > 1.5) indicates stability conditions, orange area (1 < SF < 1.5) indicates critical conditions, finally, red area (SF < 1) indicates unstable conditions.*

Effect of the volume: volume increase (from 10^3 to 10^5 m^3 in the selected examples) results in a drastic reduction of the static SF for all the considered material types (fig. 3.5a-b). Even if less evident compared to the previous cases (fig. 3.4a-b), the stability of large volume – low

angle landslides is more affected by variations of the material friction angle. Indeed, the lowest factors of safety are obtained either for rotational or translational landslides, when the lowest friction angle materials (i.e., cohesive soils) are introduced into the models. On the contrary, volume reductions (from 10^3 to 10 m^3) correspond to SF increasing (fig. 3.6a-b). In terms of SF variation, small volume – low angle landslides have similar behaviour to medium volume – low angle landslides. Indeed, also in this case the condition less favourable to stability is determined by the presence of low-cohesion materials.

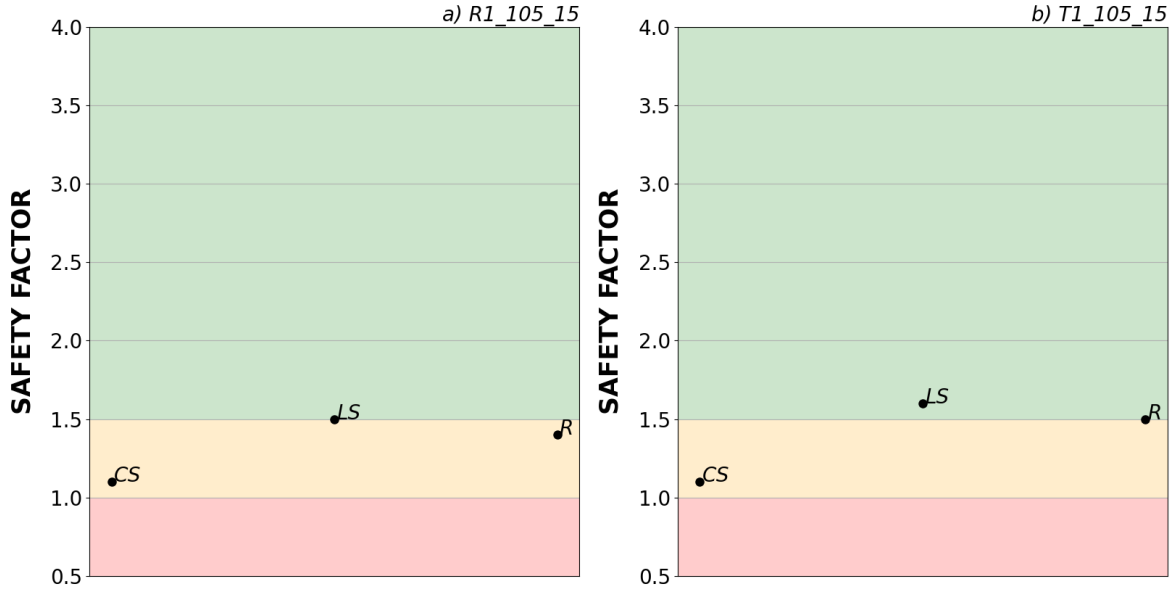

Figure 3.5: *Distributions of factors of safety for a) « R1_105_15 » and b) « T1_105_15 ».*

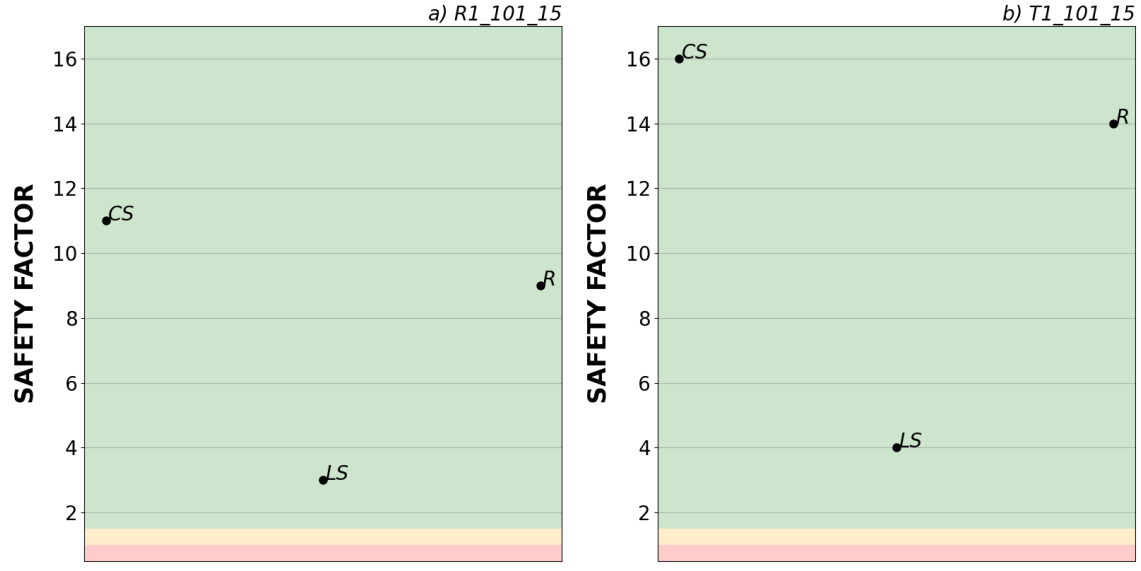

Figure 3.6: *Distributions of factors of safety for a) « R1_101_15 » and b) « T1_101_15 ».*

Effect of the slope angle: increasing the slope angle from 15° to 30° results in a reduction of slope stability, as can be observed by comparing figures 3.7a-b and 3.4a-b. When high slope angle is combined with large volume landslides, the decrease of SF results into slope instability in almost all cases (fig. 3.8a-b). According to these results, it can be concluded that landslide

models characterized by high slope angle – large volume combinations are those most prone to be destabilized. This group of models (i.e., already unstable in static conditions) will therefore be excluded from the application of Newmark's analysis that will be discussed in the next paragraphs. On the contrary, medium volume – high slope angle landslide models, experience SF reductions but remain in the stability domain, except when loose materials are considered.

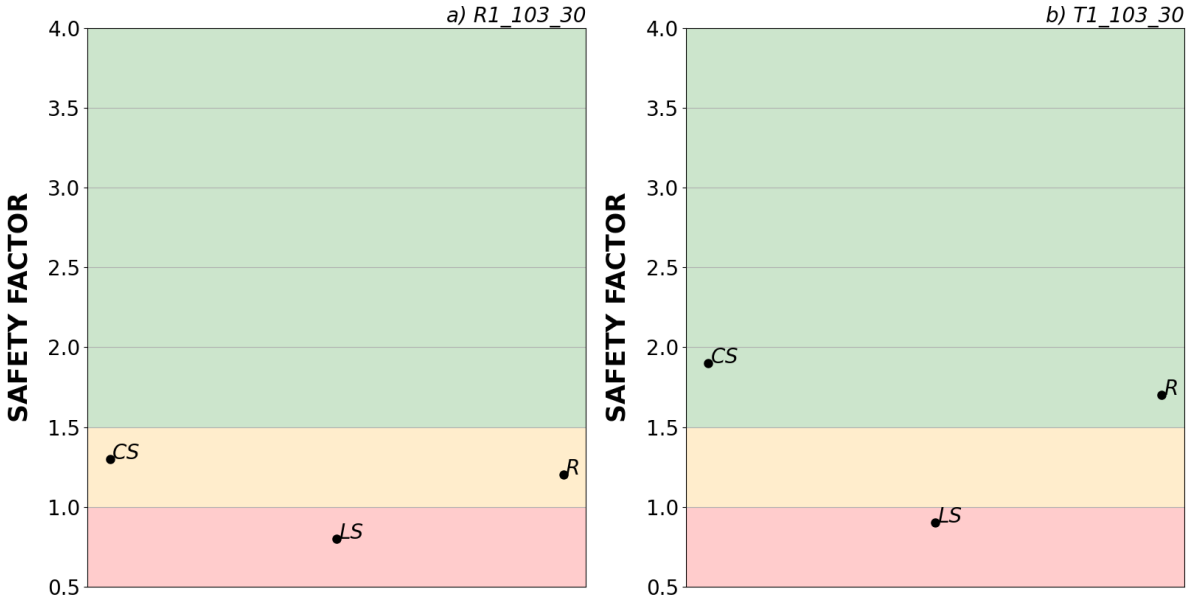

Figure 3.7: *SF distributions of the models a) « R1_103_30 » and b) « T1_103_30 ».*

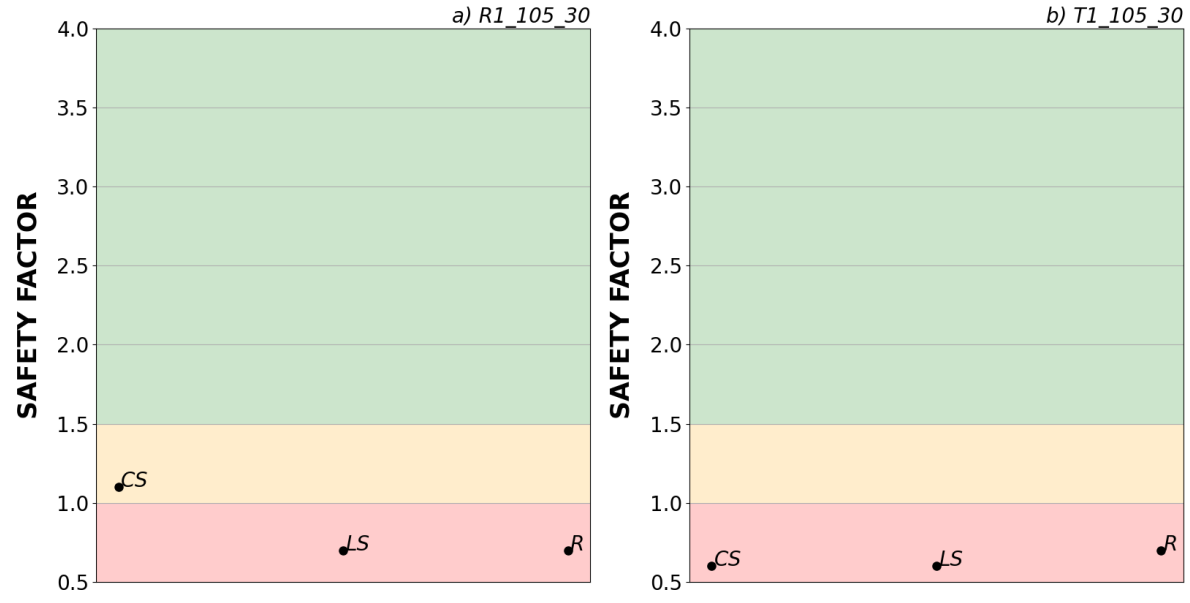

Figure 3.8: *SF distributions of the models a) « R1_105_30 » and b) « T1_105_30 ».*

Effect of landslide mass geometry: figures 3.9a and b compare SF distributions obtained for rotational and translational landslides with the same slope angle and volume but different geometry:

- rotational mechanism: landslides located at the slope toe (« R2 ») are more stable than landslides involving the whole slope (« R1 ») or extending beyond the crest (« R3 »). Additionally, « R1 » and « R3 » models show very close SF independently from material type. The SF difference between « R2 » and « R1 » - « R3 » models is reduced when loose soils are introduced into the models. The higher values of SF of « R2 » models can be interpreted as the effect of smaller landslide dimensions compared to « R1 » and « R3 » cases
- translational mechanism: results obtained for « T3 » models are similar to those of « T2 » models even if the dimensions of the landslide bodies are quite different. Nevertheless, the SFs calculated for the 3 model types become very close in the presence of low-cohesion materials. This result could be interpreted as the effect of:
    1) a different shape of the sliding surface of « T3 » models. Due to geometrical reasons, the sliding surfaces of configuration n.3 models were designed inclined with respect to the slope face generating wedge-like landslides. For this reason, other factors could contribute to their overall stability and the increasing/decreasing landslide dimensions could not be sufficient to justify SF distributions as for rotational cases
    2) factors of safety of « T3 » sliding surface models were computed by adopting a different formulation due to the wedge-like geometry being not suitable to the infinite slope approach. Therefore, results calculated by these different methods may not be fully comparable

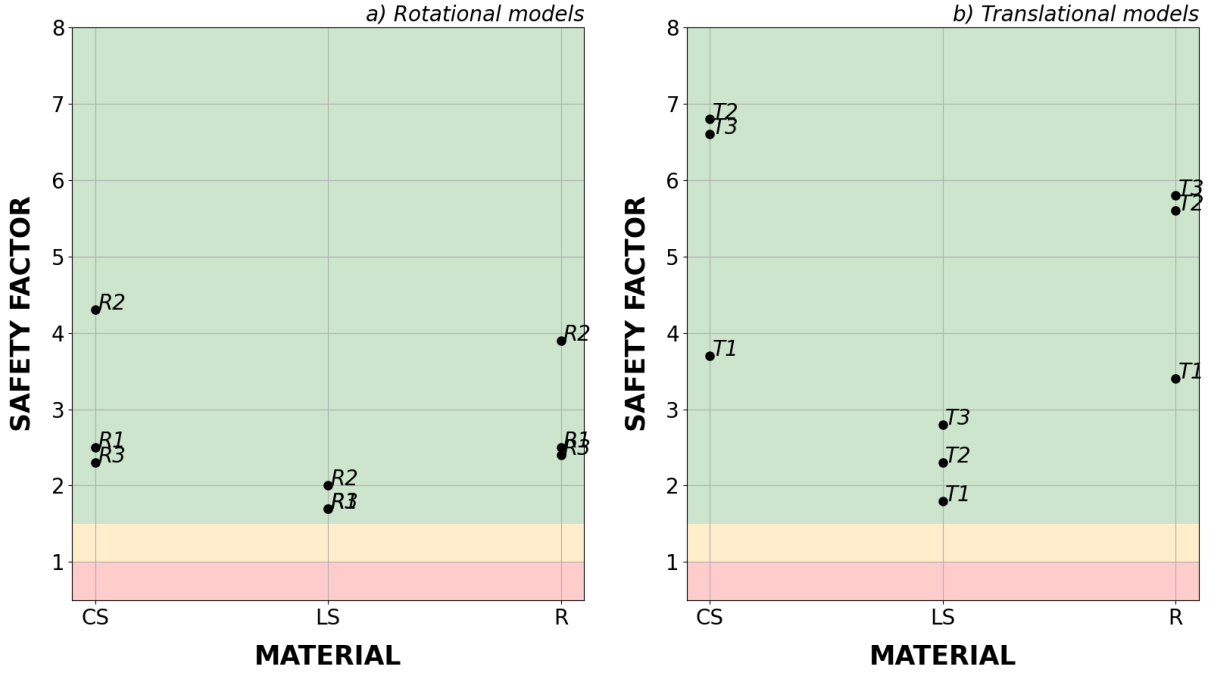

Figure 3.9: *Distribution of SF for models a) « R1_103_15 » (R1), « R2_103_15 » (R2) and « R3_103_15 » (R3) and b) « T1_103_15 » (T1), « T2_103_15 » (T2) and « T3_103_15 » (T3).*

Even if it is not possible to generalize results due to the specific geometries and geomechanical properties investigated in this study, based on the above-presented SF distributions, it can be summarized that:

- the combination of material properties with landslide volume can explain SF variations. This effect is even more evident when the lowest slope angle is considered
- increasing volume results in drastic reductions of the factor of safety independently from the material type. When large volumes are combined with high slope angles, models become unstable and variations of SF related to material geomechanical properties are less evident, suggesting a secondary role of this feature in the determination of the overall stability of the slopes
- in the majority of the cases, translational landslides are more stable than the equivalent (in terms of material type, slope angle, volume and configuration) rotational landslides

3.2 Quantification of permanent co-seismic displacements by pseudo-dynamic analysis

This section discusses the results of the conducted seismic slope stability analyses. More in particular, it will address the following topics:

- computation of critical accelerations (a_y) by pseudo-static analyses
- prediction of co-seismic displacements by Newmark's method (1965) – based approach
- discussion of the results

3.2.1 The conventional pseudo-static method

Seismic stability analyses are usually performed by the conventional pseudo-static approach. According to the latter, the seismic action is introduced into the force balance as an equivalent static inertial force applied at the mass barycenter. This force has horizontal and vertical components; however, the vertical component is generally neglected and only the horizontal downstream component is considered as it is the most problematic in terms of destabilization (fig. 3.10).

According to this assumption, the pseudo-static force is defined as (eq. 3.5):

$$F_h = k_h W \qquad \text{[Eq. 3.5]}$$

where k_h is the pseudo-static coefficient and W represents the landslide weight.

Due to pseudo-static force, equations 3.1, 3.3 and 3.4 must be modified to account for reductions of slope stability in the presence of the seismic force. For instance, the Fellenius's equation has to be re-written as (eq. 3.6):

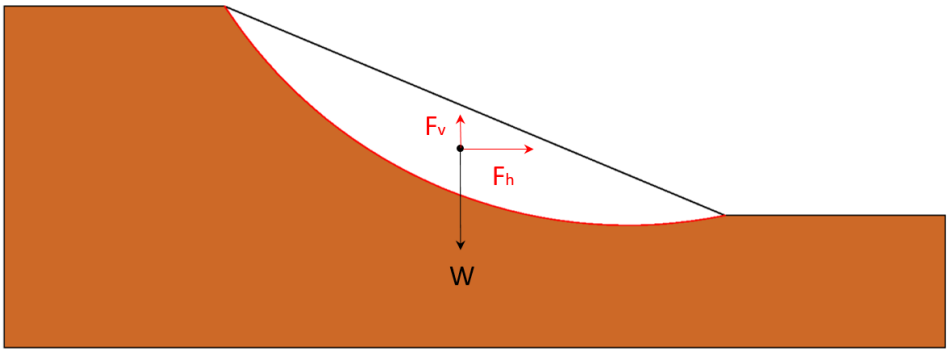

***Figure 3.10**: Sketch showing horizontal and vertical pseudo-static forces applied at the landslide baricenter.*

$$SF = \frac{\sum(c_j l_j + (W_j \cos\beta_j - W_j k_h \sin\beta_j)\tan\phi_j)}{\sum(W_j \sin\beta_j + W_j k_h (d_j/R)}$$ [Eq.3.6]

where d_j/R is the ratio between the arm of the pseudo-static force with respect to the center of rotation and R is the ray of the circular sliding surface. Since Fellenius's method works on portioned landslide masses, the pseudo-static force will not be considered as applied at the whole mass barycenter, but at the barycenter of each slice.

In the same manner, the infinite slope equation becomes (eq. 3.7):

$$SF = \frac{c}{\gamma h k_h \cos^2\beta} + \frac{-k_h \tan\beta}{k_h + \tan\beta}\tan\phi$$ [Eq. 3.7]

Finally, equation 3.4 for « T3 » models becomes:

$$SF = \frac{(cl + (W(\cos\beta - k_h \sin\beta)\tan\phi)}{(W\sin\beta + k_h \cos\beta)}$$ [Eq.3.8]

Critical pseudo-static coefficient (k_y) corresponds to the value of k_h for which the factor of safety is equal to 1 (i.e., the value that brings the slope in critical conditions). k_y can also be expressed in terms of acceleration (a_y) by multiplying it by the gravity acceleration (g).

Even if this method allows assessing reductions of the static safety factor as consequence of the application of seismic forces, it does not provide with an estimation of the expected earthquake-induced displacements of the landslide. At this regard, the pseudo-dynamic approach by Newmark's (1965) must be introduced.

3.2.2 Newmark's method (1965): advantages and limitations

The Newmark's method (1965) is a conventional approach widely used by engineers and engineering-geologists for predicting permanent co-seismic displacements of landslides. Similarly to the limit equilibrium theory, in Newmark's method (1965), the landslide is considered as a rigid block sliding under elastic-perfectly plastic conditions and characterized by perfectly elastic strain behaviour before failure occurs. Basing on this rheological hypothesis, permanent co-seismic displacements are cumulated by the « block » only if the seismic acceleration exceeds the landslide critical acceleration (a_y). The final displacement value is calculated by double integration of the seismic accelerogram peaks overcoming the landslide yielding acceleration (a_y). Newmark (1965) himself specifies that his method is quite

simple but that it can provide with a rapid estimation of the order of magnitude of the expected displacements of the landslide once seismically solicited.

The main drawbacks of Newmark's approach are:

1) simplification of the material rheology: below strain threshold, the sliding block does not deform, and internal deformations of the mass are not allowed. For this reason, the method is more appropriate for low-deformability materials
2) pore water pressures build-up during the seismic shaking are neglected: material saturation due to rainfall or water table levels might be responsible for the development of pore pressures into the slopes during ground shaking, contributing to slope instability (cf. paragraph 1.2.1). A significant disadvantage of Newmark's method consists in not accounting for shear strength modifications related to pore water pressure development and consequently, for landslide post-seismic displacements. For this reason, the method is more suitable for applications on dry materials
3) site effects: the method does not consider 1D or 2D effects related to the propagation of seismic solicitations within landsliding slopes. These effects are strictly related to the frequency content of seismic waves with respect to the landslide characteristic periods and they can produce landslide displacements larger than those predicted by the classic rigid-block analysis (cf. paragraphs 1.2.1 and 3.7.1.2)

Despite its limitations, Newmark (1965)'s method is still at the basis of many types of softwares used to assess earthquake-induced displacements of landslides (Rathje & Bray, 2000). In addition, implementations of the method on GIS (Geographic Information System) were proposed over time to perform seismic hazard predictions over large areas. These implementations are useful not only because they allow passing from slope-scale to regional-scale analyses, but also because they can help planning mitigation measures.

3.2.2.1 Application of Newmark's method (1965) to the landslide prototypes

According to the previous paragraph, the classic rigid-block analysis requires seismic accelerograms to calculate cumulated seismic displacements of landslides through a double integration of accelerogram peaks above the a_y threshold.

As discussed in paragraph 2.6, in this study 17 equivalent LEMA_DES short-duration signals (Lenti & Martino, 2010) were used to simulate seismic ground-motion. Due to the shorter duration of the equivalent signals compared to the real accelerograms from which they are derived, the number of acceleration peaks resulting for the LEMA_DES signals is strongly reduced. As a consequence, the procedure originally described by Newmark (1965) is not suitable.

To overcome this issue, the empirical equation by Hsieh & Lee (2011), which is based on data from worldwide earthquakes (i.e., the 1999 Chi-Chi earthquake, the 1999 Kocaeli earthquake, the 1999 Duzce earthquake, the 1995 Kobe earthquake, the 1994 Northridge earthquake and the 1989 Loma Prieta earthquake), was used. This equation correlates Newmark's displacements (D) of landslides with seismic properties (i.e., Arias Intensity) and landslide critical acceleration (in terms of k_y, cf. paragraph 3.2.1) as follows:

$$\mathrm{Log}_{10}(\mathrm{D}) = 0.802\log(\mathrm{AI}) - 10.981(\mathrm{k_y}) + 7.377(\mathrm{k_y})\log(\mathrm{AI}) + 1.914 \pm 0.274 \quad \text{[Eq.3.9]}$$

This equation is based on easily accessible data:

1) the Arias Intensity of the LEMA_DES signals is known. Indeed, by definition, LEMA_DES signals have an equivalent AI to the original signals
2) the critical acceleration of the landslide prototypes can be computed by conventional pseudo-static approach

Results obtained by equation 3.9 are presented in the next paragraph.

3.2.3 Interpretation of the results

In this paragraph, variability of the computed Newmark's displacements for all models is investigated.

Because Arias Intensity values related to the LEMA_DES signals are almost similar (cf. paragraph 2.6), results related to a specific model will be presented in terms of the average value of the 17 calculated displacements.

Moreover, in this section, focus will be on understanding how different the order of magnitude of displacements computed for different models may be, in agreement with comments on SF (cf. paragraph 3.1.3).

Effect of material properties: results obtained for models described in paragraph 3.1.3 are reported in this section. From figures 3.11a and b it can be inferred that Newmark's displacements calculated for medium volume-low angle rotational (a) and translational (b) landslides are negligible since they are all below the value of 1 mm that was here defined as minimum relevant displacement (i.e., below this threshold displacements are practically null).

However, it can be observed that:

- displacements computed for rotational landslides are higher compared to those calculated for translational landslides. This can be related to a lower SF for rotational models and therefore a lower a_y of landslide models (fig.3.4)
- the average Newmark's displacements computed for loose materials are more than 3 orders of magnitude higher compared to the other cases, either for rotational or translational landslides. These results confirm that according to simplified approaches, material composition has a strong impact on the overall stability of landslides

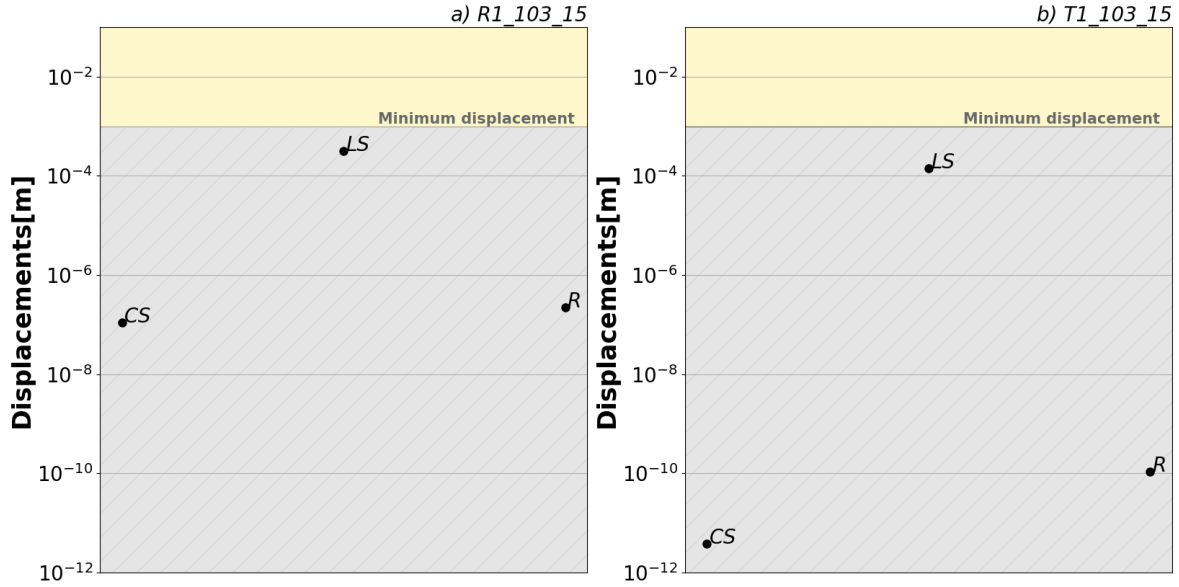

***Figure 3.11**: Comparison of the average Newmark's displacements for models a) « R1_103_15 » and b) « T1_103_15 ». Grey line marks the minimum relevant displacement, below which (grey zone) displacements are considered as null.*

Effect of landslide volume: volume increase is associated to an increase of average Newmark's displacements for both rotational (fig.3.12a) and translational (fig.3.12b) landslides. According to previous section on SF (cf. paragraph 3.1.3), the large volume – low angle geometrical combination is mostly controlled by variations of material friction angle. Indeed, models with the lowest friction angle material (i.e., cohesive soils), return the highest Newmark's displacements. To further interpret the results, the concept of « critical displacement » must be introduced. According to Romeo (2000), critical displacement is defined as the co-seismic displacement beyond which the slope general failure occurs. This threshold is generally lower for brittle materials since they have reduced capacity to accommodate large deformations. The critical displacements that Romeo (2000) reports are: 10 cm for soils slopes (that he extracts from Jibson and Keefer, 1993) and 5 cm for rocky slopes (from Wieczorek et al., 1985).

Displacements above these thresholds will be therefore considered as « failures ». This is the case for model « R1_105_15 » involving cohesive soils for which a decimetric displacement, close to critical threshold, is reached. To conclude this comparison, it must be mentioned that models characterized by a lower volume (« R1_101_15 » and « T1_101_15 ») return displacements lower than 1 mm and therefore they are considered as null. This result suggests that small volume – low angle geometrical configurations are not seismically reactivable at the seismic energy level here considered, independently from material composition.

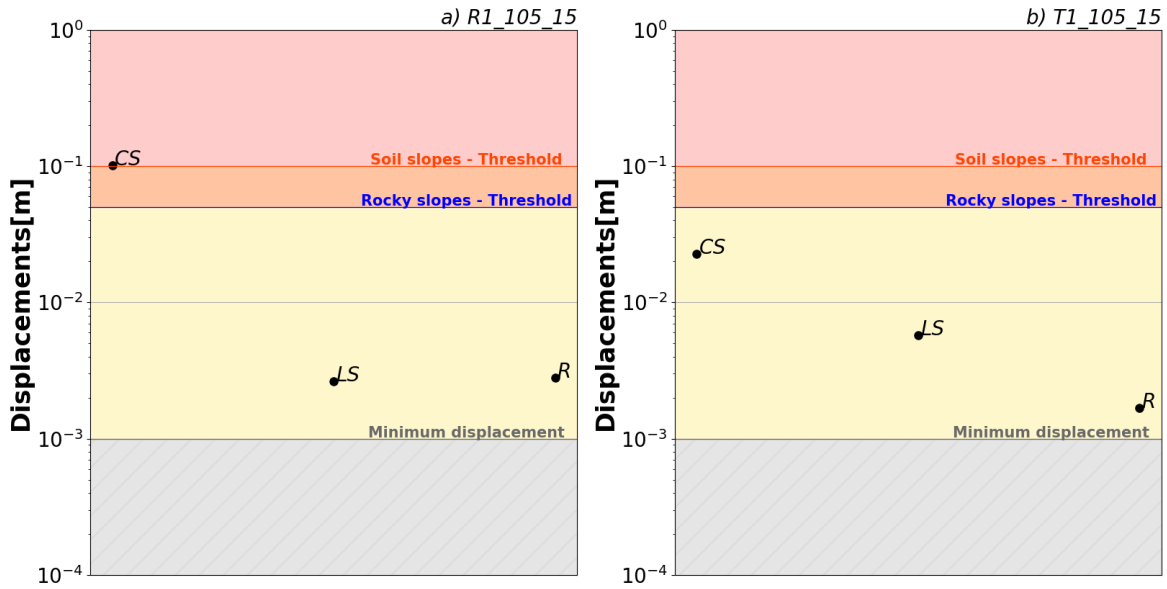

Figure 3.12: *Average Newmark's displacements of models a) « R1_105_15 » and b) « T1_105_15 ». Lines mark respectively: the minimum relevant displacement (grey), critical displacement for rocky slopes (blue) and for soil slopes (orange).*

Effect of slope angle: as already discussed in paragraph 3.1.3, increasing slope dip induces unfavourable conditions. In the reported example, this increase leads to null displacements for translational landslides (fig.3.13b) and millimetric displacements for rotational landslides (fig.3.13a). The combination large volume – high slope angle cannot be analysed since already unstable in static conditions. Finally, the effect of slope configuration is not investigated since the distribution of the factor of safety presented in paragraph 3.1.3 did not highlight relevant different features that could not be attributed to landslide dimension variation.

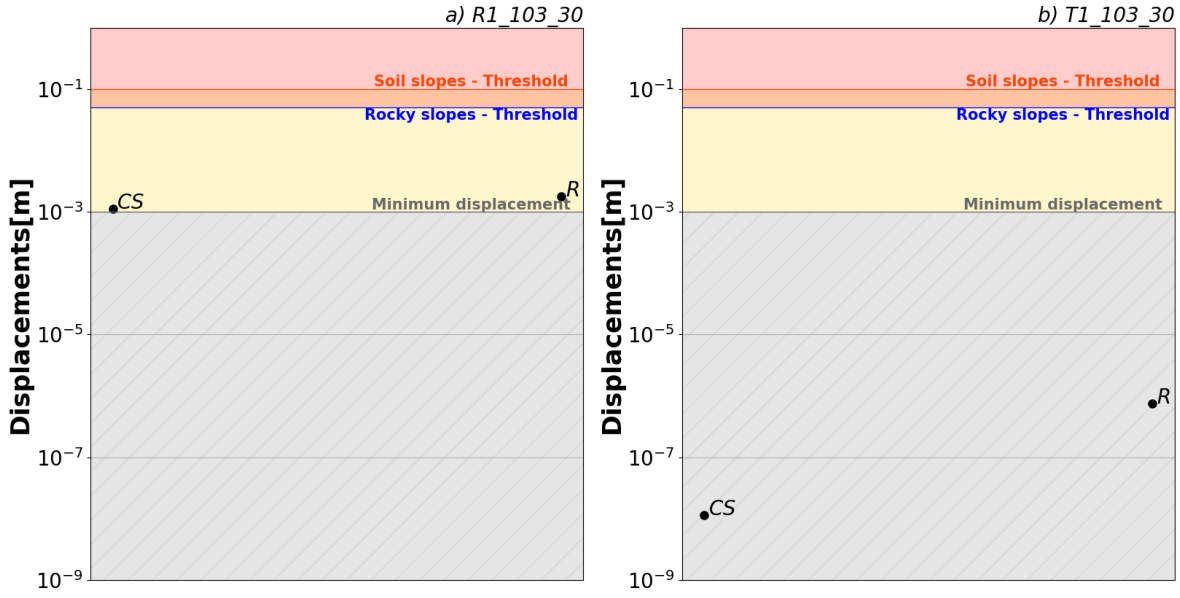

Figure 3.13: *Newmark's displacements distributions of models a) « R1_103_30 » and b) « T1_103_30 ». Results related to loose soils are missing because those models are already unstable in static conditions.*

Overview of all results: the total distribution of Newmark's displacements computed for rotational and translational landslide prototypes is presented in the following. It is important

to stress that in this case the displacements are not reported in terms of average values, but that the full set of results was considered for each model. In addition, since the solution obtained for specific models and specific material types coincides when the impedance contrast is varied (cf. paragraph 3.1.3), the corresponding set of displacement values is reported only once in the distributions. Moreover:

- data were filtered in order to exclude displacements below 1 mm
- distributions for soils and rocky slopes models are separately represented since different critical displacements were assumed for them
- the following distributions exclude rotational (~20% of all rotational prototypes) and translational (~18% of all translational prototypes) prototypes characterized by SF < 1 for which Newmark's method-based analysis was not performed (cf. paragraph 3.1.3)

The final distributions for rotational and translational landslide models in soil slopes are in figures 3.14a and b. For rotational landslides, Newmark's displacements above 1 mm represent ~30% of all cases: of the latter ~9% are above the 10 cm threshold (i.e., failure). This percentage is computed by also including Newmark's displacements resulting for models « R1_105_30, CS», characterized by critical SF that determined displacements in the order of magnitude of 10^3 m in the seismic scenario here considered. Being the latter values too large compared to other displacements in figure 3.14a, results related to model « R1_105_30, CS» were excluded for a better data visualization even if they were included in the statistics. For translational landslides, ~17% of all cases are considered as relevant (i.e., displacements ≥ 1 mm). Among them, only ~0.2% of the cases are larger than Romeo (2000)'s threshold (fig. 3.14b). Finally, comparing the two distributions it can be inferred that Newmark's displacements computed for rotational landslides are larger and span over a wider range compared to those for translational landslides (fig. 3.14a-b).

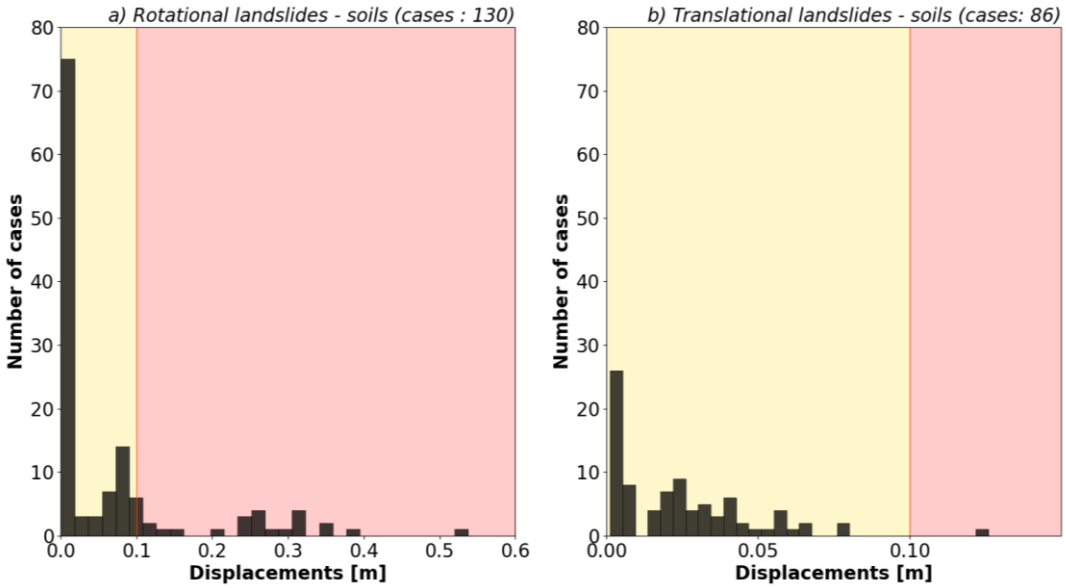

Figure 3.14: *Newmark's displacements distributions for a) rotational and b) translational landslides models in LS (=Loose Soils) and CS (= Cohesive Soils). The vertical red line marks the critical displacement according to Romeo (2000). The red area in the plot is the region of failure cases, whereas the yellow area is the region of relevant displacements (i.e., above 1mm). The total number of cases for rotational landslides (130 cases) does not include results related to models « R1_105_30, CS ».*

To identify conditions more prone to seismic reactivation, distributions in figure 3.14a-b were further classified to highlight volume (fig. 3.15) and slope angle (fig. 3.16). Such an approach allows understanding which among the parameters or their combination cause the most critical conditions in terms of co-seismic displacements.

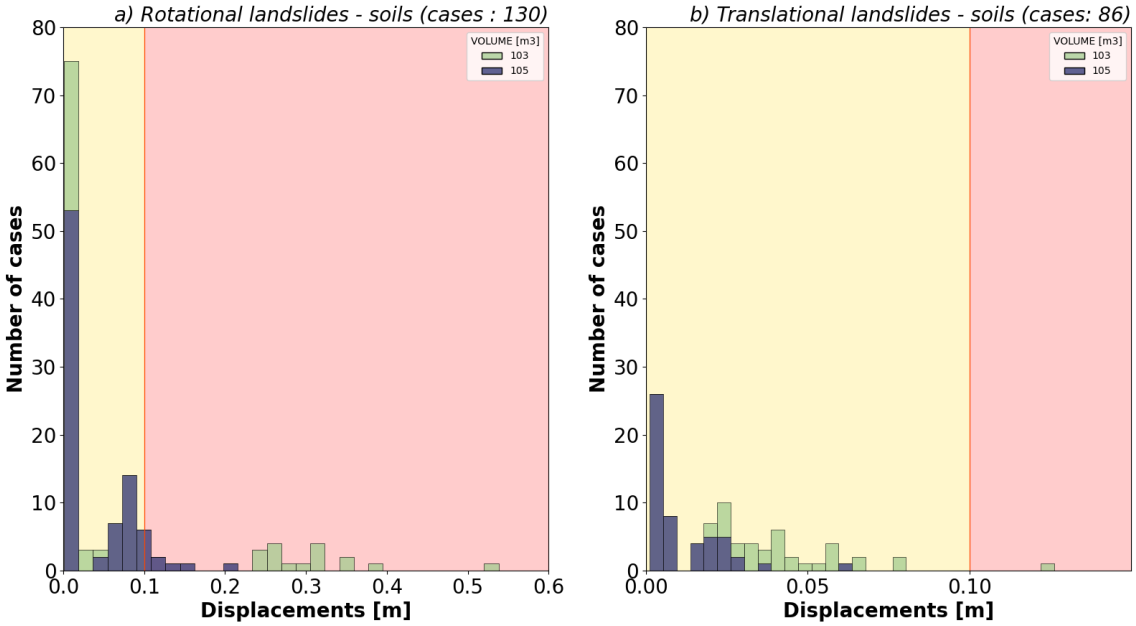

Figure 3.15: *Distribution of Newmark's displacements for rotational and translational landslide models involving soils slopes with focus on volume of landslide masses. In the legend « 103 » and « 105 » refers respectively to volume values corresponding to 10^3 and 10^5 m^3. The vertical red line marks the critical displacement according to Romeo (2000). The red area in the plot is the region of failure cases, whereas the yellow area is the region of relevant displacements (i.e., above 1mm).*

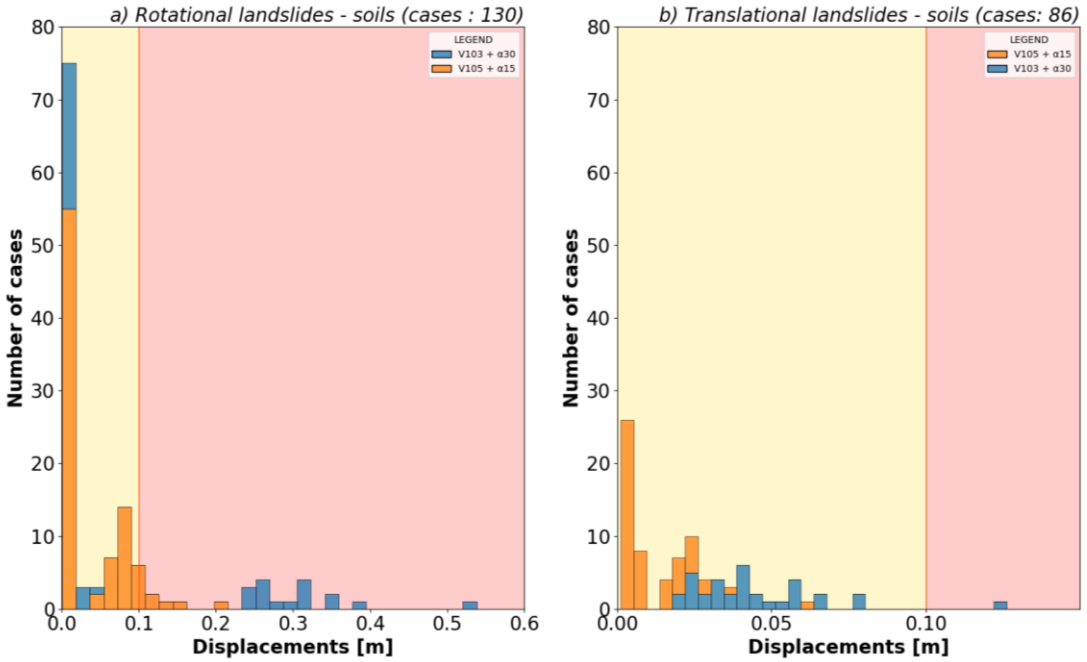

Figure 3.16: *Distribution of Newmark's displacements for rotational and translational landslide models involving soils slopes with focus on the slope angle (α) in combination with the volume (V) of landslide masses. The vertical red line marks the critical displacement according to Romeo (2000). The red area in the plot is the region of failure cases, whereas the yellow area is the region of relevant displacements (i.e., above 1mm).*

The analysis of figures 3.15-3.16 allows concluding that:

- for rotational landslides, ∼70% of all relevant displacements are associated with large volume landslides (fig. 3.15a). Similarly, for translational landslides, this percentage is ∼60% (fig. 3.15b). Smallest volume landslide models (i.e., V = 10 m^3) do not appear in distributions in figure 3.15a-b, since computed displacements for those models are smaller than 1 mm. Indeed, ∼ 96% of all Newmark's displacements below 1 mm are associated to small-medium volume landslides for rotational prototypes. The same calculation performed for translational models returned similar result: ∼ 88% of all displacements < 1 mm are associated to small-medium volume landslides. The statistics just described, characterized by clear distinction of landslide classes in terms of volume between the two considered sub-sets of data (i.e., relevant and not relevant displacements) for both rotational and translational soil landslides highlight that the parameter «volume» has a great impact on landslide expected mobility and that large volume landslides are more prone to be destabilized
- despite the previous statement, failure cases are also documented among medium volume rotational landslides. This result can be interpreted as the effect of the combination high slope angle – medium volume (3.16a). This combination of parameters is therefore one of the most unfavourable in terms stability/earthquake-induced displacements. Medium volume – high slope angle models experience the highest displacements also in the case of the translational landslides even if they do not overcome the threshold displacement leading to failure (3.16b). Models combining the two most unfavourable parameters (i.e., large volume + high slope angle) do not appear in the distributions since characterized by SF < 1. It is also interesting to stress that medium volume landslides experience relevant displacements only when 30° degrees slope angle are considered, whereas, for lower inclination, Newmark's displacements are practically null

Finally, figures 3.17a and b show the distribution of relevant Newmark's displacements computed for translational (∼ 4% of all cases) and rotational (∼25% of all cases) landslide prototypes involving rocky slopes for which a threshold displacement for failure of 5 cm is assumed (Romeo, 2000).

In figures 3.18 and b, the same distributions are classified to highlight the volume and the slope angle of the landslide models associated to the reported displacement values.

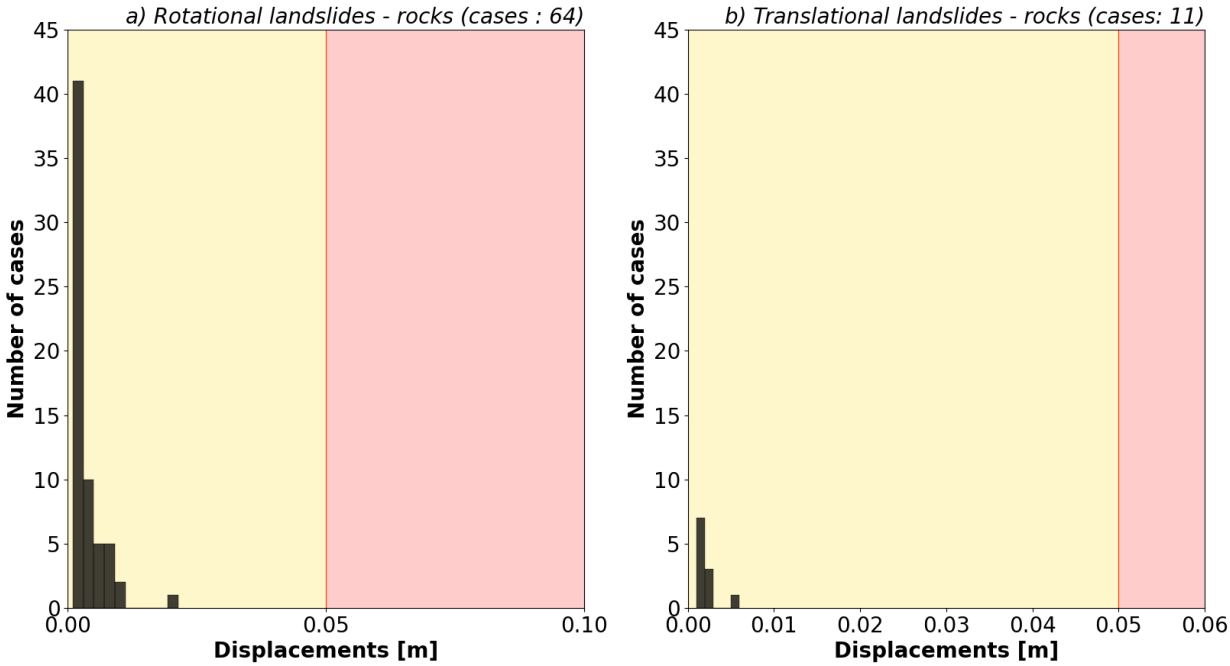

Figure 3.17: *Distribution of Newmark's displacements for a) rotational and b) translational landslide models involving rocky slopes. The vertical red line marks the critical displacement according to Romeo (2000). The red area in the plot is the region of failure cases, whereas the yellow area is the region of relevant displacements (i.e., above 1mm)*

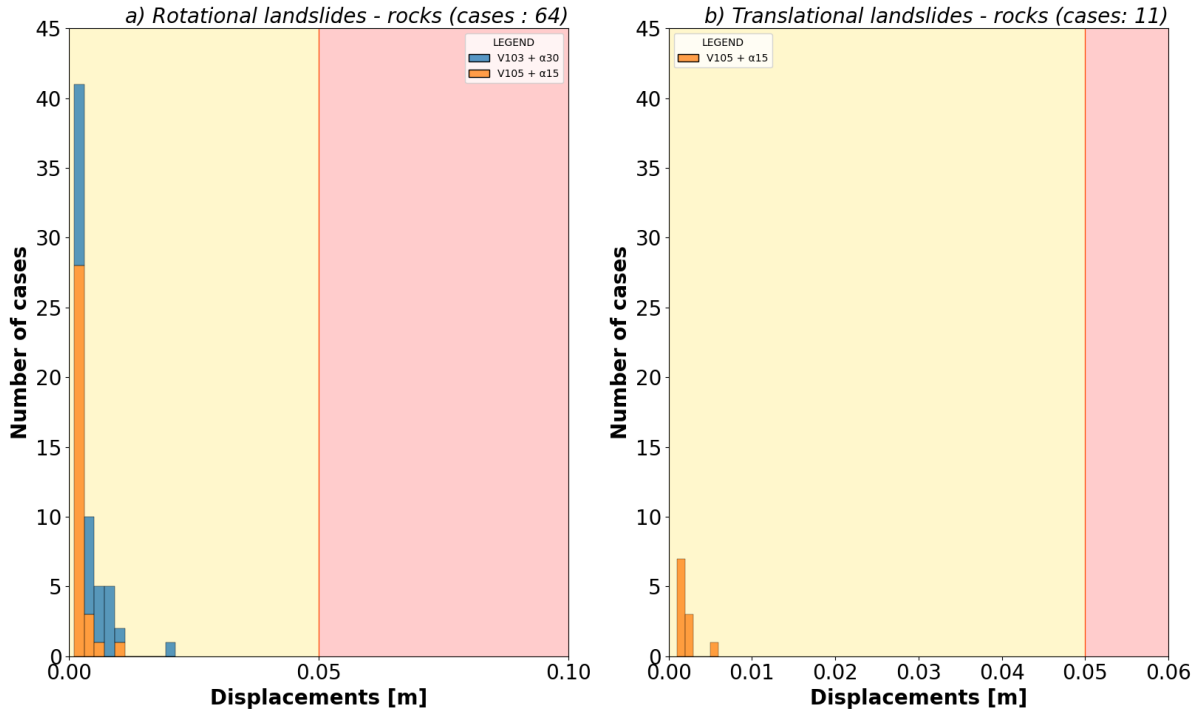

Figure 3.18: *Distribution of Newmark's displacements for rotational and translational landslide models involving rocky slopes with focus on the slope angle (α) in combination with the volume (V) of landslide masses. The vertical red line marks the critical displacement according to Romeo (2000). The red area in the plot is the region of failure cases, whereas the yellow area is the region of relevant displacements (i.e., above 1mm).*

From the analysis of the distributions shown in figures 3.17-3.18 it can be finally concluded that:

- comparing relevant displacements percentages for soil and rocky slopes, it can be argued that in the latter case, the number of displacements above the 1 mm threshold is smaller compared to the first case in particular when a translational failure mechanism is considered. This allows concluding that rocky slopes are generally less prone to move than soil slopes under the seismic and geometrical conditions here considered
- relevant displacements computed for rotational landslides are generally higher and span over a wider range compared to those for translational landslides
- the 5 cm failure threshold is never reached neither for rotational nor for translational landslides. This result is in agreement with the first argument
- 100% of the relevant Newmark's displacements are associated to large volume translational landslides in figure 3.18b. Considering a rotational failure mechanism, this percentage goes down to ~52% of the cases. Remaining cases are represented by medium volume – high slope angle landslides (fig. 3.18a). Finally, also in this case, smallest volume landslides are missing in the distributions due to null displacements returned by the performed analysis

PART 2: FDM numerical modelling

This second part of the chapter focuses on the 2D numerical modelling performed on the landslide prototypes (cf. chapter 2). The purpose of this analysis is to assess the seismic displacements of the landslide prototypes using more comprehensive methodologies than the simplified rigid-block analysis (cf. chapter 3 part 1). To begin, a general introduction on numerical methods is provided.

3.3 Generalities on stress-strain numerical methods

In practical engineering (i.e., mechanics of solids and fluids, thermodynamics and so forth) partial differential equations are used to describe the behaviour of physical systems (Dhatt et al., 2012). However, when such systems are highly complex (i.e., in terms of geometry, loadings and material properties), these equations cannot be analytically solved (Logan, 2011). At this regard, numerical methods were developed. Among the latter, the so-called « domain methods » (Zohu & Zhou, 1993) are commonly utilized. Typically, these methods discretize the systems (i.e., the « domains ») into smaller « elements » connected by points called « nodes » that overall define a « grid ». This operation reduces the complexity of a continuum medium with a consequent finite number of degrees of freedom to be considered, and it allows solving the researched observables for each point at a finite number of temporal steps. Basing on the solving strategy, discretization methods can be further distinguished. The most used are the Finite Element Methods (FEMs) and the Finite Difference Methods (FDMs). FEMs first development dates back to Hrennikoff (1941) and Courant (1943) and today are the most widely used techniques in computational mechanics (Brenner & Carstensen, 2004) for solving problems related to heat transfer, fluid flow, mass transport and electromagnetic potential (Logan, 2011). On the other side, FDMs had a widespread since 1940s to solve numerous problems such linear/non-linear and time independent/dependent problems (Zohu & Zhou, 1993). More in particular, FDMs are commonly used in seismology and earthquake ground-motion modelling since they can be applied to complex systems providing relatively accurate solutions (Moczo et al., 2004).

FDMs were selected for this research. More in particular, the FDM calculation code FLAC 7.0 (Itasca) was utilized to model the dynamic response of landslide prototypes. Its main functionalities are summarized below.

3.4 FLAC (Fast Lagrangian Analysis of Continua) code

Any information reported in this paragraph is extracted from Itasca (2015) and the Itasca website:
https://docs.itascacg.com/itasca900/flac3d/docproject/source/options/dynamic/dynamic.html

3.4.1 Generalities

FLAC (*Fast Lagrangian Analysis of Continua*) is a FDM numerical program for engineering stress-strain analyses developed in 1986. As the name suggests, the software operates with a

lagrangian calculation scheme that is particularly suitable for modelling large deformations. Materials are discretized in « elements » or « zones » that behave according to selected linear or non-linear stress/strain laws when subjected to forces and/or boundary conditions. The interconnection points among these elements are called « nodes » or « grid points » defining a « grid » or « mesh ». The element shape is usually regular, and the size is selected by the user. In FLAC all vector quantities (i.e., forces, displacements and so forth) are saved at the node locations, whereas the scalar quantities (i.e., material properties, stresses and so forth) are saved at the elements centroids.

FLAC follows an explicit calculation procedure that consists in performing computational cycles during which the differential equations are regenerating. Each cycle takes one time-step. During each time-step, the information associated to the investigated phenomenon is propagated across the elements. The disadvantage of this kind of approach is that time-steps are usually small and numerous, requiring sometimes long computation times. As it will be better explained later (cf. paragraph 3.6), this is the main drawback encountered in performing dynamic stress-strain analyses on the landslide prototypes.

FLAC allows performing both static and dynamic calculations. To reach a static solution to a problem, the software accounts also for the dynamic equations of the motion to ensure that the numerical scheme is stable. To check for the equilibrium, it is necessary to monitor the so-called « unbalanced force » (i.e., maximum nodal force vector at each node). Generally, this force does not arrive exactly at zero, however, the equilibrium is considered to be reached when its value is small compared to the initial applied forces (at this stage only the effect of gravity force is considered). Dynamic phase of the calculation is described below. Since the latter is a fundamental step in the framework of this study a separated paragraph is dedicated to it.

3.4.2 Dynamic calculation in FLAC

Once the static equilibrium is reached, the dynamic modelling is performed by applying cyclic loads as SV in-plane waves propagating upward from the base of the model. In this study, 17 equivalent signals (cf. paragraph 2.6) were applied in this phase.

FLAC performs non-linear analyses during the dynamic calculation. This method consists in updating initial shear modulus and damping values according to defined decay curves in which the shear modulus reduction is expressed as function of the strain percentage. In particular, in this work, shear modulus decay and damping increasing are updated exploiting the Hardin & Drnevich (1972) model embedded into FLAC (cf. paragraphs 2.3.2.5, 2.3.3.5, 2.3.4.5). Damping is a very important parameter in dynamic modelling, since it accounts for energy dissipation occurring when materials are seismically solicited. Without damping or failure, materials vibrations would continue indefinitely. For more reliable dynamic analyses, the hysteretic damping alone is not sufficient since it does not provide with enough energy dissipation at low-level strain. At this regard, a small amount of Rayleigh damping must be added when dynamic modelling is performed in FLAC that is only relevant at low strains respect the hysteretic damping values. The Rayleigh damping is introduced in the damping matrix (C) given by (eq. 3.10):

$$C = \alpha M + \beta K \quad \text{[Eq.3.10]}$$

where M and K are respectively the mass and stiffness matrices and α and β are respectively a mass-proportional damping constant and a stiffness proportional damping constant. The Rayleigh damping related function varies in the frequency domain reaching a minimum value at a given circular frequency (ω_{min}, eq. 3.11) at which it corresponds a minimum damping value (ξ_{min}, eq. 3.12):

$$\omega_{min} = \left(\frac{\alpha}{\beta}\right)^{1/2} \quad \text{[Eq. 3.11]}$$

$$\xi_{min} = (\alpha\beta)^{1/2} \quad \text{[Eq. 3.12]}$$

The latter are the necessary parameters for specifying a Rayleigh damping in FLAC.

At the end of the dynamic computational process, outputs of interest (i.e., seismically-induced displacements) can be finally extracted from each grid point (cf. paragraph 3.7.2.1).

3.4.3 Advantages and drawbacks of FDMs for earthquake-induced landslides predictions

Nowadays, FDM codes are a good alternative to conventional methods to simulate seismic wave propagation into slopes and to evaluate the related effects. Indeed, compared to simplified analytical approaches (such as the Newmark's method, 1965), FDMs:

- account for mass internal deformations, admitting also internal differential movements
- treat the deformation/failure process as a function of both space and time
- consider viscous and plastic constitutive laws for the materials, not only the perfectly elasto-plastic behaviour, as the limit equilibrium approaches. Moreover, FDMs also model material linearity and non-linearity in the presence of ground shaking
- account for pore pressures related to water table and/or induced by external loadings, which is one of the main drawbacks of the Newmark's method (cf. paragraph 3.2.2). This feature is particularly important when assessing post-seismic displacements of the landslide masses
- account for site effects generating de-/amplification of the amplitude of seismic waves due to pre-existing geology (i.e., soil-substratum impedance contrast), topography and/or landslide geometry

Despite these advantages, analytical approaches are still widely used to compute earthquake-induced displacements of landslides for the following reasons:

- softwares for FDM analyses require a higher expertise level compared to analytical methods
- FDM analyses have longer computation times
- FDMs softwares necessitate a good rheological characterization of the materials, which may not be always available, especially at regional scale, due to time and economical constraints

- Newmark's method (1965) – based empirical equations can be implemented in GIS for performing regional scale analyses (cf. paragraph 3.2.2)

3.5 Design of sheared-slopes by FLAC code

Technical information reported here, have been mostly extracted from Itasca (2015) and the Itasca website:

https://docs.itascacg.com/itasca900/flac3d/docproject/source/options/dynamic/dynamic.html

To design the 216 landslide prototypes (cf. chapter 2) in FLAC, x-y coordinates of points and lines generated in AutoCAD (Autodesk) were extrapolated and recreated in FLAC using the Fish Language embedded into the software. However, before that, the element size must be defined to generate the grid.

The element size quantifies the internodal distance (l_d). According to Kuhlemeyer & Lysmer (1973), l_d must be selected to ensure a reliable propagation of a maximum frequency (f_{max}) consistent with the frequency range of interest (eq. 3.13):

$$f_{max} = v_{min}/(l_d * n) \quad \text{[Eq.3.13]}$$

where v_{min} is the minimum shear wave velocity (i.e., shear wave velocity of the landslide) and n is the number of nodes per wavelength that is typically between 6 and 10. In this study, n= 10 and f_{max} = 20 Hz were substituted into equation 3.13 to calculate l_d. According to equation 3.13, l_d is function of the shear wave velocity of the material, therefore, different l_d values are associated to same geometry by varying the landslide geotechnical composition. Moreover, due to the presence of very shallow landslides (i.e., landslides characterized by centimetric thickness), the choice of l_d must assure the presence of at least 10 nodes into the landslides along the vertical direction to ensure a correct model resolution. To simplify the model design procedure, one l_d value was defined for each geometry by choosing the minimum value among those computed for the selected material types. When the resulting l_d was too large compared to the landslide thickness, l_d was obtained by dividing the thickness by 10. Following these criteria, 36 different l_d values ranging between 0.02 and 0.6 m were obtained.

Other main requirements in FLAC after the generation of the geometry are:

1) constitutive laws for the modelled materials which represent their rheological behaviour
2) conditions assumed for both lateral and basal boundaries of the numerical domain
3) dynamic properties (requested for the dynamic modelling only)

Constitutive laws expressing rheological behaviour, describe stress-strain relationships peculiar of the materials of the domain. As it regards the models designed in this study, different constitutive laws were attributed to the following regions:

- bedrock (i.e., rocks)
- landslide mass (i.e., cohesive soils, loose soils, or rocks)

Since in this study focus is on landslide, a purely elastic behaviour was assigned to the substratum. The elastic model implicates reversible deformations and stress-strain linear relationship according to the Hooke's law. Properties that must be attributed to model an elastic rheology in FLAC are: density, bulk modulus, Poisson's ratio, shear modulus and Young's modulus (cf. paragraph 2.3.2.3, tab.2.4; cf. paragraph 2.3.2.4, tab.2.5c). On the contrary, for landslide bodies, a Mohr-Coulomb constitutive law was assumed (cf. paragraph 2.3.2.2, eq. 2.3). In this case, the following parameters must be specified: density, bulk modulus, cohesion, friction angle, Poisson's ratio, shear modulus, tension cut-off and Young modulus (cf. paragraph cf.2.3.2.3, tab. 2.4; cf. paragraph 2.3.2.4, tab. 2.5a-b; cf. paragraph 23.3.3, tab. 2.7; cf. paragraph 2.3.3.4, tab.2.8a-b; cf. 2.3.4.3, tab. 2.3.4.3; cf. paragraph 2.3.4.4, tab.2.11a-b). The Mohr-Coulomb region is further distinguished between the proper landslide body, to which peak shear strength parameters are attributed, and the residual zone, which corresponds to a belt located at the location of the sliding surface and is associated to residual strength parameters. The width of this belt does not exceed the internodal distance (i.e., zones immediately along the sliding surface were considered). The introduction of this belt at the landslide mass base serves not only to simulate residual strength conditions along the existing sliding surface, but also to constrain the shape and size of the modelled landslides. Indeed, this prevents the FLAC from generating its own sliding surface during the simulations.

Boundary conditions must be specified for a correct numerical analysis. Peripheral boundaries are artificial limits set to enclose the domain, due to FLAC requirement to work with finite region of space. The values of the field variables imposed at the boundary region represent the boundaries conditions. The existence of artificial lateral and basal boundaries might affect the reliability of the computation and for this reason specific boundaries conditions must be applied as in the following:

- in the static phase, lateral fixed roller (i.e., fixed x) boundaries and basal fixed y-boundaries were applied. When these kinds of boundaries are imposed, forces are generated to counter forces that produce an acceleration of the nodes in the boundary region to maintain their positions unchanged. More in particular, at the lateral edges, the x-position of nodes is fixed while the vertical movement is allowed (i.e., settlement) to reproduce *in-situ* conditions where lateral confinement would prevent any movement in the x-direction. The contrary would occur at the basal nodes of the model
- in the dynamic phase, artificial boundaries affect seismic wave propagation generating false reflections and interferences back into the model. To avoid such an effect, lateral free-field boundaries were introduced. The latter absorbs eventual incident waves and reproduce the free-field motion that would occur in the absence of such artificial limits. In order to achieve the free-field condition, an infinite lateral extension of the model is simulated by copying into the free-field region the data (i.e., model types and current state variables such as displacements) from the adjacent zones. In addition, quiet boundaries were introduced at the models base in order to absorb incoming waves and prevent their reflection back into the model. Quiet boundaries are particularly suitable for waves incidence angle greater than 30° while they are less effective for absorbing surface waves or lower incidence angles

The dynamic properties attributed to the models include the attribution of Rayleigh damping and Hardin & Drnevich (1972) parameters. The first ones were defined based on expert judgement by distinguishing the materials in two macro-categories: soils and rocks (in this case a differentiation was done for landslide and substratum regions) while for the derivation of the second ones refer to paragraphs 2.3.2.5, 2.3.3.5 and 2.3.4.5. Parameters of interest are summarized in table 3.1.

Table 3.1: *Rayleigh damping and Hardin & Drnevich (1972) parameters used in the dynamic modelling.*

MATERIAL	PARAMETER	VALUE
Rocks - landslide	Hardin & Drnevich (1972) strain reference [%]	0.11
Cohesive soils - landslide	Hardin & Drnevich (1972) strain reference [%]	0.05
Loose soils - landslide	Hardin & Drnevich (1972) strain reference [%]	0.04
Soils landslide	Rayleigh ξ_{min} [%]	4
Soils landslide	Rayleigh f_{min} [Hz]	3
Rocks - landslide	Rayleigh ξ_{min} [%]	1
Rocks - landslide	Rayleigh f_{min} [Hz]	3
Rocks - bedrock	Rayleigh ξ_{min} [%]	0.5
Rocks - bedrock	Rayleigh f_{min} [Hz]	2

3.6 Computation time issues

2D numerical modelling on landslide prototypes requires that a static equilibrium is reached before the application of seismic signals (cf. paragraph 3.4). In order to compare solutions obtained using different approaches, the 17 equivalent signals already adopted for Newmark's-based analysis were utilized (cf. paragraph 2.6 for the full list). The total number of FDM simulations is:

- 216 static simulations
- 3672 (= 216 models x 17 signals) dynamic simulations

Among the two steps, the most time consuming is the dynamic modelling. Due to FLAC explicit calculation approach in which both time and space domains are discretized, the number of time-steps required to solve the problem depends on:

- dimension of the model in combination with internodal distance. They affect grid dimension, the total number of nodes and therefore the duration of each computational cycle
- duration of the input signals (= effective signal duration + extra time amount corresponding to half the total signal duration added to account for the generation of eventual post-seismic displacements)

According to this description, the most unfavourable computational conditions are expected to occur when dealing with models characterized by very small internodal distances and long-duration seismic signals. In particular:

- translational and rotational landslide prototypes characterized by the lowest considered volume class for which I_d varies between 0.01 and 0.06 m
- models T2_103/105_15/30 in which the resolution is between 0.05 and 0.3 m
- longest-time duration inputs: a, b, c, f and i (cf. paragraph 2.6)

For these models, the computational time-step was in the order of magnitude of 10^{-8} or 10^{-9} s requiring weeks/months of calculation before achieving all the 17 resulting files.

On the contrary, large models (T/R1/3_105_15/30) characterized by decimetric I_d (0.5-0.6 m) had much shorter computational times (i.e., time steps in the order of magnitude of 10^{-5} s) requiring hours/days of calculation to return the complete set of solutions.

3.7 Results of 2D numerical modelling

In contrast with Newmark's analysis, different types of outputs can be obtained from static and dynamic numerical analyses. In particular, in this study the focus was on deriving:

- initial position of the center of mass of the landslides → from static solution
- characteristic periods of the landslide masses → from static solution
- minimum and maximum nodal displacements into the landslide masses → from dynamic analyses
- nodal average displacements → from dynamic analyses
- displacement of the center of mass of the landslides after the application of each equivalent signal → from dynamic analyses

3.7.1 Outputs from static analysis

In this paragraph, the results of the elaborations done on data extracted from static solutions obtained in the first step of the modelling are presented.

3.7.1.1 Center of mass

The FLAC 2D numerical domain is a geometrical space discretized by a grid in which a finite number of nodes (N) can be identified. The position of each node is described by a couple of x-y coordinates. In such kind of systems, the center of mass (CM) corresponds to the physical point acting as if in it the whole mass of the system was concentrated. The location of this point is computed as the average of the mass distribution into the system according to equations 3.14-3.15:

$$x_{CM} = \frac{\sum_{i=1}^{N} x_i \left(\frac{1}{gpm_i}\right)}{\sum_{i=1}^{N} \left(\frac{1}{gpm_i}\right)} \quad \text{[Eq.3.14]}$$

$$y_{CM} = \frac{\sum_{i=1}^{N} y_i \left(\frac{1}{gpm_i}\right)}{\sum_{i=1}^{N} \left(\frac{1}{gpm_i}\right)} \quad \text{[Eq.3.15]}$$

where x_{CM} and y_{CM} are the x and y coordinates of the center of mass, x_i and y_i refer to the position of the generic node i and gpm_i is the « grid point mass » of the generic node i,

corresponding to the inverse of the mass around the node. An example of calculated CM is provided in figure 3.19.

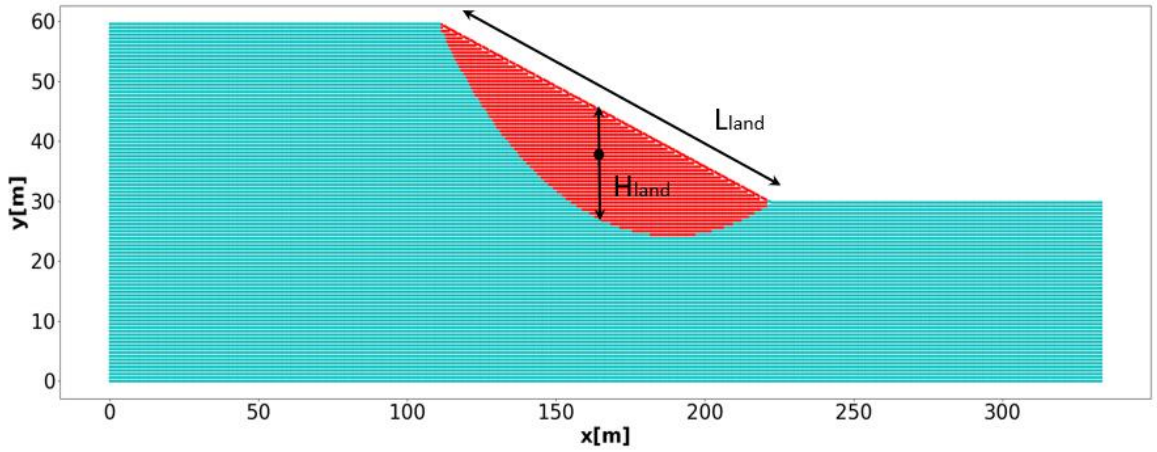

Figure 3.19: *CM (black dot) location of the landslide (red dots) in the model R1_105_15 (LS, IC = 1.5).* H_{land} *and* L_{land} *correspond to vertically measured landslide thickness and length.*

Due to the importance of CM in systems behaviour, in the next steps of this study, the displacement of this point will be computed to assess earthquake-induced landslide mobility. For the same reason, the thickness of landslides was computed at the CM x-location in order to define their resonance period (see description below for more details).

3.7.1.2 Characteristic periods ratios

Characteristic period ratios (T_s/T_m, Rathje & Bray, 2000 and T_l/T_m, Hutchinson, 1987; 1994) play an important role in landslides earthquake-induced mobility (characteristic periods – based (CPB) approach, Martino et al., 2016). The use of such ratios is limited to interpret outputs from numerical analyses since Newmark's method-based empirical correlations do not consider the frequency content of the seismic inputs (cf. paragraphs 3.2.2 and 3.2.3). A short insight about the importance of T_s/T_m and T_l/T_m ratios is provided below.

Given T_m as the mean period (Rathje et al., 1998) of the seismic solicitation (cf. paragraph 1.2.1), the earthquake-induced mobility of a landslide is expected to be maximum when one or both of the following conditions are reached:

a. $T_s/T_m = 1$ → with $T_s = 4H_{land}/v_{land}$ (Rathje & Bray, 2000) [Eq. 3.16]
b. $T_l/T_m = 0.5$ → with $T_l = L_{land}/v_{land}$ (Hutchinson 1987; 1994) [Eq. 3.17]

where, in this case, H_{land} is the landslide thickness taken at the location of the center of mass, L_{land} is the landslide longitudinal length (fig. 3.19) and v_{land} is the shear wave velocity of the landslide mass.

Equation 3.16 refers to the 1D resonance of the landslide mass that occurs when its T_s is equal or close to the T_m of the incoming seismic solicitation. In terms of seismically-induced mobility, this phenomenon is important since it is responsible for amplified oscillations of the landslide body and consequently it may impact the intensity of resulting displacements. Equation 3.17 refers to the 2D landslide – seismic wave interaction that is maximum when the signal

wavelength is two times the landslide longitudinal length (i.e., $T_l = T_m/2$). Indeed, in this condition the whole landslide mass is moving in the same direction.

Martino et al. (2018) demonstrated that in presence of dislodged landslides (i.e., landslides divided in sub-masses called « blocks ») the T_l of the blocks can be more effective on landslide mobility than the T_l of the whole mass for specific frequency ranges. However, in the present study, the determination of T_l is univocal due to the integrity of the designed landslide masses. T_s calculation is univocal only for « T1 » and « T2 » models since, in these cases, the planar shape of the sliding surfaces determines an almost constant thickness of the masses. The remaining models (i.e., « R 1 », « R2 », « R3 » and « T3 » models) are characterized by variable thicknesses, therefore, different T_s values might be computed basing on the location of thickness measurement. To overcome this issue, as previously anticipated, H_{land} was computed for all landslide prototypes at the center of mass location due to the relevant role of this geometric point in the mass displacement.

Figures 3.20 and 3.21 show the variation of the calculated characteristic ratios for 4 selected models and the different seismic inputs: « R1_101_15 », « R1_105_15 », « T1_101_15 » and « T1_105_15 ».

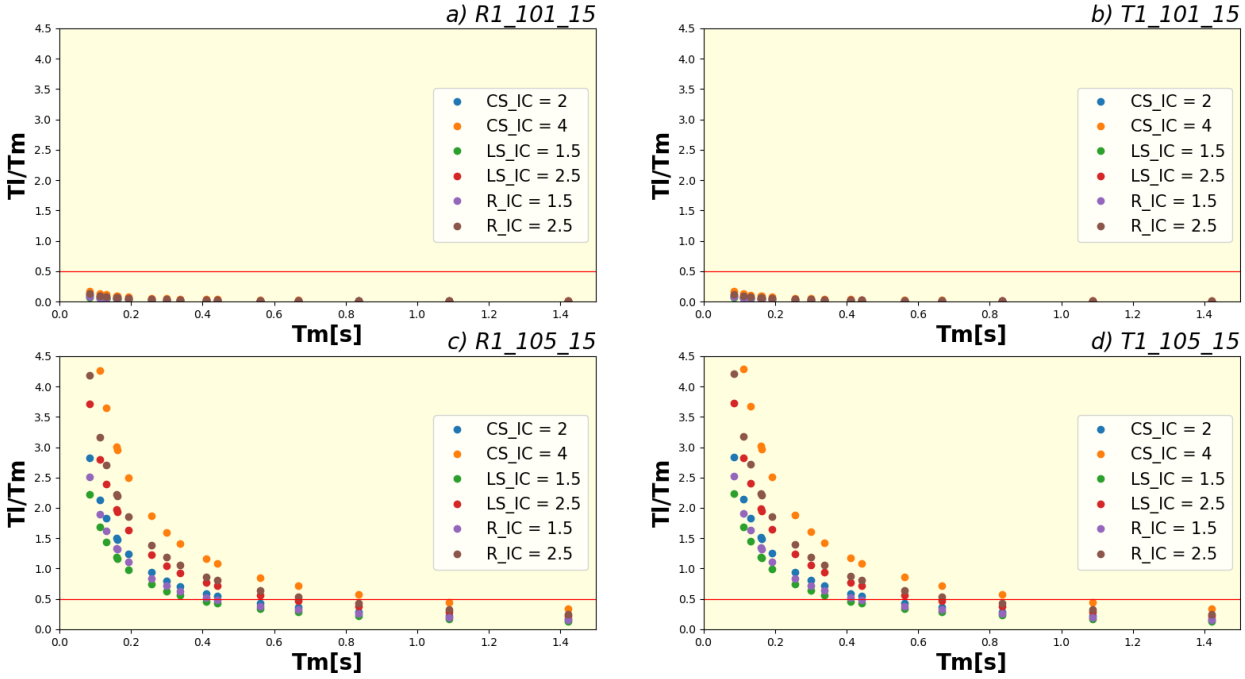

***Figure 3.20**: T_l/T_m variation of the prototypes a) « R1_101_15 », b) « T1_101_15 », c) « R1_105_15 », d) « T1_105_15 ». The red line marks the condition necessary for 2D interaction. The colourful dots represent the different material types in the different considered IC.*

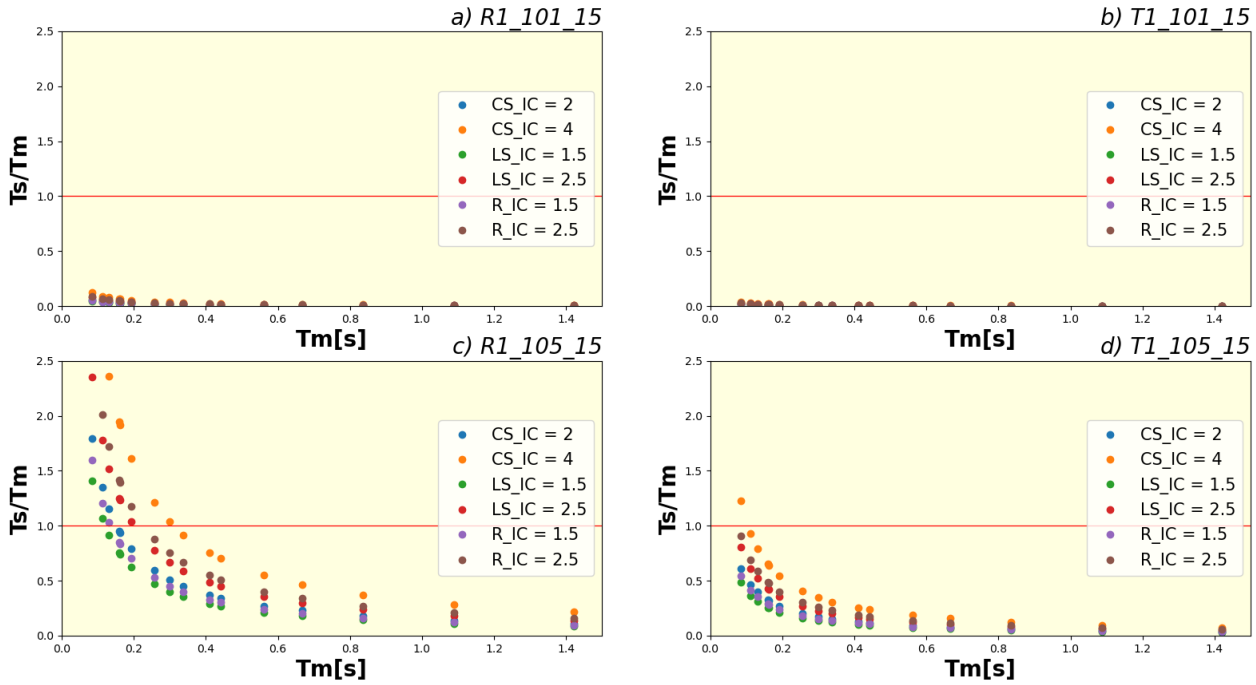

***Figure 3.21**: T_s/T_m variation of the prototypes a) « R1_101_15 », b) « T1_101_15 », c) « R1_105_15 », d) « T1_105_15 ». The red line marks the condition necessary for 1D resonance. The colourful dots represent the different material types in the different considered IC.*

According to equations 3.16 and 3.17, the parameters affecting T_s and T_l variability, and consequently the respective ratios, are the landslide dimension (i.e., H_{land} and L_{land}) and v_{land}. From figures 3.20-3.21 it can be inferred that:

- the characteristic ratios increase with decreasing v_{land} (i.e., increasing the IC)
- volume reduction corresponds to a strong decrease of T_s/T_m and T_l/T_m variation range. As shown by figures 3.20a-b and 3.21a-b, curves associated to small volume landslides do not reach neither the 1D resonance nor the 2D interaction condition. Therefore, it can be argued that the parameter « frequency content » will not significantly affect the possibility of interaction between those landslides and the selected inputs. Indeed, the computed ratios remain nearly constant within the investigated frequency range. For this reason, this category of models was forced with only 3 inputs instead of 17. At this regard, signals characterized by large, medium and small T_m (i.e., inputs « a », « c » and « r »; cf. paragraph 2.6) were selected
- increasing volume causes wider T_s/T_m and T_l/T_m variation ranges and the reaching of the conditions of interest (i.e., $T_s/T_m = 1$ and $T_l/T_m = 0.5$). This result suggests a possible major relevance of the « frequency content » parameter in the interaction of large volume landslides with the selected inputs
- the comparison of results obtained for different failure mechanisms reveals that T_s/T_m range of variation is wider for rotational than for translational landslides (3.21c-d). Indeed, keeping constant L_{land}, thickness computed for rotational landslides are larger compared to those obtained for translational landslides as consequence of a larger D/L ratio (cf. paragraph 2.5). This difference is particularly pronounced in the presence of large volume landslides. On the contrary, T_l/T_m ratios of rotational and translational landslides present the same variation range. Indeed, in this case, L_{land} as well as

material properties are the same for the two considered mechanisms. This consideration is not valid when equivalent rotational and translational landslides in configuration 3 are considered, in particular low-angle models, due to different landslide extension beyond the crest, which results in different landslide lengths (cf. paragraph 2.5)

Finally, figure 3.22 shows the distribution of all computed T_l/T_m and T_s/T_m ratios.

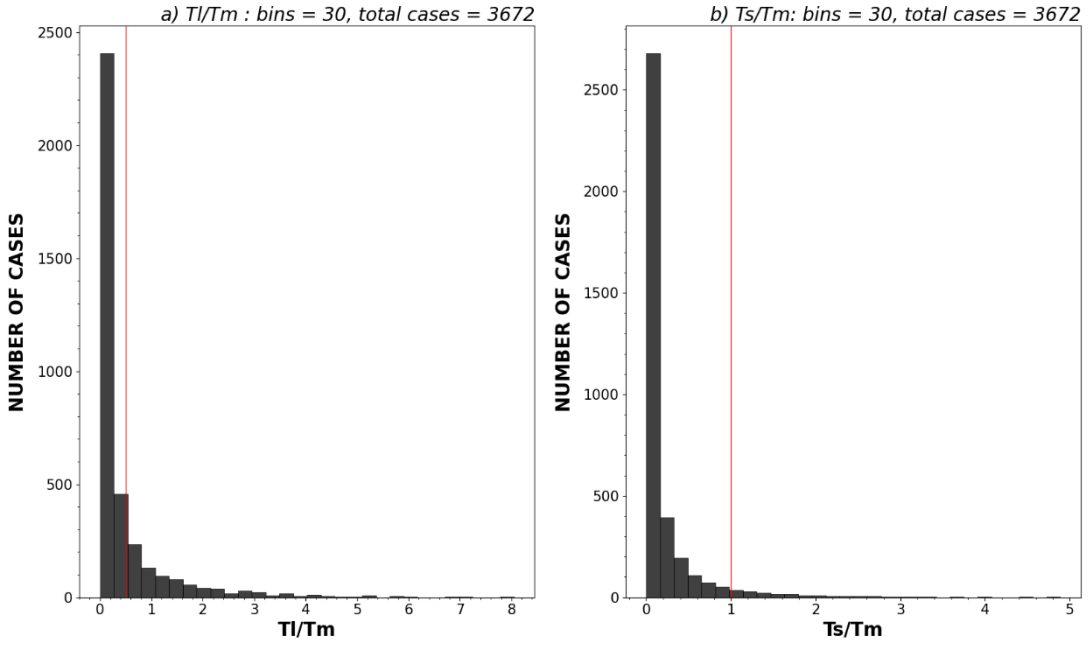

Figure 3.22: *Distribution of values for T_l/T_m (a) and T_s/T_m (b) ratios. In red are indicated the theoretical « critical » values, i.e., inducing maximum landslide displacements according to Hutchinson (1987, 1994) and Rathje & Bray (2000).*

Distribution in figure 3.22a suggests that the majority of cases (~60%) have $T_l/T_m < 0.2$ and only for ~7% of the cases this ratio is between 0.4 and 0.6. Similarly, for distribution in figure 3.22b, ~76% of the cases present a $T_s/T_m < 0.2$ and only ~2.9% of the cases have a ratio between 0.8 and 1.2. Therefore, the number of cases that present the two ratios around the values of interest are very limited compared to the entire distributions. This could affect the possibility of interpretating numerical sesimic displacements results by CPB-approach.

3.7.2 Outputs from dynamic analysis

This section discusses the outputs of the dynamic numerical modelling. All the analyses were performed by using 17 input signals characterized by their Arias Intensities and spectral features contents (cf. paragraph 2.6).

3.7.2.1 Type of outputs extracted from the results of the dynamic analyses

Dynamic numerical modelling consists in applying seismic solicitations at the bases of landslide models in order to compute the induced displacements. In contrast to Newmark's analysis in which one x-displacement value is obtained at the end of the computation, stress-strain

analyses allow extracting displacements at every node of the discretized mass, giving access to a more detailed representation of the landslide response to seismic shaking.

In order to better compare outputs from numerical and analytical methods, x-component of displacements were extracted from each grid point in order to compute the relative x-displacement of the landslide center of mass. The term « relative » refers to the fact that the computed x-displacement of the center of mass was subtracted with the mean displacement of the below stable bedrock. The center of mass displacement was computed using equation 3.14 and substituting the nodal x-displacement to the x-coordinate. Moreover, the nodal gpm values were re-extracted at the end of the dynamic simulation.

The center of mass displacement was also compared to the geometric average of all nodal displacements to verify that the two procedures returned similar results. In this manner, it can be evaluated the correctness of reporting outputs in terms of center of mass displacements.

Finally, to assess the range of variation of displacements into the landslides, relative nodal maximum and minimum displacements were computed for each model. The purpose was to verify that the computed center of mass displacement can be considered as representative of the whole mass behaviour. Indeed, if locally, nodal displacements are much larger or smaller than the computed value, this assumption cannot be done.

3.7.2.2 Performed numerical analyses

Before discussing the results, a brief explanation is needed to clarify the number of models that were effectively run compared to the initial plan.

Due to the large number of runs and the long computation times required by some of the models (cf. paragraph 3.6), it was not possible to complete all the dynamic analyses. For this reason, priority was given to models that returned relevant seismically-induced displacements in phase of post-processing of the results.

This led to exclude all small volume landslide prototypes from the list. Indeed:

- they were among the models characterized by the longest computation times due to internodal distances in the order of magnitude of 10^{-2} m that induced calculation time-steps of 10^{-8} -10^{-9} seconds
- displacements computed for a few models in this category (12 models, i.e., « R1_101_15, CS, IC = 4 », « R1_101_30, CS, IC = 4 », « R2_101_15, CS, IC = 4 », « R2_101_30, CS, IC = 4 », « R3_101_15, CS, IC = 4 », « R3_101_30, CS, IC = 4 », « T1_101_15, CS, IC = 4 », « T3_101_15 CS, IC = 4 », « R1_101_15, LS, IC = 2.5 », « R1_101_30, LS, IC = 2.5 », « R3_101_15, LS, IC = 2.5 » and « T1_101_15, LS, IC = 2.5 ») are in the order of magnitude of 10^{-8} – 10^{-5} m (i.e., much below the 1 mm threshold) and therefore they are negligible. This result is in agreement with the outputs already discussed in part 1 of this chapter, confirming not only the stability of these models under the seismic conditions here considered (T_m between 0.08s and 2.04s and Arias Intensity in the order of magnitude of 0.1 m/s), but also the necessity to prioritize the run of other types of models to obtain relevant results for this study

In addition to the previously mentioned 12 models, 105 (∼48.6% of the total) models were effectively run in FLAC. More in particular:

- for 74 models (∼34.2%), the full set of solutions is available (i.e., all the 17 inputs were applied to the initial static solution)
- for 31 models (∼14.4%) the set of solution is incomplete. This incompleteness is due to: i) incorrect saving of the output files by the software (5 models, 2.3%), ii) repeated failures of the models occurred for every tried input of the dataset (26 cases, ∼12%). The latter percentage also includes models whose set of results consist of both failures and non-failures cases. For these 26 models, inputs characterized by T_m values similar to those of other inputs that induced failure were not run since it was reasonable to expect the same result

On the contrary, the 99 not-run models (∼45.8%) include:

- small volume landslides for which no movement is expected (61 models, ∼28.2%)
- large volume landslides combined with high slope angles (18 models, ∼8.3%). For these cases, basing on the results available for similar models and SF ∼ 1 or < 1 (cf. 3.1.3), failure is expected for all the inputs
- models for which is not possible to predict the result (20 models, ∼9.2%). Out of them, 15 models (∼6.9%) were not run since they are characterized by very small internodal distances (10^{-2}/10^{-1} m)

3.7.2.3 Discussion of results

In the following, outputs from the performed stress-strain analyses are discussed. In order to highlight the effect of material, volume, slope angle, configuration and failure mechanism on the earthquake-induced mobility of the landslide prototypes, some models were selected. Additionally, the role of the characteristic periods ratios and the landslide-bedrock impedance contrast is investigated. For these analyses, models for which the set of solution is full were selected (except a few cases where the combination of geometrical and geotechnical parameters determined critical conditions for the slope, resulting in repeated failures during the dynamic phase of the modelling, cf. paragraph 3.7.2.2).

Compared to results discussed in part 1, some main differences can already be found between outputs from numerical and analytical methods:

- the set of solutions available for each geometry is 6 in the case of stress-strain analyses (i.e., material + IC) and only 3 in the case of analytical analyses (i.e., material type)
- the results are not represented in terms of averages of the 17 computed displacements since, contrary to results from Newmark's type analysis, outputs from stress-strain methods incorporate the effect of the frequency content of the input, therefore, the role of the latter can be investigated

Figures 3.23-3.26 show distributions of the x-component of the center of mass (« o ») and average (« x ») landslide displacements computed for models « R1_103_15 », « R1_105_15 », « T1_103_15 » and « T1_105_15 » after the application of each input. These figures report

also the range of variation of the nodal displacements into the landslide region by vertical bars whose top and bottom coincide with the maximum and minimum nodal displacements respectively. Since minimum displacements are generally negative (i.e., the node moves upstream), bar bottoms may not be visible from the plots due to the logarithmic scale in the y-axis. Upstream x-displacements are generally not relevant in terms of general instability of the landslide masses since they are opposite to the downstream direction along which masses are destabilized. Nevertheless, upstream x-displacements can be indicators of differential movement into the landslide mass.

The term « failure » refers to those cases in which the calculation diverges, or very large nodal displacements are returned as outputs. In order to represent failure in the plots, the inter-nodal distance was adopted as x-displacement for such models: it is the threshold displacement associated to large deformations of the mesh (i.e., failure). Additionally, critical displacements by Romeo (2000) are reported as reference. Indeed, even if it is more complex to assume a single threshold value for deformable masses, as in the rigid-block analysis, critical displacements by Romeo (2000) can still be considered reasonable for the models here presented since the adopted inter-nodal distances are smaller or in the same order of magnitude with respect to critical displacements indicated by Romeo (2000). On the contrary, if the models had larger inter-nodal distances than Romeo (2000)'s thresholds, the risk was to consider as failures, displacements for which mesh was not largely deformed (i.e., no failure).

Effect of material properties: loose soils are responsible for the larger displacements for model « R1_103_15 », especially when the higher IC (i.e., IC = 2.5) is considered (fig. 3.23).

For model « R1_103_15 », high-cohesion materials (i.e., rocks, cohesive soils) return seismic displacements that are almost below 1 mm.

On the contrary, when volume is increased up to 10^5 m^3 (fig. 3.24), larger displacements are generally registered in the presence of cohesive materials (IC = 4) and rocks (IC = 2.5) for $T_l/T_m > 1$ and $T_s/T_m > 0.5$. However, at lower ratios, loose soils give rise to failures, determining the most critical conditions. For model « R1_105_15 », the lowest displacements are related to cohesive soils (IC = 2) and rocks (IC = 1.5). Related point to these material types are indeed downward-shifted with respect to other points into the distribution in figure 3.24. Nevertheless, they follow the same variation trend with respect to characteristic periods ratios as other points.

For translational landslides, the variation of displacements with respect to material type is less clear. Similarly to model « R1_103_15 », for model « T1_103_15 » loose materials induce the highest displacements (fig. 3.25). Remaining loose soils cases give rise to failures at T_l/T_m between 0-0.6 and T_s/T_m between 0-0.15. Increasing the volume (i.e., model « T1_105_15 », fig. 3.26), failures occur for almost all the loose soils cases, determining the most critical conditions.

Contrary to rotational models, failures span over T_l/T_m and T_s/T_m wider ranges for both models « T1_103_15 » and « T1_105_15 ».

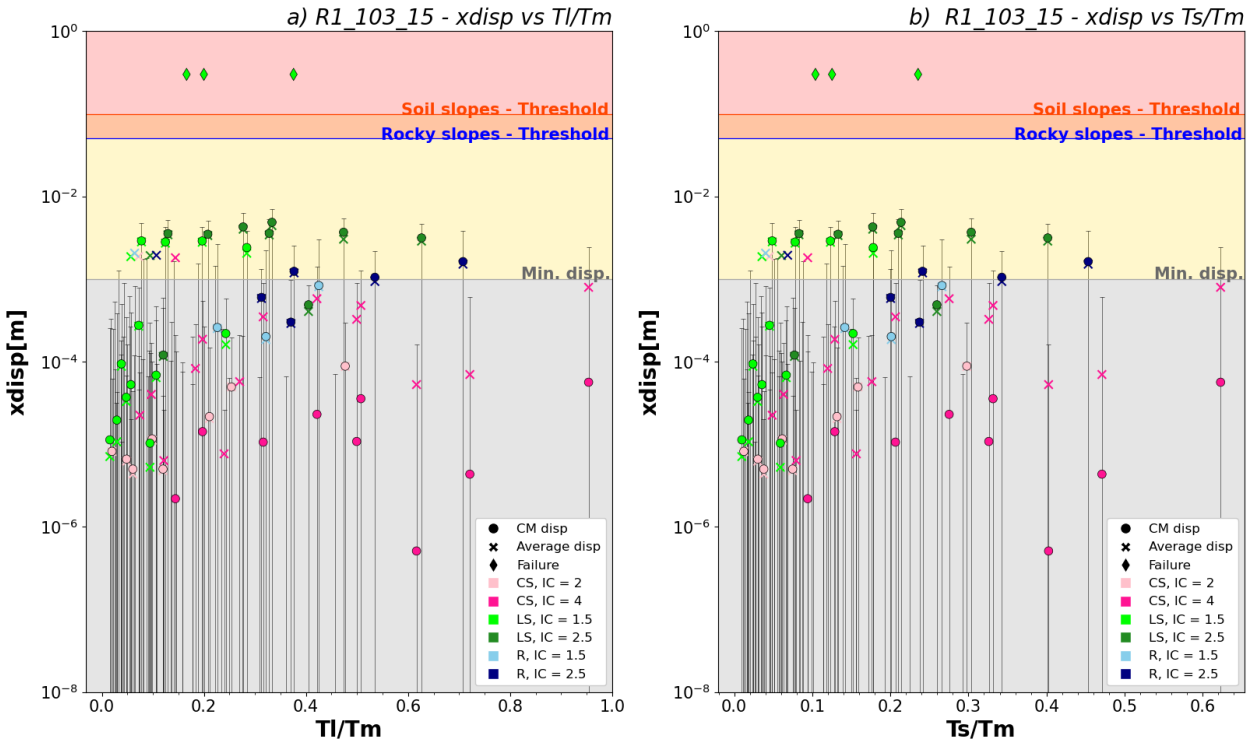

Figure 3.23: *Distribution of average, minimum, maximum and center of mass x-displacements with respect to T_l/T_m (a) and T_s/T_m (b) for model « R1_103_15 ». In the plots, bars represent the range of variability of the nodal x-displacements into the landslide mass (i.e., from minimum to maximum x-displacements), markers represent different types of displacements and colours identify material type + impedance contrast. The term « failure » indicates cases in which numerical analyses stops or returned very large displacements. In the plots, also the critical displacements indicated by Romeo (2000) are reported.*

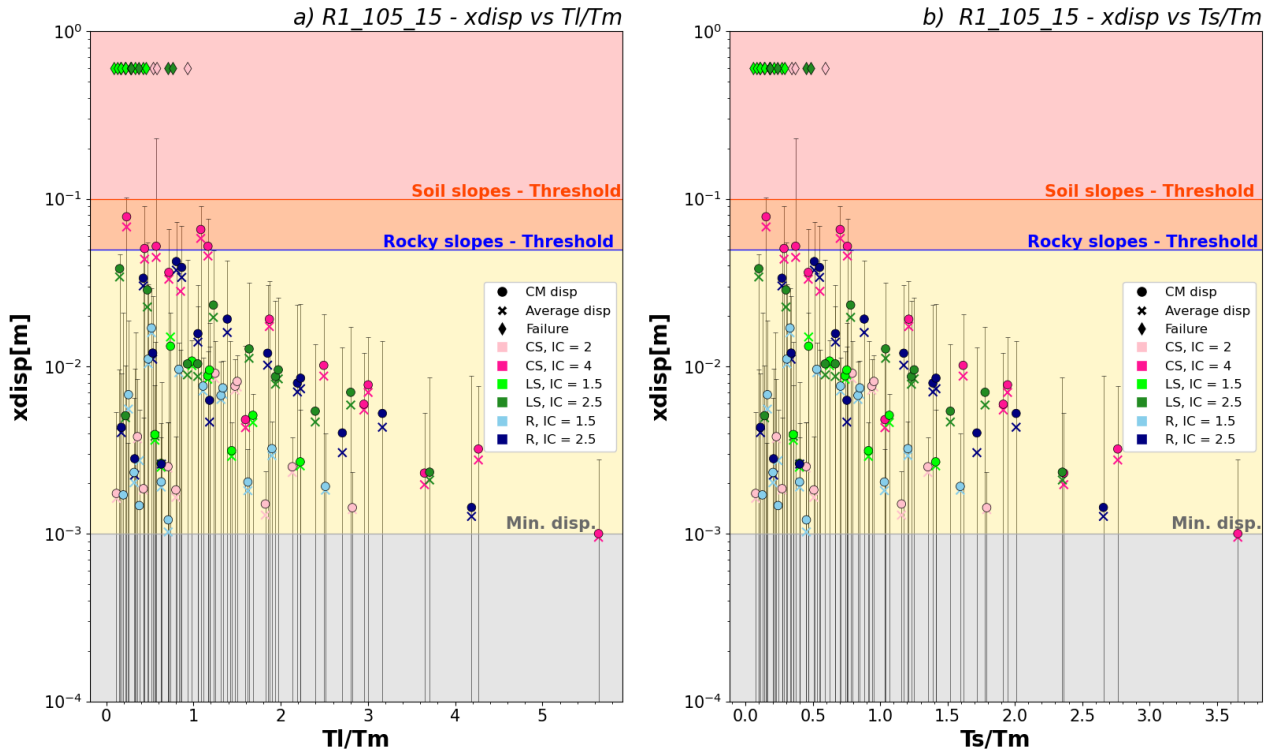

Figure 3.24: *Distribution of average, minimum, maximum and center of mass x-displacements with respect to T_l/T_m (a) and T_s/T_m (b) for model « R1_105_15 ».*

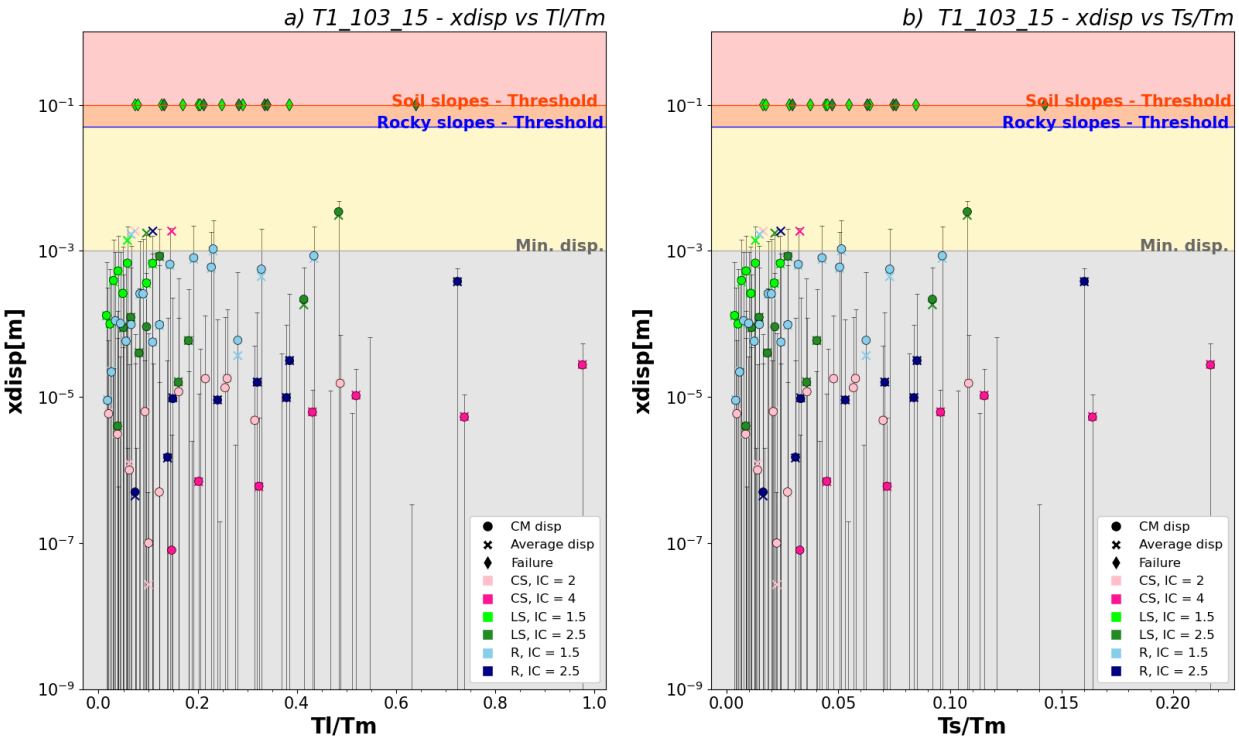

Figure 3.25: *Average, minimum, maximum and center of mass x-displacements vs T_l/T_m (a) and T_s/T_m (b) of « T1_103_15 ».*

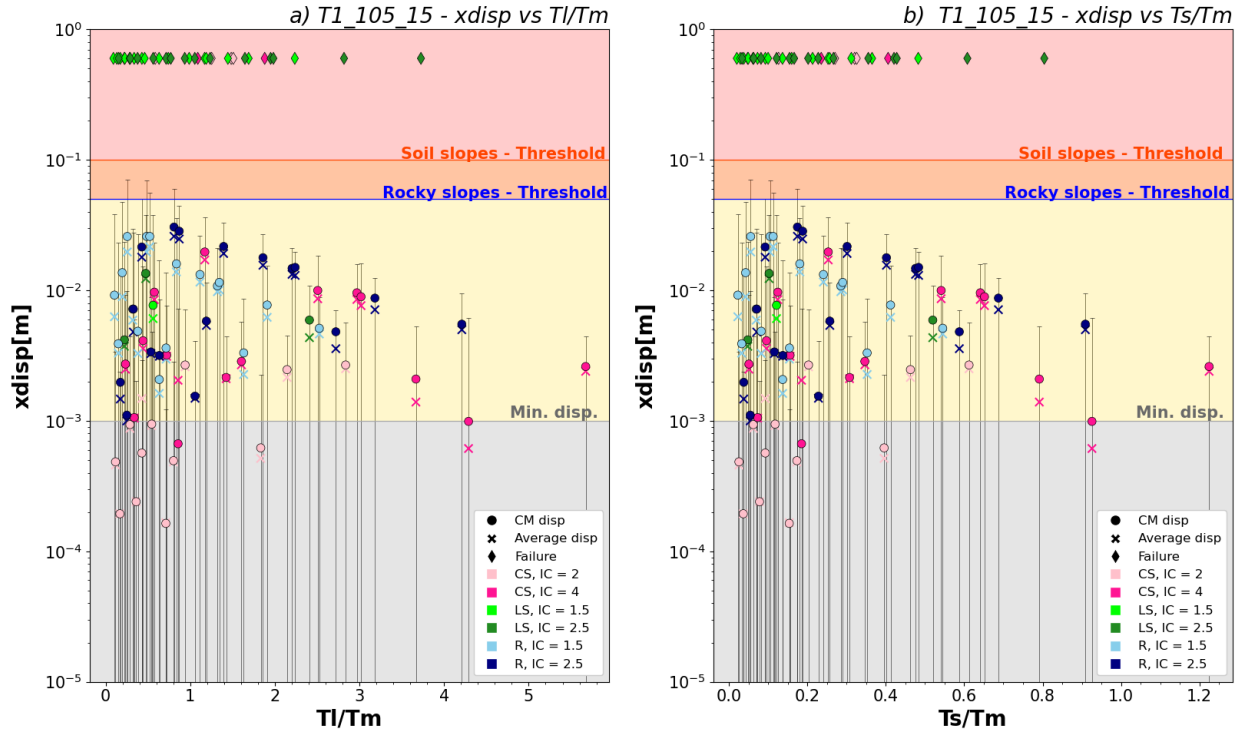

Figure 3.26: *Average, minimum, maximum and center of mass x-displacements vs T_l/T_m (a) and T_s/T_m (b) of « T1_105_15 ».*

Effect of the mechanism: displacements computed for translational models are lower compared to those for the correspondent rotational models (refer to fig. 3.23-3.25 and fig. 3.24-3.26). This outcome agrees with results already observed by Newmark's analysis (cf.

paragraph 3.2.3). One reason for this outcome can be attributed to the different dimensions of translational and rotational landslides. Indeed, according to the procedure described in paragraph 2.5, rotational landslides are characterized by greater thickness compared to the corresponding translational landslides, due to differences in their sliding surface shape and D/L. In 2D, this results in a larger total area for rotational landslides compared to translational landslides as shown in figure 3.27. Consequently, it can be interpreted that the difference in computed x-displacements between rotational and translational landslides is an indirect effect of smaller dimensions of the latter.

For further considerations regarding the impact of landslide dimensions on x-displacements reference has to be done below, where the role of the volume is discussed.

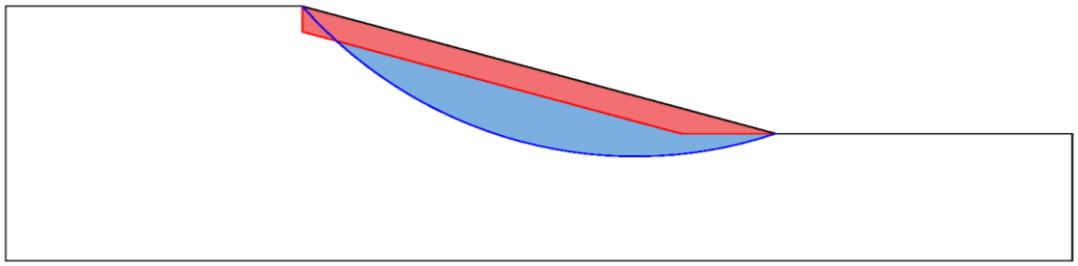

Figure 3.27: *Comparison of areas of correspondent landslide models: « R1_103_15 » (blue) and « T1_103_15 » (red).*

Effect of volume: larger volumes are associated to larger displacements. Displacements computed for models « R1_103_15 » and « T1_103_15 » and various material types/IC conditions are mostly lower than 1 mm.

Indeed, excluding failures, for model « R1_103_15 » only the 13.8% of all center of mass displacements are larger than 1 mm, whereas for model « T1_103_15 » this percentage is further reduced to 1.9%. Failure cases correspond to 1.9% of cases for « R1_103_15 » and to 14.9% of cases for « T1_103_15 ».

Increasing the volume, displacements become larger than 1 mm and the number of failures increases up to 25.7% for model « R1_105_15 » and to 36.3% for model « T1_105_15 ». The impact of volume modifications on landslide seismic displacements is better visualized in figure 3.28, in which results related to models « R1_103_15 » and « R1_105_15 » are directly compared. From figure 3.28, two different clusters of points can be clearly identified: the first located at the bottom of the plot (i.e., green points, corresponding to V = 10^3 m^3) where displacements range from ~10^{-7} to ~10^{-2} m and that are included in a narrow characteristic period range, and the second (i.e., blue points, corresponding to V = 10^5 m^3) located at the top of the plot, in which displacements are between ~10^{-3} and ~10^{-1} m and span over a large characteristic period ratios range. The difference in the shapes of the two distributions (i.e., that related to medium volume landslide and to large volume landslide) is further commented below. Indeed, for a more comprehensive analysis, the role of characteristic period ratios and therefore of the frequency content of the inputs must be further investigated.

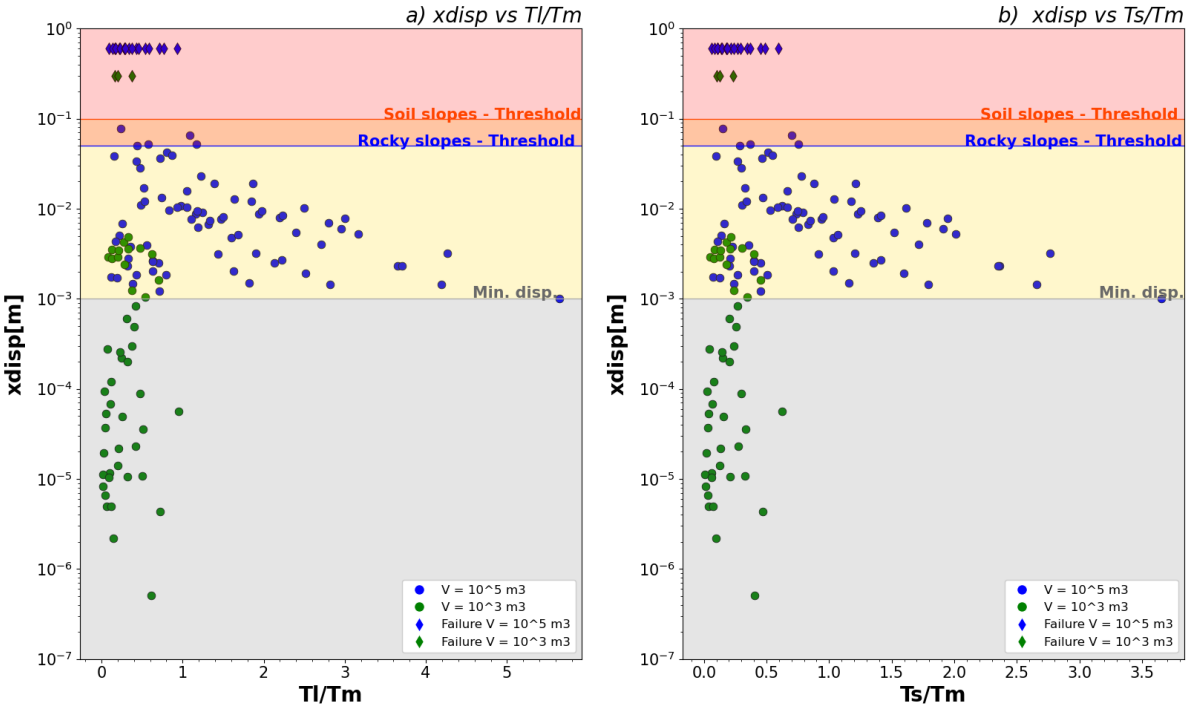

Figure 3.28: *Distribution of the center of mass displacements of « R1_103_15 » and « R1_105_15 ».*

Effect of input frequency content: as previously discussed (cf. paragraph 3.7.1.2) volume modifications strongly affect T_l/T_m and T_s/T_m variation ranges. More in particular, characteristic periods ratios of large volume landslides span over a wider range compared to those of smaller volume landslides. As a consequence, differences in the seismic displacement distributions results when the latter are plotted with respect to T_l/T_m and T_s/T_m. For medium volume landslides (fig. 3.23 and 3.25) no variation trend of displacements vs T_l/T_m and T_s/T_m is identifiable. From this evidence it can be argued that displacements computed for medium volume landslides do not seem to be significantly affected by characteristic period ratios variations in the frequency range here considered. Increasing landslide volume (fig. 3.24, 3.26, 3.28), characteristic period ratios span over a larger range of values and displacements dependency on the characteristic periods ratios appears more clearly. A peak of displacement can be seen for T_l/T_m between 0 and 1. In this range, displacements may strongly vary for small T_l/T_m increase until they reach a peak around $T_l/T_m = 0.5$. For $T_l/T_m > 1$, displacements follow a decreasing trend. This result is consistent with Hutchinson (1987; 1994). Indeed, displacements reach a peak nearly the theoretical value identified by the author and for larger ratios, their decreasing demonstrates that the interaction between high frequency content inputs (i.e., input characterized by short T_m) and high-length landslides is less effective in terms of induced displacements. On the contrary, no correlation is found between the 1D resonance condition and displacement values even if the latter follow an increasing-decreasing trend with T_s/T_m that is similar to that observed with respect to T_l/T_m.

Comparison between different extracted displacements: from figures 3.23-3.26 it can be inferred that average and center of mass displacements are comparable in almost all cases, since related points usually overlap or are very close. Nevertheless, representing landslide movement by a single value might lead to neglect displacement variations into the landslides.

Indeed, if maximum displacements are much different than computed average and/or center of mass displacements and if these maximum values occur at the ground surface, more severe damages may be registered on buildings. In figure 3.24, in 4% of the investigated cases, the computed maximum displacements overcome Romeo (2000)'s critical displacement thresholds even if the computed average/center of mass displacements stay well below these limits. The percentage is very low, and maximum displacements generally remain within the same order of magnitude as calculated center of mass displacements. This observation allows concluding that representing landslide displacements by a single average value is an accurate assumption for the landslide configurations here analysed. Nevertheless, this conclusion cannot be generalized since it would be necessary to evaluate case by case. Moreover, quantifying the difference between average and maximum displacements is not sufficient alone and must be completed with more information regarding the location of occurrence of these maximum values in order to better evaluate the associated risk. The topic, that it is not further investigated in this study, would deserve more in-depth future analyses.

Effect of slope angle: figure 3.29 compares center of mass displacements computed for models « R1_103_15 » and « R1_103_30 ».

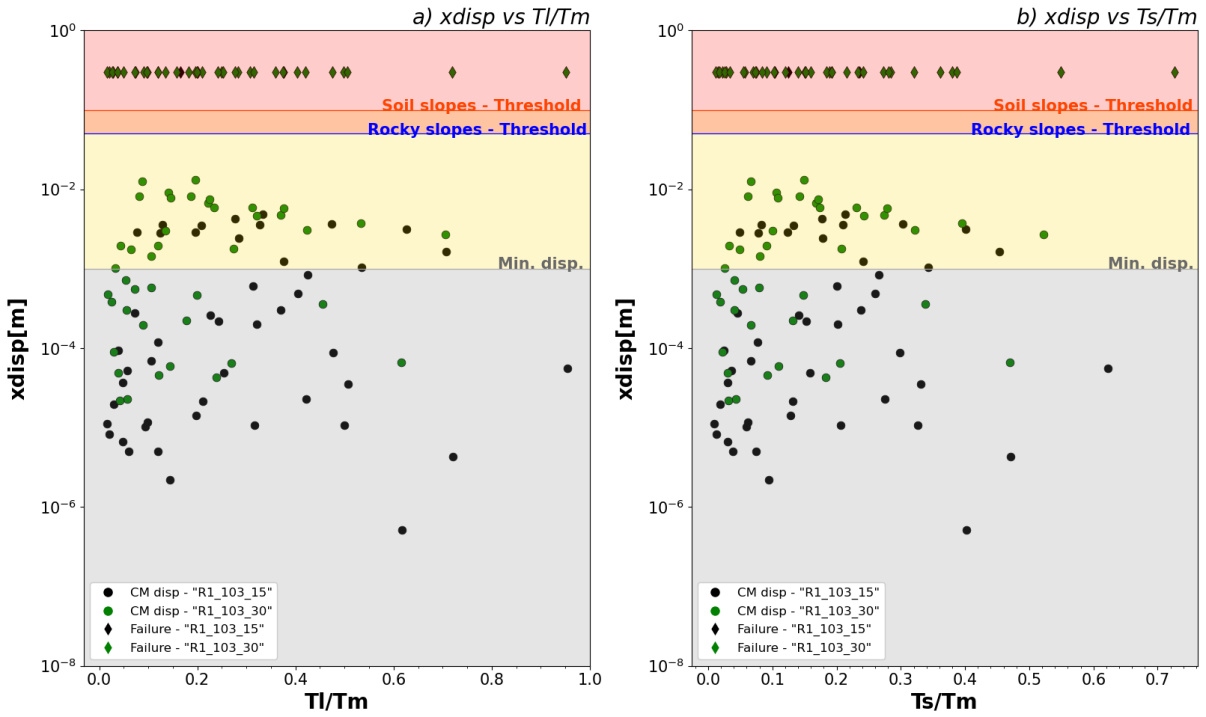

Figure 3.29: *Comparison of displacements distributions for models « R1_103_15 » and « R1_103_30 ».*

According to figure 3.29, slope angle increase does not modify displacements distribution with respect to characteristic periods ratios. Indeed, according to the adopted procedure (cf. paragraph 2.5), corresponding models, which are differentiated only for the parameter « slope angle » such as models « R1_103_15 » and « R1_103_30 », present almost same dimensions. Consequently, the investigated characteristic periods ratios range is similar. As previously observed for model « R1_103_15 », the limited range of characteristic period ratios prevents the observation of any correlation between characteristic periods ratios and displacements in the frequency range here considered. Nevertheless, from figure 3.29 it can

be inferred that increasing slope angle induces a general shift of the points towards larger displacements and a significant increase of the number of failures (it reaches ~46% of the total cases). In the case of the « R1_105_30 » model, which is characterized by a combination of large volume with high slope angle, numerical modelling returned failures for all the inputs. This result is consistent with critical/unstable conditions indicated by computed SF in static conditions (cf. paragraph 3.1.3). For this reason, it was not possible to compare outputs obtained for models « R1_105_15 » and « R1_105_30 ».

Effect of landslide configuration: figure 3.30 compares center of mass displacements computed for models « R1_105_15 », « R2_105_15 » and « R3_105_15 ». As shown by figure 3.30, modifying the landslide configuration (« R1 », « R2 » and « R3 ») does not impact displacements distribution with respect to period ratios.

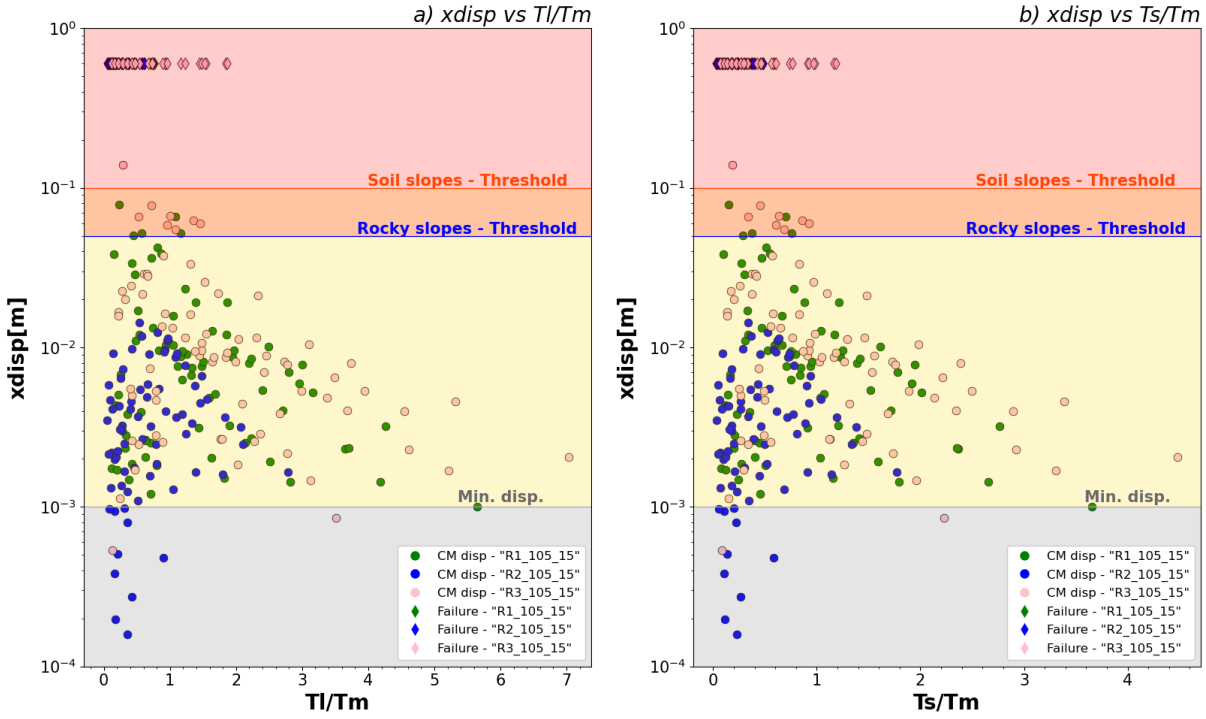

Figure 3.30: *Distribution of the center of mass displacements with respect to T_l/T_m (a) and T_s/T_m (b) for the models « R1_105_15 », « R2_105_15 » and « R3_105_15 ».*

As previously observed for Newmark's analysis, landslide configuration affects displacements in the same way as the volume. Indeed, configurations 1 and 3 behave in the same manner, i.e., displacements points almost overlap. On the contrary, due to smaller dimensions for the « R2 » model, displacements spread is narrower and displacements values are smaller.

Overview of the computed relevant (i.e., > 1 mm) displacements (~32% of run cases) is provided in frequency distribution plots in figures 3.31 and 3.32.

Figures 3.31 and 3.32 report the results related to all landslide prototypes for which the full or partially completed set of solution is available (cf. paragraph 3.7.2.2). From figures 3.31 - 3.32 the following cases were excluded:

- failures (i.e., cases in which the calculation diverged, or very large nodal displacements were returned from FDM modelling), ~24% of run cases

- center of mass displacements below 1mm, ~44% of run cases

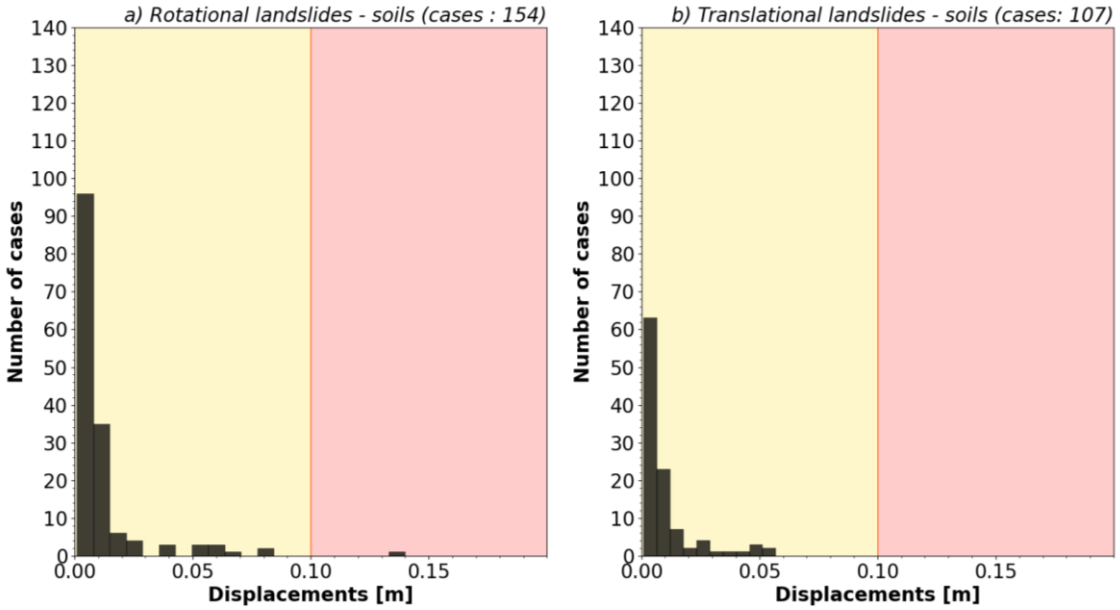

Figure 3.31: *Distribution of center of mass displacements above 1 mm calculated for rotational (a) and translational (b) landslide prototypes in soil materials (i.e., cohesive soils and loose soils). The yellow area contains displacements above 1 mm, whereas the red area contains all displacements major than Romeo (2000)'s threshold.*

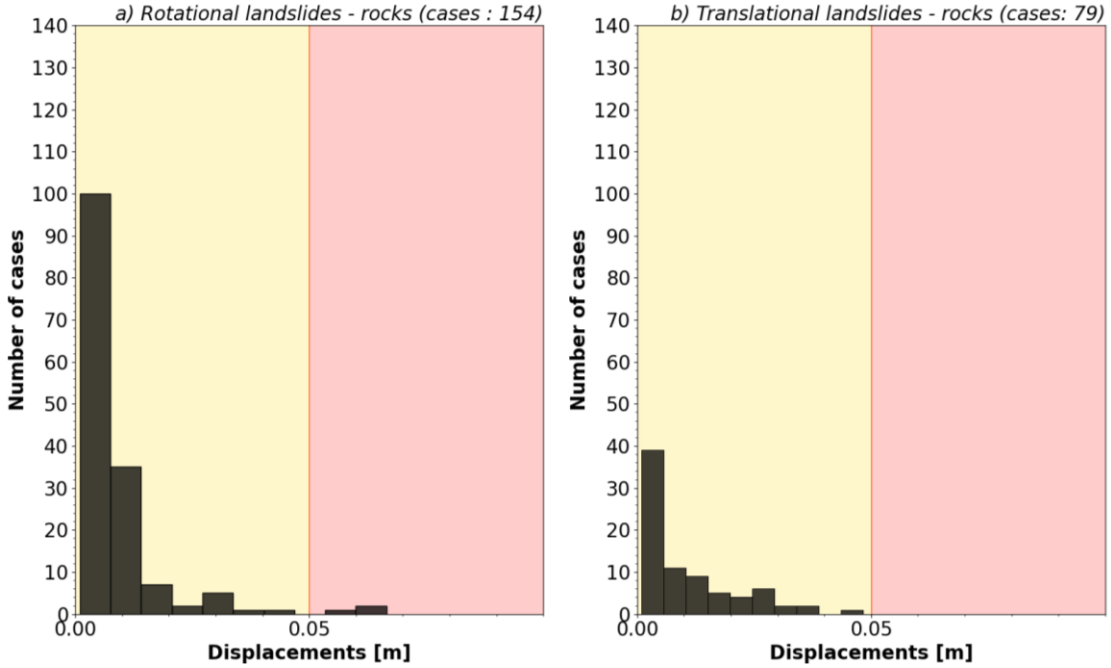

Figure 3.32: *Distribution of center of mass displacements above 1 mm calculated for rotational (a) and translational (b) landslide prototypes in rock materials. The yellow area contains displacements above 1 mm, whereas the red area contains all displacements major than Romeo (2000)'s threshold.*

From figures 3.31-3.32, it can be inferred that, excluding some cases overcoming Romeo (2000)'s thresholds, the range of displacement variation is as follows: i) it is almost the same for rotational and translational landslides involving rocky slopes (fig. 3.32), ii) it is wider for rotational landslides in the presence of soil slopes (fig. 3.31).

Independently of material type, displacements exceeding 1 mm are more numerous for rotational landslides (308 total cases) compared to translational landslides (186 total cases). This can be clearly observed by looking at figures 3.31-3.32. One reason for this difference could be attributed to the greater number of runs for rotational models (910) compared to translational prototypes (646). Indeed, independently of material type, the fraction of displacements above 1 mm is quite similar for the two mechanisms (i.e., 29% of run cases for translational models and 34% of run cases for rotational models). Despite the comparison of correspondent rotational and translational models (such as « R1_105_15 » and « T1_105_15 ») revealed that the first ones experience larger displacements and figure 3.31 demonstrated that relevant displacements for rotational landslides span over a wider range compared to translational landslides especially when soil slopes are considered, since not all models were run, at this stage, some information may be missing from figures 3.31-3.32, therefore, their analysis does not allow drawing a definitive conclusion on the topic.

In figures 3.33-3.34, relevant displacements distributions for rotational and translational landslides involving soils and rocks are classified basing on the parameter « volume ».

Similar to observations made for results from Newmark's analysis (cf. paragraph 3.2.3), the plots clearly show a prevalence of displacements belonging to landslides prototypes characterized by the largest considered volume. This occurs independently of material type and failure mechanism. In particular:

- in figure 3.33a, data related to large volume landslides represent ∼80% of the data
- in figure 3.33b, data characterized by V = 10^5 m^3 are ∼82% of the total distribution
- in figure 3.34a, data belonging to the largest-size landslides are ∼60% of the entire distribution
- in figure 3.34b, data related to V = 10^5 m^3 are ∼83% all the data

In all the 4 plots, data related to the smallest-size landslide prototypes are completely absent. Consequently, it can be concluded that, according to FDM numerical modelling, these landslides are stable in the seismic conditions considered in this research. Conversely, large volume landslides are the most susceptible.

This result further confirms the importance of the parameter « volume » for predicting earthquake-induced mobility of landslides.

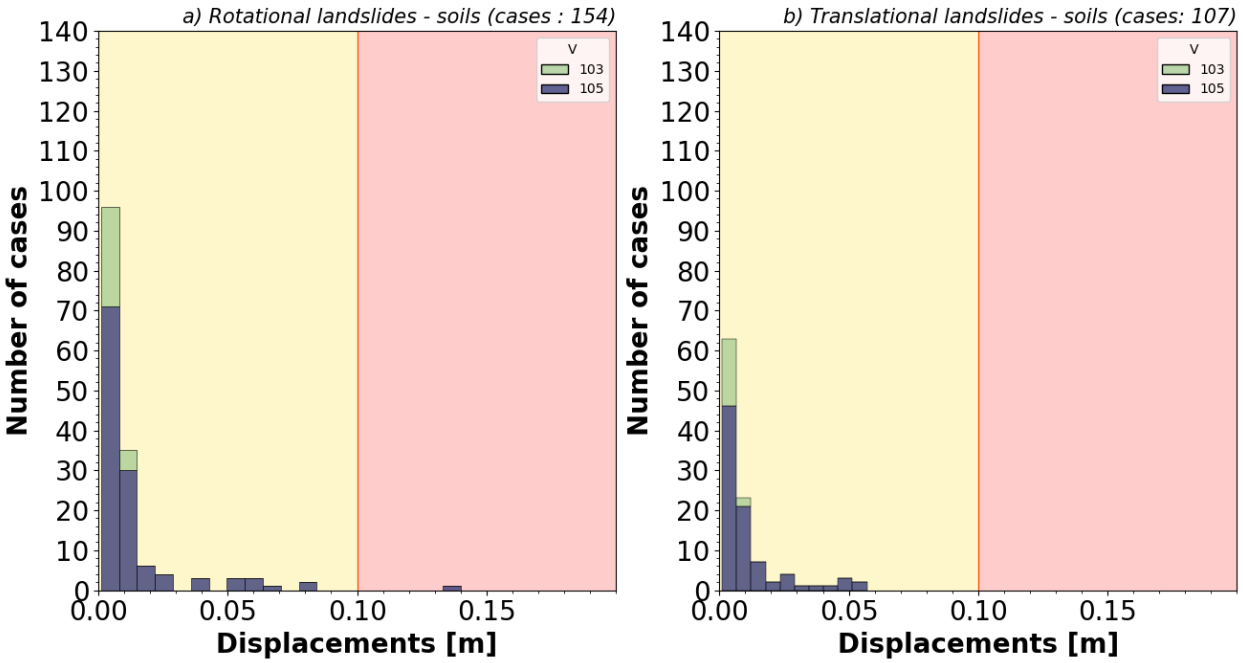

Figure 3.33: *Distribution of center of mass displacements above 1 mm calculated for rotational (a) and translational (b) landslide prototypes in soils with focus on the parameter « volume, V ». The yellow area contains displacements above 1 mm, whereas the red area contains all displacements major than Romeo (2000)'s threshold. Moreover, in the legend « 103 » indicates V = 10^3 m^3 and « 105 » indicates V = 10^5 m^3.*

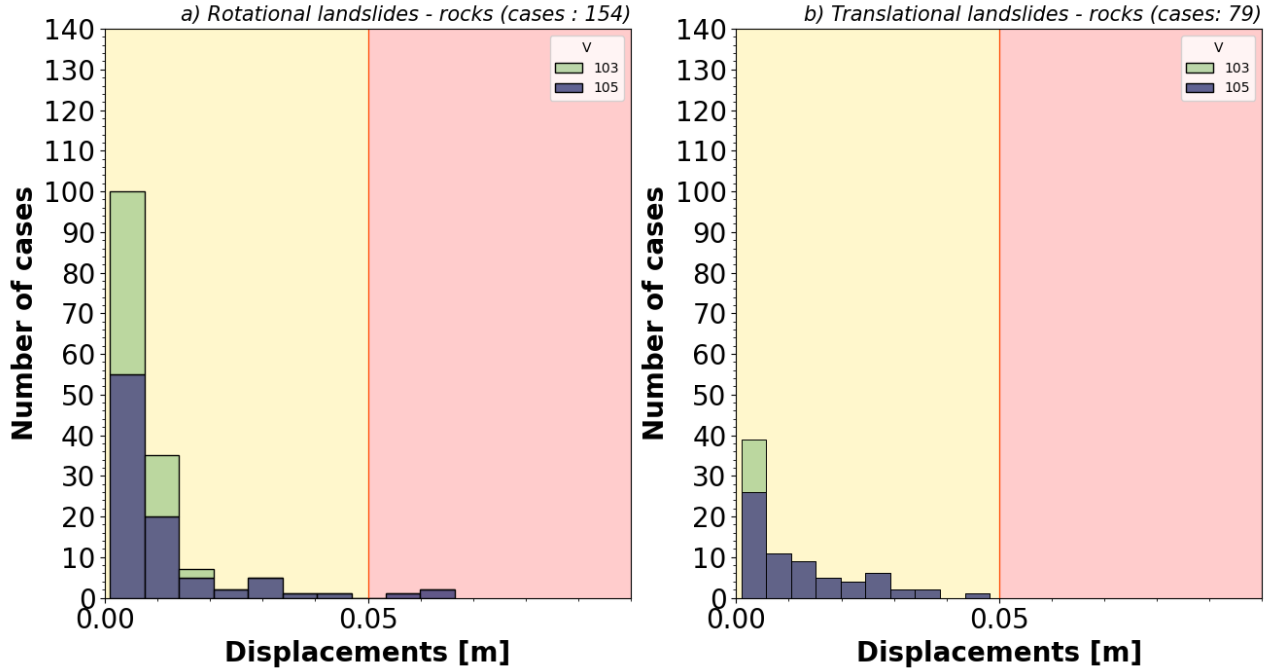

Figure 3.34: *Distribution of center of mass displacements above 1 mm calculated for rotational (a) and translational (b) landslide prototypes in rock-type materials with focus on the parameter « volume ». The yellow area contains displacements above 1 mm, whereas the red area contains all displacements major than Romeo (2000)'s threshold. Moreover, in the legend « 103 » indicates V = 10^3 m^3 and « 105 » indicates V = 10^5 m^3.*

In figures 3.35 and 3.36, results from figures 3.31 and 3.34 are plotted against the characteristic periods ratios.

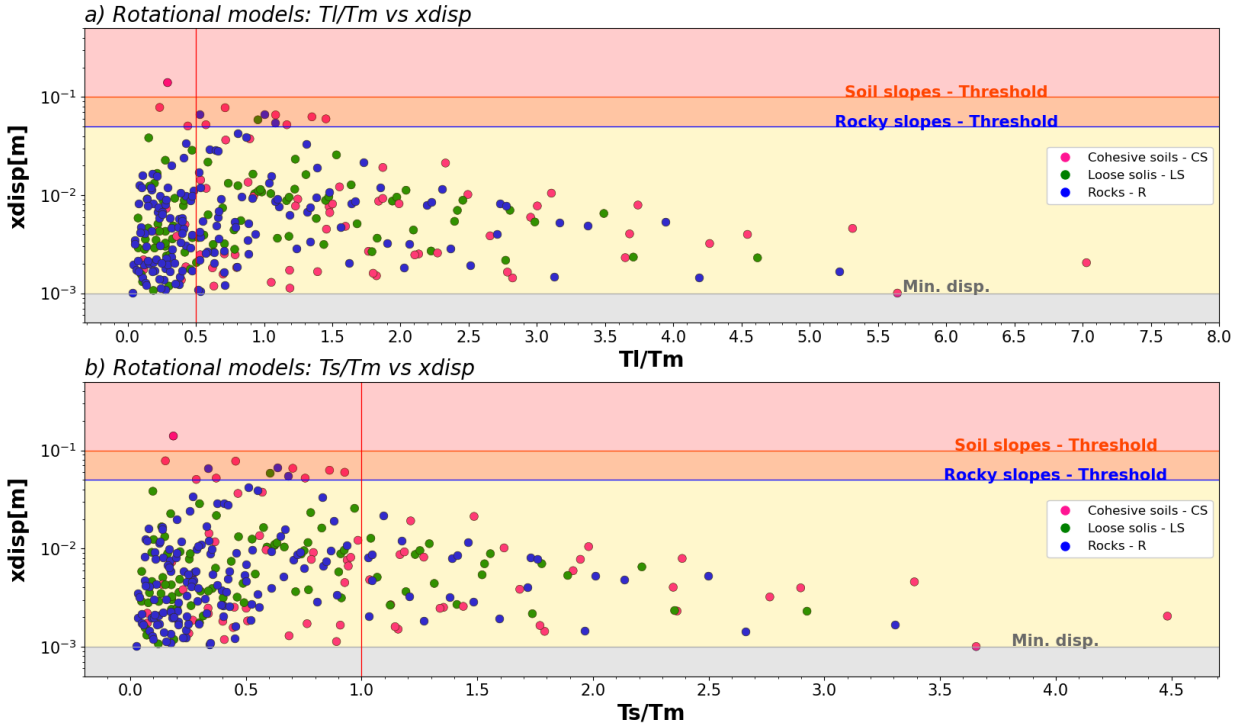

Figure 3.35: *Distribution of the center of mass displacements for rotational landslides models with respect to characteristic periods ratios.*

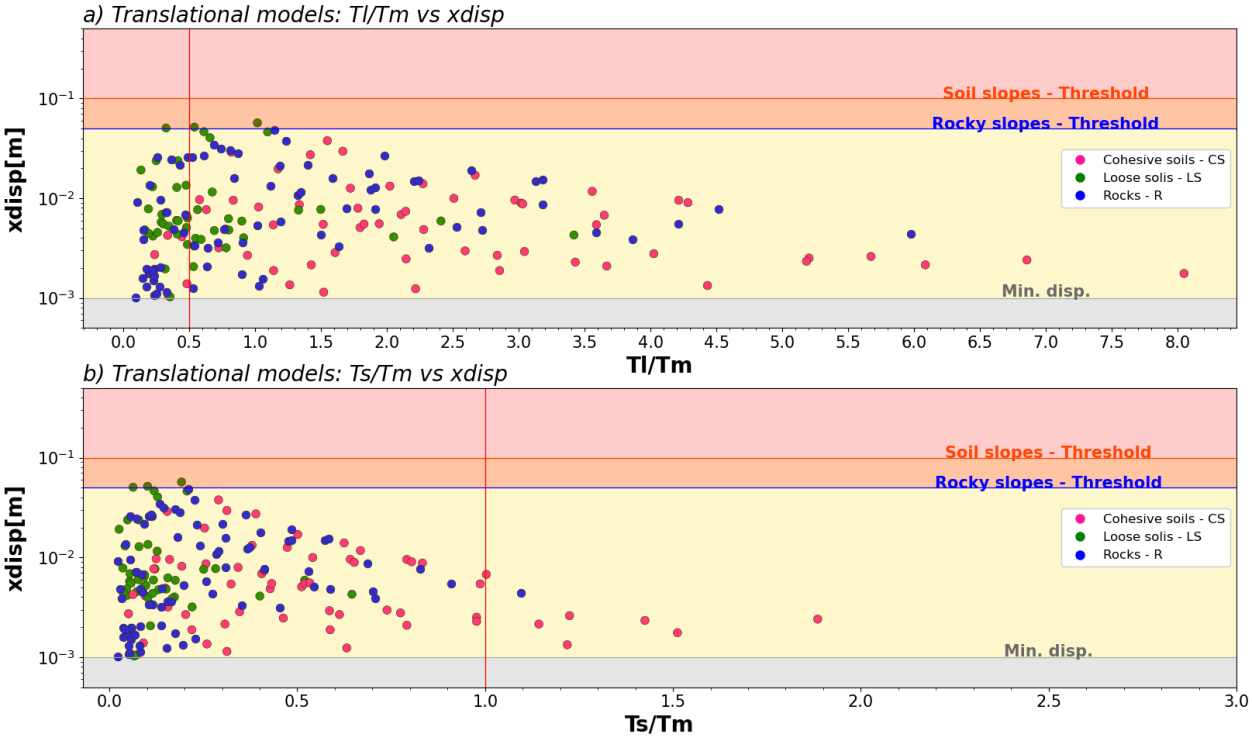

Figure 3.36: *Distribution of the center of mass displacements for translational landslides models with respect to characteristic periods ratios.*

From figures 3.35-3.36, it can be inferred that:

- landslide composition (i.e., material type) does not significantly affect displacements distribution shape. Indeed, displacements follow the same distribution trend independently of material composition
- 1D resonance is not particularly relevant for earthquake-induced mobility of landslides in the seismic conditions considered here. Indeed, no displacement peak is identifiable at $T_s/T_m = 1$. This may be because the resonance condition is rarely reached by the models in the frequency range here analysed (cf. paragraph 3.7.12, fig. 3.22). Nevertheless, the plots showing displacements vs T_s/T_m demonstrate a clear distribution variation trend resulting in an increase and then a decrease of the displacements as T_s/T_m increases, even if the peak does not occur at the expected theoretical ratio
- 2D seismic input-landslide interaction plays a fundamental role in modifying earthquake-induced mobility of landslides. Indeed, displacements distributions depend on a complex interplay between ground-motion parameters (T_m) and landslide characteristics: they reach a peak close to $T_l/T_m = 0.5$ (Hutchinson 1987; 1994). When the seismic input mean frequency increases (i.e., T_l/T_m increases) the interaction is less effective and a decreasing trend of displacements is identifiable

3.7.2.4 Insight on numerical modelling failures

Failure cases are discussed below. The purpose of this section is to investigate if the occurrence of numerical modelling failures can be explained considering the characteristic period ratios and, therefore, if specific inputs are more prone to trigger failures for specific landslide geometries. Since results shown in the previous paragraph highlighted that the 1D resonance does not significantly affect landslide mobility, focus will be on T_l/T_m.

In order to understand which failures are related to the features controlling the interaction between landslide mass and seismic input in 2D schemes, all the failures observed for models characterized by SF = 1 or < 1 were excluded. Indeed, it can be argued that in these cases, whatever input, independently from its frequency, would have induced the landslide destabilization. At this regard a short premise must be done. All generated prototypes were run in FLAC without accounting for the computed SF value, in order to identify eventual predictive differences between analytical and numerical methods. Therefore, models in critical or unstable conditions according to limit equilibrium methods (i.e., $SF \leq 1$, cf. paragraph 3.1.3) were run in FLAC in any case. All of them reached a static equilibrium, even if for some of them, failures occurred for all inputs during the dynamic phase. The latter failure cases are those excluded from this analysis. In addition, only models returning at least one failure were considered. Indeed, remaining models are probably so stable that cannot be destabilized by any of the signals here investigated. For these models, displacements distribution should be studied in order to understand the effect of the seismic input frequency on landslide mobility (cf. paragraph 3.7.2.3).

3 LEMA_DES inputs characterized by long-medium and small T_m were selected (i.e., a: T_m = 2.04 s; c: T_m = 1.09 s; p: T_m = 0.16 s) in order to illustrate failures distributions and not failures cases highlighting the parameter « landslide length, L » (fig.3.37-3.39).

At this regard 5 length classes were distinguished:

- L ≤10 m
- 10 m < L ≤ 50 m
- 50 m < L ≤ 100 m
- 100 m < L ≤ 150 m
- L > 150 m

From figures 3.37-3.39 it can be inferred that failure cases do not peak at the theoretical ratio T_l/T_m = 0.5 except for input p (fig. 3.39a). Nevertheless, mean periods affect failure occurrences. Indeed, the longest period input (i.e., a) induces failures for most of the long landslides (length in the range 100 and 150 m). On the contrary most of the short landslides (i.e., landslides with maximum length ≤ 50 m) fall in the not failure plot (fig. 3.37b). An exactly opposite behaviour occurs for input p. Input c is characterized by an intermediate behaviour. Indeed, this input is characterized by an average mean period and therefore it might be able to move a wider range of landslide length classes.

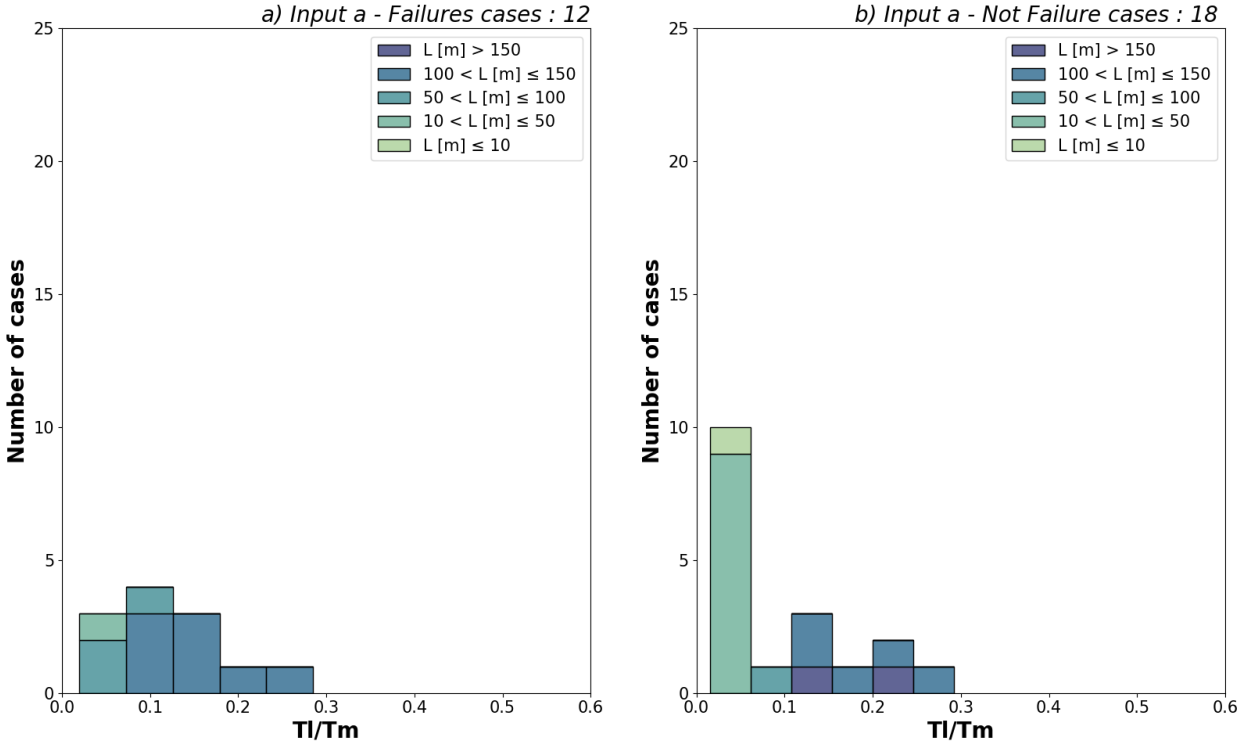

Figure 3.37: *Distribution of failure (a) and not failure (b) cases for input a.*

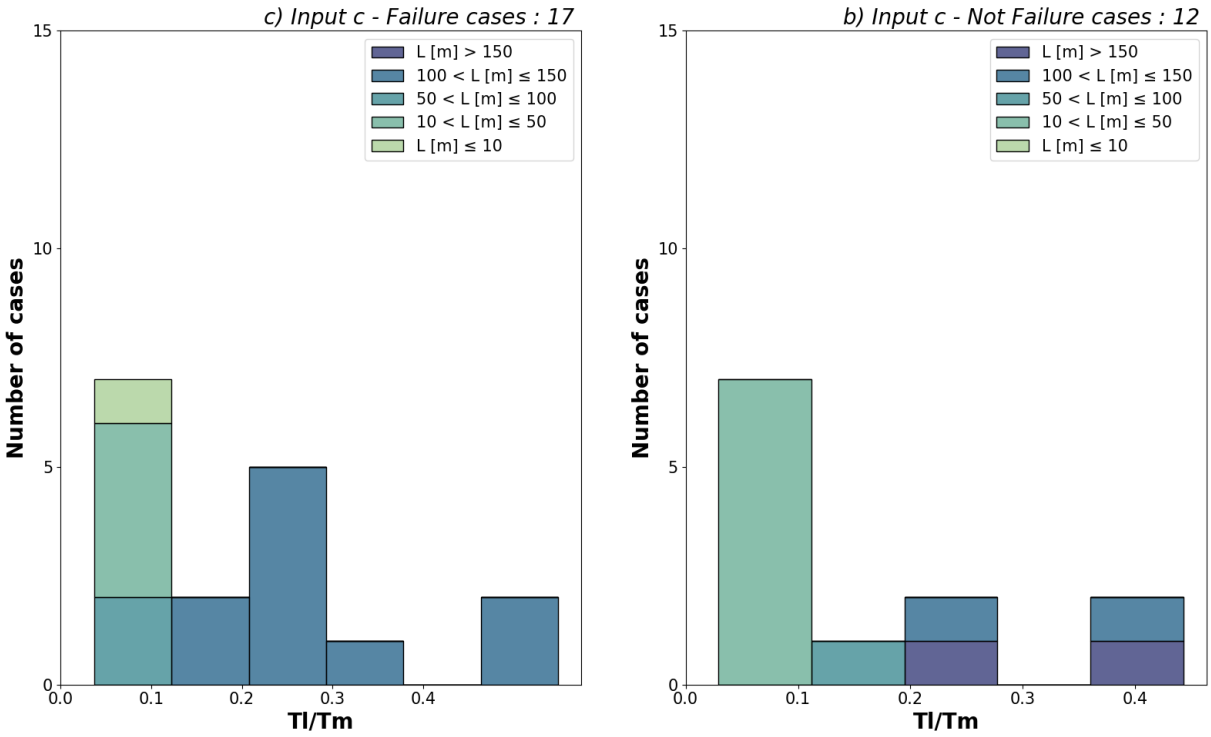

Figure 3.38: *Distribution of failure (a) and not failure (b) cases for input c.*

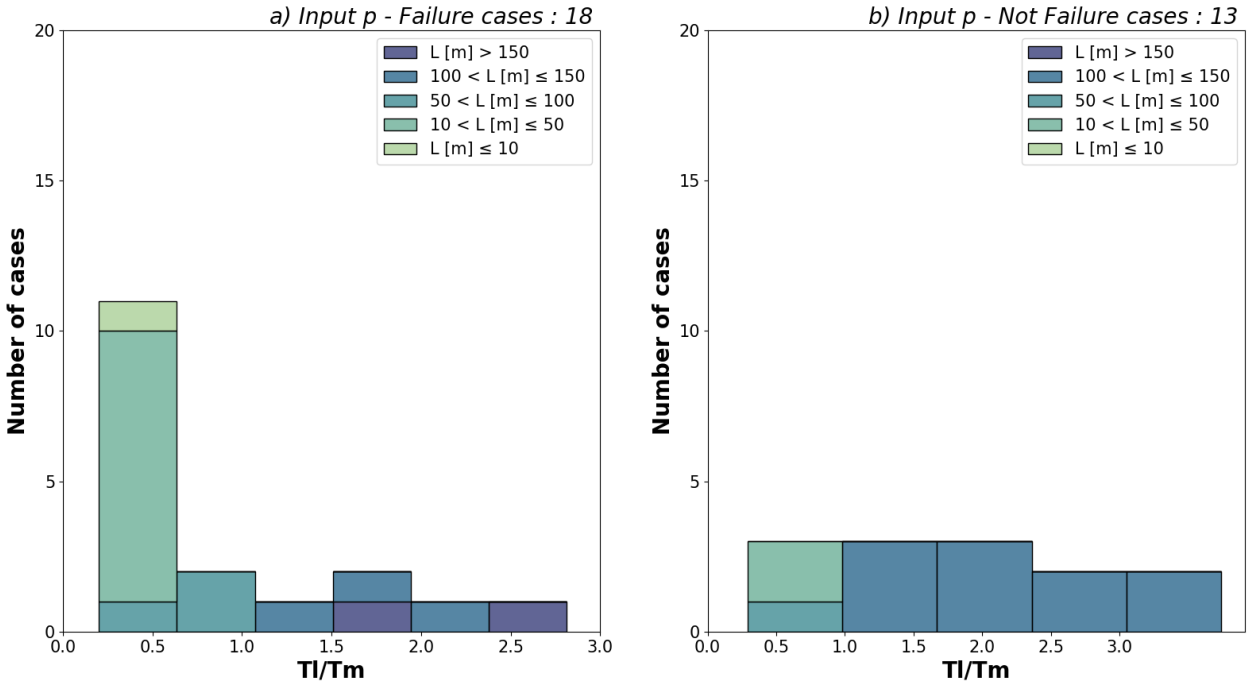

Figure 3.39: *Distribution of failure (a) and not failure (b) cases for input p.*

Distributions here described, cannot be quantitatively commented due to the general incompleteness of numerical modelling set of results and to the fact that the inputs were not

run the same number of times (cf. paragraph 3.7.2.2). Because of that, the number of cases contained into distributions in figures 3.37-3.39 cannot be compared.

However, these obtained preliminary results are consistent with landslide mass –seismic wave interaction theory.

Chapter 4: Machine Learning (ML) Random Forest (RF) analysis

4.1 Introduction

The present chapter investigates the possibility of using machine learning, in particular the random forest algorithm, on the dataset derived from this research (cf. chapter 2 and 3). The goal is to develop a preliminary predictive model for earthquake-induced displacements of landslides that can address future users towards analytical (cf. chapter 3, part 1) or numerical (cf. chapter 3, part 2) methods. More in particular, the predictive model here developed is expected to provide with an estimation, by *a priori* evaluations (i.e., knowing geometrical, geotechnical and seismic parameters of landslides under investigations), of the severity in terms of quantitative difference between predictions by conventional pseudo-dynamic approaches and numerical modelling. In other words, the random forest predictive model here developed will be able to address the following questions: i) which is the method predicting larger seismic displacements; ii) how much the expected difference between the two predictions is. Nevertheless, methodology here proposed does not express a judgement regarding the reliability/convenience of selecting one of the two methods since it must be the result of each user's choice basing on the combination of:

- scale of the study
- time available for decision-making
- cost-benefit ratio (i.e., over-estimated displacements require the adoption of over-estimated risk management measures that can be costly, therefore, the most conservative solution is not always the most optimal)

The definition of such kind of predictive model could represent a significative step forward for disciplines dealing with assessment of hazard related to earthquake-induced landslides.

Before presenting the performed analyses, the reader must be aware that results here discussed are part of a procedure that is still at its early development phase. Indeed, the dataset (i.e., the dataset including all outcomes of this study) used for the analyses is still far from being considered complete. In particular, the latter requires further enrichments in terms of variability of geometrical and geotechnical parameters considered to design the landslide prototypes and the use of seismic inputs representative of alternative seismic scenarios either in terms of frequency or energy contents. Besides, the fact that the considered variables are not continuous in terms of covered value ranges, contributes to limit the possibility of application of the algorithm out of the values here considered. This is especially for some parameters such as the Arias Intensity, which value was considered almost constant in this study.

Despite these limitations, results presented below, illustrate how data science could be used for risk management purposes and encourage towards future in-depth investigations.

4.2 Machine Learning (ML)

ML methods are discussed in the following. Except when differently specified, most of information was extracted from scikit-learn.org. The present paragraph does not claim completeness on the topic, which does not directly represent the object/main interest of this research, but it just aims at providing the reader with a summary of main functionalities of ML methods as they were used in the framework of this research.

Machine Learning (ML) (Marsland, 2014) is a sub-discipline of Artificial Intelligence (AI) (Russel & Norving, 2020) that nowadays counts variety of applications to solve problems (Diridi, 2021) due to its recognized efficiency in handling/interpreting big amount of data (Mahesh, 2020).

In recent years, ML spread in disciplines related to earth sciences, particularly those dealing with natural hazard due to the combination of:

- increase of computers computational power
- community of computer developers able to generate efficient and easily implementable algorithms

Both factors contributed to a great diffusion of scientific and technical-scientific texts describing experiences on the application of these techniques to problems related to geological hazard mitigation (Youssef et al., 2016; He et al., 2021).

Usually, ML is adopted for making predictions. More in particular, ML solves problems by learning from available datasets (that are generally composed of *n* data samples with single or multiple attributes/features) to predict, by algorithms (i.e., the model), properties of unknown data. The kind of selected algorithm depends on several factors such as type of problem and number of variables (Mahesh, 2020).

Learning problems are divided into:

- supervised learning: the model is trained on a labelled dataset in which each sample is defined by more than one attribute (they might be categorical, binary or continuous attributes), (Diridi, 2021). In supervised learning the input data are splitted into train (labelled) and test datasets (unlabelled), (Diridi, 2021). The first step consists in training the model by the train dataset. Then, the model is fed with the testing data, on which it makes predictions basing on patterns learnt on the train dataset (Diridi, 2021; Mahesh, 2020). Supervised learning problems include two groups: classification and regression. In the first case, attributes are categorical, whereas in the second case attributes are continuous
- unsupervised learning: the model is trained on an unlabelled dataset, i.e., the ML algorithms are left on their own to discover the interesting structure into the dataset (Mahesh, 2020). More in particular, unsupervised learning algorithms learn few attributes from the data and when new data are introduced, they use the previously learned attributes to recognize the class to which the data belong to (Mahesh, 2020). These ML methods groups include: clustering, dimensionality reduction and association algorithms (James et al., 2013)

Basing on the outputs obtained in this research, supervised ML methods were considered as the most suitable for the expected goals. More in particular, among the supervised learning methods, the Random Forest algorithm was selected.

Main functionalities of Random Forest method are discussed in the following.

4.2.1 Random Forest (RF) method

Random Forest (Ho, 1995; Breiman, 2001; Cutler et al., 2012) is a supervised ML algorithm commonly utilized for solving classification and regression problems. More in particular, the RF technique allows making predictions by combining outputs from randomly selected multiple « decision trees » in order to find a solution to a problem. For classification problems, the solution is the category most frequently chosen by the RF trees (Wikipedia, 2023), whereas, for regression problems, the solution is the average of predictions of individual trees (Ho, 1998; Wikipedia, 2023).

According to the above-provided description, « decision trees » are at the basis of RF method and therefore are further discussed. Similarly to RF, decision trees are used for classification and regression purposes with the goal of creating models predicting the value/category of target variables by learning simple decision rules from features of known input datasets (source: scikit-learn.org). Each tree is composed of a root node, branches, internal nodes and leaves (fig. 4.1).

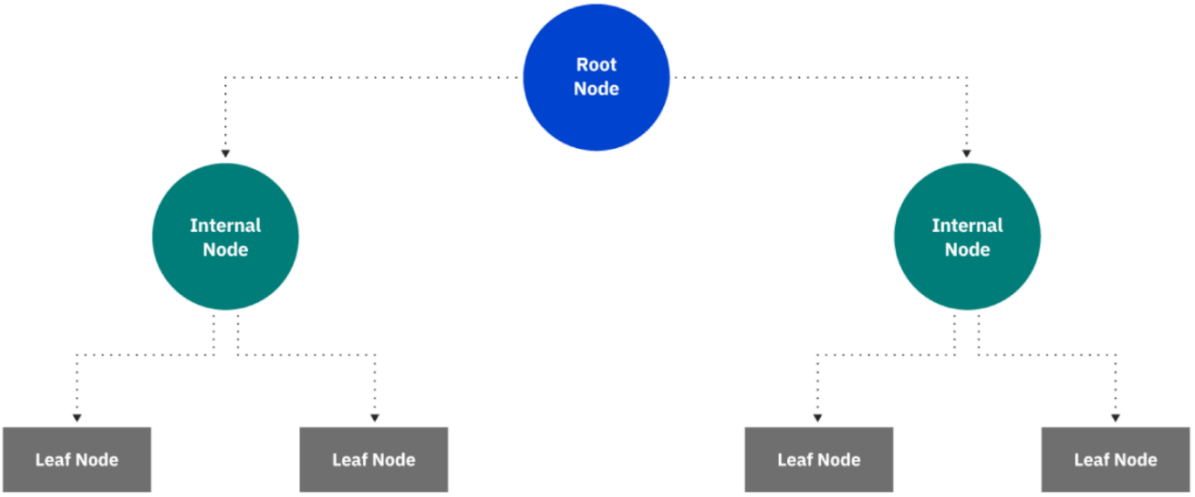

Figure 4.1: *Example of structure of a decision tree (source: ibm.com).*

To use decision trees, it must start from the root (i.e., the top), (Quinlan, 1990). From the root node, an object is classified by tracing out a path until one of the leaves of the tree (at the bottom) that returns the requested output (Quinlan, 1990). Internal nodes are connected to leaves and root node by branches. Each internal node corresponds to a test done for the given object, which output allows moving down until one of the leaves (Quinlan, 1990).

The RF is founded on the bagging method which relies on the fact that the combination of learning models (i.e., multiple decision trees) improves the overall result (source: builtin.com).

4.3 Input dataset description

The input dataset used to perform RF analysis is described in the following. More in particular, it consists in a 3672 (rows) x 33 (columns) 2D matrix (or DataFrame) gathering all outputs of this study (cf. chapter 2 and 3).

The 3672 rows derive from the combination of landslide prototypes designed according to the procedure described in paragraphs 2.5, 2.5.1 with different seismic inputs (cf. paragraph 2.6). Parameters of interest for this combination are shortly summarized below:

- kinematics: « R »: rotational landslide, « T »: translational landslide
- slope angle: 15°or 30° (cf. paragraph 2.2.4)
- configuration: « 1 »: landslide involving the whole slope face, « 2 »: landslide involving the slope bottom, « 3 »: landslide extended beyond the slope crest (cf. paragraph 2.4)
- material: « CS »: cohesive soils, « LS »: loose soils, « R »: rocks (cf. paragraph 2.3), for which 2 impedance contrast values were considered. Geotechnical properties associated to each material type are not specified in more detail in this chapter. Indeed, the geotechnical parameterization of the selected materials is univocal since, parametric analysis of shear strength parameters and physical properties for each type of material was not performed in this study
- volume: which values are in the order of magnitude of 10 m^3 (101 in the dataset), 10^3 m^3 (103 in the dataset) and 10^5 m^3 (105 in the dataset), (cf. paragraph 2.2.2)
- seismic inputs: 17 different LEMA_DES signals (cf. paragraph 2.6) characterized by different duration, frequency content (T_m), PGA, PGV and almost equivalent AI

Each dataset row (i.e., 3672 total rows = 2 (kinematics)*2 (slope angle values)*3 (configurations)*3 (material types)* 2 (impedance contrasts)*3 (volume classes)*17 (seismic signals)) represents peculiar landslide prototypes – seismic input couples for which seismic slope stability analysis by simplified and stress-strain analyses were performed in order to compute related seismically-induced displacements (cf. chapter 3).

The 33 columns contain the attributes of each data sample (row). More in particular, the 33 columns refer to parameters characterizing the geology and geometry of the landslide prototypes, the properties of the seismic inputs and different outputs from the performed FDM and Newmark (1965)'s method–based analysis. In more detail, the 33 features/attributes are:

1. « IDcsv »: it is an integer representing a univocal numerical code associated to each row for its identification (from 1 to 3672)
2. « model ID »: identifying the ID of the landslide prototype as discussed in paragraph 2.5
3. « kin »: categorical variable indicating the failure mechanism of the landslide prototypes that can be translational « T » or rotational « R »
4. « configuration », an integer from 1 to 3 (cf. paragraph 2.4)
5. « volume [m^3] », an integer equal to « 101 » (i.e., V = 10 m^3), « 103 » (i.e., V = 10^3 m^3) or « 105 » (i.e., V = 10^5 m^3)

6. « slope angle [°] », an integer equal to « 15» (i.e., 15°) or « 30 » (i.e., 30°)
7. « material », categorical variable equal to « CS » (i.e., cohesive soils), « LS » (i.e., loose soils) or « R » (i.e., rocks)
8. « IC » (i.e., impedance contrast), an integer that can take values of 1.5, 2, 2.5, or 4 basing on the corresponding material type (cf. chapter 2)
9. « mesh size [m] », a floating point indicating the value of the inter-nodal distance used to create the FLAC model (cf. chapter 3, part 2)
10. « v land [m/s] », a floating point indicating the shear wave velocity value associated with the landslide (cf. chapter 2)
11. « D [m] », a floating point indicating the thickness of the landslide mass (cf. paragraph 2.5)
12. « H slope [m] », a floating point indicating the slope height measured according to paragraph 2.5
13. « L land [m] », a floating point indicating the landslide length according to paragraph 2.5
14. « L slope [m] », a floating point indicating the slope length (i.e., crest-bottom distance along slope dip-direction)
15. « % land [%] », (i.e., percentage of slope length involved into the landslide movement) given by an integer computed according to paragraph 2.4
16. « input name », a categorical variable indicating the name of the seismic input (cf. paragraph 2.6)
17. « signal duration [s] », floating point indicating the duration of the seismic input (cf. paragraph 2.6)
18. « PGA [m/s^2] », floating point (cf. paragraph 2.6)
19. « PGV [m/s] », floating point (cf. paragraph 2.6)
20. « AI [m/s] », floating point representing Arias Intensity (cf. paragraph 2.6)
21. « T_m [s] », floating point describing mean period (cf. paragraph 2.6)
22. « T_s/T_m », floating point computed as in eq.3.16, paragraph 3.7.1.2
23. « T_l/T_m », floating point computed as in eq.3.17, paragraph 3.7.1.2
24. « CM_DISP [m] », floating point indicating the relative x-displacement of the center of mass of landslide prototypes as a consequence of the application of a given input. For more details on the computation procedure for « CM_DISP », the reader is referred to paragraph 3.7.2.1
25. « AV_DISP [m] », floating point indicating the average relative x-nodal displacement into the landslide mass
26. « MIN_DISP [m] », floating point indicating the minimum relative x-component nodal displacement into the landslide mass
27. « MAX_DISP [m] », floating point indicating the maximum relative x-component of nodal displacement into the landslide mass
28. « failures_NM [m] », floating point indicating the prototype mesh size that was used as minimum displacement value to represent numerical modelling (NM) failure cases. This column is therefore filled only in cases of failure for which values referred to « CM_DISP [m] », « AV_DISP [m] », « MIN_DISP [m] » and « MAX_DISP [m] » are missing

29. « NW_DISP [m] », floating point corresponding to Newmark's displacement computed according to equation 3.9 in paragraph 3.2.2.1
30. « SF », floating point indicating the Static Safety Factor computed as in paragraphs 3.1.1 and 3.1.2
31. « a_y [m/s^2] », floating point indicating the landslide yielding acceleration (cf. paragraph 3.2.1)
32. « DIF [m] », floating point number given by « CM_DISP [m] » - « NW_DISP [m] ». Indeed, displacements of the center of mass, were used as reference value for expressing seismically-induced displacements assessed by FDM analyses. Values in « AV_DISP [m] », « MIN_DISP [m] » and « MAX_DISP [m] » columns were neglected in this phase
33. « CLASS_DIF », categorical variable classifying results of « DIF [m] » column into 7 classes as explained below

Due to several issues (cf. paragraph 3.7.2.2), columns « CM_DISP [m] », « AV_DISP [m] », « MIN_DISP [m] » and « MAX_DISP [m] ») are incomplete. In contrast, the set of solution for the feature « NW_DISP [m] » is full (except for models characterized by SF < 1 for which Newmark (1965)'s method-based analysis was not performed, cf. paragraph 3.1.3).

As it is evident from the listed attributes, the « CLASS_DIF » feature was introduced during this phase of the research, as it will represent the target variable of the RF analysis (i.e., the feature that the algorithm aims at predicting *a priori*) according to the objectives described in paragraph 4.1. The « CLASS_DIF » attribute assigns each row to one of 7 different classes basing on the value contained in the column « DIF [m] » (i.e., basing on computed difference between center of mass displacements, « CM_DISP [m] », and Newmark's displacements, « NW_DISP [m] »). More in particular, the 7 classes (fig. 4.2) were defined by considering a reasonable difference of one order of magnitude (in negative or in positive) between adjacent classes (the limit between each class is defined according to a logarithmic scale).

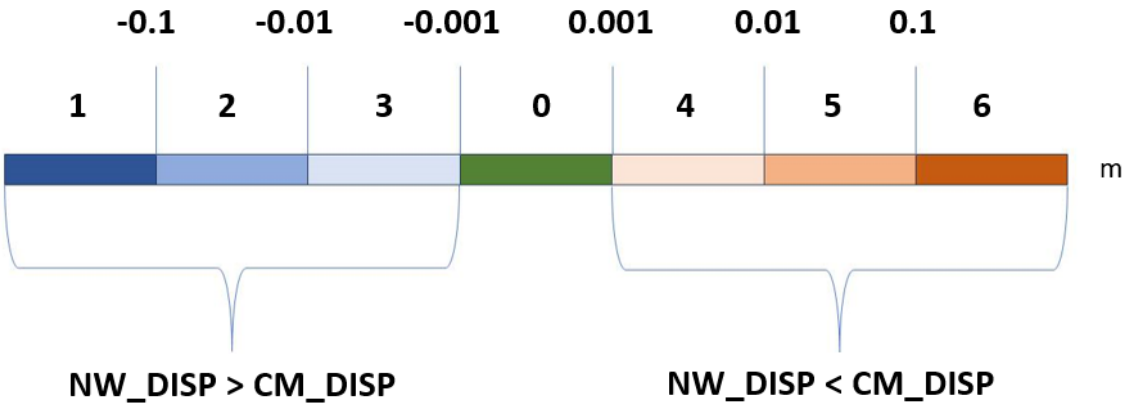

Figure 4.2: *Selected classes to identify difference between « CM_DISP » and « NW_DISP ». Classes 1-2-3 are those for which Newmark (1965)'s method-based analysis overestimates x-disp compared to FDM-analysis, whereas classes 4-5-6 are those for which the opposite occurs. When « DIF » value is in class 0, it can be reasonably assumed that predictions by the two methods are equivalent since the difference is in the order of magnitude of 1 mm.*

In more detail, the 7 classes are grouped as follows:

- classes 1-2-3 include negative « DIF » values lower than - 0.001 m. Rows belonging to these classes include data samples for which Newmark (1965)'s method – based analysis predicts larger displacements than FDM modelling. In other words, in these cases, simplified approaches are more conservative than FDM stress-strain analysis
- classes 4-5-6 include positive « DIF » values larger or equal to 0.001 m for which displacements predicted by Newmark (1965)'s method – based analysis are smaller compared to those predicted by FDM modelling
- class 0 includes all « DIF » values between -0.001 and 0.001 m. For these cases, predictions by the two methods can be reasonably considered equivalent

The above-described 7 classes represent guidelines for evaluating which method is more convenient to use, based on the criteria discussed in paragraph 4.1. Indeed, each class is an indicator of the amount of under- or over- estimation using simplified or numerical approaches.

4.3.1 Filtering of the input dataset

Before performing RF analysis, the input dataset was filtered in order to: i) exclude data samples not suitable for the purpose of the analysis, ii) reduce the number features under investigation.

More in detail:

- rows were filtered to exclude all cases in which one of the two predictions were missing. This exclusion was necessary since, for them, the « DIF [m] » and the « CLASS_DIF » variables were not computable. The filtering criterion also includes landslide prototypes characterized by Safety Factor < 1, for which Newmark's analysis was not conducted since it would have been meaningless to perform seismic slope stability analyses for landslides already unstable in static conditions. Additionally, models for which one of the two methods returned failure (234 rows, cf. chapter 3 for fixed failure criteria) were excluded since, for them, computed « DIF [m] » values would not have been comparable to other cases. For instance, in cases where failures were predicted by FDM modelling, the feature « mesh size » was assumed as minimum displacement necessary to produce the slope collapse. Consequently, in these cases, for computing the « DIF » variable it would have been necessary to subtract Newmark's prediction to a minimum displacement value. Therefore, the obtained value would not have been reliable and/or comparable to other computed values compromising the result provided by the RF algorithm. Accounting for these filters, the total number of rows reduced to 1134
- columns were filtered to eliminate all not independent variables (i.e., columns containing parameters analytically inferred from other parameters) from the dataset to avoid redundancies. For instance, « % land [%] » was computed from « L land [m] » and « L slope [m] » values (cf. paragraph 2.4). In addition, variables such as « AV_DISP [m] », « MIN_DISP [m] » and « MAX_DISP [m] », « CM_DISP [m] » and « NW_DISP [m]

» were excluded since, in this phase the interest is towards the prediction of the difference between FDM (expressed in terms of CM_DISP, cf. paragraph 3.7.2.1) and Newmark's displacements

The filtering procedure allowed reducing the number of features under investigation to 18. In particular, they are:

1. « kin »
2. « configuration »
3. « volume [m^3] »
4. « slope angle [°] »
5. « material »
6. « IC »
7. « D [m] »
8. « H slope [m] »
9. « L land [m] »
10. « L slope [m] »
11. « signal duration [s] »
12. « PGA [m/s^2] »
13. « PGV [m/s] »
14. « AI [m/s] »
15. « T_m [s] »
16. « T_s/T_m »
17. « T_l/T_m »
18. « CLASS_DIF » → TARGET VARIABLE

Consequently, the dataset became a 1134 x 18 2D matrix.

Features from 1 to 17 are fundamental since they are the features that one must define to make any prediction (i.e., feature n.18) with the RF model created in this study: indeed, this is the set of features used to train and test the RF model as will be better explained in paragraph 4.3.

For completeness, the distribution of the « CLASS_DIF » values into the filtered dataset is reported in figure 4.3.

The analysis of the « CLASS_DIF » values distribution in figure 4.3 reveals that class « 0 » (i.e., the class corresponding to negligible differences between displacements computed by numerical and simplified approaches) is the most represented into the dataset. CLASS_DIF = 6 (i.e., CM_DISP > NW_DISP and the difference is major or equal than 0.1 m) is the only class not represented into the dataset. For CLASS_DIF = 1 only 4 cases are present. The number of cases for CLASS_DIF = 2, 3 and 5 is almost equivalent (∼100 cases), whereas ∼200 cases are present for CLASS_DIF = 4.

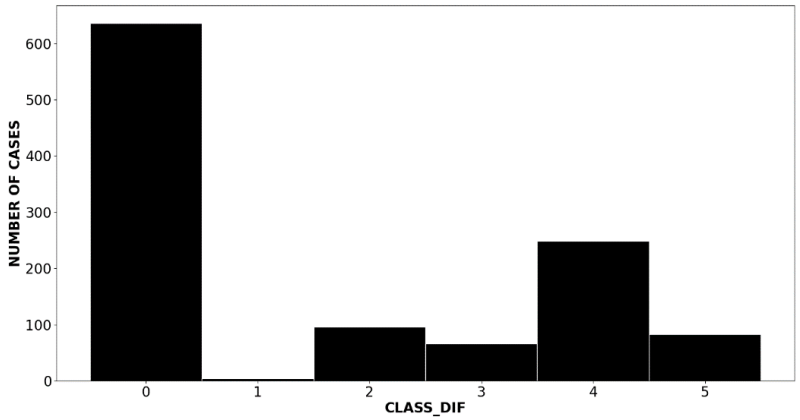

Figure 4.3: *Distribution of « CLASS_DIF » values into the dataset after filtering.*

From distribution in figure 4.3, it can be concluded that:

- in the geometrical, geotechnical, and seismic conditions analysed in this study, there is a good equivalence in terms of predictions between numerical and simplified approaches since more than half cases belong to CLASS_DIF = 0 (636 out of 1134 cases, ∼56%). This evidence is in agreement with findings from Lenti & Martino (2013), which demonstrated that for AI in the order of magnitude of 0.1 m/s, as the one considered in this research, no relevant difference in terms of predictions from Newmark (1965)'s analysis and FDM modelling can be found. According to the authors, relevant differences between outputs from the two methods are registered when: i) AI < 0.1 m/s: Newmark's method underestimates the displacements compared to stress-strain analysis and ii) AI > 0.1 m/s, when the opposite occurs
- cases in which Newmark (1965)'s method-based analysis is more conservative than FDM modelling (i.e., CLASS_DIF = 1,2,3) are the less numerous into the dataset (166 out of 1134 cases, ∼15%). Simplified method prediction overestimates displacements by more than 0.1 m only in 4 cases
- cases in which FDM modelling is more conservative (i.e., CLASS_DIF = 4 or 5) are the most abundant after cases belonging to CLASS_DIF = 0 (332 out of 1134 cases, ∼29%). Nevertheless, the difference in terms of prediction between the two methods never exceeds 0.1 m

Therefore, in most of the cases, simplified and numerical approaches return similar results. For cases in which a difference exists, the latter is, in most of the cases, lower than 0.1 m (the extreme classes either in negative either in positive, i.e., class 1 and class 6, are represented by few cases, i.e., class 1 or not represented at all, i.e., class 6).

4.4 Application of ML RF to the input dataset

RF analysis on input dataset (cf. paragraph 4.3 and 4.3.1) was performed in Python by using the different functions embedded into the « scikit-learn » or « sklearn » library. The latter is generally used to implement ML RF models in Python codes. Main steps of the Python code are following summarized:

- step 1: splitting of the input dataset into train and test datasets for training and testing the RF model. In the present study, the test size (i.e., test_size) represents the 25% (i.e., 1/4) of the whole dataset, while the remaining 75% was used to train the RF model. This operation was performed by using the function « train_test_split » of the « sklearn » library, which shuffles the dataset before the splitting (source: towards datascience.com). In addition to the parameter « test_size », the « sklearn » library requires the specification of the « random_state », which was set at the default value of 42. The « random_state » parameter controls the shuffling of the data before their splitting (source: medium.com). The specification of this parameter makes the code reproducible since it ensures that the data are shuffled always in the same manner every time the code is run (source: medium.com). Random state value can be whatever value ≥ 0. In ML RF implementations 42 is often selected as tribute to the « Hitch-hiker's Guide » books by Douglas Adams as it was supposed to be the answer to the great question of « Life, the universe, and everything» (source: quora.com)
- step 2: use of the sklearn function « RandomForestClassifier » which allows generating the RF Classifier to perform the RF analysis. This function requires selecting the random state (i.e., 42) and number of trees (i.e., 100), which were both fixed at their default values. The number of trees defines the number of decision trees composing the random forest which outputs are combined to find the solution to the problem (cf. paragraph 4.2.1). Since in this case, the target variable is categorical (i.e., « CLASS_DIF »), the RF output will correspond to the most frequent class (i.e., the most frequent « CLASS_DIF ») among those indicated by all decision trees
- step 3: the RF classifier is trained by using the training dataset
- step 4: the performance/accuracy of the model is evaluated by feeding it with the test dataset. More in particular, the « predict » function is used to forecast the « CLASS_DIF » target variable for test data by using the same set of features considered to train the model. Since the « CLASS_DIF » variable is already known for this sub-group of data, the prediction obtained from the RF model can be compared to the known values of the target variable in order to evaluate the accuracy of the prediction by the function « score ». The latter measures the number of right predictions with respect to the total number of performed predictions for the testing dataset

4.4.1 Outcomes of RF analysis

Following steps reported in the previous paragraph, a RF predictive model for the variable « CLASS_DIF », with an accuracy ~80%, was implemented in Python programming language.

Considering ML standards, such an accuracy level might not be considered satisfactory. However, for this study, this result can be regarded as strongly encouraging. Indeed, as previously commented (cf. paragraph 4.1), results here presented consist in a first attempt to use scientific results for predictive purposes in the framework of earthquake-induced landslide studies. The method here presented will require:

- in-depth analyses and optimization of the learning and prediction processes

- further enrichment of the input dataset in terms of variability of geometrical and geotechnical parameters that due to the time constraints of the PhD course were limited to few choices resulting in non-continuous values for the introduced attributes

One of the characteristics distinguishing RF from other ML techniques is the possibility to list DataFrame features in order of decreasing importance in terms of RF model prediction. In python programming language the importance of the feature can be obtained by using the attribute « feature_importances » embedded into the library sklearn. The importance of the different features involved in this study, according to the preliminary model here developed, is in figure 4.4.

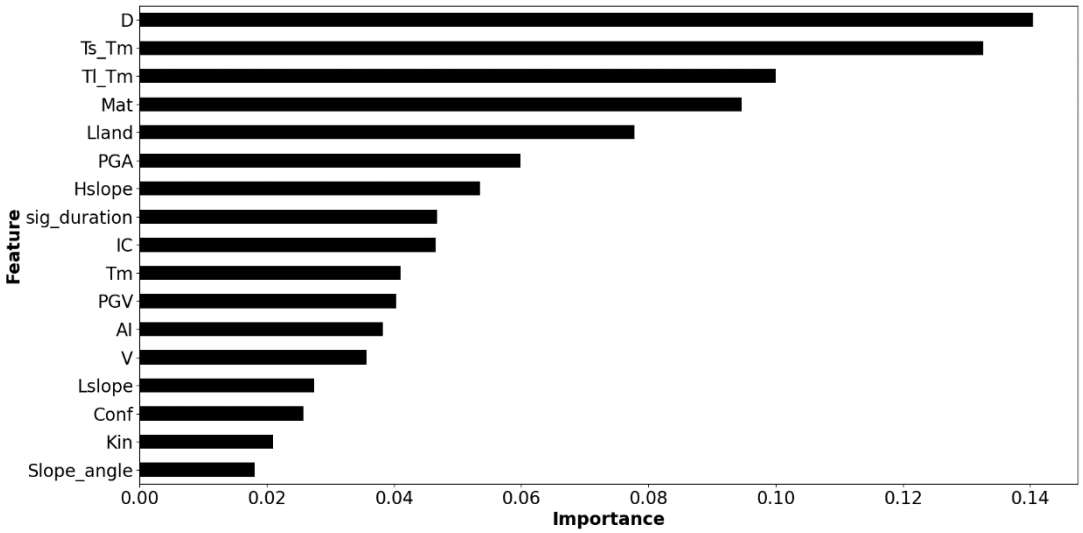

Figure 4.4: *Importance of features in the RF predictive model. In the plot: D – landslide thickness; Mat – material type; sig_duration – signal duration; V – volume; Conf – configuration; Kin – kinematics. For other parameters refers to paragraph 4.2.*

From figure 4.4, it can be argued that the 5 most important features controlling the predictive model are: landslide thickness, characteristic period ratios (i.e., T_s/T_m and T_l/T_m), material type and landslide length. For these parameters, the importance is above 0.06. Below this latter value there are all features related to seismic inputs and slope geometry, but also volume, impedance contrast and landslide kinematics. Regarding the above-mentioned list of priority parameters, it is necessary to specify that the importance of the different features must be interpreted as the « weight » that they have in affecting the outcoming discrepancy between seismic displacements predicted by simplified and numerical approaches. In other words, some of the features (i.e., the most important according to the RF model here generated) mostly affect displacements according to one of the two methods determining larger or smaller values of the « DIF » feature and consequently of the « CLASS_DIF ». For instance, the low importance of slope angle and volume, whose influence on seismic displacement variations was widely discussed in chapter 3, might be a surprise. Nevertheless, this result is reliable since slope angle and volume demonstrated to significantly affect earthquake-induced displacements of landslides according to both adopted methods (cf. chapter 3). Consequently, it can be argued that increasing/decreasing of these parameters values results in displacement variation for both simplified and numerical methods, therefore, their difference (i.e., « DIF ») will not be largely affected. On the contrary, it is interesting to note that the 5 most important

features include landslide characteristic periods ratios and related parameters (i.e., landslide length and thickness, cf. equations 3.16-3.17, paragraph 3.7.1.2) as they strongly control seismic response of landslides but are not accounted for by analytical approaches (cf. paragraphs 3.2.2 and 3.4.3). As it regards the T_s/T_m ratio, even if it was excluded any correlation between peak of numerical displacements and the resonance condition (i.e., $T_s/T_m = 1$), an increasing-decreasing trend of numerical displacements was recognized in paragraph 3.7.2.3. This could explain the high importance of this parameter according to the RF model. Nevertheless, a high uncertainty remains for the reliability of the list in figure 4.4 as it regards the major importance of the T_s/T_m compared to the T_l/T_m ratio.

This result leads to stress again that outcomes here discussed are satisfactory just for an explorative phase in terms of using ML techniques for seismic hazard evaluation purposes and that further analyses are necessary. For this reason, these results must be regarded as preliminary and no further strict conclusions can be made.

4.4.2 Analyses of dataset samples excluded from RF analysis

In this paragraph, dataset samples excluded from the RF analysis due to prediction of failure from one or both the two methods are further discussed.

Above all, results can be grouped into 5 main failure classes:

1. CLASS F1 grouping all cases characterized by SF < 1, for which FDM analyses returned failure and Newmark (1965)'s method – based analysis was not performed (160 cases). This number could be strongly underestimated since it does not count cases with SF < 1 that were not effectively run in FLAC but for which similar result is expected (cf. paragraph 3.7.2.2 and 3.7.2.4)
2. CLASS F1' including few cases for which SF < 1 but FDM modelling did not predict failure (19 cases)
3. CLASS F2 including cases with SF $\geq$ 1 for which both methods predicted failure (9 cases)
4. CLASS F3 including cases with SF $\geq$ 1 for which Newmark (1965)'s method – based analysis predicted failure but not FDM modelling (18 cases)
5. CLASS F4 gathering all cases with SF $\geq$ 1 in which FDM modelling predicted failure but not Newmark (1965)'s method – based analysis (208 cases)

The « failure » is defined according to criteria in chapter 3 (i.e., computed displacements are above Romeo (2000)'s critical threshold; FDM modelling stopped before the end of the computation due to very large displacements registered into the model that cause very large mesh deformation or returned very large displacements in post-processing of the results).

From the above reported classification, it can be inferred that FDM modelling predicts more frequently landslide failure. Indeed, CLASS F4 includes more cases compared to CLASS F3. Cases belonging to CLASS F4 can be regarded as the extreme representation of cases in which the prediction by FDM analysis is more conservative than that provided by simplified approaches (as CLASS_DIFF = 4, 5 or 6 in paragraph 4.2).

Tables 4.1 – 4.2 classify data belonging to classes F3 and F4 highlighting their most frequent material type, volume, slope angle and configuration.

Table 4.1: *Table showing the most frequent (red) material type, volume, slope angle and configurations of data belonging to CLASS F3.*

MATERIAL TYPE	**CS**	**100%**
	LS	0%
	R	0%
VOLUME [m^3]	**10**	0%
	10^3	0%
	10^5	**100%**
SLOPE ANGLE [°]	**15**	**100%**
	30	0%
CONFIGURATION	**1**	**78%**
	2	0%
	3	22%

Table 4.2: *Table showing the most frequent (red) material type, volume, slope angle and configurations of data belonging to CLASS F4.*

MATERIAL TYPE	**CS**	42.4%
	LS	**57.2%**
	R	0.4%
VOLUME [m^3]	**10**	0%
	10^3	40%
	10^5	**60%**
SLOPE ANGLE [°]	**15**	**72.5%**
	30	27.5%
CONFIGURATION	**1**	**51.4%**
	2	21.6%
	3	27%

As it can be noticed from table 4.1, the 18 cases belonging to CLASS F3 are all characterized by the largest volume, the lowest slope angle and involve cohesive soils. In addition, the majority of cases (~78%) are landslides in configuration n.1. This result is consistent with observations in paragraph 3.2.3, which suggested that landslides combining large volume, low slope angle and cohesive soils are among the most critical according to Newmark's type analysis. In contrast, for same models, displacement distributions with respect to material type was more complex according to results from stress-strain analysis (cf. 3.7.2.3).

On the contrary, from table 4.2 it can be inferred a wider variability of parameters that it can also be interpreted as the effect of the major number of cases belonging to CLASS F4. In this case, more than half of the cases involve loose materials. As it regards volume, slope angle and configuration, similarly to CLASS F3, the most frequent cases are respectively: 10^5 m^3, 15° and configuration n.1. The percentage of landslide cases in configuration n.2 and 3 is almost equivalent. In this case, it is not possible to refer to observations done in previous sections, since in this case, data are more variable (i.e., percentages are different from 100%), therefore, from table 4.2 information regarding parameter combinations cannot be inferred.

Nevertheless, these percentages are not enough to explain data distribution, since the number of cases belonging to the two classes is quite different and except for the material type other parameters have same mode.

Additionally, figure 4.5 shows the distribution of the T_I/T_m ratios of data belonging to classes F3 and F4.

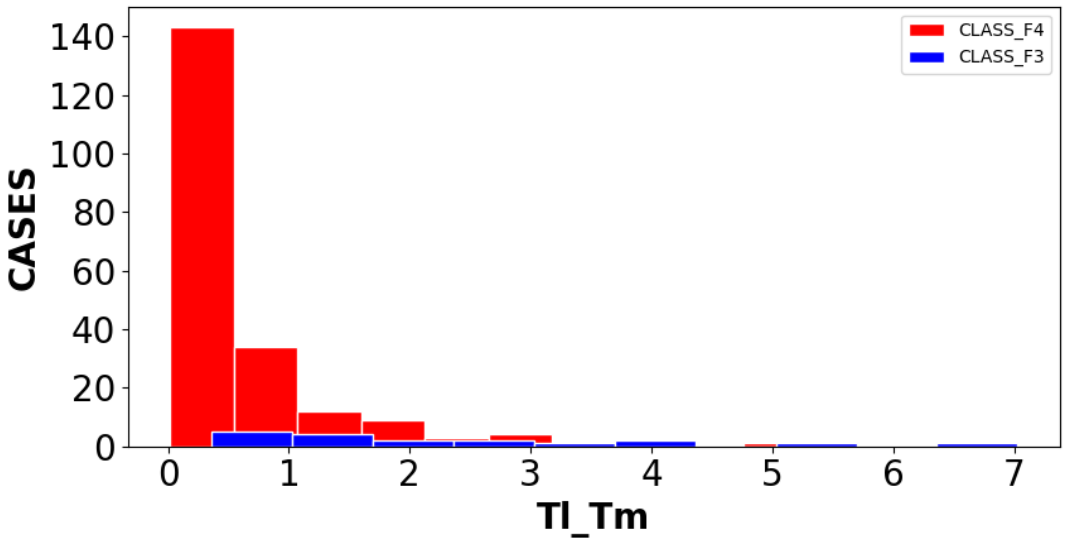

Figure 4.5: *Distribution of T_I/T_m ratio values of data from class F4 (red) and F3 (blue).*

From figure 4.5 it can be inferred that T_I/T_m ratio values span approximately between 0.5 and 7 for CLASS F3 and 0 and 6 for CLASS F4. Moreover, the distribution mode for the latter class is approximately between 0 and 0.5. In contrast, the mode of CLASS F3 distribution is slightly higher, and the associated cases are much less numerous compared to CLASS F4, due to the limited number of the data belonging to this class. The distributions in figure 4.5 do not provide any clear evidence of a significant influence of the T_I/T_m ratio parameter in explaining why one of the two methods predicts failure. This is because the range of values spanned by the two distributions is similar. Furthermore, the range of values covered by the distributions in figure 4.5, it is comparable to that of the original distribution in figure 3.22a. This evidence suggests that T_I/T_m values covered by the frequency distributions in figure 4.5 are not controlled by the repartition of the data between classes F3 and F4. On the contrary, they reflect the fact that T_I/T_m values initially computed for the designed landslide prototypes span over this range of values and especially between 0-1.

The only conclusion that can be done up to now, is that in the analysed conditions, stress-strain analyses predict more frequently the failure. Therefore, even if as it regards not failure cases, the predictions by simplified and numerical approaches result similar in more than half of the cases, discordant results are obtained when failure cases are considered. Indeed, the two methods predict both failures only in 9 cases (i.e., CLASS F2). These 9 cases do not include models belonging to CLASS F1 (i.e., landslide prototypes for which the combination of geometrical parameters, i.e., usually $V = 10^5$ m^3 and $\alpha = 30°$, determines instability conditions

already in static conditions according to limit equilibrium approaches but that once run in FLAC reach a static equilibrium to fail in most of the cases after the application of whatever input).

Therefore, up to now, high uncertainty remains in defining a general criterion explaining why and in which conditions Newmark's analysis returns a more conservative solution and *viceversa*. At this regard, further investigations are necessary.

Chapter 5: Conclusions and future perspectives

This chapter provides with a comprehensive overview of the key findings of this study. Furthermore, its objective is to stress limitations and innovations of this research with the aim of identifying open questions and issues, which could require further in-depth analyses.

5.1 2D landslide prototypes

In this study, 216 2D step-like-slope landslide prototypes were designed (cf. chapter 2) by combining geometrical (i.e., thickness-to-length ratio, slope angle and volume) and geotechnical (i.e., shear strength and physical parameters of the 3 material types most frequently involved in landslide movements) parameters statistically inferred from literature review. The analysed state of art allowed compiling sub-datasets for each parameter of interest to compute for them mean values at worldwide scale. According to this procedure, generated landslide prototypes can be considered as representative of common real landslides in terms of geometry, dimension, and geotechnical composition. As it regards the failure mechanism, the present study considers exclusively purely rotational and translational slides (*sensu* Varnes, 1978). Landslide kinematics is indirectly expressed by the thickness-to-length ratio (D/L) that assumes typical ranges of values basing on the prevalence of the rotational or the translational component of movement (Skempton & Hutchinson, 1969).

Multiple representative values were derived for both geometrical and geotechnical parameters to be regarded as possible controlling factors for landslide displacements up to failure. Main findings from the performed literature review are summarized below:

- in agreement with Skempton & Hutchinson (1969), most frequent D/L values at worldwide scale are 0.05 for translational slides and 0.16 for rotational slides (cf. paragraph 2.2.3)
- slope angles at worldwide scale span approximately between minimum and maximum values of 15° and 30° considering mainly slide-type landslides (cf. paragraph 2.2.4)
- most frequent volume value at worldwide scale is 10^3 m^3. Additionally to the latter, two other values (i.e., 10 m^3 and 10^5 m^3) were considered in this study (cf. paragraph 2.2.2) to represent smaller and larger size landslides
- material types most frequently involved in landslide movements are cohesive soils, loose soils, and rocks. These three material types were therefore geotechnically characterized in paragraph 2.3
- 3 principal landslide positions along slope can be identified to represent common real landslides (cf. paragraph 2.4)

The above-listed parameters were combined according to the procedure outlined in paragraph 2.5 to design the 216 landslide prototypes. At the base of each prototype a rocky bedrock was considered with a shear wave velocity of 800 m/s.

The procedure outlined in chapter 2 revealed some limitations:

- landslide prototypes presented in this study were 2D modelled (i.e., the width is considered infinite) whereas real landslides are 3D bodies characterized by finite length, width, and depth/thickness. The approximation of 3D bodies with 2D bodies is reliable when: i) the involved material is homogeneous in the third direction, ii) the landslide width is significantly larger if compared to the landslide length (i.e., the landslide width can be regarded as infinite). This feature is particularly important for earthquake-induced landslide studies since landslide edges can give rise to reflections and refractions of seismic waves that can contribute to modify the local seismic response. Consequently, such a kind of approximation might not be fully reliable for real case studies in which the relationship between landslide length and width is different with respect to that just described
- due to time constraints few values only were considered to represent the variability of the parameters of interest at worldwide scale. For instance, this study takes into account only volume values up to 10^5 m^3. Consequently, larger size landslides are not represented in this research
- some of the statistical analyses (cf. chapter 2) were based on quite limited amount of data leading to high uncertainties in the resulting values for some of the introduced geotechnical parameters. Furthermore, for time issues, single values for geotechnical parameters were considered to characterize the three material types. However, at this stage, the selected values cannot be considered representative of all materials in nature, even if, in this case, they were intended in terms of geotechnical units rather than lithological units. Therefore, additional values of considered geotechnical parameters for each material type would be necessary to represent a broader range of real cases

5.2 Earthquake-induced displacements by simplified and numerical methods

17 equivalent LEMA_DES signals (Lenti & Martino, 2010) characterized by Arias Intensity in the order of magnitude of 0.1 m/s and mean period (T_m, Rathje et al., 1998) between 0.08 and 2.04 s (cf. paragraph 2.6) were used to compute earthquake-induced displacements of the designed landslide prototypes by simplified (cf. chapter 3, part 1) and numerical (cf. chapter 3, part 2) methods.

The goal of such investigations was to better understand in which conditions, methods commonly utilized to predict earthquake-induced displacements of landslides at regional scale (i.e., Newmark (1965)'s method-based analysis) return significantly different results with respect to more advanced FDM stress-strain methods, which use is usually limited to slope-scale analyses. Drawbacks and advantages of the two methods were widely discussed in chapter 3.

In chapter 3, results obtained by simplified and numerical methods were separately discussed. The purpose was to identify the most relevant parameters (among those related to the

geometry and geotechnics of the landslide prototypes and the seismic inputs) that mainly control the variation of computed earthquake-induced displacements according the two methods. Basing on results discussed in chapter 3, the following conclusions can be drawn:

- relevant earthquake-induced displacements computed in this study span over a range of values between 0.001 and 0.08 m for both numerical and simplified methods (fig. 5.1). This outcome aligns with previous findings from Lenti & Martino (2013), who demonstrated that simplified and numerical approaches predict similar results when the Arias Intensity of the seismic solicitations is in the order of magnitude of 0.1 m/s

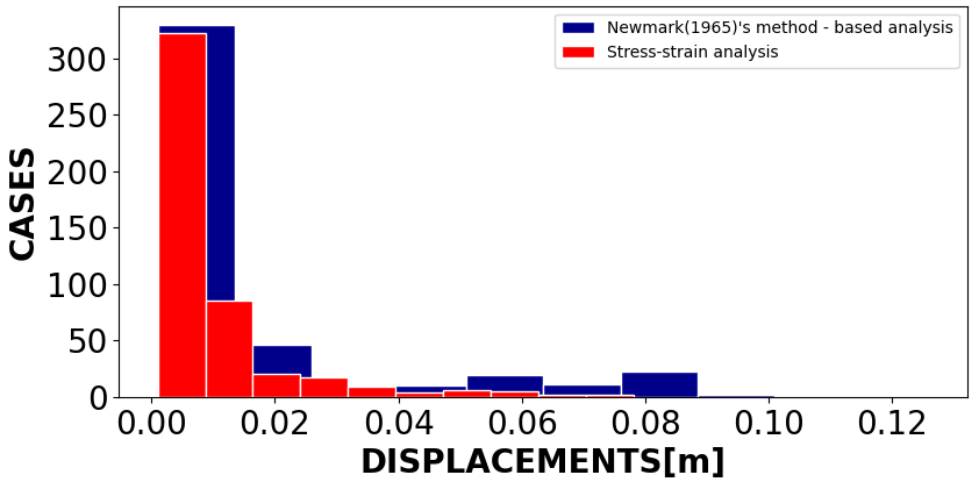

Figure 5.1: *Distribution of displacements computed by Newmark (1965)'s method – based analysis (blue) and FDM numerical modelling (red). The distributions do not include: i) displacements below 1 mm threshold, ii) displacements above Romeo (2000)'s failure threshold.*

- the comparison of results related to correspondent translational and rotational landslide prototypes reveals that the latter experience larger displacements according both numerical and analytical methods
- being equal other parameters, increasing landslide volume, displacements increase by using either numerical either analytical methods
- being equal other parameters, slope angle increase corresponds to increased displacements using either numerical or analytical approaches
- the weight of geometry related to a specific configuration is comparable to that of the volume. Outputs from numerical modelling reveal that seismic displacements related to landslide prototypes in configuration 2 (fig.3.30) are smaller compared to displacements computed for the equivalent prototypes in configuration 1 and 3. Same effect is inferred for results obtained by simplified approaches (fig. 3.9) even if this result is less clear for translational landslides (fig.3.9b) and it could be affected by the use of different approaches for assessing initial slope stability conditions (cf. paragraph 3.1.3)
- the role of the types of materials is clearer by looking at outputs from Newmark (1965)'s method-based analysis. Results from the latter method show that the highest displacements occurs in the presence of low-cohesion materials (i.e., loose soils) for medium volume – low angle landslides (models R1_103_15 and T1_103_15 in fig. 3.11)

and in the presence of material with low friction angle (i.e., cohesive soils) for large volume – low angle landslides (models R1_105_15 and T1_105_15 in fig. 3.12). Conversely, results from stress-strain analyses obtained for the same models are more complex to be interpreted since, in this case, it is necessary to also evaluate the IC and the input frequency content for better understanding displacements distribution. Finally, when large volume is combined with high slope angle, landslide prototypes show SF < 1 independently from the material type. Same models reach a static equilibrium in FLAC but fail in almost all cases (except few cases) in the following dynamic phase after the application of whatever seismic input. Such models may be in critical static conditions

- earthquake-induced displacements computed by Newmark (1965)'s method –based analysis are not affected by variation of input mean period since this parameter is not accounted for by equation 3.9 used for their computation. On the contrary, this parameter is fundamental to explain the variation of earthquake-induced displacements by stress-strain analysis. The influence of input mean period must be read in relation to landslide characteristic periods (T_s and T_l) computed with respect to landslide mass thickness and longitudinal length (cf. paragraph 3.7.1.2). The here performed analyses demonstrated that the T_l/T_m characteristic period ratio strongly affects displacement variation and that its effect is much more pronounced by increasing the volume since, in this case, the T_l/T_m ratio spans over a larger range of values. More in particular, for $0 < T_l/T_m < 0.5$ displacements are subjected to high increases for low T_l/T_m variations until they reach a peak in correspondence of the theoretical value $T_l/T_m = 0.5$. Indeed, in correspondence of the latter, the interaction between seismic waves and landslide masses should reach the highest efficiency (Hutchinson, 1987; 1994). For $T_l/T_m > 0.5$ displacements progressively decrease. On the contrary, displacements distributions do not peak in correspondence of the 1D resonance condition ($T_s/T_m = 1$, Rathje & Bray, 2000), even if this fact could also be explained by the low number of models that reach this theoretical value in the frequency range here investigated. Nevertheless, displacement variation according to an increasing-decreasing trend with respect to the T_s/T_m was identified, especially for large volume landslides

5.3 Random Forest analysis

A preliminary predictive model based on the Random Forest algorithm (cf. chapter 4) was developed starting from the dataset compiled in this study. The goal of such an investigation was to define a model to predict, a *priori* (i.e., starting from a set of known attributes), the target variable CLASS_DIF, i.e., an integer between 0 and 6 corresponding to a range of values associated to the expected difference between computed numerical and Newmark (1965)'s displacements. To define this model, the initial dataset was filtered in order to erase all dependent attributes as well as data samples related to landslide prototypes failing according to one or both the two approaches. Indeed, for these latter cases, the CLASS_DIF variable was not computable. Obtained results demonstrated that:

- the CLASS_DIF value mostly represented into the dataset is the CLASS_DIF = 0 which means negligible difference between displacements by numerical and simplified approaches. This result is in agreement with distributions in figure 5.1 and findings from literature (Lenti & Martino, 2013)
- the efficiency of the model is roughly 80%
- the 5 most important parameters which resulted relevant in controlling RF model predictions are: landslide thickness, T_s/T_m, T_l/T_m, material type and landslide length. The latter attributes are those mostly affecting the expected discrepancy between displacements returned by numerical and simplified approaches. This result is consistent with findings from chapter 3, according to which characteristic periods ratios play a role in explaining only outcomes from numerical modelling but they do not affect Newmark (1965)'s method – based analysis

As mentioned in chapter 4, the RF predictive model presented in this study is still at its preliminary phase, therefore, it is not yet prepared for practical applications. To be suitable for such purpose, further enrichments of the input dataset in terms of variability and continuity of considered parameters are requested. Indeed, this will allow representing a larger number of cases either in terms of geometrical and geotechnical composition of the designed landslide masses or in terms of considered seismic scenarios (especially as it regards the energy level of the seismic signals). Therefore, at this stage, the applicability of the RF model may not be suitable out of the values considered for the relevant parameters introduced in this study.

5.4 Future perspectives

Basing on above-discussed innovations and drawbacks, results achieved in this study require further investigations into the following topics:

- conclusion of incomplete numerical simulations which were not run due to time constraints
- enrichments of the sub-datasets compiled to compute mean values of the geotechnical parameters used to characterize the landslide prototypes
- generation of new landslide prototypes to schematize a larger number of real cases. In particular, new models could account for larger volume classes or different configurations along slope. At this regard, it might be particularly interesting to introduce landslide masses involving the upper half part of the slope face which occurrence is frequent during seismic events due to topographic site effects near the slope crest. Additionally, parametric analysis of displacements could be performed by modifying materials shear strength properties (that in this study were kept constant for the same material), impedance contrasts, bedrock properties and introducing more complex rheological laws for materials. It would be also interesting to investigate the role of pore pressure modifications in landslides mobility. The consideration of new landslide prototypes will also contribute to further enrich the input dataset used for the random forest analysis

- consideration of new seismic scenarios especially in terms of Arias Intensity, which value was kept constant in this study due to time constraints. This latter aspect is fundamental to ensure the applicability of the predictive model here developed to seismic regions where expected seismic events have Arias Intensity different from 0.1 m/s or also to make predictions for the same area by accounting for seismic inputs with different return times
- comparison of results from 2D and 3D models in order to evaluate which is the approximation introduced in the results when the third dimension is assumed infinite; in this case importance should be given also to the incidence of waves and their 3D nature (i.e., consideration of seismic waves of the SH and P-SV types at the same time)
- comparison of earthquake-induced displacements computed by adopting equivalent signals and real earthquakes
- test of the developed preliminary Random Forest predictive model to case studies. At this regard, some elaborations were already performed, although the results are not yet prepared to be presented in this manuscript

References

Alfaro, P., Delgado, J., García-Tortosa, F. J., Giner, J. J., Lenti, L., López-Casado, C., Martino, S., & Scarascia Mugnozza, G. (2012). The role of near-field interaction between seismic waves and slope on the triggering of a rockslide at Lorca (SE Spain). Natural Hazards and Earth System Sciences, 12(12), 3631-3643.

Ambraseys, N. N., & Menu, J. A. M. (1988). Earthquake-induced ground displacements. Earthquake engineering & structural dynamics, 16(7), 985-1006.

Amirahmadi, A., Pourhashemi, S., Karami, M., & Akbari, E. (2016). Modeling of landslide volume estimation. Open Geosciences, 8(1), 360-370.

Athanasopoulos, G. A., Pelekis, P. C., & Xenaki, V. C. (2001, March). Topography effects in the Athens 1999 earthquake: the case of hotel Dekelia. In Proceedings of fourth international conference on recent advances in geotechnical earthquake engineering and soil dynamics, San Diego, March (in CDROM).

Bard, P. Y., & Bouchon, M. (1985). The two-dimensional resonance of sediment-filled valleys. Bulletin of the Seismological Society of America, 75(2), 519-541.

Barlow, J., Barisin, I., Rosser, N., Petley, D., Densmore, A., & Wright, T. (2015). Seismically-induced mass movements and volumetric fluxes resulting from the 2010 Mw= 7.2 earthquake in the Sierra Cucapah, Mexico. Geomorphology, 230, 138-145.

Bird, J. F., & Bommer, J. J. (2004). Earthquake losses due to ground failure. Engineering geology, 75(2), 147-179.

Bishop, A. W. (1955). The use of the slip circle in the stability analysis of slopes. Geotechnique, 5(1), 7-17.

Bakavoli, M. K., & Haghshenas, E. (2010). Experimental and numerical study of topographic site effect on a hill near Tehran.

Bouckovalas, G. D., & Papadimitriou, A. G. (2005). Numerical evaluation of slope topography effects on seismic ground motion. Soil Dynamics and Earthquake Engineering, 25(7-10), 547-558.

Bozzano, F., Lenti, L., Martino, S., Montagna, A., & Paciello, A. (2011a). Earthquake triggering of landslides in highly jointed rock masses: Reconstruction of the 1783 Scilla rock avalanche (Italy). Geomorphology, 129(3-4), 294-308.

Bozzano, F., Lenti, L., Martino, S., Paciello, A., & Scarascia Mugnozza, G. (2011b). Evidences of landslide earthquake triggering due to self-excitation process. International Journal of Earth Sciences, 100, 861-879.

Bozzano, F., Lenti, L., Martino, S., Paciello, A., & Scarascia Mugnozza, G. (2008). Self-excitation process due to local seismic amplification responsible for the reactivation of the Salcito landslide (Italy) on 31 October 2002. Journal of Geophysical Research: Solid Earth, 113(B10).

Bozzano, F., Martino, S., Esposito, E., Montagna, A., Lenti, L., Paciello, A., & Porfido, S. (2010). Numerical modelling of earthquake-induced rock landslides: the 1783 Scilla case-history (Southern Italy).

Breiman, L. (2001). Random Forests. Machine Learning 45, 5–32. https://doi.org/10.1023/A:1010933404324.

Brenner, S. C., & Carstensen, C. (2004). Finite element methods. Encyclopedia of computational mechanics, 1, 73-118.

Conti P. (2012). Analisi geomeccanica. Dispense realizzate per il Corso di Laurea Magistrale in Scienze e Tecnologie Geologiche, Università di Siena, 2012.

Corominas, J., Mavrouli, O., & Ruiz-Carulla, R. (2018). Magnitude and frequency relations: are there geological constraints to the rockfall size?. Landslides, 15(5), 829-845.

Courant R. Variational methods for the solution of problems of equilibrium and vibration. Bull. Am. Math. Soc. 1943; 49:1-23.

Cruden, D. M., & Varnes, D. J. (1958). Landslide types and processes. Special Report-National Research Council. Transp. Res. Board, 247, 20-47.

Cruden, D.M. & Varnes, D.J. (1996). Landslide Types and Processes, Transportation Research Board, US National Academy of Sciences, Special Report, 247: 36-75. Landslides Eng. Pract, 24, 20-47.

Cutler, A., Cutler, D. R., & Stevens, J. R. (2012). Random forests. Ensemble machine learning: Methods and applications, 157-175.

Delgado, J., Garrido, J., Lenti, L., Lopez-Casado, C., Martino, S., & Sierra, F. J. (2015). Unconventional pseudostatic stability analysis of the Diezma landslide (Granada, Spain) based on a high-resolution engineering-geological model. Engineering Geology, 184, 81-95.

Delgado, J., Garrido, J., López-Casado, C., Martino, S., & Peláez, J. A. (2011). On far field occurrence of seismically induced landslides. Engineering Geology, 123(3), 204-213.

Dhatt, G., Lefrançois, E., & Touzot, G. (2012). Finite element method. John Wiley & Sons.

Dridi, S. (2021). Supervised learning-a systematic literature review.

Domej, G., Bourdeau, C., Lenti, L., Martino, S., & Piuta, K. (2017). Mean landslide geometries inferred from a global database of earthquake-and non-earthquake-triggered landslides. Ital. J. Eng. Geol. Environ, 17, 87-107.

Domej, G., Bourdeau, C., Lenti, L., Martino, S., & Pluta, K. (2020). Shape and Dimension Estimations of Landslide Rupture Zones via Correlations of Characteristic Parameters. Geosciences, 10(5), 198.

Domej G. & Pluta K., 2018. L'EquT Database. Accompanying dataset of doctoral thesis and publications. Zenodo. (DOI: 10.5281/zenodo.7653511).

Dussauge, C., Grasso, J. R., & Helmstetter, A. (2003). Statistical analysis of rockfall volume distributions: Implications for rockfall dynamics. Journal of Geophysical Research: Solid Earth, 108(B6).

Dussauge-Peisser, C., Helmstetter, A., Grasso, J. R., Hantz, D., Desvarreux, P., Jeannin, M., & Giraud, A. (2002). Probabilistic approach to rock fall hazard assessment: potential of historical data analysis. Natural hazards and earth system sciences, 2(1/2), 15-26.

Fan, X., Scaringi, G., Korup, O., West, A. J., van Westen, C. J., Tanyaş, H., Hovius, N., Hales, T. C., Jibson, R. W., Allstadt, K. E., Zhang, L., Evans, S. G., Xu, C., Li, G., Pei, X., Xu, Q., & Huang, R. (2019). Earthquake-induced chains of geologic hazards: Patterns, mechanisms, and impacts. Reviews of geophysics, 57(2), 421-503.

Fellenius, W. (1927). Erdstatische Berechnungen mit Reibung und Kohäsion (Adhäsion) und unter Annahme kreiszylindrischer Gleitflächen. W. Ernst & Sohn.

Fellenius, W. (1936). Calculation of the stability of earth dams. In Proc. of the second congress on large dams (Vol. 4, pp. 445-463).

Final Draft International Standard ISO/FDIS 14688-1:2017 Geotechnical investigation and testing – Identification and classification of soil – Part 1: Identification and description.

Fredlund, D. G., & Krahn, J. (1977). Comparison of slope stability methods of analysis. Canadian geotechnical journal, 14(3), 429-439.

García-Rodríguez, M. J., & Malpica, J. A. (2010). Assessment of earthquake-triggered landslide susceptibility in El Salvador based on an Artificial Neural Network model. Natural Hazards and Earth System Sciences, 10(6), 1307-1315.

Gercek, H. (2007). Poisson's ratio values for rocks. International Journal of Rock Mechanics and Mining Sciences, 44(1), 1-13.

Gischig, V. S., Eberhardt, E., Moore, J. R., & Hungr, O. (2015). On the seismic response of deep-seated rock slope instabilities—Insights from numerical modeling. Engineering Geology, 193, 1-18.

Glinsky, N., Bertrand, E., & Régnier, J. (2019). Numerical simulation of topographical and geological site effects. Applications to canonical topographies and Rognes hill, South East France. Soil Dynamics and Earthquake Engineering, 116, 620-636.

Gorum, T., Fan, X., van Westen, C. J., Huang, R. Q., Xu, Q., Tang, C., & Wang, G. (2011). Distribution pattern of earthquake-induced landslides triggered by the 12 May 2008 Wenchuan earthquake. Geomorphology, 133(3-4), 152-167.

Gorum, T., van Westen, C. J., Korup, O., van der Meijde, M., Fan, X., & van der Meer, F. D. (2013). Complex rupture mechanism and topography control symmetry of mass-wasting pattern, 2010 Haiti earthquake. Geomorphology, 184, 127-138.

Guthrie R.H., Evans S.G. (2004). Analysis of landslide frequencies and characteristics ina natural system, coastal British Columbia. Earth Surface Processes and Landforms 29, 1321–1339.

Guzzetti, F., Ardizzone, F., Cardinali, M., Galli, M., Reichenbach, P., & Rossi, M. (2008). Distribution of landslides in the Upper Tiber River basin, central Italy. Geomorphology, 96(1-2), 105-122.

Guzzetti, F., Ardizzone, F., Cardinali, M., Rossi, M., & Valigi, D. (2009). Landslide volumes and landslide mobilization rates in Umbria, central Italy. Earth and Planetary Science Letters, 279(3-4), 222-229.

Guzzetti, F., Malamud, B. D., Turcotte, D. L., & Reichenbach, P. (2002). Power-law correlations of landslide areas in central Italy. Earth and Planetary Science Letters, 195(3-4), 169-183.

Guzzetti, F., Reichenbach, P., Ghigi, S. (2004). Rock-fall hazard and risk assessment in the Nera River Vally, Umbria Region, central Italy. Environ Manag 34(2): 191-208.

Hardin, B. O., & Drnevich, V. P. (1972). Shear modulus and damping in soils: design equations and curves. Journal of the Soil mechanics and Foundations Division, 98(7), 667-692.

Havenith, H. B., Jongmans, D., Faccioli, E., Abdrakhmatov, K., & Bard, P. Y. (2002). Site effect analysis around the seismically induced Ananevo rockslide, Kyrgyzstan. Bulletin of the seismological society of America, 92(8), 3190-3209.

He, Q., Wang, M., & Liu, K. (2021). Rapidly assessing earthquake-induced landslide susceptibility on a global scale using random forest. Geomorphology, 391, 107889.

Hendron Jr, A. J., & Patton, F. D. (1985). The vaiont slide. A geotechnical analysis based on new geologic observations of the failure surface. Volume 1. Main text. ARMY ENGINEER WATERWAYS EXPERIMENT STATION VICKSBURG MS GEOTECHNICAL LAB.

Ho, T. K. (1995, August). Random decision forests. In Proceedings of 3rd international conference on document analysis and recognition (Vol. 1, pp. 278-282). IEEE.

Ho, T. K. (1998). The random subspace method for constructing decision forests. IEEE transactions on pattern analysis and machine intelligence, 20(8), 832-844.

Hrennikoff, A. (1941). Solution of problems of elasticity by the framework method.

Hsieh, S. Y., & Lee, C. T. (2011). Empirical estimation of the Newmark displacement from the Arias intensity and critical acceleration. Engineering Geology, 122(1-2), 34-42.

Huggel, C., Zgraggen-Oswald, S., Haeberli, W., Kääb, A., Polkvoj, A., Galushkin, I., & Evans, S. G. (2005). The 2002 rock/ice avalanche at Kolka/Karmadon, Russian Caucasus: assessment of extraordinary avalanche formation and mobility, and application of QuickBird satellite imagery. Natural Hazards and Earth System Sciences, 5(2), 173-187.

Hungr, O., Leroueil, S., & Picarelli, L. (2014). The Varnes classification of landslide types, an update. Landslides, 11, 167-194.

Hungr, O., McDougall, S., Wise, M. & Cullen, M. (1999). Magnitude-frequency relationships of debris flows and debris avalanches in relation to slope relief. Geomorphology, 96 :355-365.

Hungr, O., McDougall, S. & Bovis, M. In Debris-Flow Hazards and Related Phenomena (eds Jakob, M. & Hungr, O.) (Springer, Berlin, 2005).

Hutchinson, J. N. (1987). Mechanism producing large displacements in landslides on pre-existing shears, Mem. Soc. Geol. China 9, 175–200.

Hutchinson, J. N. (1994). Some aspects of the morphological and geotechnical parameters of landslides, with examples drawn from Italy and elsewhere. Geologica Romana, 30, 1-14.

ISMR. Terminology (English, French, German). Lizbon: ISMR ; 1975.

Itasca (2015). FLAC 8 Basics. An introduction to FLAC 8 and a guide to its practical application in geotechnical engineering. Available on https://www.itascacg.com/software/flac-8-basics.

James, G., Witten, D., Hastie, T., & Tibshirani, R. (2013). An introduction to statistical learning (Vol. 112, p. 18). New York: springer.

Janbu, N. (1954). Stability analysis of slopes with dimensionless parameters. (No Title).

Jibson, R. W. (1993). Predicting earthquake-induced landslide displacements using Newmark's sliding block analysis. Transportation research record, 1411, 9-17.

Jibson, R. W. (2007). Regression models for estimating coseismic landslide displacement. Engineering geology, 91(2-4), 209-218.

Jibson, R. W., & Keefer, D. K. (1993). Analysis of the seismic origin of landslides: examples from the New Madrid seismic zone. Geological Society of America Bulletin, 105(4), 521-536.

Makdisi, F. I., & Seed, H. B. (1978). Simplified procedure for estimating dam and embankment earthquake-induced deformations. Journal of the Geotechnical Engineering Division, 104(7), 849-867.

Keefer, D. K. (1984). Landslides caused by earthquakes. Geological Society of America Bulletin, 95(4), 406-421.

Kuhlemeyer, R. L., & Lysmer, J. (1973). Finite element method accuracy for wave propagation problems. Journal of the Soil Mechanics and Foundations Division, 99(5), 421-427.

Larsen, M. C., & Torres-Sánchez, A. J. (1998). The frequency and distribution of recent landslides in three montane tropical regions of Puerto Rico. Geomorphology, 24(4), 309-331.

Lenti, L., & Martino, S. (2010). New procedure for deriving multifrequential dynamic equivalent signals (LEMA_DES): a test-study based on Italian accelerometric records. Bulletin of Earthquake Engineering, 8, 813-846.

Lenti, L., & Martino, S. (2012). The interaction of seismic waves with step-like slopes and its influence on landslide movements. Engineering Geology, 126, 19-36.

Lenti, L., & Martino, S. (2013). A Parametric Numerical Study of the Interaction between Seismic Waves and Landslides for the Evaluation of the Susceptibility to Seismically Induced DisplacementsA Parametric Numerical Study of the Interaction between Seismic Waves and Landslides. Bulletin of the Seismological Society of America, 103(1), 33-56.

Logan, D. L. (2011). A first course in the finite element method cengage learning.

Mahesh, B. (2020). Machine learning algorithms-a review. International Journal of Science and Research (IJSR).[Internet], 9(1), 381-386.

Malamud, B. D., Turcotte, D. L., Guzzetti, F., & Reichenbach, P. (2004). Landslides, earthquakes, and erosion. Earth and Planetary Science Letters, 229(1-2), 45-59.

Malamud, B. D., Turcotte, D. L., Guzzetti, F., & Reichenbach, P. (2004a). Landslide inventories and their statistical properties. Earth Surface Processes and Landforms, 29(6), 687-711.

Martin, Y., Rood, K., Schwab, J. W., & Church, M. (2002). Sediment transfer by shallow landsliding in the Queen Charlotte Islands, British Columbia. Canadian Journal of Earth Sciences, 39(2), 189-205.

Martino, S. (2015). Earthquake-induced reactivation of landslides: recent advances and future perspectives. Earthquakes and their impact on society, 291-322.

Martino, S. (2017). Eartquake-induced landslides in Italy. From the distribution of effects to the hazard mapping. Italian Journal of Engineering Geology and Environment, 1, 53-67.

Martino, S., Bozzano, F., Caporossi, P., D'angiò, D., Della Seta, M., Esposito, C., Fantini, A., Fiorucci, M., Giannini, L.M., Iannucci, R., Marmoni, G.M., Mazzanti, P., Missori, C., Moretto, S., Piacentini, D., Rivellino, S., Romeo, R.W., Sarandrea, P., Schilirò, L., Troiani, F. & Varone, C. (2019). Impact of landslides on transportation routes during the 2016–2017 Central Italy seismic sequence. Landslides, 16, 1221-1241.

Martino, S., Lenti, L., & Bourdeau, C. (2018). Composite mechanism of the Büyükçekmece (Turkey) landslide as conditioning factor for earthquake-induced mobility. Geomorphology, 308, 64-77.

Martino, S., Lenti, L., Delgado, J., Garrido, J., & Lopez-Casado, C. (2016). Application of a characteristic periods-based (CPB) approach to estimate earthquake-induced displacements of landslides through dynamic numerical modelling. Geophysical Journal International, 206(1), 85-102.

Martino, S., Marmoni, G. M., Fiorucci, M., Ceci, A. F., Discenza, M. E., Rouhi, J., & Tedoradze, D. (2022). Role of antecedent rainfall in the earthquake-triggered shallow landslides involving unsaturated slope covers. Applied Sciences, 12(6), 2917.

Martino, S., & Mugnozza, G. S. (2005). The role of the seismic trigger in the Calitri landslide (Italy): historical reconstruction and dynamic analysis. Soil Dynamics and Earthquake Engineering, 25(12), 933-950.

Martino, S., Prestininzi, A., & Romeo, R. W. (2014). Earthquake-induced ground failures in Italy from a reviewed database. Natural Hazards and Earth System Sciences, 14(4), 799-814.

Marsland S. (2014). Machine learning: an algorithmic perspective. Second edition. Boca Raton, FL: : Chapman & Hall/CRC.

Meunier, P., Hovius, N., & Haines, J. A. (2008). Topographic site effects and the location of earthquake induced landslides. Earth and Planetary Science Letters, 275(3-4), 221-232.

Moczo, P., Kristek, J., & Halada, L. (2004). The finite-difference method for seismologists. An Introduction, 161.

Newmark, N. M. (1965). Effects of earthquakes on dams and embankments. Geotechnique, 15(2), 139-160.

Petley, D. (2012). Global patterns of loss of life from landslides. Geology, 40(10), 927-930.

Pudasaini, S. P., & Krautblatter, M. (2021). The mechanics of landslide mobility with erosion. Nature communications, 12(1), 6793.

Quinlan, J. R. (1990). Decision trees and decision-making. IEEE Transactions on Systems, Man, and Cybernetics, 20(2), 339-346.

Rathje, E. M., Abrahamson, N. A., & Bray, J. D. (1998). Simplified frequency content estimates of earthquake ground motions. Journal of geotechnical and geoenvironmental engineering, 124(2), 150-159.

Rathje, E. M., & Bray, J. D. (2000). Nonlinear coupled seismic sliding analysis of earth structures, J. Geotech. Geoenviron. Eng. ASCE 126, no. 11, 1002–1014.

Rault, C., Robert, A., Marc, O., Hovius, N., & Meunier, P. (2019). Seismic and geologic controls on spatial clustering of landslides in three large earthquakes. Earth Surface Dynamics, 7(3), 829-839.

Roback, K., Clark, M. K., West, A. J., Zekkos, D., Li, G., Gallen, S. F., ... & Godt, J. W. (2018). The size, distribution, and mobility of landslides caused by the 2015 Mw7. 8 Gorkha earthquake, Nepal. Geomorphology, 301, 121-138.

Rodríguez, C. E., Bommer, J. J., & Chandler, R. J. (1999). Earthquake-induced landslides: 1980–1997. Soil Dynamics and Earthquake Engineering, 18(5), 325-346.

Rohatgi, A. (2021). Webplotdigitizer: Version 4.5, 2021. URL https://automeris. io/WebPlotDigitizer, 4(2).

Romeo, R. (2000). Seismically induced landslide displacements: a predictive model. Engineering Geology, 58(3-4), 337-351.

Russel, S., & Norvig, P. (2020). Artificial intelligence: a modern approach. 1136 p.

Sato, H. P., Hasegawa, H., Fujiwara, S., Tobita, M., Koarai, M., Une, H., & Iwahashi, J. (2007). Interpretation of landslide distribution triggered by the 2005 Northern Pakistan earthquake using SPOT 5 imagery. Landslides, 4, 113-122.

Saygili, G., & Rathje, E. M. (2008). Empirical predictive models for earthquake-induced sliding displacements of slopes. Journal of geotechnical and geoenvironmental engineering, 134(6), 790-803.

Yagi, H., Sato, G., Higaki, D., Yamamoto, M., & Yamasaki, T. (2009). Distribution and characteristics of landslides induced by the Iwate–Miyagi Nairiku Earthquake in 2008 in Tohoku District, Northeast Japan. Landslides, 6, 335-344.

Seal, D. M., Jessee, N., Hamburger, M. W., & Allstadt, K. E. (2022). Comprehensive Global Database of Earthquake-Induced Landslide Events and Their Impacts. US Geological Survey data release, https://doi. org/10.5066/P9RG3MBE.

Seed, H. B., & Idriss, I. M. (1969). Influence of soil conditions on ground motions during earthquakes. Journal of the Soil Mechanics and Foundations Division, 95(1), 99-137.

Sepúlveda, S. A., Serey, A., Lara, M., Pavez, A., & Rebolledo, S. (2010). Landslides induced by the April 2007 Aysén fjord earthquake, Chilean Patagonia. Landslides, 7, 483-492.

Simonett, D. S. (1967). Landslide distribution and earthquakes in the Bavani and Torricelli Mountains, New Guinea. Landform Studies from Australia and New Guinea, 64-84.

Skempton, A. W., & DeLory, F. A. (1957). Stability of natural slopes in London clay. Thomas Telford Publishing, London, UK, 15, 378-381.

Skempton, A. W., & Hutchinson, J. (1969). Stability of natural slopes and embankment foundations. In Soil Mech & Fdn Eng Conf Proc/Mexico/.

Stock, G. M., Collins, B. D., Santaniello, D. J., Zimmer, V. L., Wieczorek, G. F., & Snyder, J. B. (2013). Historical Rock Falls in Yosemite National Park, California (1857-2011) (p. 17). US Department of the Interior, US Geological Survey.

Tang, C., Tanyaş, H., van Westen, C. J., Tang, C., Fan, X., & Jetten, V. G. (2019). Analysing post-earthquake mass movement volume dynamics with multi-source DEMs. Engineering geology, 248, 89-101.

Tanyaş, H., Van Westen, C. J., Allstadt, K. E., Anna Nowicki Jessee, M., Görüm, T., Jibson, R. W., Godt, J.W., Sato, H.P, Schmitt, R.G., Marc, O. & Hovius, N. (2017). Presentation and analysis of a worldwide database of earthquake-induced landslide inventories. Journal of Geophysical Research: Earth Surface, 122(10), 1991-2015.

Tanyaş, H., van Westen, C. J., Allstadt, K. E., & Jibson, R. W. (2019). Factors controlling landslide frequency–area distributions. Earth surface processes and landforms, 44(4), 900-917.

Varnes, D. J. (1978). Slope movement types and processes. Special report, 176, 11-33.

Voight, B., Janda, R. J., Glicken, H., & Douglass, P. M. (1983). Nature and mechanics of the Mount St Helens rockslide-avalanche of 18 May 1980. Geotechnique, 33(3), 243-273.

Wieczorek, G.F., Snyder, J.B., Alger, C.S., Isaacson, K.A. (1992). Rock falls in Yosemite Valley, California U.S. Geological Survey Open-File Report 92-387, 38 p., 2 appendixes, 4 plates.

Wieczorek, G. F., Wilson, R. C., & Harp, E. L. (1985). Map showing slope stability during earthquakes in San Mateo County, California (No. 1257-E).

Wikipedia contributors. (2023, September 9). Random forest. In Wikipedia, The Free Encyclopedia. Retrieved 10:21, September 15, 2023, from https://en.wikipedia.org/w/index.php?title=Random forest&oldid=1174573646.

Youssef, A. M., Pourghasemi, H. R., Pourtaghi, Z. S., & Al-Katheeri, M. M. (2016). Landslide susceptibility mapping using random forest, boosted regression tree, classification and regression tree, and general linear models and comparison of their performance at Wadi Tayyah Basin, Asir Region, Saudi Arabia. Landslides, 13, 839-856.

Zhang, Z., Fleurisson, J. A., & Pellet, F. (2018). The effects of slope topography on acceleration amplification and interaction between slope topography and seismic input motion. Soil Dynamics and Earthquake Engineering, 113, 420-431.

Zhou, P. B., & Zhou, P. B. (1993). Finite difference method. Numerical Analysis of Electromagnetic Fields, 63-94.

Licences

AutoCAD, 2022. Free version for students.

FLAC 7.00, Itasca. Licence serial number 213-033-0764, Univ. Gustave Eiffel, SRO laboratory.

Annex 1: Velocity time histories of input signals

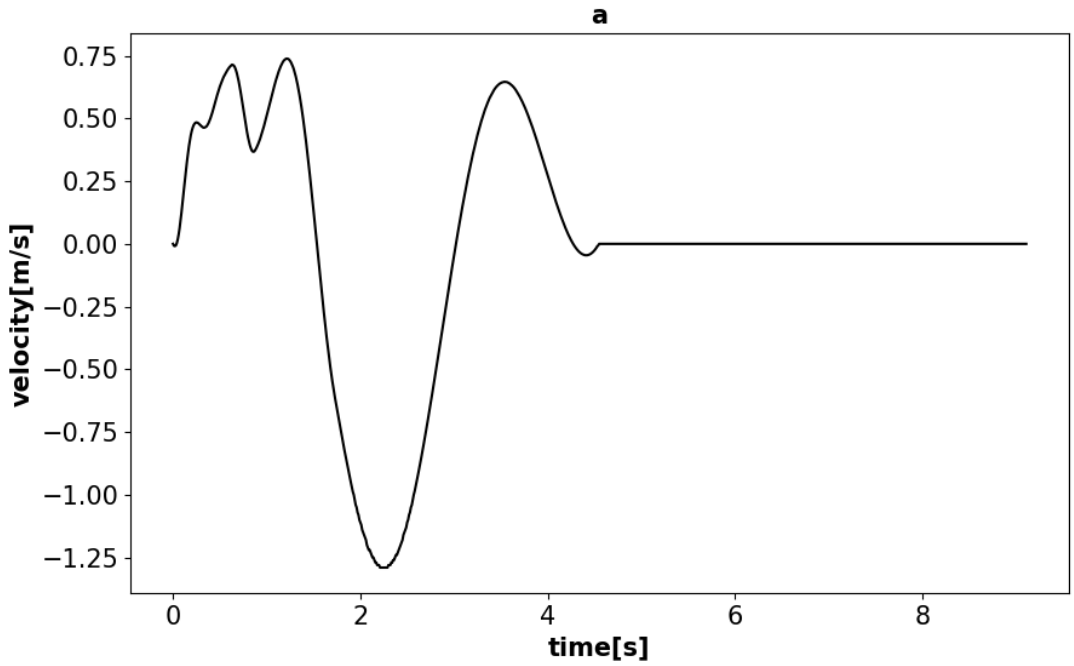

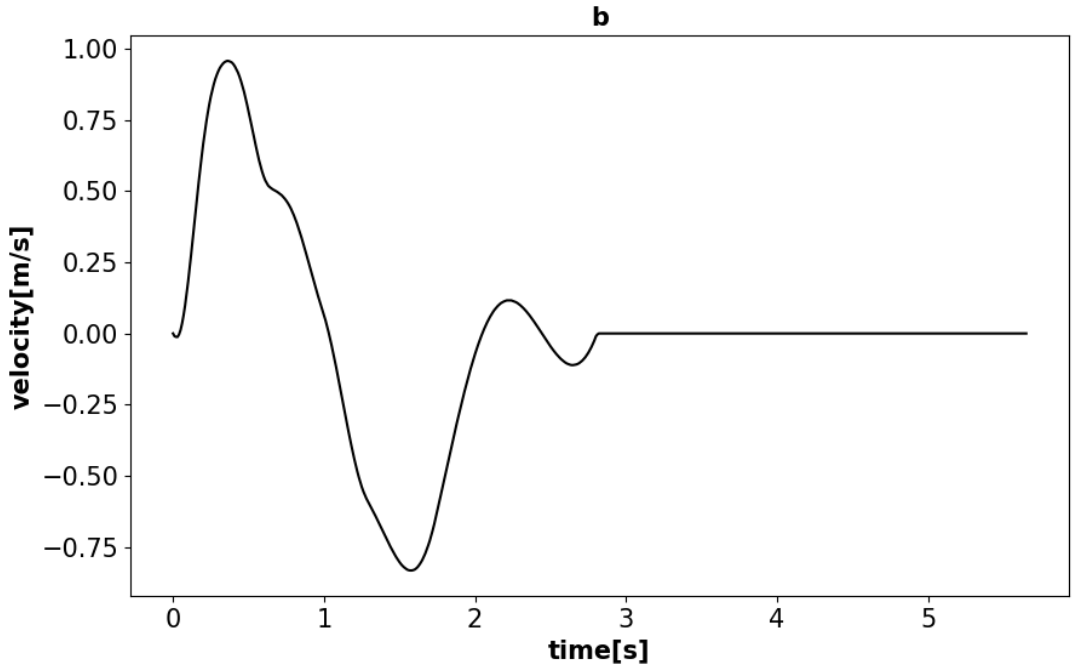

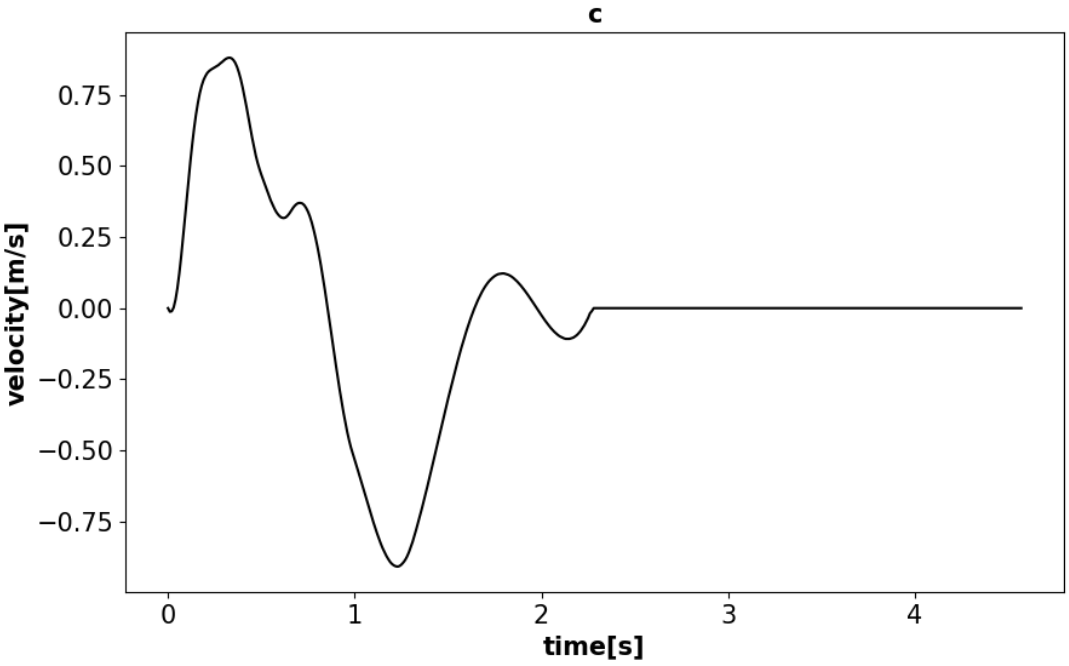
c
velocity[m/s]
0.75
0.50
0.25
0.00
−0.25
−0.50
−0.75
0
1
2
3
4
time[s]

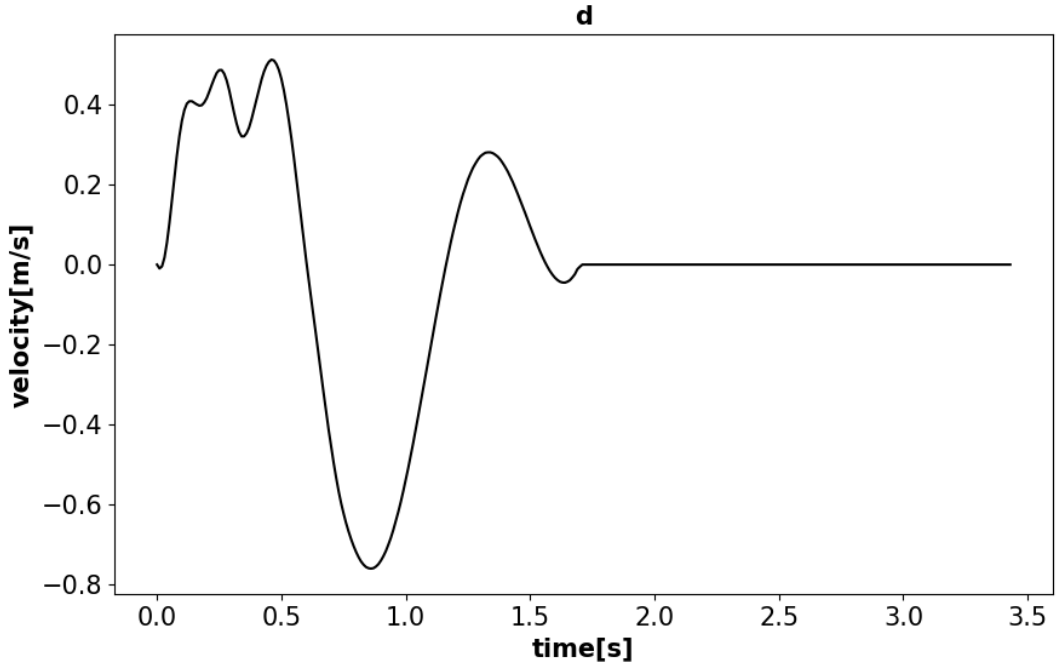
d
velocity[m/s]
0.4
0.2
0.0
−0.2
−0.4
−0.6
−0.8
0.0
0.5
1.0
1.5
2.0
2.5
3.0
3.5
time[s]

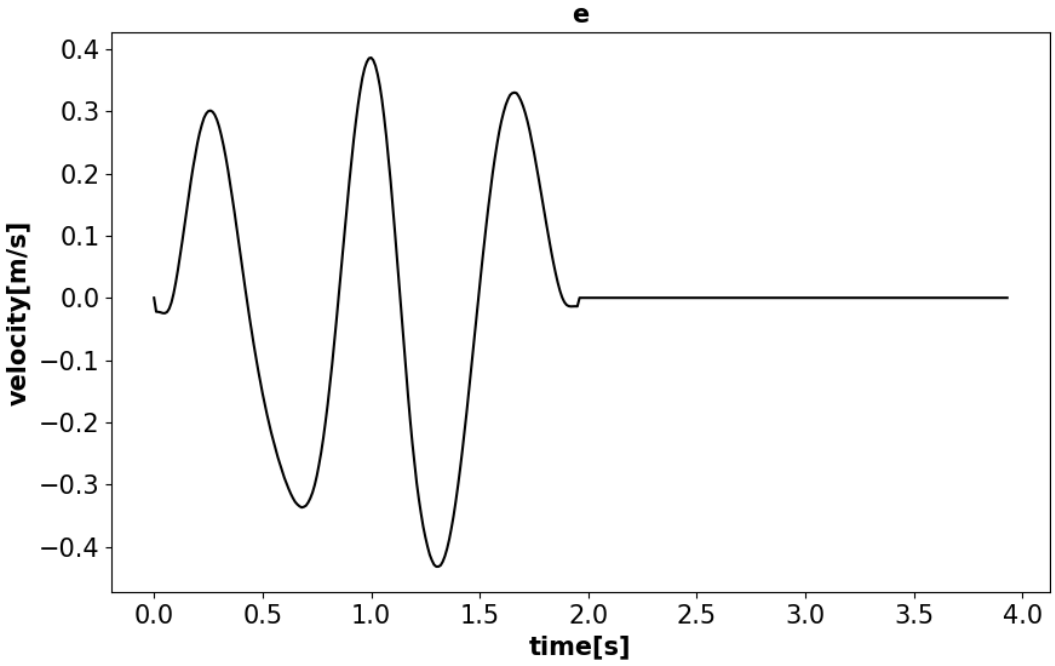
e
velocity[m/s]
time[s]
0.4
0.3
0.2
0.1
0.0
−0.1
−0.2
−0.3
−0.4
0.0
0.5
1.0
1.5
2.0
2.5
3.0
3.5
4.0

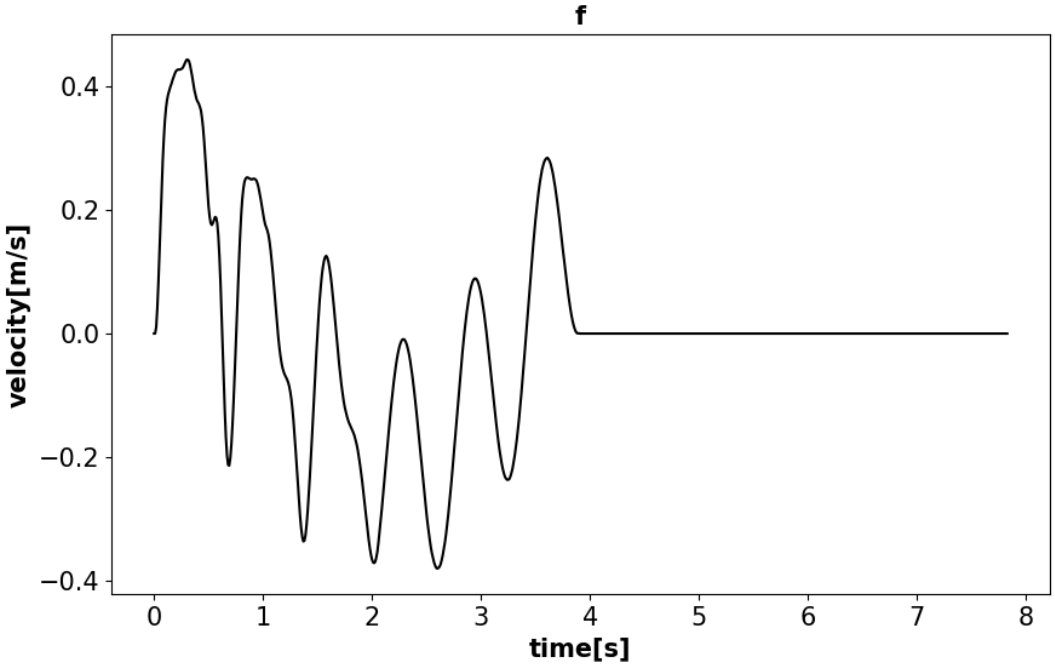
f
velocity[m/s]
time[s]
0.4
0.2
0.0
−0.2
−0.4
0
1
2
3
4
5
6
7
8

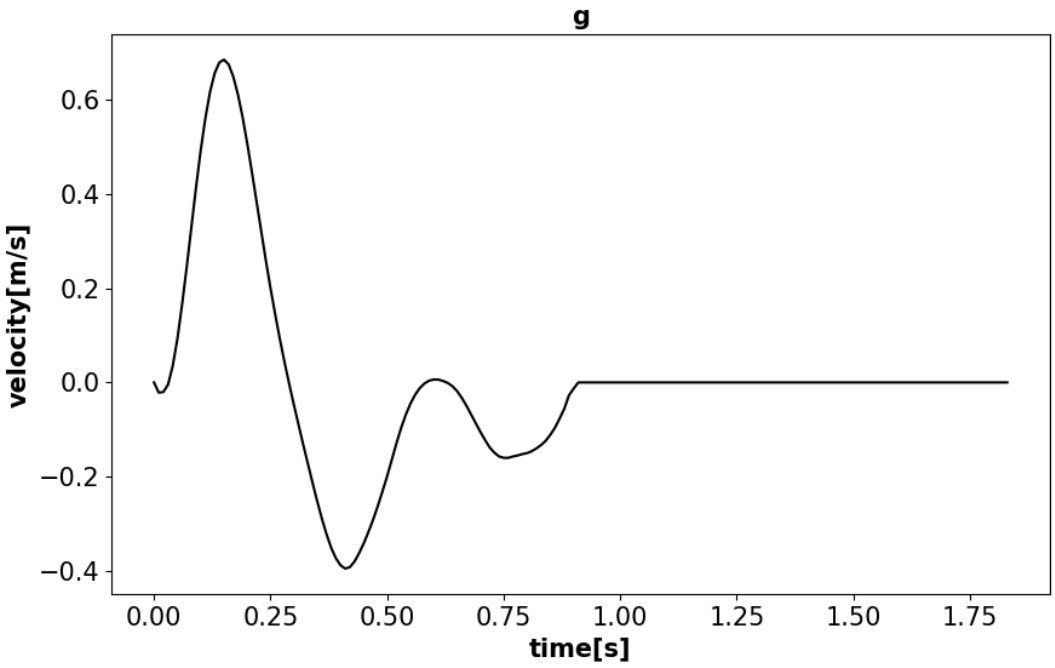
g
velocity[m/s]
0.6
0.4
0.2
0.0
−0.2
−0.4
0.00
0.25
0.50
0.75
1.00
1.25
1.50
1.75
time[s]

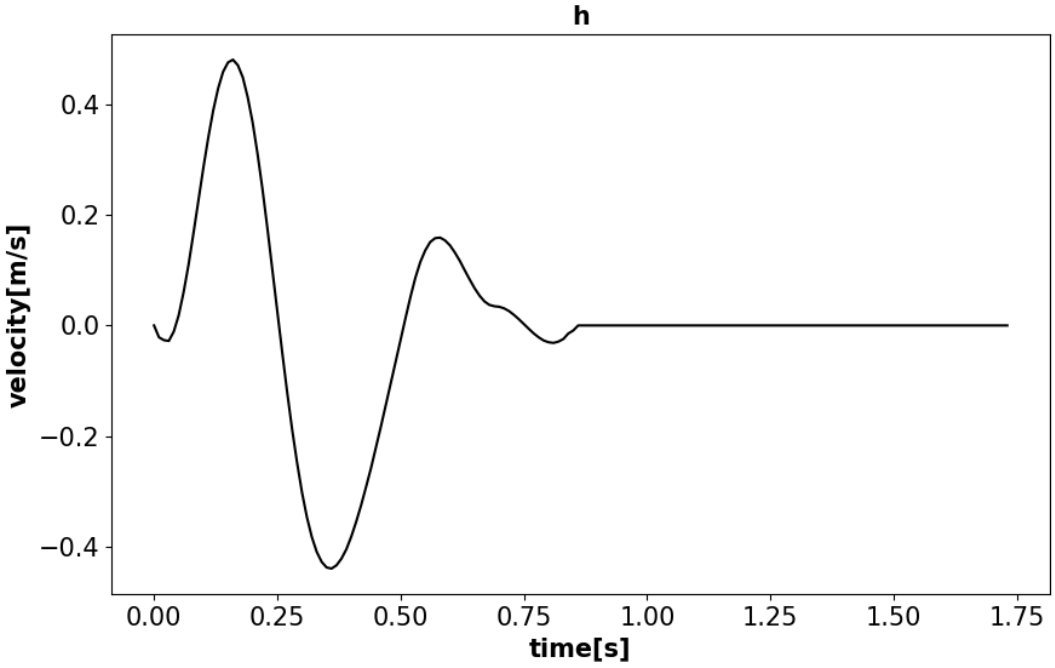
h
velocity[m/s]
0.4
0.2
0.0
−0.2
−0.4
0.00
0.25
0.50
0.75
1.00
1.25
1.50
1.75
time[s]

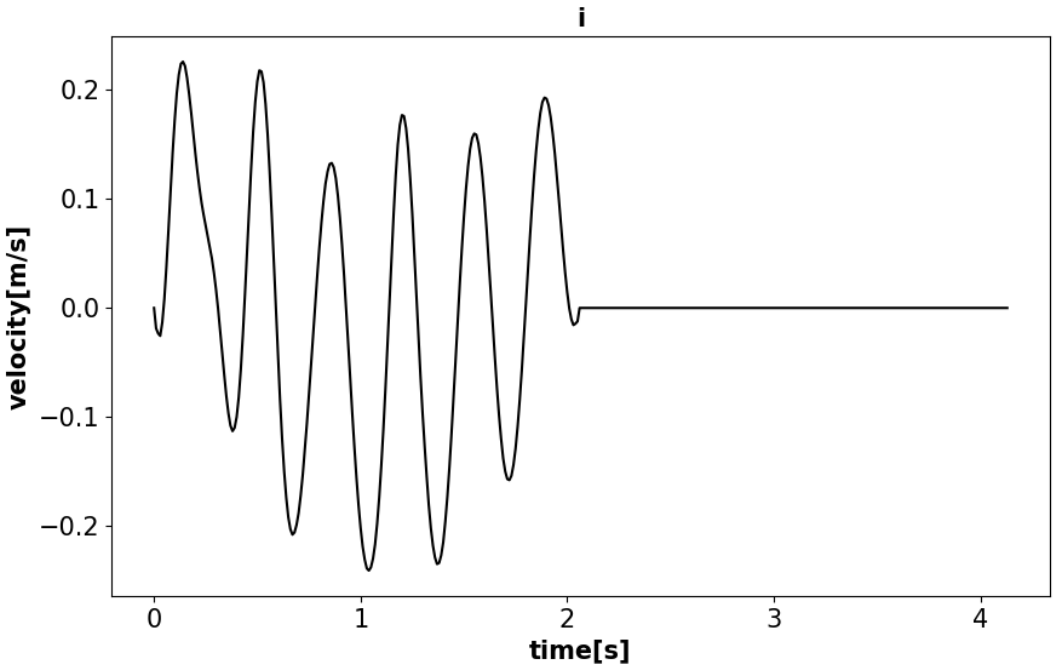
i
velocity[m/s]
0.2
0.1
0.0
−0.1
−0.2
0
1
2
3
4
time[s]

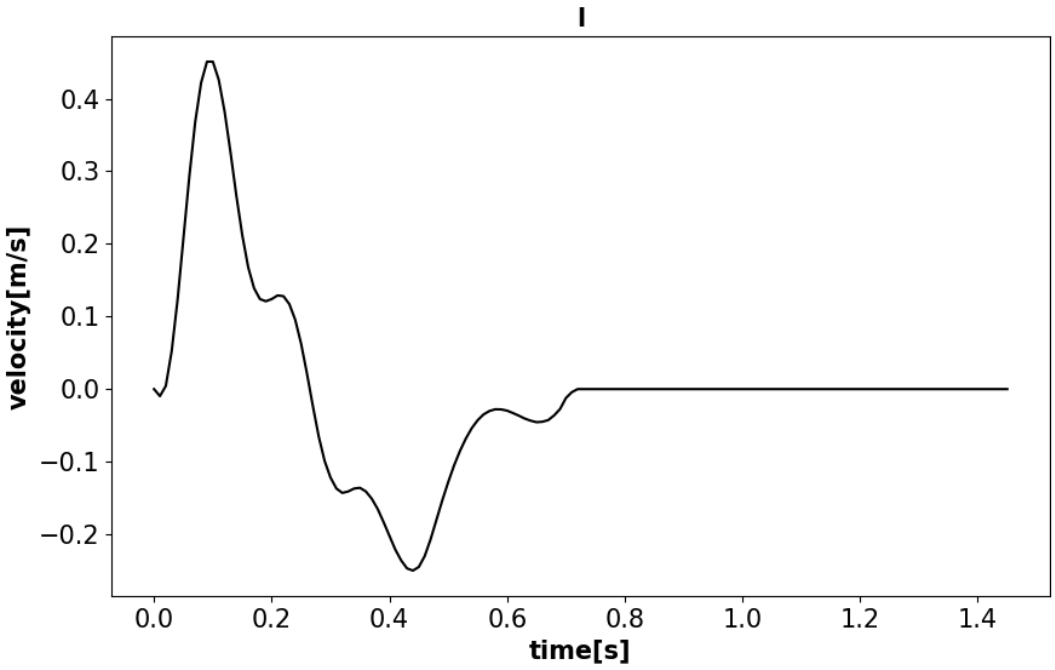
I
velocity[m/s]
0.4
0.3
0.2
0.1
0.0
−0.1
−0.2
0.0
0.2
0.4
0.6
0.8
1.0
1.2
1.4
time[s]

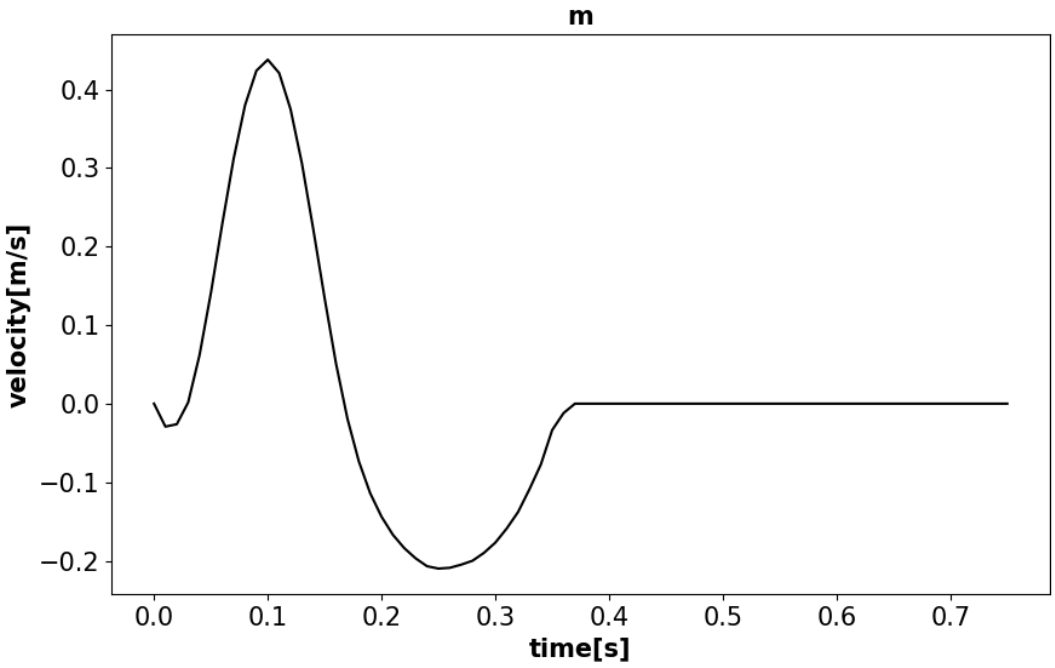
m
velocity[m/s]
time[s]
0.4
0.3
0.2
0.1
0.0
−0.1
−0.2
0.0
0.1
0.2
0.3
0.4
0.5
0.6
0.7

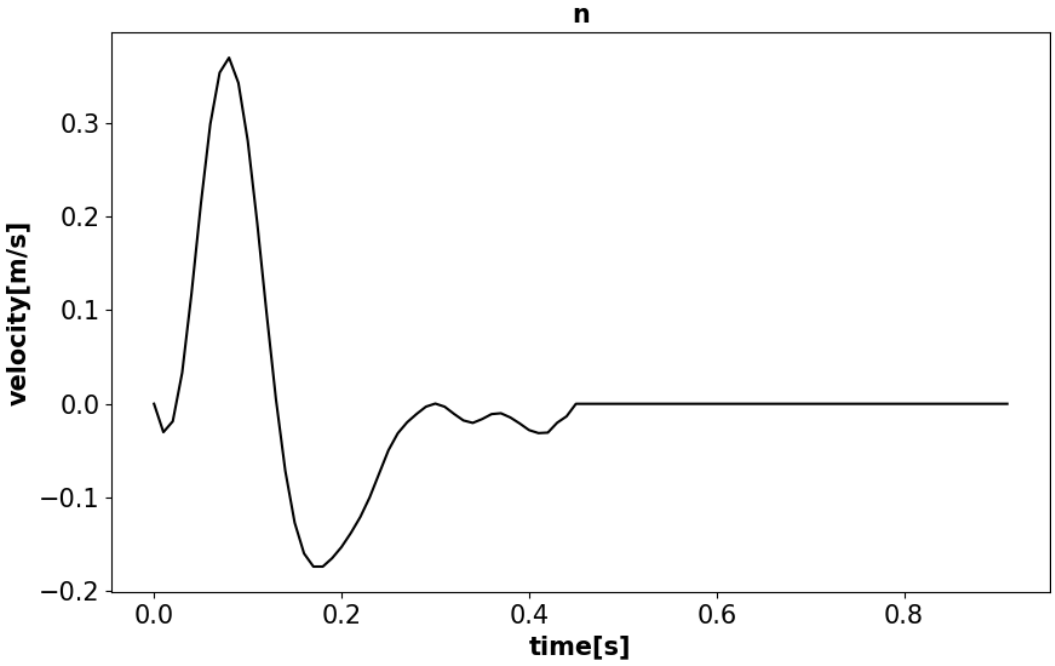
n
velocity[m/s]
time[s]
0.3
0.2
0.1
0.0
−0.1
−0.2
0.0
0.2
0.4
0.6
0.8

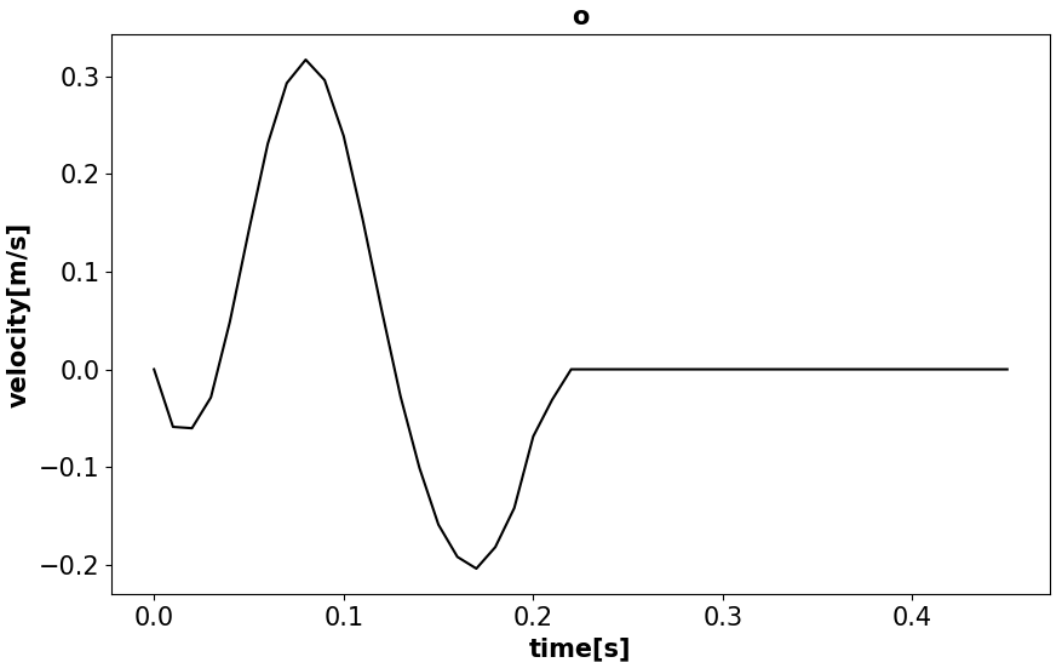
o
velocity[m/s]
time[s]
0.3
0.2
0.1
0.0
−0.1
−0.2
0.0
0.1
0.2
0.3
0.4

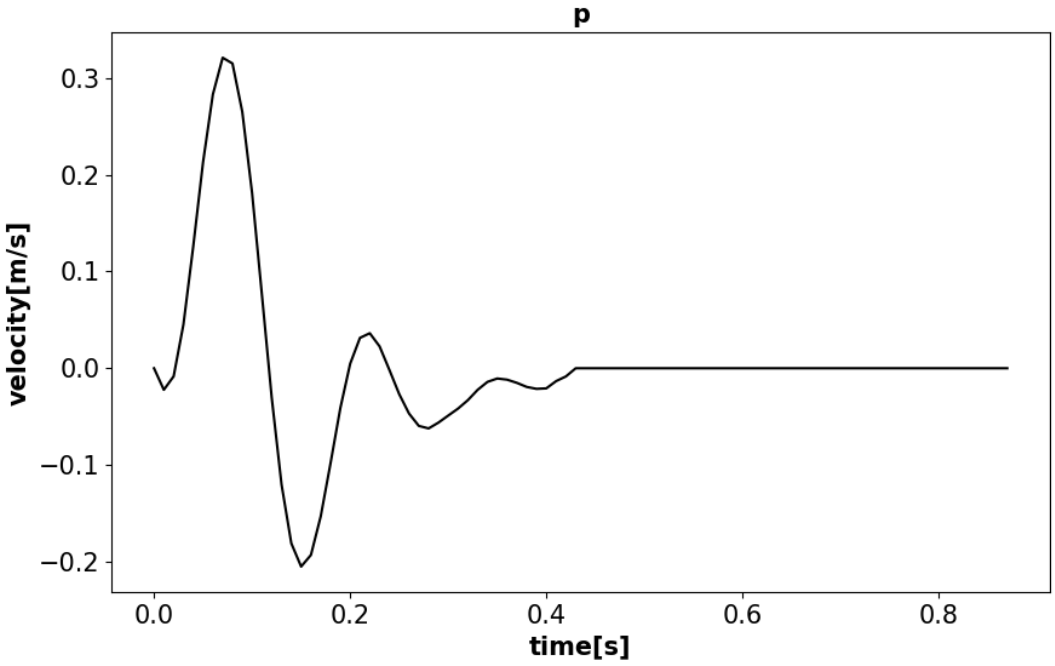
p
velocity[m/s]
time[s]
0.3
0.2
0.1
0.0
−0.1
−0.2
0.0
0.2
0.4
0.6
0.8

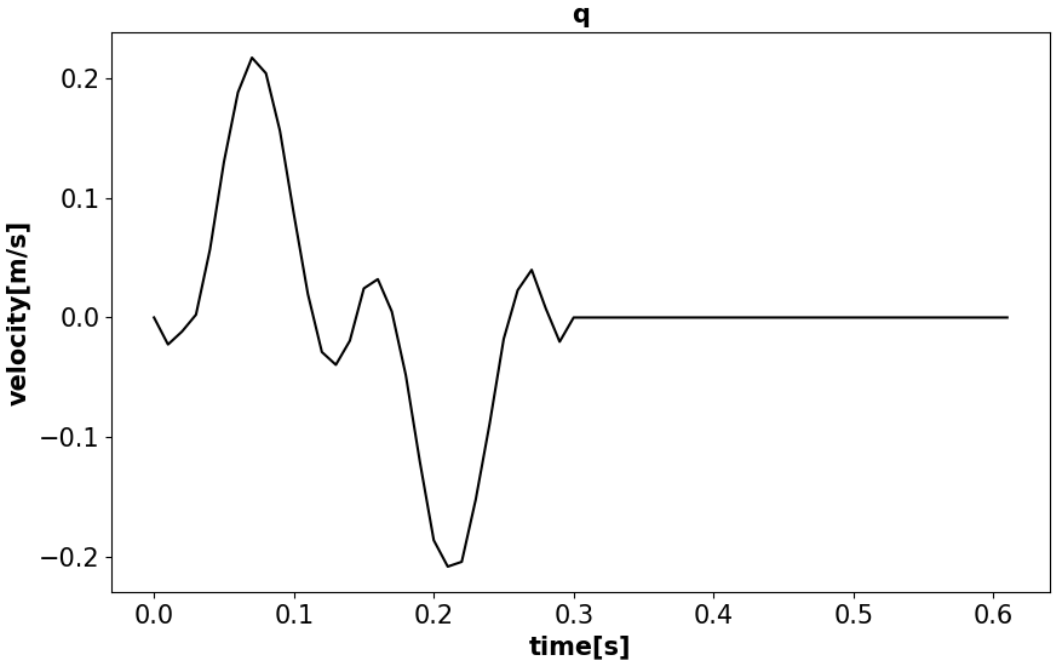
q
velocity[m/s]
time[s]
0.2
0.1
0.0
−0.1
−0.2
0.0
0.1
0.2
0.3
0.4
0.5
0.6

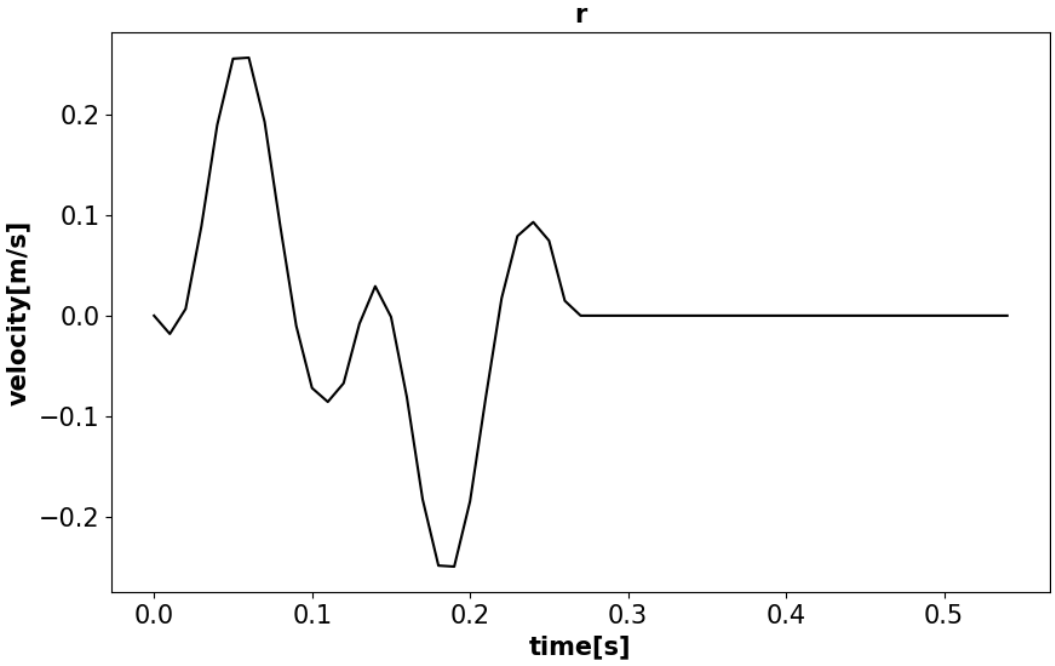
r
velocity[m/s]
time[s]
0.2
0.1
0.0
−0.1
−0.2
0.0
0.1
0.2
0.3
0.4
0.5

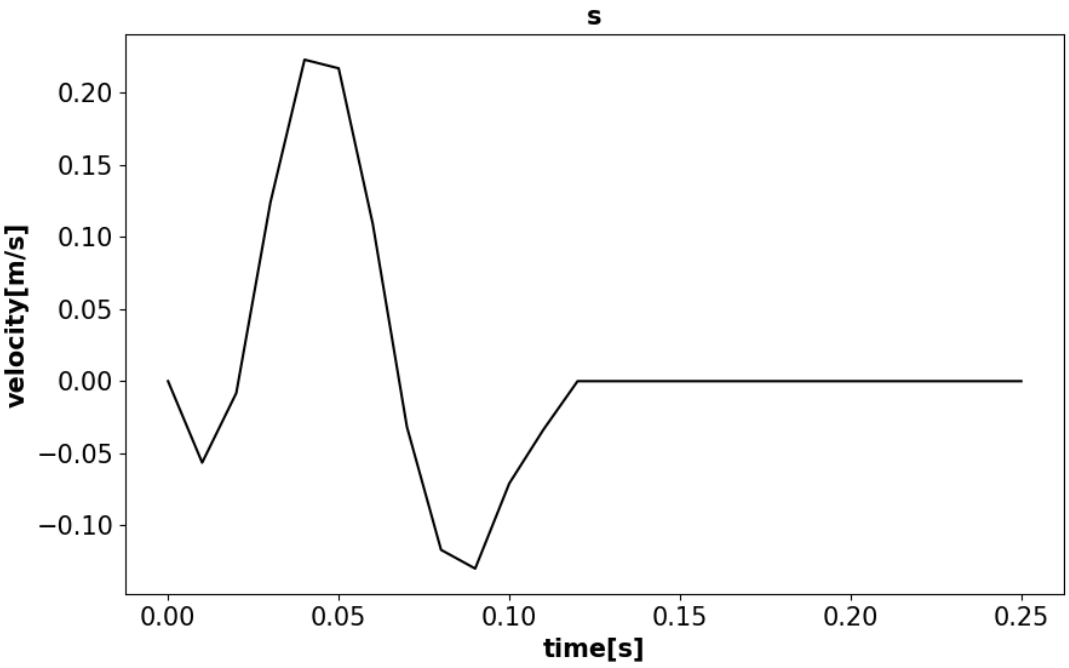
s
velocity[m/s]
0.20
0.15
0.10
0.05
0.00
−0.05
−0.10
0.00
0.05
0.10
0.15
0.20
0.25
time[s]